Thèse
de doctorat
de l'UTT

Ali RIDA

Study of the Mechanical Properties of Nanocrystalline Materials by Molecular Dynamics Simulations

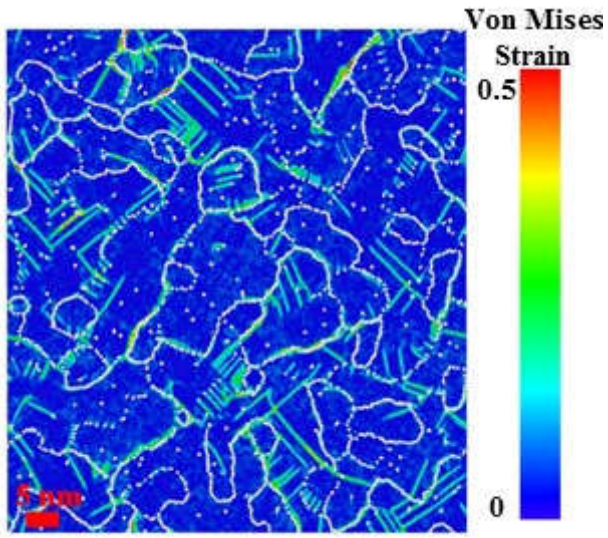

Champ disciplinaire :
Sciences pour l'Ingénieur

2018TROY0031

Année 2018

utt
UNIVERSITÉ DE TECHNOLOGIE
TROYES

THESE

pour l'obtention du grade de

DOCTEUR
de l'UNIVERSITE DE TECHNOLOGIE DE TROYES

EN SCIENCES POUR L'INGENIEUR

Spécialité : MATERIAUX, MECANIQUE, OPTIQUE, NANOTECHNOLOGIE

présentée et soutenue par

Ali RIDA

le 5 octobre 2018

Study of the Mechanical Properties of Nanocrystalline Materials by Molecular Dynamics Simulations

JURY

M. M. PEREZ	PROFESSEUR DES UNIVERSITES	Président
M. O. POLITANO	MAITRE DE CONFERENCES - HDR	Rapporteur
Mme A. TANGUY	PROFESSEURE DES UNIVERSITES	Rapporteure
M. R. BRENNER	DIRECTEUR DE RECHERCHE CNRS	Examinateur
M. R. PELLENQ	SENIOR RESEARCH SCIENTIST	Examinateur
M. Y. YUE	PROFESSOR	Examinateur
M. M. MICOULAUT	PROFESSEUR DES UNIVERSITES	Directeur de thèse
Mme E. ROUHAUD	PROFESSEURE DES UNIVERSITES	Directrice de thèse

Personnalité invitée

M. A. MAKKE	CHERCHEUR	Directeur de thèse

Acknowledgements

This thesis could not have been finished without the help and support from many people. Herein, it is my great pleasure to acknowledge them.

Foremost, I would like to express my sincere gratitude to my advisors Prof. Emmanuelle Rouhaud, Prof. Matthieu Micoulaut and Dr. Ali Makke for their constant guidance and continuous support throughout my Ph.D. study. Their immense knowledge, experience, and encouragement helped me all the time including building this thesis from the first draft to the last version. Also, I would like to thank them for supporting me in broadening my understanding of related fields and presenting this project in international conferences and workshops, as well as for providing advice on my personal development and career.

My sincere thanks are extended to Prof. Anne Tanguy, and Dr. Olivier Politano for their time in reviewing this manuscript. I also thank Prof. Rolland Pellenq, Prof. Yuanzheng Yue and Dr. Renald Brenner for joining the examination committee, and to Prof. Michel Perez for chairing the examination procedure. They provided me with their insightful comments and suggestions, and let my defense be an enjoyable moment.

I also would like to thank all the members of the LASMIS team of the ICD laboratory for their support and friendship. They made contributions in many ways: sharing knowledge, providing advice and support, and creating a pleasant atmosphere in the group. I also thank the UTT doctoral school, in particular, the director Khemais Saanouni, and the secretaries Pascale Denis, Isabelle Leclercq, and Thérèse Kazarian.

My thanks go to all my colleagues and all the friends I made during these last three years. Words cannot express my infinite love and gratitude for all of you. Thank you for your patience and encouragement throughout this thesis!

Finally, I would like to thank my family for all their love and encouragement. For my parents Samar and Hussein who raised me with their unwavering love, for my sisters Rana and Roua for always supporting me unconditionally throughout my entire life, for my brother Hassan for always managing to put a smile on my face, they are appreciated. I love all of them forever.

Abstract

Polycrystalline materials with crystallite diameters below hundred nanometer are called nanocrytsalline materials. These materials are found to exhibit extraordinary strength which goes along with a decrease in ductility. In order to tailor tough materials, which combine strength and ductility, the underlying deformation mechanisms have to be understood. As a result, considerable effort has been spent on the characterization of possible new deformation mechanisms that give rise to this remarkable response of nanocrystalline materials. To this aim, in this dissertation molecular dynamics simulations are performed to extend the understanding of the fundamental deformation mechanisms which mediate the plasticity in bulk nanocrystalline materials.

In the first part of this thesis, a recent melting cooling method has been applied to generate initial numerical atomic configurations for molecular dynamics simulations. This method produces realistic samples that contain point and line defects inside the grains such as dislocations, vacancies and interstitials. The curvature of the grain boundaries is one of the additional advantage of this method in comparison with the standard polycrystalline geneation methods such as the Voronoï tessellation method.

The second part investigates the influence of the mean grain size on the mechanical behavior of nanocrystalline FCC Copper and HCP α-Titanium. The melting cooling method has been used to generate an initial columnar nanocrystalline Copper with variable mean grain size, whereas the Voronoï tessellation method has been used to generate initial full 3D nanocrystalline α-Titanium. The results of uniaxial tensile tests applied to these systems reveal the presence of a critical mean grain size d_c = 16 nm for Copper and 15 nm for α-Titanium, for which there is an inversion of the conventional Hall-Petch relation. A combination of dislocations, twinning and grain boundaries mediated processes (Atomic shuffling, grain boundary and triple junction migrations, grain coalescence) control the deformation behavior of the samples. In addition, a new deformation mechanism has been found where edge dislocations present inside the grains from the cooling process propagate on specific planes generating shear bands inside the grains.

Strain rate studies of polycrystalline materials can, furthermore, provide

information on atomic scale mechanisms in tensile strain experiments. In the third part of this manuscript, we used the simulations to investigate the influence of the strain rate on the mechanical properties of nanocrystalline Copper systems. Series of uniaxial tensile tests were performed at 3 orders of magnitude strain rates lower than that usually used in atomic simulations ranging from 10^4 to $10^9 s^{-1}$. We found that above a certain value ($\dot{\varepsilon} \geqslant 5.10^5 s^{-1}$), the system is not able to equilibrate with the ongoing deformation over the ns timescale. This observation is confirmed by relaxation tests in the elastic and the plastic regime. The time evolution of the stress suggests features that are typical of glassy relaxation with a stretched exponential behavior for the stress relaxation that is only encountered for large deformation rates.

Furthermore, the increase of the flow stress with the strain rate is attributed to the delay in the onset of dislocation propagation while increasing the strain rate. The sensitivity of the latter and the flow stress activation volume are calculated, and their values are found to be consistent with experiments. The enhancement of the strain rate sensitivity confirms the increase of the contribution of grain boundary mediated mechanisms to plasticity in nanocrystalline materials.

Finally, the influence of the strain rate on dislocations, twinning and grain boundaries processes has been investigated on the atomic level. An increase of the fraction of perfect dislocations is evidenced with the decrease of the strain rate. However, at high strain rate, a transition from partial dislocations to twinning is predicted whereas grain growth mechanism appears to be limited at high strain rate.

KEYWORDS: Molecular dynamics, Nanostructured materials, Dislocations in metals, Plasticity, Grain boundaries, Materials - - Mechanical properties

Contents

List of Figures

List of Tables

Introduction

Motivation

The landmark paper by Gleiter [1] reoriented the global research efforts in materials science to nanocrystalline materials. The mechanical behavior of these materials has become the subject of widespread research over the past couple of decades. Nanocrystalline materials are polycrystals with a mean grain size less than 100 nm. The microstructure of these materials is characterized by a large volume fraction of grain boundaries which alter their mechanical properties in comparison with their conventional coarse-grained counterparts with a mean grain size higher than 1 μm [2–6]. As the mean grain size decreases, the strength of the material increases which is known as the Hall-Petch relation [7, 8]. The paradigm "Smaller is Stronger" has created routes to ultra-high-strength materials. The pile-up of dislocations to grain boundary is considered as the main deformation mechanism in coarse grained materials. With a further decrease of grain size, the fraction of grain boundary increases. Thereby, the motion of dislocations is impeded by grain boundary which causes the strengthening of the material. However, several models predict a breakdown of the pile-up mechanism in nanocrystalline metals [9, 10]. With even further grain refinement, some experiments evidence even a softening of the material this is called " inverse Hall Petch " [11–13].

Nanocrystalline materials are found to have high strength/hardness [12, 14–17], improved toughness, and enhanced diffusivity [18]. However, the high density of grain boundary reduces the elastic modulus and the ductility of these materials. The idea of a material with a gradient of grain size along the depth going from nanometer to micrometer is a compromise between strength and ductility. In such way, the surface of the material which is the origin of failure initiation is hardened. While the bulk of the material conserves its ductility. To this aim, Surface Mechanical Attrition treatment (SMAT) has been recently developed. This surface treatment technique leads to a nanocrystalline layer on the surface of metallic materials [19–21]. To date, this technique has been

successfully applied in achieving surface nanocrystallization in a variety of materials either pure metals, alloys or steels [19–23]. The understanding of the deformation mechanisms of each layer allows establishing a direct link between the process parameters (e.g. frequency of impacts, the velocity of the shots...) and the resultant microstructure (e.g thickness of the nanocrystalline layer, mean grain size in the nanocrystalline layer ...). This relation allows the optimization of the parameters of the process as a function of the desired microstructure and the mechanical properties. Therefore, the study of the mechanical behavior of nanocrystalline materials is indispensable to establish constitutive models that describe the deformation mechanisms in these materials.

Molecular dynamics simulations have the ability to describe the evolution of a system of atoms in real time which is not possible experimentally. This technique has been widely used to elucidate and exploit the deformation behavior of nanocrystalline materials [24–26]. Molecular dynamics simulations showed significant grain boundary activity during the deformation of nanocrystalline atomistic models [27–29]. Grain rotation [30, 31], grain boundary migration, triple junction migration [32, 33], and discrete atomic diffusive events in the interface such as atomic shuffling and stress assisted free volume migration have been reported in nanocrystalline materials [34, 35]. Moreover, molecular dynamics simulations showed that the grain boundaries are the sources and sinks to dislocations in nanocrystalline materials [36, 37]. The reported dislocations are of Shockley partial type or perfect dislocations dissociated on two Shockley partials [36, 38].

The interplay between these deformation mechanisms is still controversial. This justifies the lacking of a precise constitutive model to describe each mechanism. For example, the nucleation and absorption of dislocation at the grain boundary are found to engender large discrete atomic activities at this boundary (e.g. atomic shuffling and stress assisted free volume migration) [27, 35]. Also, a great influence of the initial sample in molecular dynamics simulations on the above mechanisms indicates the possibility of the presence of other mechanism limited by these samples. For example, curvature driven grain boundary migration and grain growth are not yet elucidated by molecular dynamics simulation since the initial configuration is generated with straight grain boundaries (by Voronoï tessellation).

Therefore, there is a need for more realistic initial nanostructures for deformation tests in molecular dynamics.

The mechanical properties of nanocrystalline materials have been reviewed many time [5, 6, 39–41], but the current understanding of the deformation mechanisms of such materials is still controversial. The deformation behavior in nanocrystalline materials is strongly dependent on the grain size, the temperature, the nanostructure (grain size distribution, grains shapes), and the strain rate. The study of these parameters uses usually an experimental approach to investigate the underlying deformation mechanism of nanocrystalline materials. The objective of this thesis is to develop a better understanding of the influence of these parameters on the deformation mechanisms presented above using molecular dynamics simulations.

Outline of the thesis

This thesis consists of 5 chapters and it is organized as follows:

In Chapter 1, the SMAT process and the characteristic of the smatted materials have been presented followed by a review of the experimental and the molecular dynamics simulations studies of the mechanical behavior of nanocrystalline materials.

In Chapter 2 the basic theory of molecular dynamics simulations and the main analysis techniques at the atomic level are introduced. Also, the validation of the used interatomic potentials has been presented. Finally, a description of the recent melting-cooling method applied to generate the initial atomic nanocrystalline samples is shown.

In Chapter 3 the influence of the grain size on the mechanical properties and the deformation mechanisms of nanocrystalline Copper and α-Titanium is investigated. Moreover, the mechanical behavior of different nanostructured Copper (quasi-2D, Columnar 3D, and 3D) have been compared. The deformation mechanisms are also analyzed at the atomic level.

In Chapter 4 the strain rate dependence of the mechanical behavior of two kinds of nanocrystalline Copper (columnar 3D and quasi-2D) samples with 9 nm mean grain size have been investigated. The equilibrium of the system on

the timescale of molecular dynamics has been elucidated by a series of relaxation tests in the elastic and the plastic regime. Finally, the rate dependence of each deformation mechanism is studied and analyzed at the atomic level.

In Chapter 5 the main conclusions and the perspectives for future works are given.

Chapter 1

Literature Review

Contents

1.1 Surface mechanical attrition treatment

Surface Mechanical Attrition Treatment is a surface plastic deformation process to generate a nanocrystalline layer on the surface of a metal with coarse grained polycrystalline microstructure. This process is based on surface severe plastic deformation induced by repetitive impacts of spherical shots with high velocity on the surface of the material in treatment.

Figure 1.1 (a) illustrates the SMAT process. Spherical shots are contained in a treatment chamber and are propelled by a vibrator called "sonotrode". The size of these shots is between 1 to 10 mm, whereas their impact velocity is between 1-20 m/s depending on the vibration frequency which is in the order of 50 to 20000 Hz. The incidence angle of the shots with respect to the sample surface is random, which facilitates the grain refinement of the surface layer. The high frequency or velocity of impacts leads to a high plastic deformation on the surface because of the partial indentation of shots in the surface at large strain rate in the order of (10^2 to 10^4 s^{-1}) [43] . The impact of each shot on

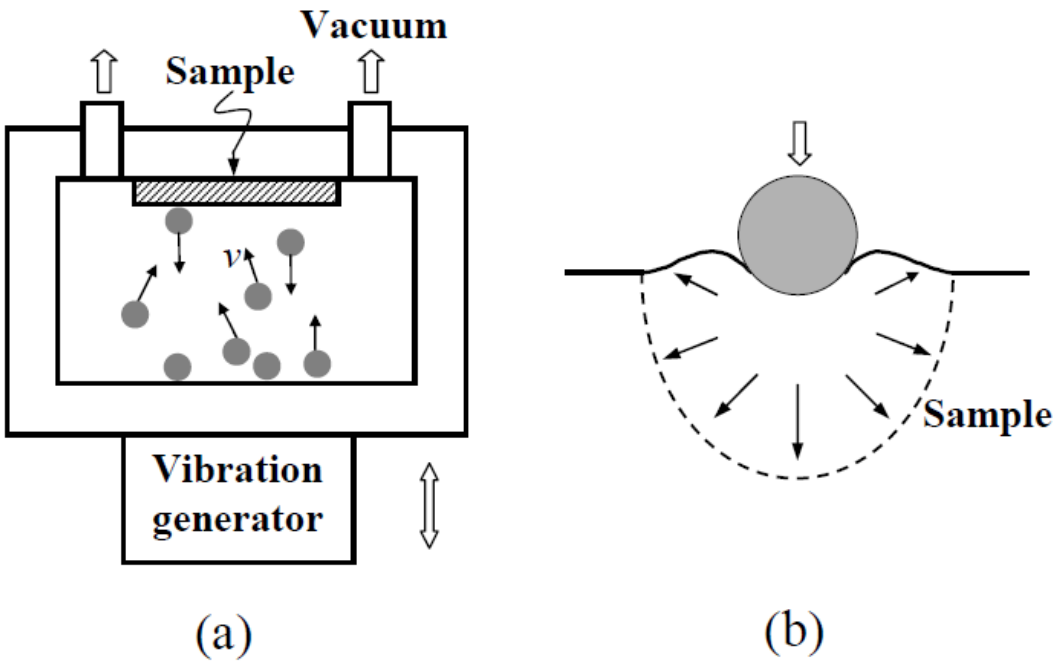

FIGURE 1.1: (a) Schematic representation of the SMAT process, (b) The localized plastic deformation on the surface caused by the impact of a shot [42].

the specimen generates severe local plastic deformation (dimple) as seen in Figure 1.1 (b). Therefore, the material tries to regenerate its original shape thereby producing a compressive residual stress field just below the surface which increases the fatigue strength of the material [44].

1.1.1 Microstructure of the smatted samples

A nanocrystalline layer has been successfully generated in the surface of pure metals and alloys by means of SMAT (Fe [19], Copper [45], Titanium [46], Al-Alloy [22, 23], Stainless steel [20, 47]). These studies have found that the average grain size and the thickness of the nanocrystalline layer depend on the processing conditions (the treatment duration, the shots velocities...), and the treated materials (crystal structure, stacking fault energy) [42]. In SMAT, even if the plastic strain is high, its influence does not exceed a few hundred of micrometer in the depth. This layer has a strong gradient of grain size going from hundreds of nm at the surface of the material to 1μm in the bulk (*i.e.* the non-affected region by treatment) as shown in Figure 1.2. The schematic plot shows the evolution of the strain and the strain rate with respect to the depth. The high strain and strain rate are located at the surface, thus nanocrystalline layer is generated. Below the surface, these quantities (the strain and the strain rate) start to decrease progressively to reach zero. Therefore, this type

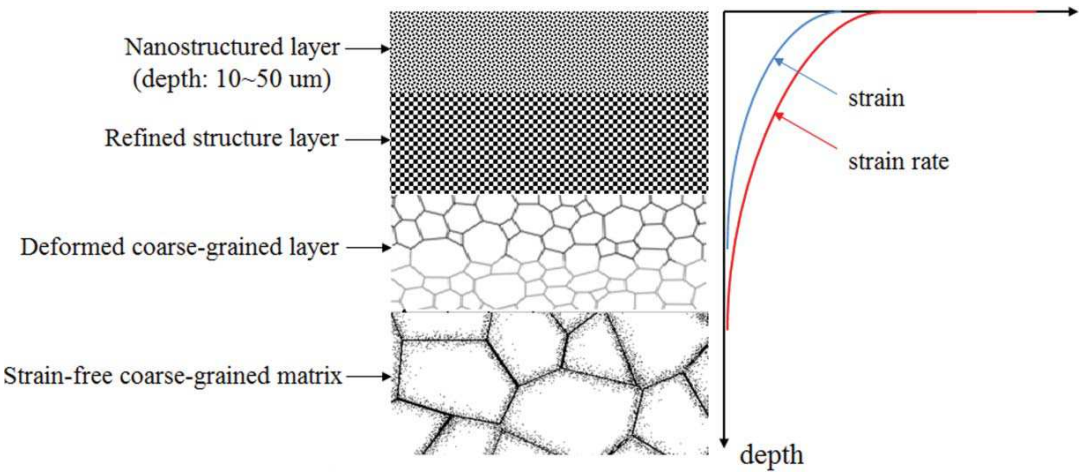

FIGURE 1.2: Schematic illustration of microstructure characteristics and the distributions of strain and strain rate with respect to the depth in a surface layer subjected to SMAT [43].

of microstructure is a comprise between high hardness and acceptable ductility because of the difference in grain size between the surface and the core of the material [48].

1.1.2 Grain refinement mechanisms in SMAT

The microstructural evolution and the formation of the nanocrystalline layer have been investigated several times [19, 20, 22, 23, 45, 46, 49]. Two formation mechanisms were found and related to the stacking fault energy of the metal: (i) Deformation via dislocation slip for high stacking fault energy, (ii) Deformation via dislocation slip and mechanical twinning for low stacking fault energy.

For high stacking fault energy materials such as BCC iron Fe, dislocations slip and dislocations interactions are responsible for the grain refinement [19]. Figure A.3 (a) shows the mechanism of grain refinement observed in Fe. Firstly, the high strain and strain rate at the surface of the material will generate a large density of dislocations. These dislocations will be organized in a dense dislocation walls along (110) slip planes (Figure A.3 $A1$) or will interact between each other to form dislocation tangles in the original coarse grains (Figure A.3 $B1$). Due to the high value of strain rate, the annihilation process is lower than the nucleation process of dislocations, therefore, a large density of dislocation is present inside the grains. These dislocations are accumulated and rearranged to minimize the total energy state in the form of dense dislocation walls. In addition, the random angle of impact of the shots induces the activation of different slip systems. Consequently, the coarse grains will

be divided into small regions bounded by dense dislocation walls or dislocation tangles (Figure A.3 $A1$ and $B1$).

Secondly, when the dislocation density is stabilized with deformation (i.e the dislocations nucleation and annihilation are balanced); Dense dislocation walls and dislocation tangles will be transformed into sub-boundaries with small misorientation (Figure A.3 $A2$ and $B2$). Thirdly, the sub-boundaries evolve into highly misoriented grain boundaries because of the rotation of these subgrains induced by the accumulation and annihilation of dislocations on the sub-boundaries (Figure A.3 A_3 and B_3). With further increase of strain, dense dislocation walls and dislocation tangles could also divide the subgrain generated in the previous deformation to finer subgrains (Figure A.3 $AA3$ and $BB3$).

For low stacking fault materials such as FCC Copper, a combination via dislocations slip and mechanical twinning have been found as the main refinement mechanism [45] . The high strain rate induced by the high-speed shots impacts on the surface leads to a stress concentration in the surface which exceeds the critical stress of twin nucleation. As a consequence, there is a large density of twin boundaries in the surface. These twin boundaries decompose the coarse grains into lamellar twin-matrix blocks with a nanometer-sized thickness as seen in Figure A.3 (b) (i). Then, these lamellae are divided into rhombic blocks because of the interaction of two twins with different slip system or to the interaction between dislocation arrays and twins. After that, the high strain and strain rate of the deformation induce the formation of small angle boundaries from these blocks with a size of few nanometers. Finally, these blocks transformed into small grains with high misorientation angle due to twin-twin interaction and/or twin-dislocation interaction.

1.1.3 Tensile strength of the “smatted” samples

The mechanical properties of smatted samples show an increase in the hardness and the tensile strength [45, 48, 49]. Figure 1.4 shows the stress-strain curves of a stainless steel treated by SMAT at different SMAT timespan conditions. Compared with the untreated samples, the Smatted samples shows three significant modifications in their mechanical properties: (i) high value of yield stress and ultimate stress, (ii) less pronounced strain hardening and (iii) the ultimate strain decreases which means that the material becomes less ductile. This increase of the yield and ultimate strength is related to the nanocrystalline layer induced by SMAT [48].

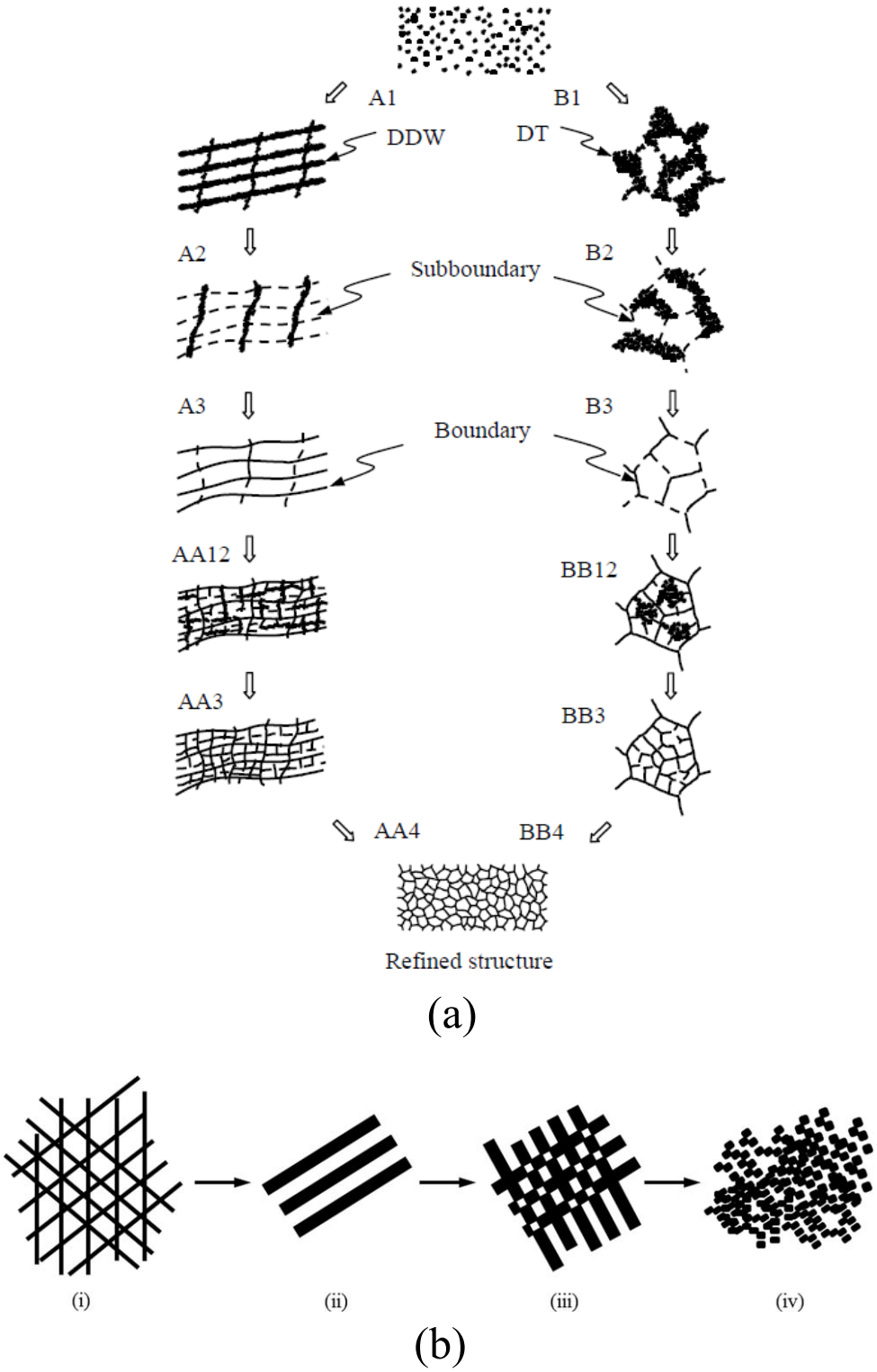

FIGURE 1.3: (a) Schematic illustration of the grain refinement mechanism in Fe [42], (b) An illustration showing the grain refinement in the materials with a plastic deformation induced by mechanical twins and dislocations: (i) formation of planar dislocation arrays, (ii) formation of twins, (iii) interaction of dislocations with mechanical twins, and (iv) formation of refined grains with random orientations [43].

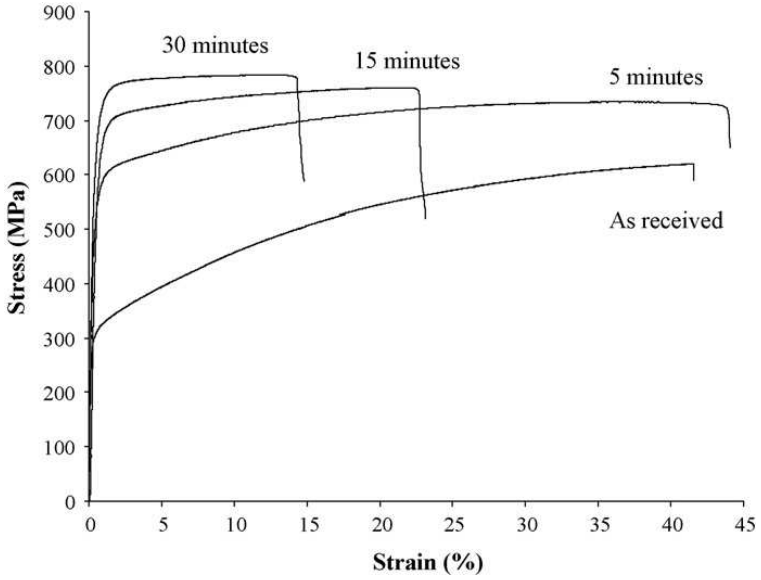

FIGURE 1.4: Tensile stress-strain curves obtained for different SMAT timespans of stainless steel [48].

1.2 Nanostructured and Nanocrystalline materials

Nanostructured Materials are materials with a sub-microstructure of a characteristic length scale on the order of a few nanometers (1-100) nm. A classification of nanostructured materials (see Figure 1.5) , based on their chemical composition and crystallite geometry, was proposed in Gleiter's pioneering work [50]. Nanostructured materials can be divided into three families: (1) layer-shaped, (2) rod-shaped, and (3) equiaxed crystallites as shown in Figure 1.5. For each family the chemical composition of the crystallites in one structure can be the same or different. Also, the chemical composition of the crystallites can be different from that of the boundaries or the interphase between crystallites. Finally, the crystallites can be dispersed in a matrix with a different composition.

Nanocrystalline materials is a kind of nanostructured material with equiaxed crystallites called grains. The grain size is less than 100 nm. Three constituents compose nanocrystalline materials: (1) grain cores also referred to as crystallites, (2) grain boundaries, and (3) triple junctions also referred to as triple lines. Grain cores exhibit a crystalline structure (e.g., Face Center Cubic FCC, Hexagonal Compact HC, Body Center Cubic BCC). Grain boundaries correspond to the regions of the junction between two grains. This means that

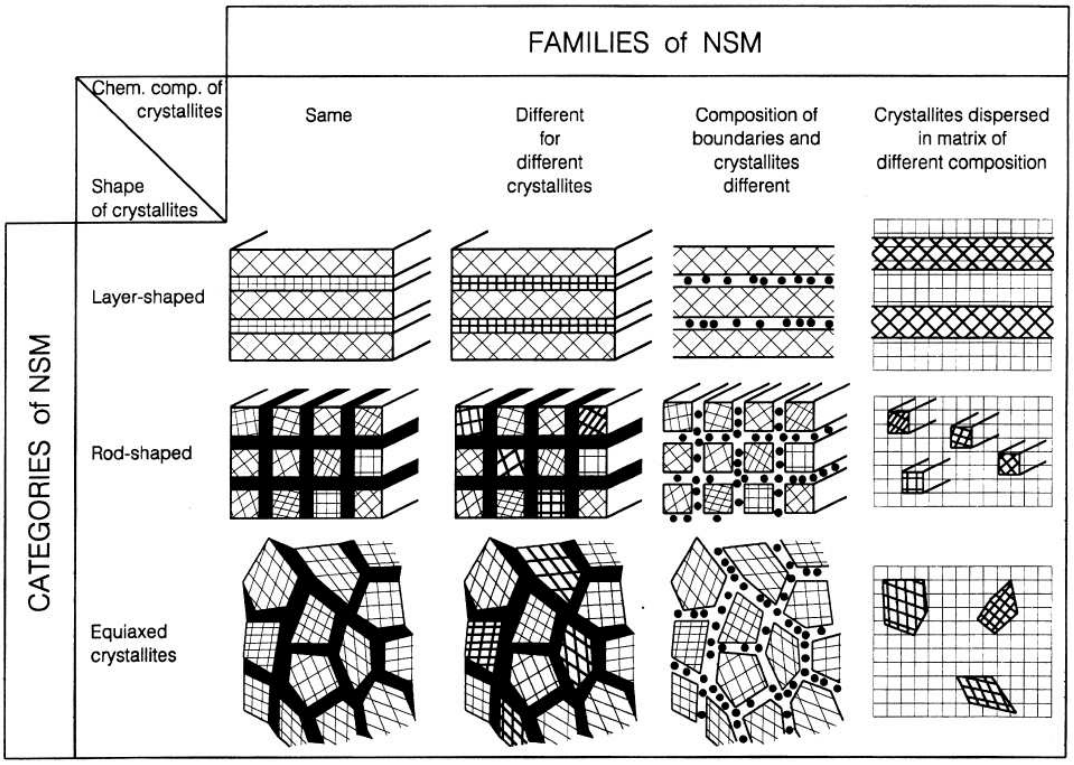

FIGURE 1.5: Classification of the nanostructured materials according to their chemical composition and the dimensionality (shape) of the crystallites (structural elements) forming the nanostructured materials. The boundary regions of the first and second family of nanostructured materials are indicated in black to emphasize the different atomic arrangements in the crystallites and in the boundaries. The chemical composition of the black boundary regions and the crystallites is identical in the first family. In the second family, the black boundaries are the regions where two crystals of a different chemical composition are joined together [50].

a decrease in the grain size leads to an increase in the volume fraction of the grain boundaries.

1.2.1 Mechanical properties of nanocrystalline materials

1.2.1.1 The elastic modulus

The elastic response of a material is directly correlated to its atomic structure as depicted previously. The volume fraction of the grain boundary increases with the decrease of the mean grain size. As the structure of the grain boundaries is different from the perfect crystal lattice, it is obvious to expect a size effect in the elastic response of nanocrystalline materials. Also, because of the increase of the fraction of the grain boundaries having a density lower than that of the grain interior one can expect a decrease in the elastic modulus of nanocrystalline materials. Nieman *et al* reported a reduced Young's modulus

(E) for nanocrystalline Copper and Pd with a grain size between 5 to 50 nm prepared by inert gas-condensation/vacuum consolidation [14]. They related this decrease of E to the porosity in these samples. Sanders *et al* also reported a decrease of Young's modulus for nanocrystalline Copper and Pd Samples with grain sizes of 10 - 100 nm. These samples have been produced by inert-gas condensation and warm compaction. Also, the density of these samples is greater than 98% [12]. Shen *et al* measured Young's modulus of nanocrystalline Fe, Copper, Ni, and Cu-Ni alloys prepared by mechanical milling/alloying using the nanoindentation technique. They found that Young's modulus of nanocrystalline Copper, Ni, and Cu-Ni alloys with a grain size ranging from 17 to 26 nm are similar to those of their corresponding polycrystals [51]. Figure 1.6 shows a summary of the experimental results found for different nanocrystalline materials elaborated by different conception methods. An ambiguity is still present regarding the elastic modulus of nanocrystalline materials measured experimentally due to the difference in the sample porosity, artifacts, and impurities.

Molecular dynamics simulations carried out by Gao *et al* showed that the grain boundary deforms more locally compared with the grain core region under thermal vibrations and is elastically less stiff than the core component at finite temperature. The elastic modulus of the grain boundary is found to be more than 70% lower than that of the grain interior [52]. Valat *et al* [53] performed a series of deformation tests (compression, tensile and shear tests) on nanocrystalline tungsten samples presenting various microstructures with a mean grain size between 2.7 and 6.7 nm. They found that both Young's modulus and the shear modulus decrease by over 60% as the average grain diameter decreases below 3 nm. They related this decrease to the grain boundary volume fraction.

1.2.1.2 The ductility

Ductility is the ability of a material to change irreversibly its shape without fracture. It is of critical importance for engineering materials in both manufacturability and performance. Measures of ductility include the percent of elongation (uniform plastic flow prior to mechanical instability necking or fracture) and the decrease in cross-section. In the conventional grain size regime, usually, a reduction in grain size leads to an increase in ductility. Thus, one should expect that the ductility increases as the grain size decreases to reach the nanoscale [55]. However, nanocrystalline materials often exhibit low

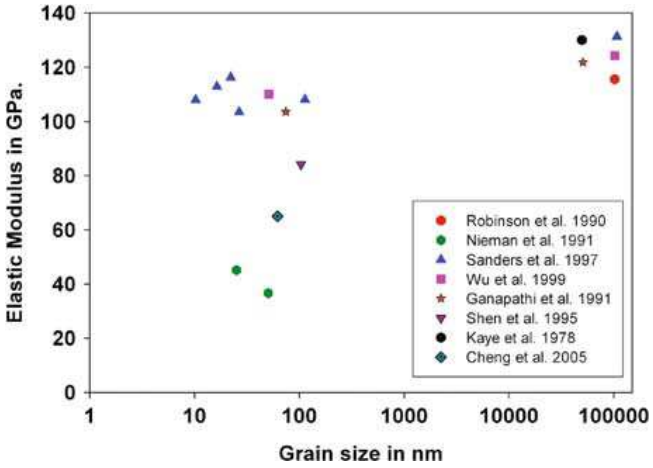

FIGURE 1.6: Experimental measurements of the Young's modulus as a function of grain size[54].

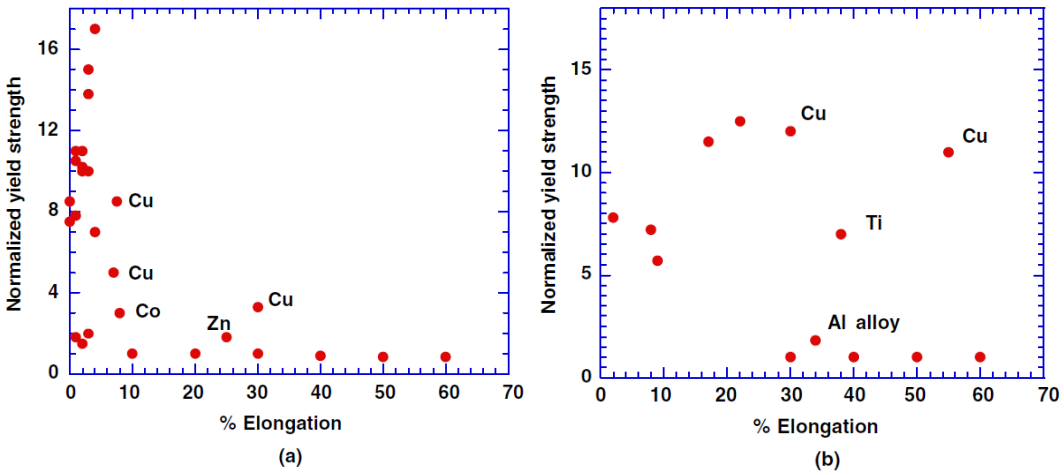

FIGURE 1.7: Normalized yield stress versus % elongation (a) for nanocrystalline materials, (b) ultrafine grained metal [5].

tensile ductility at room temperature because of the poor sample quality, which limits their practical utility. The ultimate strain of nanocrystalline materials is typically less than a few percents. The experimental results about the ductility of single-phase nanocrystalline materials indicated little ductility in tension for grain sizes less than about 25 nm [5].

Figure 1.7 shows the normalized yield strength [1] versus the percentage tensile elongation for metals with grain sizes in the nanocrystalline range and ultrafine grained metals. There is a clear decrease in the ductility while the strength increases for nanocrystalline materials. However, ultrafine grained materials Figure 1.7 (b) exhibit an increased yield strength along with good

[1]The ratio of the yield strength of nanocrystalline or ultrafine grained metals over the yield strength of the bulk polycrystalline metal

ductility in comparison to nanograined materials. Weertman and co-workers have studied the tensile behavior of high density and high purity nanocrystalline Copper and Pd with a mean grain size going from 10-110 nm. The yield strength of nanocrystalline Copper and Pd was from 10 to 15 times greater than that of the annealed coarse-grained metals. For samples with grains size below 50 nm, the ultimate strain does not exceed the 4%. Whereas for the sample with grain size of 110 nm the ultimate strain reaches 8% [12]. Wang *et al* described a thermomechanical treatment of Copper that results in a bimodal grain size distribution, with micrometer-sized grains embedded inside a matrix of nanocrystalline and ultrafine grains. The inhomogeneous microstructure leads to a strain hardening behavior that increases the ductility of the material [56].

Until now, there has been a debate about the potential causes of the low tensile elongation in nanocrystalline materials. However, it has been demonstrated that the mechanical properties of nanocrystalline materials are strongly dependent on the internal structure and impurities (i.e. porosity, defects...) [12].

1.2.1.3 The strain hardening rate

Basically, the hardening in a crystalline and polycrystalline structure occurs because these materials deform plastically through the irreversible movement of dislocations. These latter interact directly among themselves, with the grain boundaries and with other imperfections. Dislocations can also interact indirectly with the internal stress field of various imperfections and obstacles. All these interactions lead to a reduction in the mean dislocations mobility. Therefore, the dislocations require a greater stress to accomplish further movement (i.e., with continuing plastic deformation, we need to apply a greater stress for further plastic deformation); hence the phenomenon of work-hardening (strain hardening).

In nanocrystalline materials, there is no strain hardening or rapid strain hardening over a small plastic strain regime (1–3%), which is different from their coarse-grained counterparts. The main cause of the absence of strain hardening is the dynamic recovery or the annihilation of dislocations at grain boundary. In nanocrystalline materials, grain boundaries act as sources and sinks to dislocations [5]. Therefore, a competition between the generation of

dislocations during plastic deformation and the annihilation during stress recovery determines the steady-state dislocation density.

1.2.1.4 The strain rate sensitivity

The understanding and the prediction of the mechanical properties of materials imply a detailed knowledge of the elementary mechanisms that govern the plastic behavior at atomic scale. In particular, those which control the dislocation mobility and how this mobility changes under the influence of stress, strain rate, and temperature. The sensitivity of the deformation mechanisms to the change in the imposed strain allows one to analyze the strain rate threshold that limits these mechanisms. The transient testing is a suitable method to evaluate the response of the material to the variation of the stress or strain rate. Two main methods can be applied in a transient test:

1. The variation of the strain rate once the material is in a plastic flow. This is called strain rate jump test [57–59].

2. The applying of a sudden change in the imposed stress. This is followed by a stress relaxation i.e. the plot of the variation of strain at constant stress and then the variation of the strain rate is calculated as a function of stress [60, 61]. This is called stress transient test.

Two main parameters can be extracted from these tests: (i) the strain rate sensitivity (m) and (ii) the activation volume (V^*). They are defined as:

$$m = \frac{\partial \ln(\sigma)}{\partial \ln(\dot{\varepsilon})} \tag{1.1}$$

$$V^* = \sqrt{3} k_B T \frac{\partial \ln(\dot{\varepsilon})}{\partial \sigma} \tag{1.2}$$

$$m = \frac{\sqrt{3} k_B T}{\sigma V^*} \tag{1.3}$$

where k_B is the Boltzmann constant, T the temperature in $^\circ K$, $\dot{\varepsilon}$ the strain rate, and σ the flow stress.
These parameters (m and V^*) depend on the active deformation mechanism in the polycrystalline material.

A series of experimental studies have investigated the strain rate dependence of the flow stress in nanocrystalline materials. A strong dependence of m and V^* on grain size have been distinguished. For FCC nanocrystalline metals. Very low values of V^* have been found in the order of $1b^3 - 20b^3$ (b is the Burger's vector length.) as well as an increase of m one to two orders of

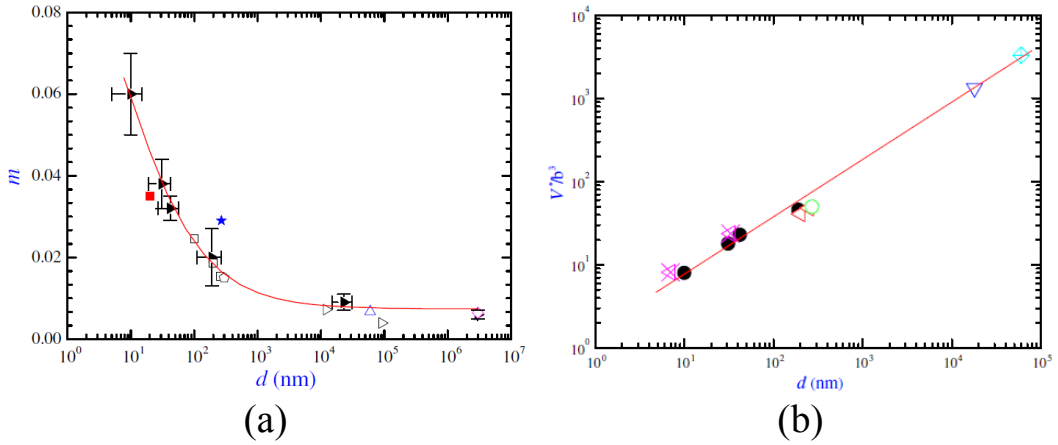

FIGURE 1.8: Summary of the experimental data from the literature of the variation of (a) m and (b) V^* as a function of d for Copper [15].

magnitude than coarse-grained materials [16, 17, 62]. These authors suggest that grain boundaries have a significant contribution to the plastic deformation and they proposed a transition from dislocations-dislocations interactions to dislocations-grain boundaries interactions. Also, it has found that m increases with the decrease of the mean grain size. Figure 4.9 (a) shows the variation of m with the grain size down to the nanoscale regime. Despite some inconsistencies in the absolute values of m due to different synthesis techniques or different testing methods, a consistent trend has been found. The value of m increases with the decrease of mean grain size d from the macro to the nanoscale [15]. Figure 4.9 (b) shows the variation of V^* with respect to the grain size down to the nanoscale regime. A clear decrease of V^* with the grain size from thousands of b^3 for coarse-grained to $1-50b^3$ for nanocrystalline materials. In coarse-grained materials, forest lattice dislocations interaction is the main deformation mechanism. These dislocations are nucleated from Frank-Read sources and piled-up to grain boundary. Therefore, large V^* corresponds to the localization of the plastic deformation inside the grains by means of propagating dislocations. Whereas, a small contribution of grain boundary to plastic deformation leads to a small value of m. While going down to the nanoscale, the dislocations nucleation from Frank-Read sources is no longer valid [63]. The plastic deformation becomes localized on grain boundaries that act as sources and sinks to dislocations as mentioned above. Consequently, the V^* decreases and the m increases.

Molecular dynamics simulations have been used to investigate the effect of strain rate on the deformation behavior of nanocrystalline FCC metals [24, 25,

28, 29, 64]. Brandl *et al* found that when the strain rate is decreased by two orders of magnitude (10^7 to $10^9 s^{-1}$) the flow stress decreases and cross-slip occurs frequently in nanocrystalline Aluminium [29]. They suggest that at this strain rate the grain boundary cannot assimilate all arriving dislocations. Also, they reported that cross-slip facilitates the depining process of the full dislocation in nanocrystalline Al. Recently, Dupraz *et al* [37] applied a series of stress drop test to 3D nanocrystalline Al with 12 nm mean grain size by molecular dynamics simulations. They found that at reduced strain rates ($10^6 s^{-1}$ in molecular dynamics), dislocations can propagate using low Schmid factor slip system, a mechanism that requires significant grain boundary assimilation processes. The high strain rates commonly used in molecular dynamics simulations make it however very challenging to determine the rate-limiting deformation mechanisms occurring in experiments timescale. It has been shown that the application of higher strain rates results in higher flow stresses. Under such a stress and as grain boundary accommodation mechanisms are mainly stress-driven [64], the dislocations are enabled to propagate athermally [29].

However, in molecular dynamics simulations, the strain rate used is very high in the order of $10^7 s^{-1}$ to $10^{10} s^{-1}$ because of the small time-window of these simulations (1-5 fs). The short timescale of molecular dynamics and the high strain rate in these simulations limits their capacity to investigate the deformation mechanisms that take place at low strain rate such as diffusion process. On the other hand, the main advantage of these simulations is the description of the trajectory of the atoms in the configuration in real time. This allows one to analyze the evolution of the plastic deformation mechanisms at the atomic level.

To overcome this restriction, Yamakov *et al* [65] performed molecular dynamics simulations on nanocrystalline Pd at elevated temperature. A distinct grain boundary diffusion creep was identified. However, Van Swygenhoven *et al* [66] indicates that the activation energy and the strain rate calculated by Yamakov *et al* are calculated from a non-equilibrium state. This means that the strain rate in the flow regime is variable as we will see later in Figure 1.11. Therefore, the calculated strain rate varies in the flow regime if the simulations are conducted to more than 100 ps. Thus, the validated constitutive equation for Coble creep model is not precise.

Consequently, a basic issue arises about the ability of the nanocrystalline

materials to relax the applied mechanical load within the timescale of molecular dynamics simulations (the nanosecond scale) at very high strain rate. Also, if the deformation mechanisms observed in molecular dynamics simulations are relevant even if high strain rate is applied in the simulations and if they can be compared to the experimental outcomes.

Next, we review the important results of molecular dynamics simulations and experiments that study the deformation behavior of nanocrystalline materials and their mechanical properties. Nowadays, molecular dynamics simulation systems have become large enough to cover the entire range of grain size. Thus, the transition from dislocation-based deformation mechanisms to grain boundary mediated process becomes observable.

1.2.2 Deformation mechanisms of nanocrystalline materials

The mechanical behavior of nanocrystalline materials has become the subject of an excessive research since the first synthesis of a nanocrystalline metal with a mean grain size less than 100 nm [1, 67]. The large density of grain boundary changes the mechanical behavior of these metals. For microcrystalline metals (d > 1 μm), dislocations generated from sources inside the grains such as Frank-Read sources pile-up to grain boundaries [68]. These boundaries act as barriers to the motion of dislocations. Once the stress concentration at the head of the pileup overcomes the threshold stress of the grain boundary, the pile-up will traverse the grain boundary. Thus, the macroscopic stress is relaxed and local plastic deformation is generated. This phenomenon is known as the strain hardening. As the grain size decreases, the fraction of the barriers to dislocations increases and hence, the metals are strengthened which is known as the Hall-Petch effect [7, 8]. The Hall-Petch relation is expressed as:

$$\sigma = \sigma_0 + K_{HP} d^{-1/2} \tag{1.4}$$

Where σ is the yield stress, σ_0 is the friction stress, and K_{HP} the so-called Hall-Petch constant.

For ultrafine grain size i.e. polycrystalline materials with a mean grain size between 100 nm and 500 nm [5], the number of dislocations inside the grains decreases and also the length of dislocations (distance traversed by dislocation from the source to the grain boundary). Therefore, the slope of the Hall-Petch K_{HP} decreases but strengthening still occur with the decrease of the mean grain size as seen in Figure 1.9 [69, 70].

As the grain size decreases to the nanocrystalline regime (d $\leq$ 100 nm), the dislocations pile-up mechanism begins to decrease. The number of dislocations

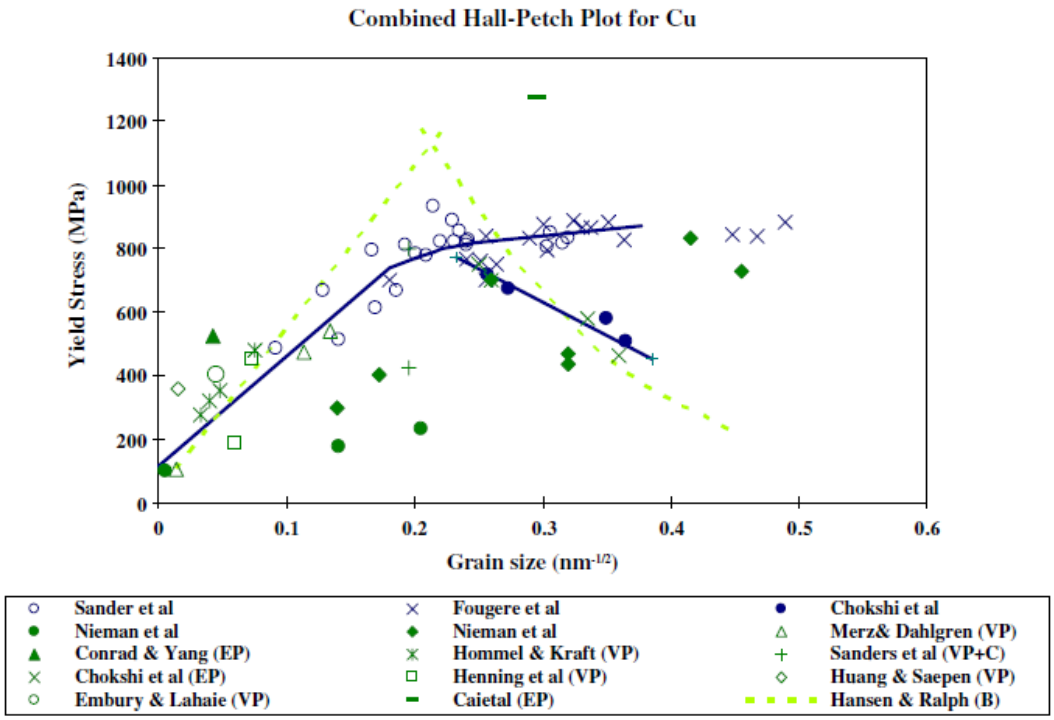

FIGURE 1.9: Compiled yield stress versus grain size plot for Copper from various sources ranging from coarse to nanograin size. The plots show a different trend as the grain size falls below a critical size [5].

inside grains and their boundaries is reduced. The slope of the Hall-Petch relation continues to decrease [71–73], until a critical mean grain size d_c where the Hall-Petch tendency is inverted and the metal starts to soften as the mean grain size decreases. This is known as the inverse Hall-Petch effect. A debate is always present about the value of this critical grain size that leads to the strongest polycrystalline system. d_c is assumed to be between 10 to 30 nm [11, 12, 24, 25, 74, 75]. Below 10 nm, experimental studies indicate that the strength decreases with further grain refinement [11, 71, 76]. In this regime, grain boundary mediated mechanisms are considered as the dominant deformation modes In molecular dynamics simulations. Van Swygenhoven *et al* identified a critical mean grain size for Copper at about 8 nm and for Nickel at about 11 nm [77]. Another molecular dynamics study realized by Schiötz and Jacobsen [28] indicates that a maximum flow strength of Copper is reached when $10\ nm \leqslant d \leqslant 15\ nm$. This grain size corresponds to a switch in the microscopic deformation mechanisms from dislocation-mediated plasticity to grain boundary sliding.

An ambiguity about the critical grain size is clearly present in the results

of molecular dynamics simulations. This can be related to the different approaches used to the study of the mechanical properties of nanocrystalline materials e.g. different inter-atomic potentials, the generation of initial configuration, and finally to the different strain rate or load applied. The investigation of this transition is one of the objectives of this thesis.

1.2.2.1 Grain boundary mediated plasticity

Diffusion creep Diffusion creep can take place by two main deformation mechanisms. The first one is proposed by Nabarro and Herring and shown in Figure 1.10 (a). This mechanism involves a flux of vacancies inside the grain. This migration of vacancies from the inside to the grain boundaries induces an increase of the grain length in the loading direction. The boundaries perpendicular to the loading direction, are the sources of vacancies. In contrast, the boundaries parallel to this direction act as sinks to the flow of vacancies [78].

The other diffusion mechanism is proposed by Coble as shown in Figure 1.10 (b). In case of Coble creep the diffusion of vacancies occurs in the grain boundaries only instead of the grain interior. This diffusion process results in a sliding of the grain boundaries. We can observe in Figure 1.10 (b) that the elongation of the grain in the loading direction is caused by the grain boundaries sliding [79].

The diffusional creep is governed by the following constitutive equation:

$$\dot{\varepsilon} = \frac{\sigma\Omega}{K_B T}\left[A_{NH}\frac{D_L}{d^2} + A_C\frac{\delta D_{GB}}{d^3}\right] \tag{1.5}$$

where σ is the applied stress, Ω is the activation volume, K_B is the Boltzman constant, T is the temperature, δ is the diffusional grain boundary width, D_L and D_{GB} are the diffusivities in the lattice and grain boundaries, respectively, and A_{NH} and A_C are constants related to the grain shape during Nabarro Herring and Coble creep.

In equation 1.5 the strain rate $\dot{\varepsilon}$ is proportional to the stress σ. Also, $\dot{\varepsilon}$ is proportional to d^{-2}) for Nabarro-Herring creep and d^{-3} for Coble creep. Therefore, to validate this mechanism, a series of creep tests should be performed at different stress, grain size, and temperature. Thus, the slope of the Log-Log plot between σ and $\dot{\varepsilon}$ should be equal to one. Also, the slope of the Log-Log plot between the $\dot{\varepsilon}$ and d allows one to detect which mechanism is active: Coble or Nabarro-Herring mechanism. In addition, to calculate the activation energy of

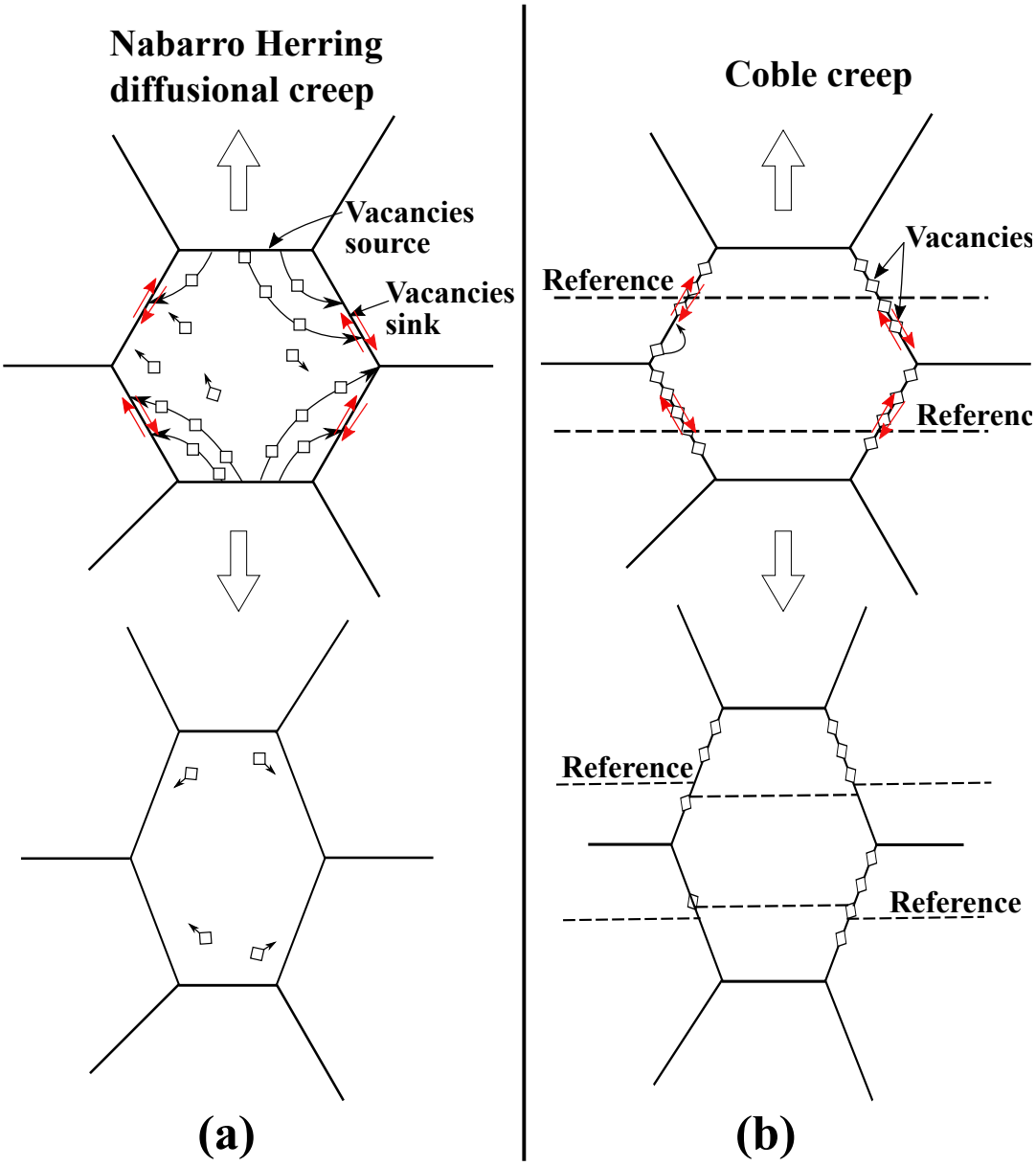

FIGURE 1.10: Grain boundary slides with respect to each others because of the diffusion of vacancies (a) from grain boundaries to the grain interior so-called "Nabarro Herring" diffusional creep mechanism, and (b) at grain boundaries Coble creep mechanism [78].

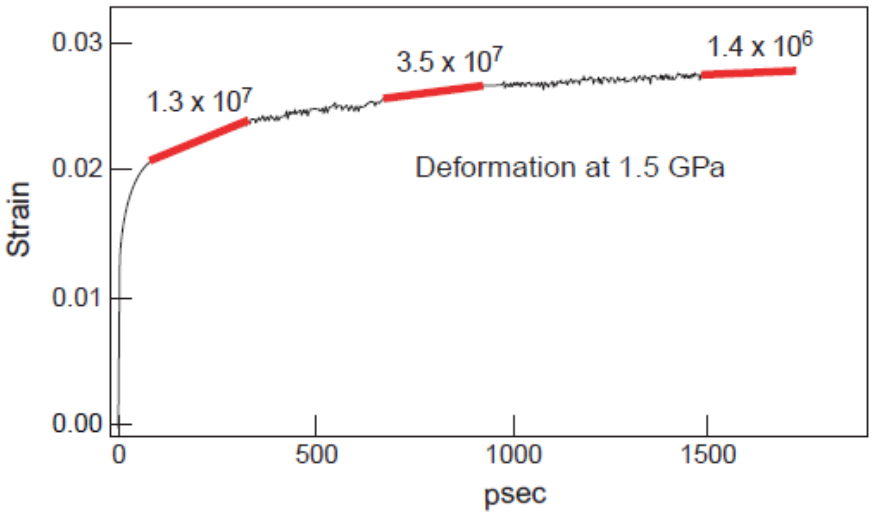

FIGURE 1.11: Reduction in strain rate during deformation at constant uniaxial stress for a nanocrystalline Nickel sample with mean grain size of 5 nm[66].

grain boundary diffusion (in Coble mechanism) or bulk diffusion (in Nabarro-Herring mechanism) an Arrhenius plot should be investigated between the $\dot{\epsilon}$ and the T at constant d and σ.

Chokshi *et al* [11] firstly suggested that nanocrystalline Copper and Pd deform by grain boundary diffusional creep or Coble creep at room temperature. To investigate the proposition of Chokshi *et al*, Yamakov *et al* performed molecular dynamics simulations of fully 3D nanocrystalline Pd with a mean grain size up to 15.2 nm [65]. To overcome the short time-scale limitations of molecular dynamics simulations, they performed their simulations at elevated temperatures 900K The creep tests are simulated for just 100 ps physical simulation time. The microstructures of these simulations were carefully prepared to have a uniform grain size and shape thus eliminating the topological driving force for grain growth (grain size distribution). The grains were randomly misoriented to form high-energy structurally disordered grain boundaries known to exhibit rather fast liquid-like self-diffusion. The results of their work showed that Coble and Nabarro Herring creep are both the main deformation mechanisms. Moreover, They suggested that this mechanism can be extrapolated to the room temperature [65].

Van Swygenhoven *et al* [66] have shown that the steady-state strain rate is not reached even after 1.5 ns simulation time. The steady state strain rate is the slope of the strain versus time in the second stage of a creep test. Figure 1.11 shows the evolution of the strain versus time for a creep test applied

on a nanocrystalline Nickel sample with 5 nm mean grain size [66]. We can see that the strain rate decreases by one order of magnitude over the first 1.5 ns. Thus, no constitutive model can be validated at this timescale. Hence, the strain rate and the activation energy calculated by Yamakov *et al* over the first 100 ps should be reconsidered. This argument reveals an important issue concerning the effect of strain rate or the simulation time on the steady state or equilibrium state of the system in molecular dynamics simulations.

One of the remarkable studies on the diffusional creep in nanocrystalline metals using molecular dynamics simulations is done by Millett *et al* [80] who performed molecular dynamics simulations at high temperature (T> 0.75 T_{melt}) to nanocrystalline BCC Molybdenum using the same method of Yamakov *et al*. The major difference is in the loading time. Their simulations have been run until 2 ns. In this case, the strain rate is calculated assuming that the system is in a steady state. Remarkably the creep rates exhibit a double-exponential dependence on temperature and a double power-law dependence on grain size. This indicates that both grain boundary diffusion of vacancies (Coble creep) and lattice diffusion of vacancies (Nabarro–Herring creep) contribute to the overall deformation. The strain versus time has been plotted for a nanocrystalline Mo with d = 12 nm at different temperatures going from 2400 K to 2900 K and a constant load of 800 MPa. The results are illustrated in figure 1.12 (a). The strain-rate values can be fit very well by a double-exponential function that is represented by the two contributions of exponential terms plot by the dashed lines. The lower-activation-energy slope (1.79 eV), corresponding to the grain boundary diffusion, dominates the creep at low temperature. As the temperature increases, a larger relative contribution is provided from the higher activation energy slope (6.69 eV), corresponding to lattice diffusion.

The Log-Log plot of $\dot{\varepsilon}/\sigma$ versus d switches from a linear dependence with d^{-2} for higher grain size to d^{-3} for the lower grain size as seen in Figure 1.12 (b). In fact the double power law of the diffusional creep is seen and the deviation from d^{-2} dependence as the grain size increases confirms the proposed equation 1.5. In contrast with the simulations of Yamakov *et al* that show a dependence on d^{-3} for higher grain size and d^{-2} for the lower grains.

Constant load with compression stress creep experiment applied to an electrodeposited nanocrystalline Nickel with d = 40 nm revealed an extensive primary creep region and no evidence for steady-state deformation [81]. Also,

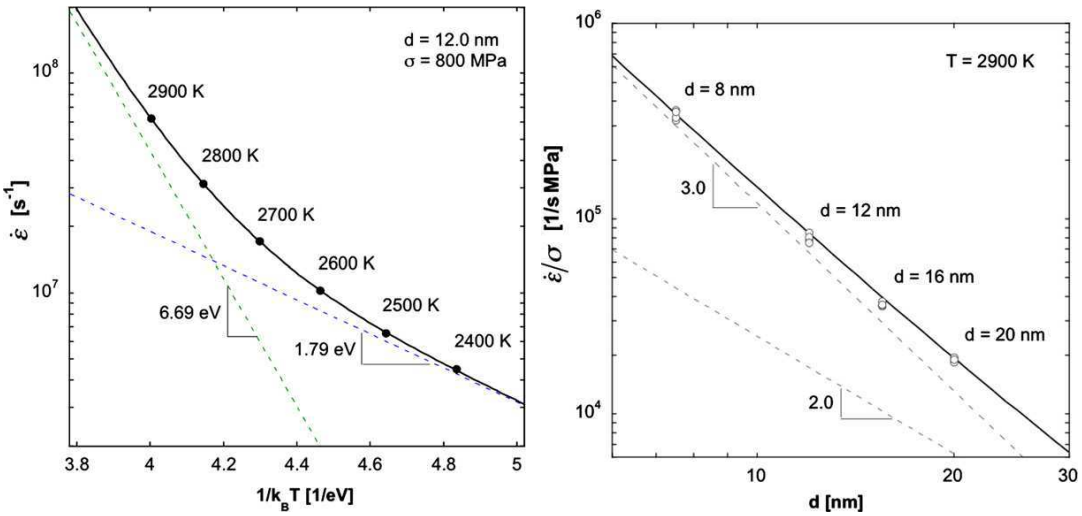

(a) (b)

FIGURE 1.12: (a) Arrhenius diagram of the creep rates for nanocrystalline Mo with d = 12 nm loaded at σ = 800 MPa, (b)Log-Log plot of $\dot{\varepsilon}/\sigma$ with respect to d gathers all the data points obtained at 2900 K in a single curve [80].

Coble creep was not considered as the main deformation mechanism because of the divergence of the stress and the grain size exponents from that proposed by Coble. However, grain boundary based mechanisms accompanied with intragranular dislocations are found to be the main deformation mechanisms in this work [81].

The underlying challenges are now (i) to prove experimentally that diffusional creep is the main deformation mechanism for nanocrystalline materials at high temperature, and (ii) to generate more realistic nanocrystalline samples for molecular dynamics simulations because most of them consist of idealized samples with generally high angle grain boundaries and defect free nanograins, and (iii) to investigate if the diffusional creep is also the deformation mechanism in the case of a wide distribution of grain size with low and high angle grain boundaries at room temperature.

Grain boundary sliding Grain boundary sliding is the relative motion between two grains and it occurs by localized shear deformation along the grain boundary plane. Molecular dynamics simulations showed that grain boundary sliding in a nanocrystalline material is accompanied by local atomic events at the interface between two adjacent grains *e.g.* uncorrelated atomic shuffling and stress assisted free volume migration [27, 63]. Moreover, a direct coupling between the grain boundary migration and the triple junction migration with

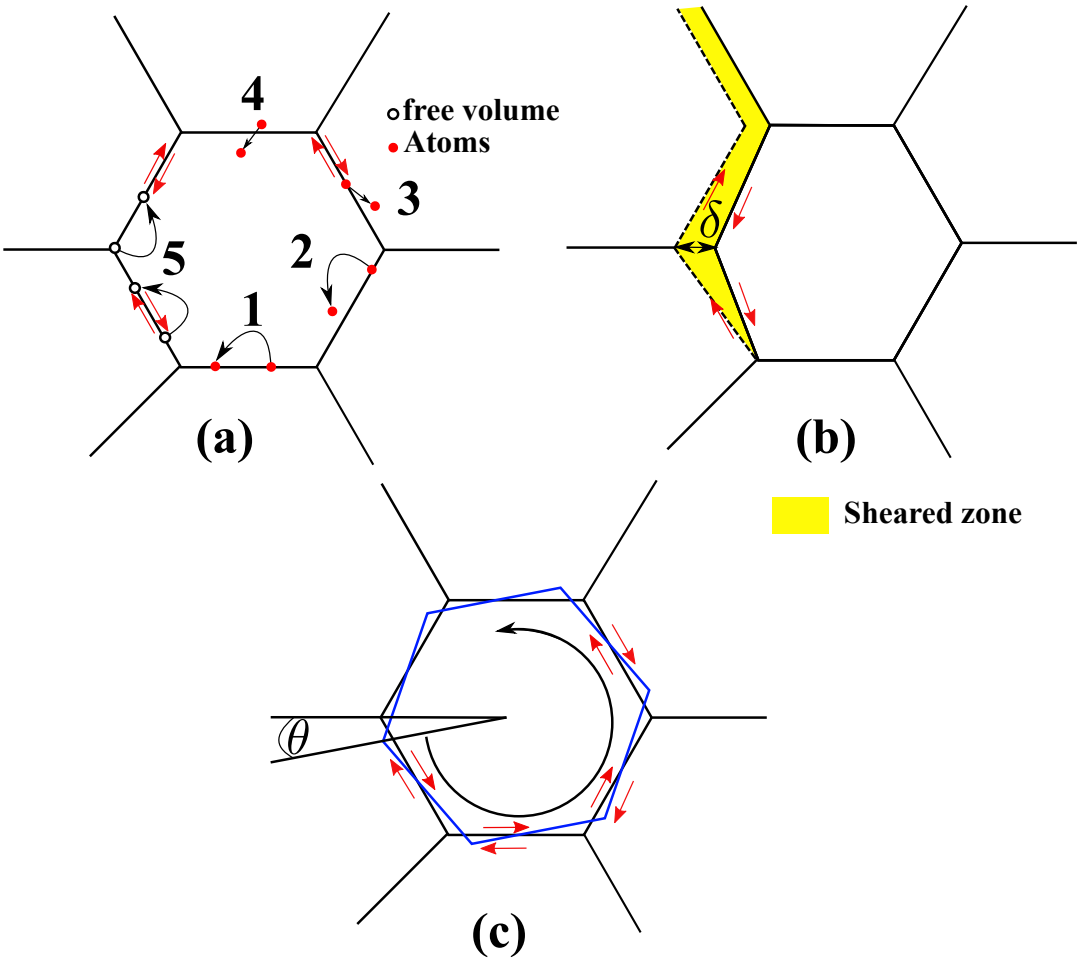

FIGURE 1.13: Deformation mechanisms in nanocrystalline FCC metals (a) Atomic shuffling and stress assisted free volume migration, (b) grain boundary and triple junction migrations, (c) grain rotation

the shear deformation have been shown using molecular dynamics simulations[32, 82, 83].

- **Uncorrelated atomic shuffling**: This mechanism involves the motion of a group of atoms independently on the grain boundary (mark 1 in the Figure 1.13 (a), or from one grain to its neighboring one (mark 4 in the Figure 1.13 (a)), or from a grain boundary to a neighboring grain interior (marks 2 and 3 in Figure 1.13 (a)). In qualitative terms, this means that when a heterogeneous shear stress is applied to a grain boundary or around the grain boundary, each atom in this vicinity will feel a different net force. Thus during the time, certain atoms will reach the conditions to leave their saddle point and migrate to a new location. Thereby, the local stress at the grain boundary will be relaxed. In this way, the combination of these localized processes leads to a homogeneous slide of grains with respect to each other. These processes do not involve long-range mass transport and therefore they are different from diffusion process. These processes contribute to the total plastic strain [27].

- **Stress assisted free volume migration**: An important characteristic of the grain boundary structure is the distribution of free volumes with sizes below that of a vacancy. When shear stress is applied on a grain boundary, free volumes migrations in the grain boundary is triggered. These migrations relax a part of this local stress (mark 5 in Figure 1.13 (a)). Moreover, Swygenhoven *et al* have employed the term of "stress assisted free volume migration" because some types of migration barrier exist via an average activation enthalpy to these activities [63].

- **Triple junction and grain boundary migration** In contrast with coarse-grained materials, the grain boundary mobility is an important deformation mechanism in nanocrystalline materials. A direct relationship has been found between the grain boundary migration and the shear deformation [83]. Figure 1.13 (b) shows a schematic description of the migration of a grain boundary and triple junction by a distance δ. This migration induces a shear deformation. The stress buildup across the grain boundary can be released by the motion of the grain boundary and triple junction [32]. With the application of stress, each grain can respond differently because the amount of stored strain energy density will vary because of the elastic anisotropy and the relative orientation of each grain. This difference in the strain energy density from grain to another

will create a driving force for grain boundary migration [32]. Another form of grain boundary motion has been revealed by Tang *et al*. Grain boundary motion will results when the atoms located at both sides of it move in the same direction normal to the boundary [31].

- **Grain rotation** Grain rotation has been found to be an important deformation mechanism in nanocrystalline materials especially for small grains size [30, 84, 85]. Figure 1.13 (c) shows a schematic plot of the grain rotation mechanism due to the sliding of different grain boundaries in the same counter-clockwise direction. Grain rotation may also lead to a stress assisted grain growth. Shan *et al* used in-situ dynamic transmission electron microscope to observe the nanocrystalline Nickel films under tensile strain ($\bar{d} = 10nm$) [84]. Grain rotation induced grain coalescence was observed. Also, They found a competition between the deformation controlled by the nucleation and the propagation of dislocations and the deformation controlled by the diffusion-assisted grain boundary processes. Wang *et al* also proposed that grain growth in electrodeposited nanocrystalline Nickel with 20 nm mean grain size is caused by the grain rotation [85].

To summarize: the atomic shuffling, the stress assisted free volume migration, the grain boundary migration, the grain growth, and the grain rotation are the mechanisms that engender a sliding of the grain boundary. The mobility of grain boundary is the common behavior that results from the combination of these mechanisms in nanoscale grain size, in contrast with coarse-grained polycrystals. Therefore, it is necessary to understand the influence of each mechanism on the deformation of the sample. In the other hand, the effect of the microstructure (i.e. grain size distribution, grain boundaries energies, and mean grain size), the stress and the strain rate on the behavior of each deformation mechanism is a very important issue to be studied. This would be helpful to propose a constitutive model for the mechanical response of nanocrystalline material taking into account the contribution of all local stated mechanisms.

1.2.2.2 Inverse Hall Petch effect

Overview of experimental studies In 1990 Chokshi *et al* were the leaders that investigate if the Hall-Petch relation is still valid for nanocrystalline Copper and Pd [11]. They found an inverse Hall-Petch tendency and they attributed this effect to the occurrence of diffusional creep at room temperature. They

suggested that diffusion creep occur by the transport of vacancies along the grain boundaries which is known as the Coble creep [79].

In 1991, Nieh and Wadsworth [10] firstly revealed the presence of a critical grain size for dislocations pileup, below which softening mechanisms led to a decrease in hardness with decreasing grain size. They assumed that there is a critical diameter from which the Hall-Petch relation broke down. This diameter is defined when the grain size becomes smaller than the critical length l_c between two dislocations.

Fougere *et al* reported a softening of nanocrystalline Copper and Pd prepared by Inert Gas Condensation followed by consolidation [86]. They demonstrated that the hardening or softening of nanocrystalline metals can depend upon the method used to vary the grain size. They attributed that the softening results from the increased ease in forming and moving dislocations as the grain size increases. Sanders *et al* have investigated the elastic properties of nanocrystalline Copper and Pd with a mean grain size varying from 10 to 110 nm [12]. They found that the hardness measurements follow the predictions of the Hall-Petch relationship for the coarse-grained Copper until a grain size of 15 nm below this value the hardness remains unchanged. Also, they reported a decrease of Young's modulus of nanocrystalline materials with respect to the grain size because of the porosity.

The mechanisms of deformation and damage evolution in electrodeposited, fully dense, nanocrystalline Nickel with an average grain size of 30 nm and a narrow grain size distribution were investigated by Kumar *et al* through in-situ Transmission Electron Microscope (TEM) and High-Resolution TEM (HR-TEM) [87]. They found that the dominant deformation mechanisms depend on: (i)dislocation emission from grain boundaries,(ii) intragranular slip and (iii) the grain boundary sliding that facilitates the nucleation of voids at boundaries and triple junctions.

Direct experimental evidence of grain boundary accommodation mechanisms is seen as the grains coarsening during deformation of nanocrystalline materials [88]. An important question is to know whether grain coarsening is a stress or strain-driven mechanism. Jin *et al* reported a strain-driven coarsening mechanism by grain boundary motion or migration during in situ nanoindentation

in an electron microscope of thin films ultrafine-grained and nanograined Aluminium [89].

In contrast, Brandstetter *et al* studied the grain coarsening during compression of bulk nanocrystalline nickel and Copper [90]. They reported that the growth rate is higher in load driven tests than in strain-driven tests for nanocrystalline Copper. This confirms that the grain growth is stress driven. However, no evidence of grain growth has been seen in electrodeposited nanocrystalline nickel. Legros *et al* and Rupert *et al* also reported that stress-driven grain growth is the origin of the grain boundary mobility in nanocrystalline Al thin film during tensile experiment [91, 92].

Overview of molecular dynamics simulations Molecular dynamics simulations come to the front in order to elucidate the main mechanisms that induce the inverse Hall-Petch response in nanocrystalline materials. Inspired by the experimental studies, Schiøtz *et al* [24, 25, 28] and Van Swygenhoven *et al* [26, 27, 77, 93, 94] launched a series of molecular dynamics simulations to investigate the low temperature plastic deformation behavior of nanocrystalline Copper and Ni. Three-dimensional microstructures have been generated that contain a distribution of grain size with an average less than 50 nm. Different simulation strategies have been employed by these authors to understand the active deformation mechanism: (i) Schiøtz *et al* [28] applied a series of tensile tests by imposing a constant strain rate to nanocrystalline samples with different mean grain sizes. Then the mechanical properties such as the yield stress, the flow stress, and Young's modulus have been calculated with respect to the grain size. (ii) Van Swygenhoven *et al* [66, 95] applied a series of tensile tests by controlling the stress to different nanocrystalline samples and they focused on the strain vs. time behavior. Then the strain rate has been extracted to analyze the active mechanism.

To simulate a large strain sample deformation by molecular dynamics, a very high stress of the order of $1 \sim 3$ GPa or very high strain rate of the order of $10^7 \sim 10^9 s^{-1}$ have to be applied because of the small time-step used in molecular dynamics (i.e.between 1 and 5 fs). The simulation results confirmed the earlier experimental suggestion that grain boundary sliding is the dominant deformation mechanism for $\bar{d} < 10\ nm$.

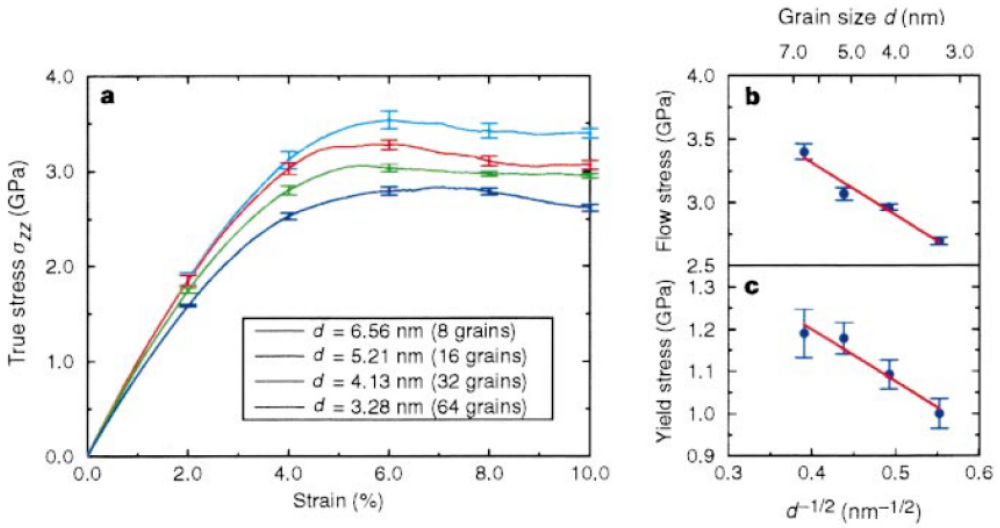

FIGURE 1.14: The effect of grain size on the stress-strain curve. (a) The average stress in the tensile direction (σ_{zz}) versus strain for each grain size sample. (b) and (c), The maximal flow stress and the yield stress as a function of grain size. The yield stress decreases with decreasing grain size, resulting in a reverse Hall-Petch effect. The maximal flow stress corresponds to the plateau of the stress-strain curves; the yield stress is defined as the stress where the strain departs 0.2% from linearity [24].

The early molecular dynamics simulations of Schiøtz *et al* revealed the decrease of the yield stress and the flow stress when the mean grain size decreases from 6.56 to 3.28 nm as seen in Figure 1.14 [24, 25]. By visualizing the non-affine displacement of atoms during the sample deformation, they showed the evidence of grain boundary sliding as the atoms move upward on one side of the boundary and downward on the other side. They have also suggested that grain rotation plays a significant role in the relaxation of the stress of these nanograins. In some of the larger grains (d $\geq$ 5.2 nm), they observed the nucleation of partial dislocations from the grain boundaries. These incomplete extended dislocations travel across the grains, leaving behind intrinsic stacking faults. However, in these simulations, the mechanism of the accommodation process of plastic deformation during grain boundary sliding was not addressed nor clearly described.

The earliest study performed by Van Swygenhoven *et al* on the plastic deformation behavior at a low temperature of nanocrystalline Nickel with a mean grain size $3nm \leqslant \bar{d} \leqslant 5nm$ revealed that the grain boundary sliding, the grain boundary migration, and the grain rotation are the main mechanisms of the plastic deformation [26]. No dislocations activity has been shown inside the

grains. In addition, they showed that at constant stress the strain rate increases linearly with the inverse of the mean grain size. This means that at the same stress level when the grain size decreases the metal becomes easier to deform which is the inverse Hall-Petch effect. Later on, the grain size in their simulations has been increased to 12 nm [94], and to 20 nm [96]. Grain boundary sliding was found to be the main deformation mechanism that results in a build-up of the stress across the neighboring grains, which in turn released by grain boundary and triple junction migration [96]. The display of the atomic processes during interfaces sliding indicates that grain boundary sliding is facilitated by atomic shuffling and some stress-assisted free volume migrations [27]. The work of Derlet *et al* [96] shows that the atomic shuffling process involves short-range atomic motions and not a long-range mass transport like diffusion of vacancies as in Coble creep mechanism.

Later on, Tang *et al* studied the mechanical behavior of nanocrystalline BCC Tantalum with a mean grain size varying from 2.5 to 30 nm under uniaxial tensile and compression loading by molecular dynamics simulations [31]. They found that the mechanical behavior in tensile is significantly different from that in compression. Also, they present an inverse Hall-Petch effect for von Mises equivalent stress in compression. For small grains, all plastic deformations are accommodated by the grain boundaries. They identified several mechanisms that relax the stress on grain boundary: (a) grain boundary migration, (b) grain boundary diffusion or atomic shuffling, (c) grain boundary sliding and (d) Grain rotation. Also, they indicate that the grain is elongated by shear when the sliding of its different grain boundaries is in different clockwise or counterclockwise direction.

Since pure grain boundary sliding is not fully compatible with strain condition, it requires other cooperative processes to release the stress built up across neighboring grains. A combination of grain boundary migration via grain boundary sliding or intragranular slip and grain rotation was proposed as the dominant process by which the shear planes form. The collective grain boundary sliding becomes highly important plastic deformation mechanism for a grain size of about 5 nm [30, 35].

Some molecular dynamics simulations studies tried to investigate whether grain growth is stress or strain-driven. Schiøtz proposed that strain-induced coarsening in nanocrystalline Copper with 5.5 nm mean grain size under cyclic

deformation [97]. He proposed that the system underwent a relaxation of the total energy because of the grains coarsening. This coarsening is attributed to atomic shuffling. Whereas, coupled grain boundary motion to shear deformation has been found in three-dimensional nanocrystalline Al grain boundary network using molecular dynamics simulation [98]. Haslam *et al* declared that the grain rotation and grain boundary curvature are auspicious for grain growth in nanocrystalline Pd at high-temperature [99, 100]. Also, they suggested that the increase of the stress enhances the rate of these mechanisms.

At present, there is a confirmation among researchers that grain boundary sliding is a relevant deformation mechanism in nanocrystalline metals. The domination of this mode leads to inverse Hall-Petch relation below a critical grain size d_c. But the debate on its nature and the underlying atomistic mechanism is still active. Two opinions have been introduced:

1. As mentioned above grain boundary sliding is a result of the atomic shuffling and stress assisted free volume migration [27, 66, 96]

2. Grain boundary sliding is caused by grain boundary diffusion which at low T involves an individual movement of vacancies and interstitials or collective motion of small clusters of atoms [75].

The difference between (1) and (2) is that while the diffusion is a long-range random-walk process, the stress-assisted migration is a short range direct movement in response to the applied stress without any preferred direction (on the grain boundary or in the grain) as the case of Coble or Nabarro Herring creep [96, 101].

1.2.2.3 Crossover to dislocation based plasticity

Dislocation in nanocrystalline materials In nanocrystalline regime, grain boundaries are considered as sources and sinks to dislocations. Molecular dynamics simulations suggest the presence of three types of intragranular deformation mechanisms: (i) Partial dislocations emission from grain boundary that propagate across the grain to vanish on the opposite boundary as shown in Figure 1.15 (a), (ii) Perfect dislocations dissociated into two Schokley partials that nucleate on grain boundary and absorbed by the opposite boundary (Figure 1.15 (b)), (iii) Twinning formed by extensive emission of partial dislocations on adjacent slip planes. Note that the first and the last mechanisms leave behind some kinds of dislocation "debris", while in the case of full dislocations

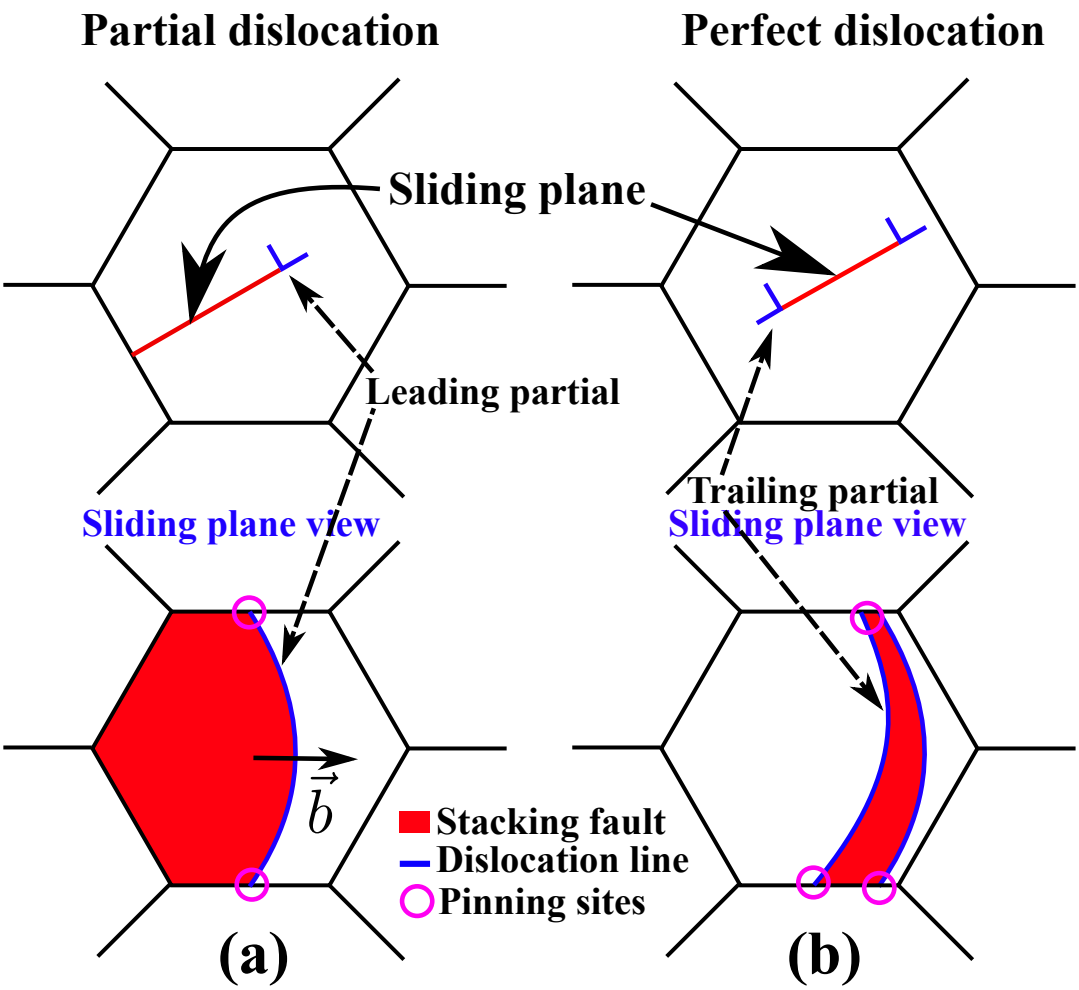

FIGURE 1.15: Partial (a) and perfect (b) dislocations in nanocrystalline materials.

nothing can be observed after the propagation of dislocations.

Schiøtz *et al* and Van Swygenhoven *et al* have firstly observed the presence of extended partial dislocations in nanocrystalline Copper and Nickel [24–28, 93]. These dislocations are nucleated from grain boundary and propagate inside the grains generating two ribbons of stacking faults behind the core of the partial dislocation as seen in Figure 1.15 (a). These dislocations are absorbed by the opposite grain boundary. Van Swygenhoven et al have investigated the atomic mechanism responsible for the emission of partial dislocations from grain boundary in nanocrystalline materials [102, 103]. They showed that grain boundary atomic shuffling combined with stress-assisted free volume migration from the vicinity of triple junction or grain boundary dislocations provide the appropriate conditions to emit a partial lattice dislocation. The stress assisted free volume migration leads to the displacement of grain boundary atoms of about a partial burger vector. This mechanism is the same as that proposed for grain boundary sliding (discussed above). The nucleation and propagation of partial dislocation induce changes in the resultant grain boundary dislocation distribution. Another structural relaxation is observed in the grain boundary and nearby triple junction. Swygenhoven *et al* related the non-observation of full dislocation with the low stress concentration on grain boundary after a structural relaxation of this boundary once a leading partial is nucleated [102].

Yamakov *et al* have first observed the nucleation and propagation of a trailing partial from grain boundary in columnar nanocrystalline Al. This partial leads to a full dislocation emission and propagation to the opposite grain boundary [74, 104]. This dislocation is dissociated into two Schokley partials separated by a stacking fault zone as shown in Figure 1.15 (b). They proposed that the comparison of the splitting distance with respect to d represents a critical length scale controlling the low-temperature mechanical behavior of nanocrystalline materials. They also revealed that above a critical grain size, the deformation is dominated by the motion of full dislocations. If the grain size was not large enough, only partial dislocations nucleated, leaving behind stacking faults transecting the grain. As the plastic strain increases, the density of dislocation increases leading to dislocation-dislocation interaction. A Lomer–Cottrell locks were observed in their simulations. Also, deformation twinning occurred by the overlapping of the stacking fault ribbon of partial dislocations at adjacent slip planes [75].

To summarize molecular dynamics simulations have revealed the following explication concerning the emission and the propagation of dislocations:

1. High hydrostatic pressure concentration on grain boundary is present before the nucleation of partial dislocation and then it is released after the emission [63, 105].

2. The emission of dislocations is accompanied by atomic shuffles and usually stress-assisted free volume migration [36].

3. The splitting distance between leading and trailing partials is determined, in part, by the stress distribution in the grain boundary [106].

4. Leading and trailing partial dislocations should not necessarily emit at the same ledge, even not at the same grain boundary, suggesting that the grain boundary dislocation nucleation cannot be simply represented by Frank-Read source [36].

5. Grain boundaries ledges can hinder the dislocation propagation that depends on the geometrical conditions of the ledge and the Burgers vector. Dislocations can become pinned at these areas resulting in a pileup of kinks and a subsequent local increase in dislocation curvature. [36]. The increase of the dislocation line curvature is caused by the stacking of the first pinning site and the sliding of the second pinning side.

Deformation twinning in nanocrystalline materials Basically, deformation twins in FCC metals are formed by the glide of Shockley partial dislocations on successive slip planes. In FCC lattice a twin boundary is defined as an inversion of the stacking sequence of the (111) plane ABCABC to produce a mirror plane as seen in Figure 3.9. Deformation by twinning depends on the grain size, the stacking fault energy, the temperature, and the strain rate. For example, coarse-grained materials with high stacking fault energy such as Al and Nickel usually deform by dislocation slip because of their lower critical stress required for dislocation slip onset in comparison with the onset of twinning (i.e. critical twinning stress) [107]. In contrast, FCC metals with low stacking fault energy such as Copper promote twinning. In conventional coarse-grained materials, the decrease of the grain size is believed to impede the deformation by twinning. Meyer *et al* have shown that the Hall-Petch slope that corresponds to twinning deformation is higher than that of dislocation slip [108]. Therefore, In coarse-grained range, the decrease of the grain size induces an increase in

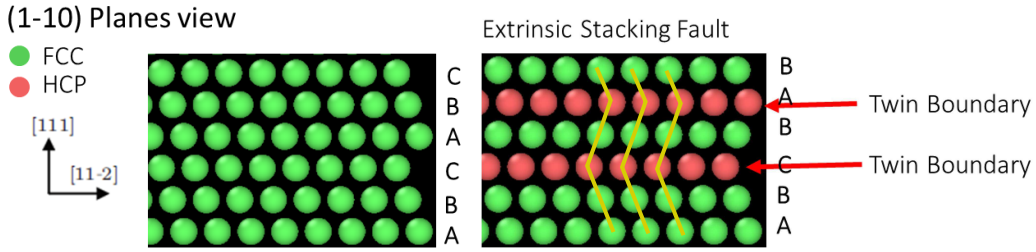

FIGURE 1.16: Micro twin (extrinsic stacking fault) that change the normal stacking sequence in FCC metals.

the onset stress of twinning much more than that of dislocation slip. The low temperature and high strain rate favored the deformation by twinning [107]. This can be understood by the increase of the flow stress of FCC materials with the decrease in temperature or the increase of the strain rate. Consequently, the critical stress of twinning can be attainable.

Molecular dynamics simulations have shown that the emission of partial dislocations from grain boundaries is a common deformation mechanism for all nanocrystalline FCC metals [28, 93, 95, 109]. As mentioned above, trailing partials have been seen in the case of nanocrystalline Al but not in the case of nanocrystalline Nickel nor Copper [38, 110]. Van Swygenhoven *et al* have shown that the emission of trailing partial cannot be seen in the timescale of molecular dynamics simulation for Copper and Ni. They explained this phenomenon in terms of the time required to re-build the stress concentration needed to overcome the energy barrier (= unstable stacking fault energy - stable stacking fault energy). Therefore, they suggested that for materials with a ratio of the stable stacking fault energy over the unstable stacking fault energy close to a unit, a perfect dislocation can be seen within the molecular dynamics timescale

Similarly, it was suggested that the ability of nanocrystalline to twin nucleation via an extended partial on an adjacent plane depends on the ratio between the unstable twinning fault and the unstable stacking fault energy [111].

Recently, a nature publication [112] gave an insight about the ultimate limits of metal plasticity by molecular dynamics simulations. In other words, they found that above a strain rate of $8.10^8 s^{-1}$ Tantalum BCC single crystal cannot dissipate the imposed mechanical load by dislocations and twinning becomes dominating to the dynamic response.

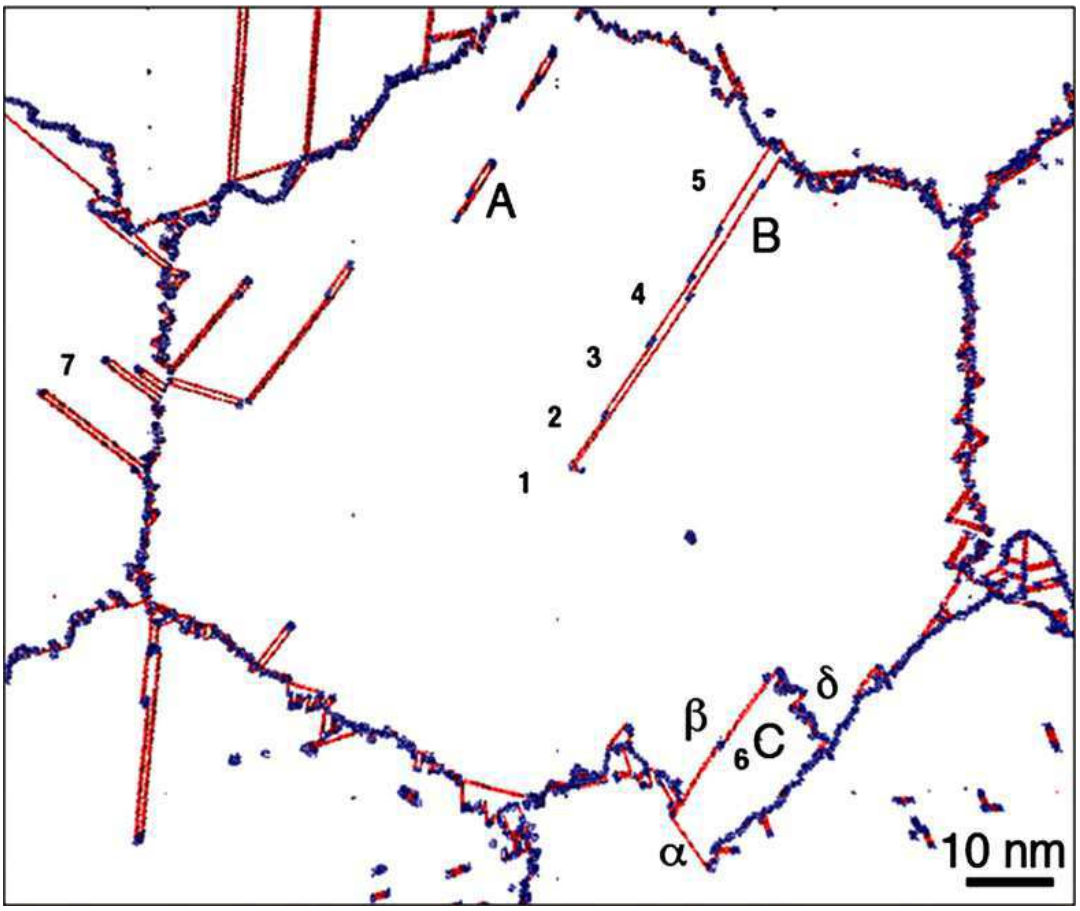

FIGURE 1.17: Snapshot for a grain with a diameter of 70 nm at 10.3% plastic strain revealing three twinning mechanisms : (A) shows a twin nucleus formed by the overlapping of two extended dislocations on adjacent slip planes, (B) represents a twin formed by successive emission of Shockley partials from the grain boundary, and (C) represents a twin formed by grain boundary splitting and migration. Zone 7 marks the emission of extrinsic dislocations from grain boundary [107].

Three twinning mechanisms have been shown by molecular dynamics simulation of nanocrystalline Al with columnar structures [75]. These simulations use idealized columnar, <110> textured lattice, that contains four grains of identical size with a regular hexagonal shape. Three twinning mechanisms have been seen:

1. The first one is indicated by the letter A in Figure 1.17 where the two stacking fault ribbons of two extended dislocations on two adjacent slip planes overlap.

2. The second mechanism is marked by the letter B in Figure 1.17 where successive Shockley partials are emitted from the same grain boundary at adjacent slip planes. The change of the stacking sequence resulting from the propagation of these partials is shown in the figure zone enumerated from 1 to 5 below the main Figure. There is an illustration that describes the modification of the atomic sequence due to the twinning. Line 1 indicates the normal stacking sequence for an FCC metal. As a consequence of the propagation of the first partial 1 an intrinsic stacking fault is formed and two HCP planes can be seen marked by red. An HCP plane is formed when the stacking sequence is ABABAB (BCBCBC or CACACA). After the emission of the second partial 2 on an adjacent slip plane, an extrinsic stacking fault or micro-twin is formed because of the overlapping of the two stacking fault ribbons as explained in Figure 3.9. The stacking sequence 3 indicates the new sequence after the passing of the second partial where two twin boundaries can be seen marked by red. Then the width of the micro-twin begins to increase by the emission of Shockley partials on adjacent slip planes to finally attain two twin boundaries with 3 slip planes between them.

3. The third mechanism is marked by C in Figure 1.17 where two twin boundaries marked by α and β are formed because of the grain boundary migration (marked by δ) that consists of the cores of partial dislocations. There is a mirror symmetry between the zone C and the grain interior. The two twin boundaries are α and β. Also, the propagation of δ to the opposite grain boundary increases the twinning zone C.

Crossover to the Hall-Petch effect Recent molecular dynamics simulations have captured that the crossover from Hall-Petch to inverse Hall Petch is related to the transition in the dominant deformation mechanism from dislocation-based plasticity to grain boundary mediated process in full three-dimensional

nanocrystalline metals [28, 30, 77, 104, 113]. Firstly, Swygenhoven *et al* [77] pointed to the presence of a critical grain size below which all plastic deformation is accommodated in the grain boundary and no intragranular deformation is observed. This conclusion was made after applying a molecular dynamics simulation to 3D nanocrystalline Nickel and Copper sample with mean grain size below 20 nm. They found that the nucleation of Shockley partial dislocations that generates stacking fault inside the grains during the propagation is present at a grain size of 8 nm in Copper and 11 nm in Ni. Therefore, they suggested a transition from grain boundary mediated process to dislocation based deformation mechanism and an increase of the critical grain size with the stacking fault energy.

Yamakov *et al* investigate the interplay between the dislocations and grain boundary processes in nanocrystalline Al 3D model consisting of 4 grains with a mean grain size going from 7 to 32 nm [104]. They showed the nucleation and the propagation of dislocation loops or extended $\frac{1}{2}$[110] dissociated in two $\frac{1}{6}$[112] Shockley partials for large grain size (d > 18 nm). In Figure 1.18 (a),(b), and (c) we can see the presence of these loops marked by 1 which consist of two blue curved lines (the cores of the two Shockley partials) separated by red atoms (Stacking fault ribbon). In contrast, no presence of this type of dislocation has been seen below 18 nm mean grain size. Only a partial dislocation that nucleates at the grain boundary and crosses the grain to vanish on the opposite boundary. The propagation of the partial dislocation generate stacking fault ribbons as seen in Figure 1.18 (a), (c) and (d) labeled by 2. Therefore, they proposed that the competition between the slip distance between the two partials and the grain size is the cause to the existence of a lower limit in the grain size $d_c = r_{split}$ below which the dislocation slip process cannot operate and a grain boundary-based deformation process takes over. Instead of determining the magnitude of the flow stress as a function of the grain size they calculated the strain rate during stress relaxation. The critical grain size is defined as the hardest sample to deform (i.e. the sample with the lowest strain rate). They found a critical grain size of 18 nm. However, at this grain size, the grains are too small to support the dislocation slip process. At the same time, they are still too large for grain boundary processes to be active as deformation mechanisms. The larger critical grain size of a metal depends on its stacking fault energy [77]. However, In contrast with Swygenhoven *et al*, partial dislocations are present in grain size below the critical grain size. In addition, Coble creep is assumed to be the dominant deformation mechanism due to the scaling of

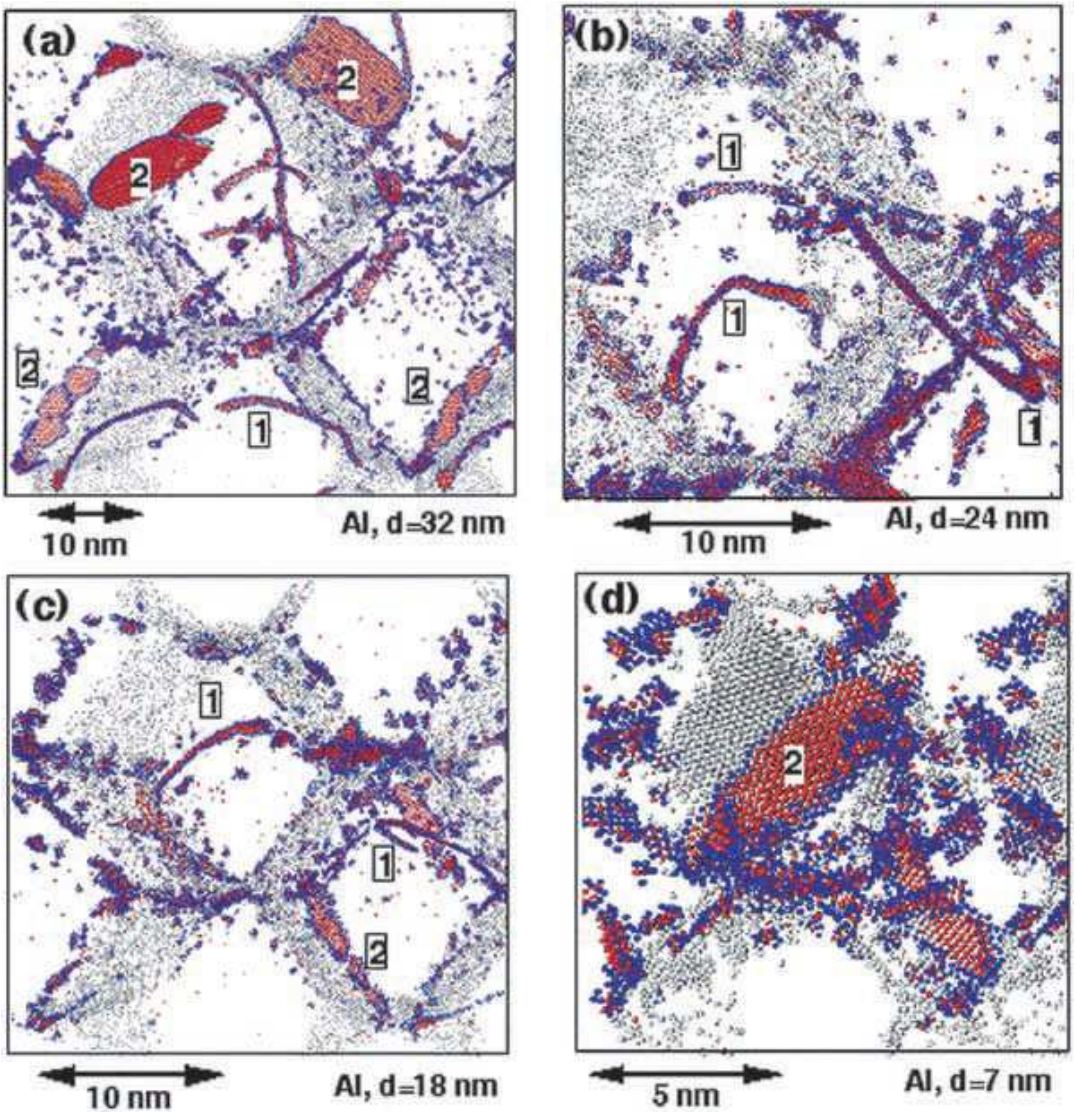

FIGURE 1.18: Snapshots of our four-grain fully 3D microstructure at about 1.5% plastic strain. The common-neighbour analysis was used to identify atoms as being either in a local hcp (red atoms) or fcc environment (not shown). The grain boundaries are seen as walls of grey atoms. The viewing direction is along the [110] diagonal of the simulation box. Two distinct types of dislocation configuration are labeled as 1, indicating a complete extended $\frac{1}{2}$[110] dislocation, and 2 indicating a stacking-fault plane produced by a single Shockley partial dislocation [104].

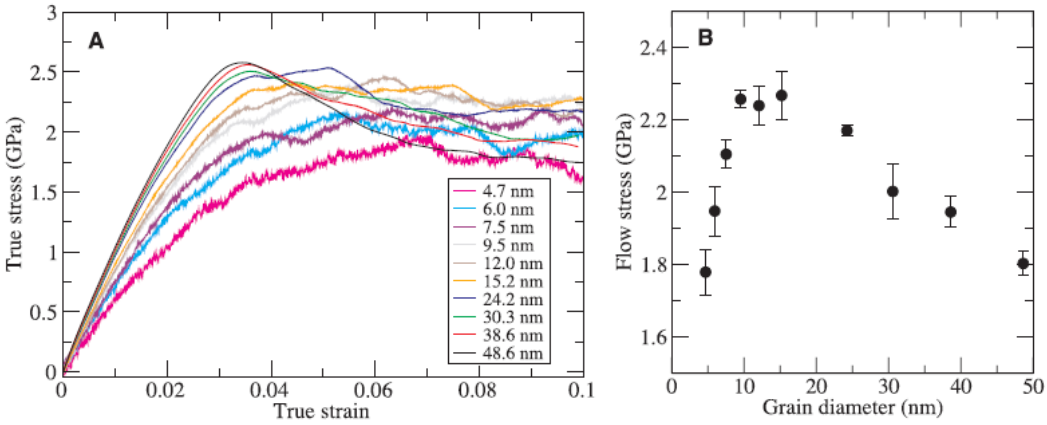

FIGURE 1.19: The grain-size dependence of the flow stress. (A) Stress-strain curves for 10 simulations with varying grain sizes. (B) The flow stress as a function of grain size [28].

the strain rate with $d^{2.1-2.6}$.

In the study of Schiøtz and Jacobsen [28], samples with large number of grains and with different average grain size ranging between 5 and 50 nm were used. Figure 1.19 shows the stress-strain curves from 10 simulations with varying grain sizes. The strength exhibited a maximum at a grain size between 10 and 15 nm (Figure 1.19). This maximum stress indicated a shift in the underlying deformation mechanism, from dislocation-mediated plasticity in samples with large grains to grain boundary sliding in small grains. They observed the formation of pile-up dislocations nucleated from grain boundary and then pileup to opposite grain boundary for large grain size. Also, some deformation twins have been seen in some simulations especially at large grain size.

Yamakov *et al* proposed a deformation-mechanism map for nanocrystalline materials based on molecular dynamics simulations at low temperature as seen in Figure 1.20. This map describes the aspects of the transition from dislocation based to grain boundary mediated plasticity. Also, the dependence of the stacking fault energy, the elastic properties of the metal and the magnitude of the applied stress are taken into consideration. The physical interpretation of the crossover between the Hall-Petch and inverse Hall-Petch effect is based on the relation between the splitting distance separated two successive Schokley partials dislocations, the stacking fault energy, and the applied stress. The

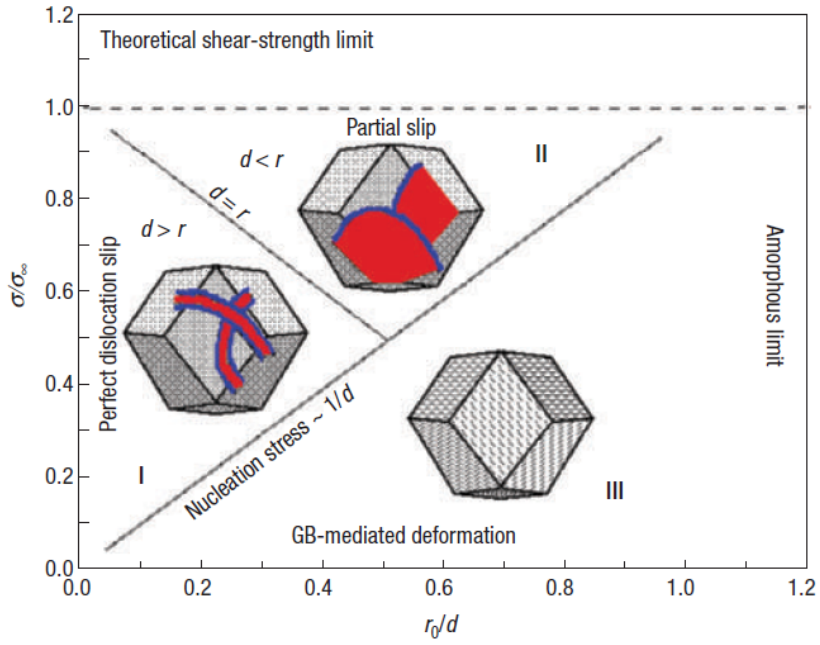

FIGURE 1.20: Proposed deformation-mechanism map incorporating the role of the stacking-fault energy in the deformation behaviour [38]

splitting distance is defined as follow :

$$r = \frac{r_0(\gamma)}{1 - \frac{\sigma}{\sigma_\infty}(\gamma)} \tag{1.6}$$

where $r_0 = K_1 b^2/\gamma$ is the equilibrium splitting distance at $\sigma = 0$; b is the Burgers vector of the Shockley partial dislocation, and $\sigma_\infty(\gamma) = K_2\gamma$ is the resolved shear stress at which the splitting distance becomes infinitely large. The constants K_1 and K_2 depend on the elastic modulus of the material and the particular types of the two Shockley partials.

As seen in Figure 1.20, this map is decomposed into three regions. In region I $d > r$ and/or high stacking fault energy, perfect dislocations dissociated into two Schokley partials nucleated from grain boundary and propagate across the grains. In the region II characterized by a small grain size and/or a low stacking fault energy metal, only incomplete dislocations can be nucleated; the grains are therefore transected by stacking faults that inhibit dislocation propagation thus giving rise to strain hardening. Region III characterizes the very small grain-size or low-stress regime in which no dislocations are present at any stress, and the deformation is therefore controlled by grain boundary-mediated processes [38].

The transition in deformation mechanisms and their related mechanical response with decreasing grain size depends on the stacking fault energy, the elastic properties of the material, and the applied stress level. For metals with a high stacking fault energy, the change was governed mainly by the transition from perfect slip to grain boundary-mediated process i.e. the $1/d$ line between Region I and III. For metals with low stacking fault energy or under high stress, the crossover involves partial slip in Region II as an intermediate stage. Stacking faults transected the small grains and grain boundary processes increased with decreasing grain size. The strongest grain size corresponds to the zone between region I and II and it increases with decreasing the stacking fault energy. They have also claimed that the strongest size increases with decreasing stacking fault energy. But this is in contrast with the molecular dynamics simulation results of Copper and Nickel where the crossover is found at grain size lower than Al [28, 77, 104]. This suggests that there is no monotonous scaling exists between the strongest size and stacking fault energy.

Later on, Van Swygenhoven *et al* showed that the nature of slip in nanocrystalline materials seen in molecular dynamics cannot be interpreted in terms of the absolute value of the stacking fault energy [111]. Also, the crossover of slip via perfect or extended dislocations cannot be only described in terms of the absolute value of the stacking fault energy. A correct interpretation should be related to the generalized planar fault curve including both stable and unstable stacking fault energy. The dependency of the slip to the type of the metal is explained in terms of the ratio of the unstable stacking fault energy to the stable stacking fault energy. Once this ratio close to unity, the emission of trailing partial dislocation is possible due to a small energy barrier defined as the difference between the stable stacking fault energy and the unstable stacking fault energy. This mechanism is seen in nanocrystalline Al where close loops of full dislocations consisting of two Schokley partials have been seen [104]. In contrast, because of the low ratio between the stable and the unstable stacking fault energy in Copper and Nickel only extended partials dislocations have been observed in the timescale of molecular dynamics [28, 77]. A change of the deformation mechanism from one that is governed by extended partial dislocations to one that includes all types of slip which are extended partials, full dislocations, and twinning as the stress is increased by a factor of 2. This suggests that these mechanisms are plausible to be seen in experiments and only extended partial dislocations is observed in molecular dynamics simulations because of the short timescale covered by the method [111].

Experimental observations Stacking fault generated by the emission of Shockley partials, full dislocations, and twins have been seen experimentally in many works using HRTEM [87, 107, 114–117]. The three mechanisms seen by Yamakov *et al* for deformation twinning in nanocrystalline Al have been experimentally validated. Firstly, the overlapping of two extended dislocations with a stacking fault is seen in [114, 116]. Also, the formation of deformation twins via emission of Shockley partials from grain boundaries have been verified by high-resolution electron microscopy [118, 119]. Finally, the grain boundary splitting and migration thereby generating twin boundaries have also been observed experimentally in many work [114].

Molecular dynamics simulations showed that twinning is favorable in nanocrystalline Al and difficult of Copper and Nickel due to the large barrier to emit twinning partial at the timescale of molecular dynamics simulations [111]. Whereas experiments showed that bulk 3D nanocrystalline Nickel and Copper deformed readily by twinning [87, 114, 116, 117]. Wu *et al* suggested that the generalized planar fault energy curve lonely is not sufficient to explain the tendency to nanocrystalline materials and found an inverse grain size effect on twinning below a critical grain size in an electrodeposited nanocrystalline Nickel with 25 nm mean grain size [115, 120]. The new twinning route in FCC nanocrystalline Pt have been observed by Wang *et al* [121]. Deformation twinning has initiated through the formation of two stacking faults separated by a single atomic layer and proceeded with the emission of a partial dislocation in between these two stacking faults.

1.3 Research objectives

The above discussion shows that, until now, the mechanical behavior of the nanocrystalline materials is not well understood. In this respect, a vast research area is still available to elucidate the current understanding of the interplay between the deformation mechanisms presented. As mentioned above there is a need to initial samples that represent faithfully the nanocrystalline structure in molecular dynamics. These samples should contain low and high angle grain boundaries, curved grain boundaries and different type of defects and impurities. A recent melting cooling method has been applied to generate initial nanocrystalline samples as relevant as possible. This method allows producing columnar nanocrystalline samples with curved grain boundaries, in addition to the presence of defects inside the grains of these samples such as

vacancies, interstitials, and dislocations.

Moreover, the influence of the mean grain size and the strain rate on the interplay between the deformation mechanisms of nanocrystalline materials is still controversial. For example, Vo *et al* showed that for nanocrystalline Copper sample with a 5 nm grain size, dislocations contribute to 50% of the total plastic strain during steady-state deformation at a rate of $10^8\ s^{-1}$, but this fraction decreases to 35% at a rate of $10^{10}\ s^{-1}$. When the grain size is increased to 20 nm, dislocations contribute on the assimilation of about 90 % of the strain, even at $10^{10}\ s^{-1}$ [122]. In this context, we firstly investigate the influence of the mean grain size on the mechanical behavior of nanocrystalline materials. Also, in order to elucidate how the deformation mechanisms of nanocrystalline materials evolve in a different crystal structure. Two types of structures have been investigated in our study, an FCC Copper and an HCP Titanium α.

Furthermore, large strain rate sensitivity has been found for nanocrystalline materials [16, 123]. An enhancement of the grain boundary accommodation processes with the decrease of the strain rate has been shown. Molecular dynamics simulations suggest that dislocations can propagate on planes with high resolved shear stress through the stress intensity of grain boundary at high strain rate [29, 37]. Farkas *et al* [32] found that grain boundary accommodation mechanisms (section 1.2.2.1) are mainly stress driven at high strain rate. On the other hand, very large strain rates are normally used in atomic simulations e.g. above $10^7\ s^{-1}$, far away from the experimental limit.

Therefore, a clear question deals with the effect of reducing the strain rate in molecular dynamics simulations on dislocations and grain boundary mediated processes. In this aim, the influence of the strain rate on the mechanical behavior of nanocrystalline Copper has been explored at different orders of magnitude going from 10^4 to $10^{10}\ s^{-1}$. A range of the strain rate used in our simulations is attainable experimentally (e.g $10^4 s^{-1}$ is reached by SMAT [43]). The strain rate dependence of twinning, dislocations and grain boundary accommodation processes has been analyzed on the atomic level. Moreover, the relaxation behavior of nanocrystalline Copper has been studied in order to explore the equilibrium properties of these nanocrystalline models on the timescale of molecular dynamics simulations.

Chapter 2

Methodology

Contents

2.1 Classical molecular dynamics simulations

2.1.1 Time evolution of positions and velocities

Molecular dynamics simulation is a technique that permits to compute the equilibrium and transport properties of a classical many body system composed of a group of atoms. The basic numerical technique in molecular dynamics builds on the solution of the equation of motion for each atom out of which the position, the velocity and the energy of each atom can be predicted as a function of an external constraints (e.g. displacement, temperature, stress). Therefore, molecular dynamics simulation appears to be particularly attractive for the study of the response of nanocrystalline materials under mechanical deformation. The system of equation to be solved is as follow:

$$F_i = m_i \ddot{r}_i \qquad \forall i \in \Omega \tag{2.1}$$

here, F_i, m_i and r_i denote the total force applied on atom i by its neighbors, the mass and the position of atom i.

The total force on atom i is calculated as a sum of the force f_{ij} resulting from the interaction of atom i with each neighboring atom j within a specific cutoff radius r_c. The force of interaction between two atoms is simply given by:

$$f_{ij} = -\nabla U(r_{ij}) \tag{2.2}$$

where $r_{ij} = \mid r_i - r_j \mid$ denotes the distance between the atoms i and j and $U(r_{ij})$ is the associated potential energy. The total force acting on atom i is:

$$F_i = \sum_{\substack{j=1 \\ j \neq i}}^{N} f_{ij} \tag{2.3}$$

Once, the calculation of the total force on each atom has been achieved, Newton's equation of motion is integrated. The Verlet algorithm is used to solve the equation of motion and is based on a Taylor expansion of the positions r_i around time t:

$$r_i(t+\Delta t) = r_i(t) + \dot{r}_i(t)\Delta t + \frac{F_i(t)}{2m_i}\Delta t^2 + \dddot{r}_i(t)\Delta t^3 + O(\Delta t^4) \tag{2.4}$$

$$r_i(t-\Delta t) = r_i(t) - \dot{r}_i(t)\Delta t + \frac{F_i(t)}{2m_i}\Delta t^2 - \dddot{r}_i(t)\Delta t^3 + O(\Delta t^4) \tag{2.5}$$

$$r_i(t+\Delta t) = 2r_i(t) - r_i(t-\Delta t) + \frac{F_i(t)}{m_i}\Delta t^2 + O(\Delta t^4) \tag{2.6}$$

$$v_i(t) = \frac{r_i(t+\Delta t) - r_i(t-\Delta t)}{2\Delta t} + O(\Delta t^2) \tag{2.7}$$

From equation (2.6) one can calculate the new position of atom i and from equation (2.7) the velocity of atom i is calculated. Note that the new position is estimated at order Δt^4. At each timestep, positions and velocities are updated starting from an initial configurations at t = 0. The information of the initial particles positions depends on the microstructure to be studied e.g. to simulate a single crystal, atoms are arranged into a specific crystal structure according to the type of the metal. The initial velocities are assigned for particles in a Maxwell-Boltzmann distribution so that the relation of the kinetic energy and temperature holds:

$$\frac{3N}{2}k_B T(t) = \frac{1}{2}\sum_{i=1}^{N} m_i \dot{r}_i(t)^2 \tag{2.8}$$

As described above, the molecular dynamics simulation of N particles in a volume V is equivalent to ensemble average in the microcanonical (constant NVE) ensemble. This means that the energy and the volume are constant with time. However, to simulate the behavior of the system at constant pressure or temperature, molecular dynamics simulations in other ensemble such as canonical (NVT ensemble) and isobaric isothermal (NPT) ensemble should be done. Therefore, dynamical approach have been introduced that reformulate the equation of motion of the system to respect the macroscopic state of the ensemble [124]. In the literature these approach are described very well and are implemented in various molecular dynamics codes such as the Nosé-Hoover thermostat and barostat, Berendsen thermostat and barostat, Andersen thermostat ... [125–128].

All molecular dynamics simulations of this work were performed using LAMMPS which is a molecular dynamics code that models the behavior of particles in a liquid, solid, or gas state. It can model rather efficiently atomic, polymeric, biological, metallic, granular, and coarse-grained systems using different types of

force fields and boundary conditions [129].

2.1.2 Virial stress

The average stress tensor for the system is calculated using the virial formulation [130]:

$$\sigma_{ij}^{V} = \frac{1}{V}\sum_{\alpha}\left[\frac{1}{2}\sum_{\beta\neq\alpha}^{N}\left(r_i^{\beta}-r_i^{\alpha}\right)F_j^{\alpha\beta}-m^{\alpha}v_i^{\alpha}v_j^{\alpha}\right] \tag{2.9}$$

$$F_j^{\alpha\beta} = \frac{\partial U(r^{\alpha\beta})}{\partial r^{\alpha\beta}}\frac{r_j^{\alpha\beta}}{r^{\alpha\beta}} \tag{2.10}$$

$$\sigma_{ij}^{V} = \frac{1}{V}\sum_{\alpha}\left[\frac{1}{2}\sum_{\beta\neq\alpha}^{N}\frac{\partial U(r^{\alpha\beta})}{\partial r^{\alpha\beta}}\frac{r_i^{\alpha\beta}r_j^{\alpha\beta}}{r^{\alpha\beta}}-m^{\alpha}v_i^{\alpha}v_j^{\alpha}\right] \tag{2.11}$$

where σ_{ij}^{V} is the average component ij of the stress tensor of the system, V is the volume of the system, m^{α} is the mass of atom α, $r_j^{\alpha\beta}$ is the j^{th} component of the distance between atom α and β, $F_j^{\alpha\beta}$ is the j^{th} component of the force of interaction between atom α and β, and $U(r^{\alpha\beta})$ is the potential energy corresponding to the distance $r^{\alpha\beta}$.

2.1.3 Periodic boundary conditions

Similar to Finite Elements or Finite Differences simulations, molecular dynamics simulations use boundary condition imposed to the physical system. Remembering that billion atoms correspond to a box size of less than a micrometer, there are spatial limitations for molecular dynamics simulations, even when using massively parallel computing. A commonly used approach is to impose periodic boundary conditions. In such a way, the simulation box is virtually replicated infinitely in all periodic dimensions as seen in Figure 2.1. As a result, each atom leaving the simulation box from one side will necessarily enter from the opposite side. If periodic boundary conditions are used in all directions, the system is considered as the bulk of the material.

2.1.4 Length and time scale restrictions

The time scale of molecular dynamics simulations is governed by the atomic frequencies at the scale of the typical phonon frequencies (Debye frequency $\approx 10^{13}$ Hz). Hence, to describe accurately these trajectories a timestep from 1 to 5 femto-second (fs) is usually used. In this work, we use a timestep of 3 fs

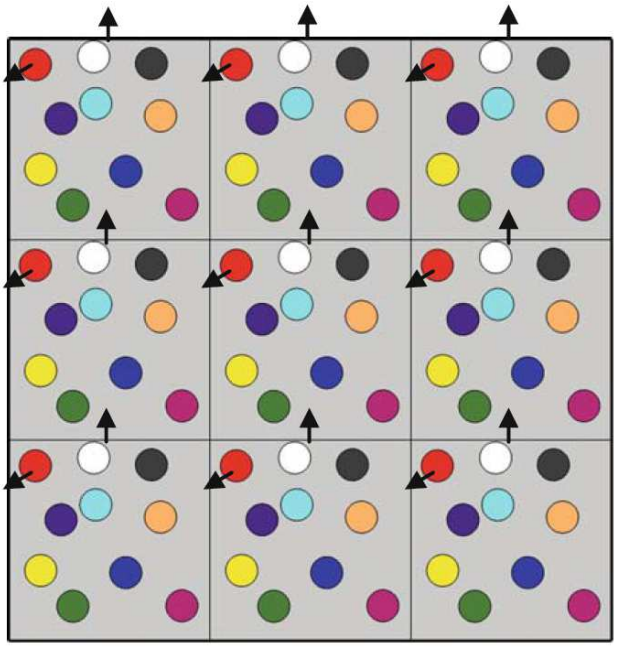

FIGURE 2.1: Sketch of a two dimensional primary cell periodically repeated in all directions [54] .

which ensures conservation of energy. As a consequence, very high strain rates (e.g. above $10^7\ s^{-1}$ are essential to attain considerable plastic deformation.

We will see in the following, a detailed study focusing on the effect of strain rate on the mechanical properties of nanocrystalline materials.

As mentioned above, another important limitation of molecular dynamics simulations is the size of the simulation box. To overcome this restriction periodic boundary conditions are used.

2.2 Interatomic potential

2.2.1 Embedded atomic method

In molecular dynamics simulations, the accuracy of the interatomic potential is crucial and permits to predict the structural properties of the etomic system (such as equilibrium lattice distance, the defects formation energy, the sublimation energy, the elastic constants...). For metals, the Embedded Atomic Method (EAM) potential has been proposed to overcome the limitation of the pair interaction potentials and to take into account in an effective way the metallic character of the bonding. Within the framework of Density Functional Theory (DFT), the starting point of the EAM potential is the observation of the electron density in the vicinity of each atom seen as the superposition

of contribution from surrounding atoms. The total energy on each atom can be therefore defined as the sum of an embedding energy of the electron density of this atom in the background electron density of the surrounding atoms in addition to a pairwise core core repulsion energy. This leads to the approximation of the total energy of the system as [131]:

$$E_{total} = \sum_i E_i = \sum_i F_i(\rho_{h,i}) + \frac{1}{2}\sum_i \sum_{j \neq i} \Phi(r_{ij}) \tag{2.12}$$

where, $\rho_{h,i}$ is the host electron density of the atom i due to the surrounding atoms, $F_i(\rho)$ is the embedding energy and $\Phi(r_{ij})$ is the pair repulsion energy. The electron density of atom i is approximated by the superposition of neighbor atomic densities:

$$\rho_{h,i} = \sum_{j \neq i}^{N} \rho_j^a(r_{ij}), \tag{2.13}$$

Here, $\rho_j^a(r_{ij})$ denotes the contribution of the atom j to the density of atom i. $\rho_j^a(r_{ij})$ can be further approximate by:

$$\rho_j^a(r_{ij}) = n_s \rho_s^a(r) + n_d \rho_d^a(r) \tag{2.14}$$

where n_s and n_d are the number of outer s and d electrons and ρ_s^a and ρ_d^a are the densities associated with the s and d wave function. The pair-wise interaction between atom i and j being defined as:

$$\Phi_{ij}(r_{ij}) = \frac{Z_i(r_{ij}) Z_j(r_{ij})}{|r_{ij}|}, \tag{2.15}$$

Where $Z(r_{ij})$ denotes the effective charge of a given atom. Both the embedding function F_i and the pair repulsive energy Φ_{ij} are typically obtained via an empirical fit of intrinsic material properties which are then uniquely defined by the potential.

We used the EAM potential proposed by Foiles *et al* to simulate the mechanical properties of nanocrystalline Copper [132] and the EAM potential proposed by Bonny *et al* to study the mechanical properties of Iron alloys ($FeNi_{14}Cr_{18}$). [133].

2.2.2 Modified embedded atomic method

The modified embedded atomic method (MEAM) formalism is an extension of the EAM developed by Baskes [134]. The MEAM includes an angular dependent electron density to model the effects of bond bending which is not the case of the EAM potential. Lenosky *et al* modified the original MEAM potential by using cubic splines for the functional form [135]. Henning *et al* used this functional form to generate a spline based MEAM potential for Titanium [136] and this potential has been used in chapter 3 for the study of the mechanical properties of HCP α-Titanium.

2.2.3 Validation of the EAM potential for Copper

Before the application of such potentials to large scale atomic systems, we have analyzed the accuracy of the interatomic potential developed for Copper by Foiles *et al* [132]. The equilibrium lattice distance, the elastic constants and the generalized stacking fault curve for monocrystalline Copper have been calculated and the obtained values are compatible with the experimental results.

Zero temperature equilibrium lattice parameter calculation In this test case, a cubic simulation box with 20 FCC lattices have been taken along x[100], y[010] and z[001] that contains 32 000 atoms with periodic boundary conditions in x, y and z as seen in Figure 2.2 (a). To compute the equilibrium lattice distance of this potential model, we have set the lattice distance for Copper at 3.58 Å, i.e. lower than the experimental value of 3.615 Å [137]. Then we applied an energy minimization to the whole simulation box to obtain a minimum potential energy corresponding to the equilibrium lattice distance (red curve in Figure 2.2 (b)). We used conjugate gradient algorithm with a specific convergence criteria of 10^{-10} for energy and force. We applied the same test but with different lattice and final results of this test is also illustrated in Figure 2.2 (blue curve). We can see that the potential energy per atom decreases to reach a minimum at an equilibrium lattice distance a = 3.615 Å. Which exactly matches the experimental data. The calculated cohesive energy is $E_{coh} = -3.54eV$ which agrees very well with the experimental value of the sublimation energy [138] (table 2.1).

Zero temperature elastic constants In linear elasticity, the most general linear relation among all the components of the stress and strain tensor is

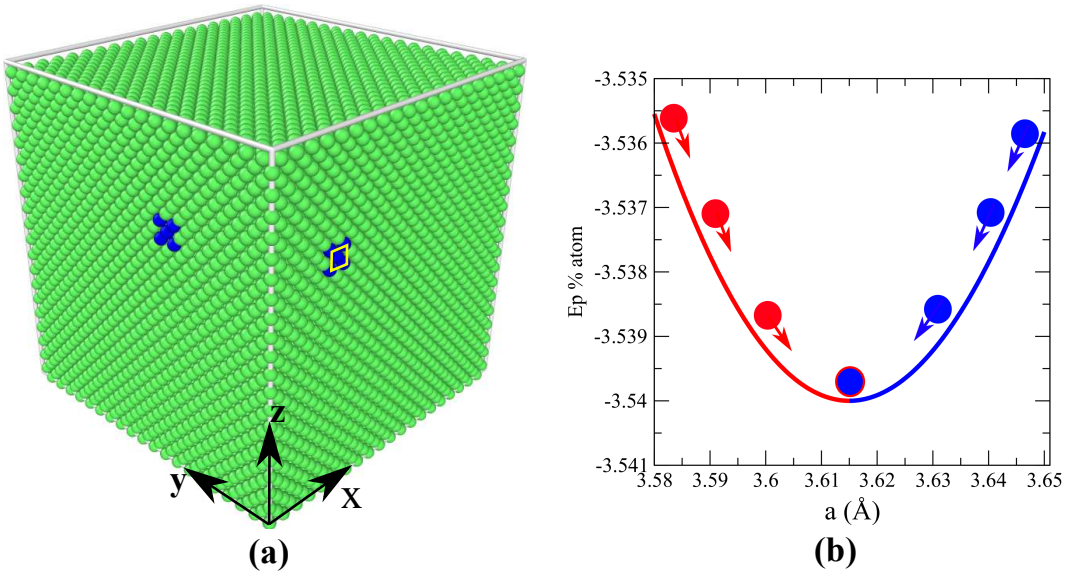

FIGURE 2.2: (a) simulation box of pure Copper at 0K, (b) Variation of the potential energy per atom as a function of lattice constant of Copper.

defined by the generalized Hooke's law:

$$\sigma_{ij} = C_{ijkl}\varepsilon_{kl} \tag{2.16}$$

Here C_{ijkl} are the components of the fourth order stiffness tensor of material properties. However, due to the symmetries of the stress and strain tensor and to the equivalence of the mixed partial derivatives in strain calculation, the number of independent elements of the stiffness tensor can be reduced for the most anisotropic linear elastic material. Moreover, due to the cubic FCC symmetry the x, y and z directions are identical. The number of the elastic matrix component is reduced to three independents constants that can be written in Voigt notation as C_{11}, C_{12} and C_{44}. To find C_{11} and C_{12} a simulation box with 10 lattice distance in the x[100], y[010] and z[001] has been constructed with periodic boundary conditions in all directions. Then an energy minimization with a conjugate gradient algorithm is performed to ensure that the pressure on the simulation is zero in all directions. After that, the box is rescaled in the x direction $L_x = L_0(1+\varepsilon_{xx})$ with a very small strain $\varepsilon_{xx} = 10^{-5}$ in the elastic regime. An energy minimization is then applied to obtain a relaxed potential energy and virial stress σ_{ij} leading to $C_{11} = \frac{\sigma_{xx}}{\varepsilon_{xx}}$ and $C_{12} = \frac{\sigma_{yy}}{\varepsilon_{xx}} = \frac{\sigma_{zz}}{\varepsilon_{xx}}$.

These simulations have been repeated in the y and z directions. We found $C_{11} = 167\ GPa$, $C_{12} = 124\ GPa$ and $B = 138\ GPa$ that are very well compatible with the experimental values (table 2.1) and those obtained by Foiles *et al*[132].

TABLE 2.1: Comparison of the pure metal properties calculated by EAM potential with Experimental values

	EAM Copper	Exp
a_0 (Å)	3.615	3.615 [137]
E_{coh} (ev)	-3.54	-3.54 [138]
C_{11} (GPa)	167	170 [139]
C_{12} (GPa)	124	122.5 [139]
C_{44} (GPa)	76	75.8 [139]
B (GPa)	138	138 [139]

The bulk modulus is calculated to be:

$$B = \frac{C_{11} + 2C_{12}}{3} \tag{2.17}$$

To calculate the C_{44} constant, a shear stain $\varepsilon_{xy} = 10^{-5}$ is applied to the simulation box, C_{44} is calculated as $C_{44} = \frac{\sigma_{xy}}{\varepsilon_{xy}}$. The calculated values of C_{44} is 76 GPa which corresponds very well to the value obtained in the initial study of the potential [132].

Generalized stacking fault energy curve for EAM Copper The {111} planes are the highest close packed planes in FCC metals. Therefore, they are the main slip systems for dislocations in these metals and the Burgers vector are usually of $< 112 >$ type due to energy consideration [68] . Therefore the slip resistance of partial dislocation is associated with $< 112 >$ paths on the (111) γ energy surface. When going to nanoscale, grain boundaries have been found to be the sources and sinks to dislocations. Therefore, one of the key criterion is the energy barrier to nucleate a dislocation from grain boundary. This can be derived from the shape of the generalized stacking fault energy (GSFE) curve.

By definition, the GSFE curve represents the energy cost of rigidly shifting two semi-infinite blocks of crystal on a (111) plane along the $[11\bar{2}]$ direction. Figure 2.3 shows a schematic plot of the shape of the GSFE curve with respect to the displacement magnitude. A number of points enumerated from 1 to 5 have been marked on the curve where snapshots of the stacking sequence have been taken. In position 1, the stacking sequence is a perfect FCC sequence (ABC ABC ABC...). The FCC lattice is oriented to the basis axis seen in the Figure. Once a shear deformation is applied along the $[11\bar{2}]$ direction, a transition from 1 to a maximum energy state (position 2) obtained. It correspond to a $b/2$ displacement where b is the magnitude of the Burger vector for a Shockley partial

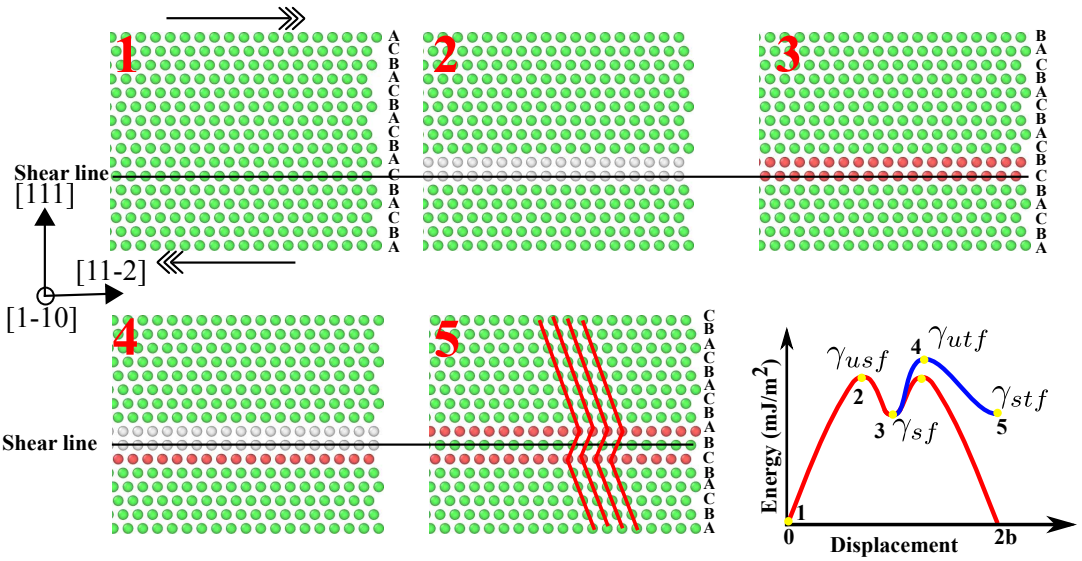

FIGURE 2.3: The GSFE curve for the < 112 > direction in an FCC crystal. The points 1 to 5 are represented by a snapshots of the atomic configuration.

dislocation of amplitude $a\sqrt{6}/6$ [68]. This position corresponds to the unstable stacking fault energy γ_{usf} which is also the energy barrier needed to nucleate a dislocation on a grain boundary. Once shear deformation continues to reach a displacement of the Burger vector b, the energy evolves to a stable position 3 corresponding to the stable stacking fault energy γ_{sf}. In this position, the lattice is in equilibrium sheared state and a stacking fault ribbon forms due to the change of the stacking sequence as shown in Figure 2.3 3. In this position, the region above the shear line in 1 is sheared with respect to the one below this line by a distance equal to b. Two HCP planes have been formed and colored in red, the stacking sequence of these planes are BCB and CBC corresponding to the HCP structure. Thus, the barrier to the nucleation of a trailing partial corresponds to $\gamma_{usf} - \gamma_{sf}$.

Also, the twinning tendency of nanocrystalline materials can be explained in terms of the GSFE curve. If the configuration 3 is taken and a shear deformation is applied on adjacent shear plane to the shear line in 1. The GSFE will continue on the blue line in the Figure 2.3 and not the red line. Two positions can be remarked, (i) the maximum one corresponding to the unstable twinning fault energy γ_{utf} and (ii) the equilibrium one at 2b displacement which is the stable twinning fault energy γ_{stf}. The stacking sequence will form 2 HCP planes (Figure 5) and between them an FCC plane, and the energy barrier corresponding to such stacking fault is $\gamma_{utf} - \gamma sf$. The twinning tendency of a material depends on the ratio between the energy barrier for the emission of

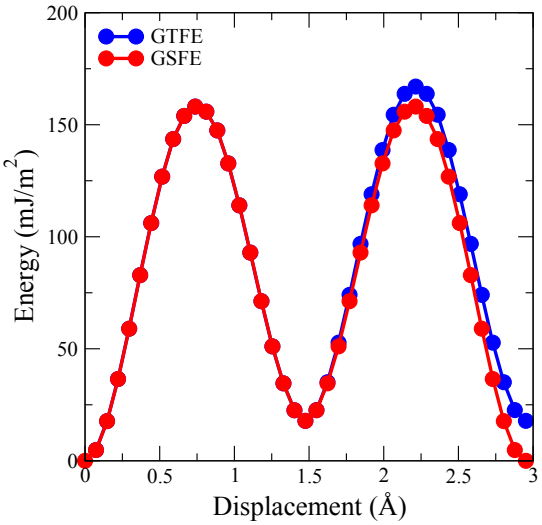

FIGURE 2.4: The GSFE curve for the < 112 > direction in an FCC crystal Copper calculated using the EAM potential of Foiles *et al* [132].

a trailing partial and the energy barrier to nucleate a micro-twin or extrinsic stacking fault $\frac{\gamma_{utf}-\gamma sf}{\gamma_{usf}-\gamma_{sf}}$. If this ratio is close to one twinning mechanism will be an important deformation mechanism [111].

To compute the GSFE curve we created a cubic simulation box with 20 FCC lattice distance along x[11$\bar{2}$], y [111] and z [1$\bar{1}$0] at 0K. Then, the simulation box has been decomposed into 2 regions and the upper region is shifted with respect to the lower one in the [11$\bar{2}$] by a magnitude b. During the deformation the energy is calculated as follows:

$$E(mJ/m^2) = \frac{E(t) - E(0)}{A} \tag{2.18}$$

where A is the area of the cross section of the simulation box in the [111] direction, $E(t)$ is the total energy of the system at time t and $E(0)$ is the energy of the system before deformation.

Figure 2.4 shows the GSFE and the generalized twinning fault energy (GTFE) curve calculated for Copper using the EAM potential [132]. The results of the two curves are presented in the table 2.2. The values of the stacking fault parameters are somewhat lower than that of the DFT calculation. However, the fitting of an EAM potential does not take the stacking fault parameters into consideration. From the ratio of γ_{sf}/γ_{usf} we can predict that trailing partial should be barely observed because the value of $\gamma_{utf}/\gamma_{usf}$ is close to 1 (Figure 2.4). As a consequence twinning will play an important role in the deformation

TABLE 2.2: The values of the stacking fault parameter extracted from the curves in Figure 2.4

	EAM Copper	exp.	DFT [140]	Ref. [141]
γ_{usf} (mJ/m^2)	158		210	164
γ_{sf} (mJ/m^2)	17.8	45 [142]	49	38
γ_{utf} (mJ/m^2)	167			
γ_{stf} (mJ/m^2)	17.8			
γ_{sf}/γ_{usf}	0.11		0.23	0.23
$\gamma_{utf}/\gamma_{usf}$	1.06			

behavior of nanocrystalline Copper as associated energy barriers are comparable (see Figure 2.3 and 2.4).

2.2.4 Validation of the EAM potential for $FeNi_{14}Cr_{18}$

In order to study the deformation mechanisms responsible for the formation of the nanocrystalline layer in the austenitic 316L stainless steel. We used the chemical composition of the iron alloy of ref. [143] but restricted to the three main elements with the highest weighting fraction (Fe, Ni and Cr), i.e. the iron alloy studied is the $FeNi_{14}Cr_{18}$ with 14% and 18% composition of Ni and Cr respectively.

The elastic constants, the equilibrium lattice position and the parameters of the stacking fault energy of this potential have been calculated using the same procedure described above for Copper. The results reproduce exactly the calculated values by Bonny *et al* [133], and a summary of these values are presented in Figure 2.5.

In addition, the same processes applied to validate the interatomic potential used for Copper have been done for the $FeNi_{14}Cr_{18}$ to validate the use of the interatomic potential developed by Bonny *et al* [133]. Firstly, the elastic constant and the equilibrium lattice position have been calculated (table 2.3). The results are consistent with the experimental values which indicate that the potential can reproduce rather well the mechanical properties of the iron alloys.

The GSFE and the GTFE curves have been also calculated (Figure 2.6 (b)), and a snapshot of an atomic configuration is shown (Figure 2.6 (a)). The shear

	Iron		Nickel		Chromium	
Configuration	Target	EAM-13	Target	EAM-13	Target	EAM-13
E_{coh} (fcc) (eV/at)	—	4.40	4.45	4.45	—	4.20
E_{coh} (bcc) (eV/at)	4.28	4.28	4.35	4.35	4.10	4.10
E_{coh} (hcp) (eV/at)	—	4.40	4.42	4.43	—	4.16
a (fcc) (Å)	3.450–3.562	3.562	3.519	3.522	3.520–3.610	3.534
a (bcc) (Å)	2.832–2.860	2.860	2.801	2.800	2.878–2.885	2.882
a (hcp) (Å)	—	2.519	—	2.485	—	2.490
c/a (hcp)	—	1.633	—	1.642	—	1.663
C_{11} (GPa)	154	154	247	247	249	245
C_{12} (GPa)	122	122	147	144	178	173
C_{44} (GPa)	77	77	125	108	143	148
E_{SF} (mJ m^{-2})	4	0	111–128	130	156–341	221
E_m (Vac) (eV)	0.62	0.64	1.09	1.09	—	0.84
E_f (Vac) (eV)	1.82–1.95	1.87	1.37–1.45	1.39	2.14	2.19
E_b (di-Vac 1nn) (eV)	0.04–0.18	0.24	0.02	0.12	0.15	0.28
E_b (di-Vac 2nn) (eV)	−0.06–0.07	0.04	−0.08	0.04	0.03	0.07
E_f(⟨1 0 0⟩ SIA) (eV)	3.20–3.62	5.25	4.07–4.11	5.83	—	4.85
E_f(⟨1 1 0⟩ SIA) (eV)	4.17–4.82	5.70	4.91–4.99	6.42	—	5.41
E_f(⟨1 1 1⟩ SIA) (eV)	4.56	6.57	4.69–4.72	7.01	—	5.44
E_f(Octa SIA) (eV)	4.35	5.65	4.25–4.32	6.16	—	4.97
E_f(Tetra SIA) (eV)	3.66–4.32	7.06	4.69–4.71	7.16	—	5.39

FIGURE 2.5: Overview of some elemental properties of the potential and their comparison with experiment and DFT [133].

TABLE 2.3: Comparison of the elastic and equilibrium properties between the potential for the $FeNi_{14}Cr_{18}$ alloy and 316L stainless steel [133].

	EAM $FeNi_{14}Cr_{18}$	Exp
a_0 (Å)	3.511	
E_{coh} (ev)	-3.54	
C_{11} (GPa)	224	204-226
C_{12} (GPa)	142	132-134
C_{44} (GPa)	132	111-122
B (GPa)	170	157-164

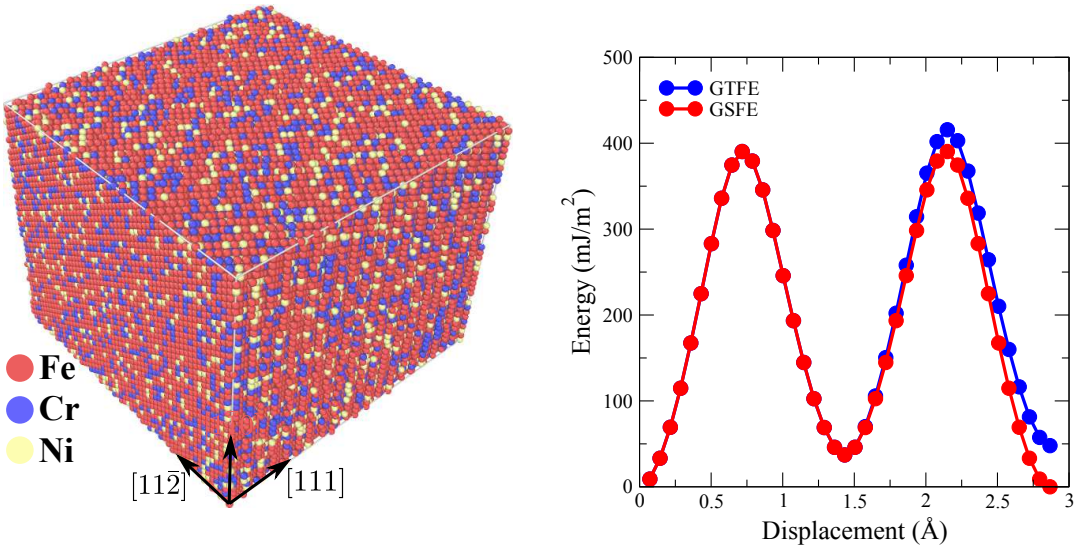

FIGURE 2.6: (a) snapshot of the atomic configuration of $FeNi_{14}Cr_{18}$ used to calculate the GSFE and the GTFE, (b) GSFE curve for the < 112 > direction in the FCC crystal $FeNi_{14}Cr_{18}$ calculated using the EAM potential of Bonny *et al* [133].

TABLE 2.4: Values of the stacking fault parameter extracted from the curves in Figure 2.6 (b)

	EAM Copper
γ_{usf} (mJ/m^2)	390.3
γ_{sf} (mJ/m^2)	37.1
γ_{utf} (mJ/m^2)	415.7
γ_{stf} (mJ/m^2)	47.9
γ_{sf}/γ_{usf}	0.095
$\gamma_{utf}/\gamma_{usf}$	1.065

deformation is applied to this sample along the [11$\bar{2}$] direction and the parameters of the generalized planar fault curves have been summarized in the table 2.4. The ratio $\gamma_{sf}/\gamma_{usf} = 0.095$ and $\gamma_{utf}/\gamma_{usf} = 1.065$ are very close to that calculated for Copper, as shown in table 2.2. Therefore, one should expect the same deformation behavior of Copper and $FeNi_{14}Cr_{18}$. However, the value of the γ_{usf} for $FeNi_{14}Cr_{18}$ is more than two times higher than the one of Copper. Thus, the barrier to the nucleation of dislocation should be larger for this iron based alloy.

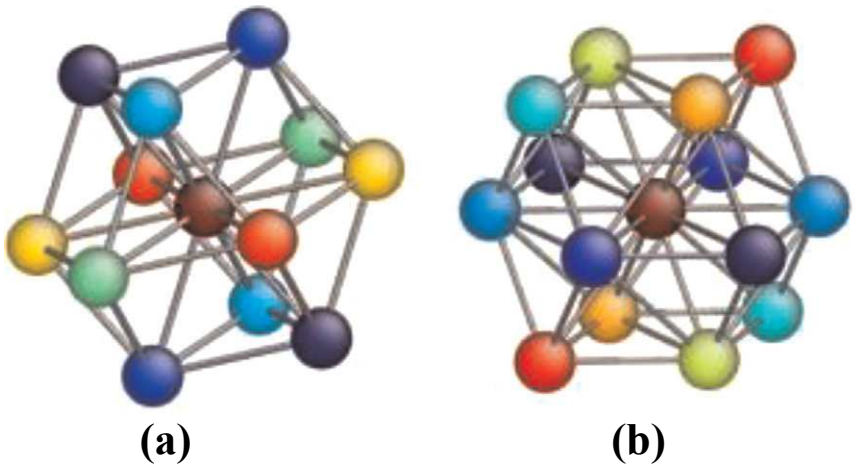

FIGURE 2.7: Pairs of atoms diametrically opposed from a central atom re-identified by the same color (a) FCC, 6 pairs and (b) BCC, 7 pairs.

2.3 Analysis techniques

The simulated configurations can be visualized using the scientific software package Open Visualization Tool (OVITO) [144]. This three-dimensional visualization software has been widely used to post-process atomistic data obtained from molecular dynamics simulations.

Several visualization methods have been developed which provide a detailed characterization of the atomic configurations. An arbitrary number of physical and structural properties can be calculated and assigned to individual atoms during the simulation. Using these quantities, a classification scheme can be developed to visualize each component of the atomic structure, including perfect atoms, dislocation cores, stacking faults, twin boundaries, grain boundaries, etc. The main visualization criteria that are currently used in the study of mechanical behavior of nanocrystalline materials are summarized in this section.

2.3.1 Centrosymmetric parameter

The CentroSymmetric Parameter (CSP) can be used to characterise whether the atom is part of perfect lattice, or a local defect (dislocations, twinning faults or stacking faults), or at a surface. The parameter is defined by [145]:

$$CSP = \sum_{i=1}^{N/2} \left| \vec{R}_i + \vec{R}_{i+N/2} \right|^2 \tag{2.19}$$

where N is the number of nearest neighbors, $\vec{R}_i$ and $\vec{R}_{i+N/2}$ are the separation vector from the central atom to a given pair of opposing neighbor atoms (Figure 2.7). This parameter is only marginally affected by elastic distortions of the crystal, but it is sensitive to random thermal fluctuation. A proper threshold should be chosen to distinguish defect atoms from perfect lattice atoms especially at elevated temperatures. In the following, atom with $CSP < 1$ is considered in a perfect position, whereas, atoms with $CSP \geqslant 1$ are considered as defect atoms (grain boundary atom, stacking fault,..).

2.3.2 Common neighbor analysis

Common neighbor analysis (CNA) is a method to characterize the local structure of each atom, i.e. if this atom belongs to an FCC, BCC, HCP or other structure [146, 147]. In CNA a characteristic signature is computed from the topology of bonds that connect the surrounding neighbor atoms. Two atoms are said to be nearest neighbors (or bonded) if they are within a specific cutoff radius r_{cut}. Therefore, CNA is based on the determination of three parameters resulting from the determination of the nearest neighbors of each atom. Firstly, to determine the bonded neighbors a specific cutoff radius should be specified. For densely packed structures (FCC and HCP) the cutoff distance is set to be between the first and second neighbor shell, giving for FCC:

$$r_{cut}^{FCC} = \frac{1}{2}\left(1+\sqrt{\frac{1}{2}}\right)a_{FCC} \simeq 0.854 a_{FCC} \tag{2.20}$$

where a_{FCC} is the lattice constant of the crystal structure. For the BCC lattice, two neighbor shells need to be taken into account, and atoms are considered to be bonded with their first and second-nearest neighbors:

$$r_{cut}^{BCC} = \frac{1}{2}\left(1+\sqrt{2}\right)a_{FCC} \simeq 1.207 a_{BCC} \tag{2.21}$$

After the determination of the bonded neighbors of each atom within the specified cutoff radius, three parameters are determined:

1. the number of neighbor atoms n_{cn} the central atoms and its bonded neighbor have in common

2. the total number of bonds between these common neighbors, n_b

3. the number of bonds in the longest chain of bonds connecting the common neighbors (n_{lcb})

TABLE 2.5: Reference triplets for each structure type where N is the number of nearest neighbor

FCC (N=12)	HCP (N=12)	BCC (N=14)	Cubic diamond (N=16)
12x(421)	6x(421)	8x(421)	12x(543)
	6x(422)	6x(444)	4x(663)

This yields N triplets (n_{cn}, n_{cn}, n_{lcb}), which are compared with a set of reference signatures to assign a structural type to the central atom (table 2.5)

Later, Stukowski [148] developed new CNA method called adaptive common neighbor analysis (ACNA). The ACNA is an extension of the CNA but with the definition of a local cutoff radius for each atom. In contrast with the CNA where a specified cutoff radius is imposed for the whole set of atoms, the ACNA allows one to characterize the structure of multi-phase systems where the choice of the cutoff parameter is adapted.

2.3.3 Shear strain analysis

The shear strain analysis is an effective method to visualize the plastic or irreversible deformation. The shear strain is calculated by comparing an running configuration with a reference one. The shear strain tensor is then calculated as the relative displacement of each atom with respect to its nearest neighbor selected in the reference configuration [149]. The coordinate of the atom i in the reference configuration is $\{x_i^0\}$ and $\{x_i\}$ in the actual one. For each neighbor j of atom i, their current separation vector is $d_{ij} = x_j - x_i$ and their reference separation is $d_{ij}^0 = x_j^0 - x_i^0$.

The relative position vector $d_{ij}^0$is transformed into d_{ij} by a locally affine transformation tensor for each atom i $\mathbf{F}_i$. $\mathbf{F}_i$ is determined by minimizing:

$$\sum_{j \in N_i^0} \left| d_{ij}^0 \mathbf{F}_i - d_{ij}^0 \right|^2 \tag{2.22}$$

$$\Rightarrow \quad \mathbf{F}_i = \left(\sum_{j \in N_i^0} d_{ij}^{0T} d_{ij}^0 \right)^{-1} \left(\sum_{j \in N_i^0} d_{ij}^{0T} d_{ij} \right) \tag{2.23}$$

Then the local Lagrangian strain matrix is computed as follows [149]

$$\mathbf{E}_i = \frac{1}{2} \left(\mathbf{F}_i \mathbf{F}_i^T - \mathbf{I} \right) \tag{2.24}$$

The shear strain called also Von-Mises strain E_i^{Mises} is computed as follow:

$$\mathbf{E}_i^{Mises} = \sqrt{\frac{\left(E_{xx}-E_{yy}\right)^2+(E_{xx}-E_{zz})^2+\left(E_{yy}-E_{zz}\right)^2}{6}+E_{xy}^2+E_{xz}^2+E_{yz}^2} \quad (2.25)$$

The visualizing of the shear strain allows one to distinguish dislocations, stacking fault and twinning inside the microstructure during the mechanical deformation.

2.3.4 Dislocation extraction analysis

The dislocation extraction algorithm (DXA) proposed by Stukowski and Albe [150, 151] is a general and powerful method for characterizing the topological structure of dislocations from atomic simulations. It converts identified dislocation networks into continuous lines and determines their Burgers vectors in a fully automated fashion even in highly distorted crystalline subregions. At the first step, the dislocation core atoms are characterized through the standard CNA method. Then, an oriented, closed, two-dimensional manifold called interface mesh is built. It distinguishes the crystalline atoms from the disordered ones. Finally, on this manifold for each dislocation segment, an initial Burgers circuit is constructed.

2.4 Nanocrystalline sample generation

Several methods have been proposed in the literature to generate initial samples. The Voronoï tessellation [152] method is often used to generate columnar or 3D samples. A method consisting in grain growth from randomly distributed initial germs [153], has been also proposed. Moreover, fully dense three-dimensional nanocrystalline materials have been constructed by Phillpot *et al* from the crystallisation of the melt [154–156]. The method consists of embedding a preoriented single-crystal seed in the melt that is subsequently cooled below the melting point to enable the growth of the crystal. This method is similar to the grain growth method that also starts from random seeds with random orientation, except that thermodynamics is lacking for the latter. It is rather efficient numerically and generates samples in which all grains have the same size. Further, the grain orientation is predetermined.

We have followed an alternative strategy and have used a recent melting–cooling method to generate initial samples of columnar nanocrystalline Copper. This

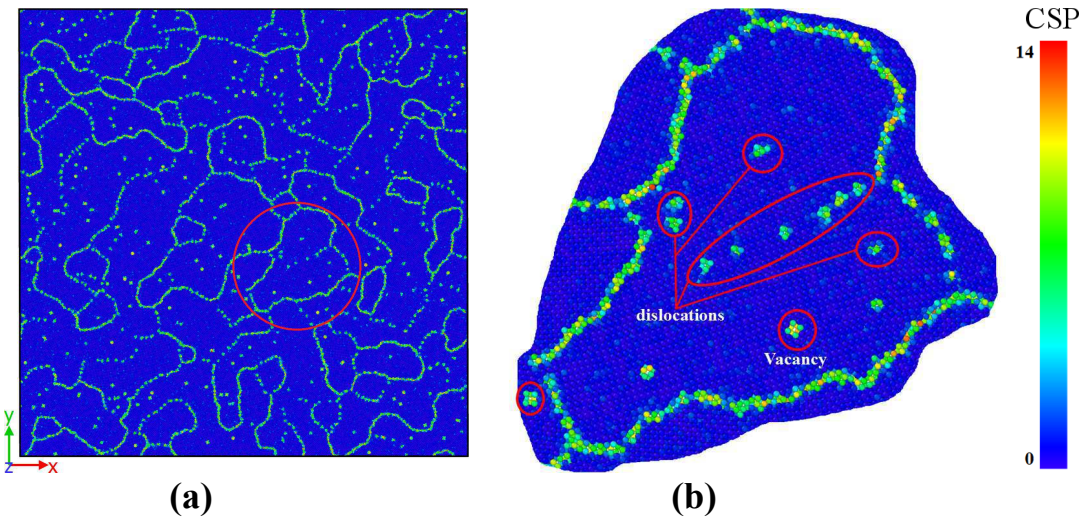

FIGURE 2.8: (a) Nanocrystalline copper created with the melting-cooling method. The mean grain size is 9.0 nm. The color of the atoms corresponds to the value of their CSP: dark blue atoms are in perfect FCC position. (b) Close-up on a grain from this sample to observe the defects.

method produces realistic samples that contain defects even inside the grains such as dislocations and vacancies.

2.4.1 Melting cooling method

quasi-2D systems

The method consists of heating a perfect FCC Copper crystal (perfect monocrystalline Copper) to 2000K in an isothermal-isobaric ensemble (NPT) using a Nosé- Hoover thermostat [125, 128]. The dimension of the initial simulation box is fixed to 72.3nm x 72.3nm x 0.3615nm (200 units cells x 200 units cells x 1 unit cell) and initially contains 160 000 atoms of Copper, leading to quasi-2D samples. The components of the pressure tensor in all directions are set to zero during the heating and the relaxation processes. Therefore, dynamic heating allows the increase of the volume of the simulation box to relax the atomic configuration during the increase of the T.

Once the melting is achieved, the liquid state system is cooled down to 300K in NPT ensemble. The cooling rate is controlled by the number of time steps selected for the cooling process. During the cooling process the volume of the simulation box decreases with the decrease of the T (Figure 2.9). It appears that the decrease of the cooling rate slightly increases the crystallization transition and decreases the volume of the sample (Figure 2.9).

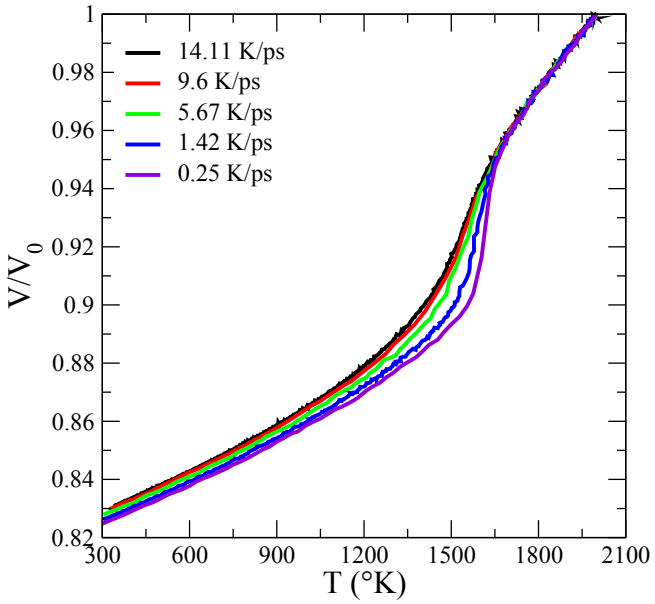

FIGURE 2.9: Variation of the sample volume versus the temperature during the cooling process for different cooling rates. Here V_0 is the starting volume at $2000K$.

After cooling, the barostat is set to 0 GPa for 200 ps. It is verified that the system has reached a stable minimal potential energy and that the internal stresses are relaxed. This melting cooling method allows generating a sample in which the grain orientation is random and the result of seed crystallization. In addition, the grain size varies, and it generates curved grain boundaries and realistic defects inside the grains (Figure 2.8). It is then possible to count the number of grains and to evaluate an average grain size. Inside the grains, it is possible to identify edge dislocations, vacancies and self interstitials (Figure 2.8 (b)).

It is important to stress that the mean grain size is controlled by the cooling rate. An increase in the cooling rate decreases the recrystallization time, leading to a decrease of the mean grain size (Figure 2.10 and 2.11). The cooling rate has been varied nearly one order of magnitude from $14.17K/ps$ (9 nm mean grain size) to $0.25K/ps$ (36 nm mean grain size). The generated samples have a mean grain size of 9, 10.5, 14.6, 16.4, 19.4, 24, 26, 30 and 36 nm (Figure 2.10).

The samples with a number of grains lower than eight (26, 30 and 36 nm) have been discarded in the study of the influence of the grain size on the mechanical behavior of nanocrystalline Copper (inset of Figure 2.10). These samples do not present a variability in the size of grains due to the limited number of grains. Moreover, the critical grain size in Copper is localized between 10 and

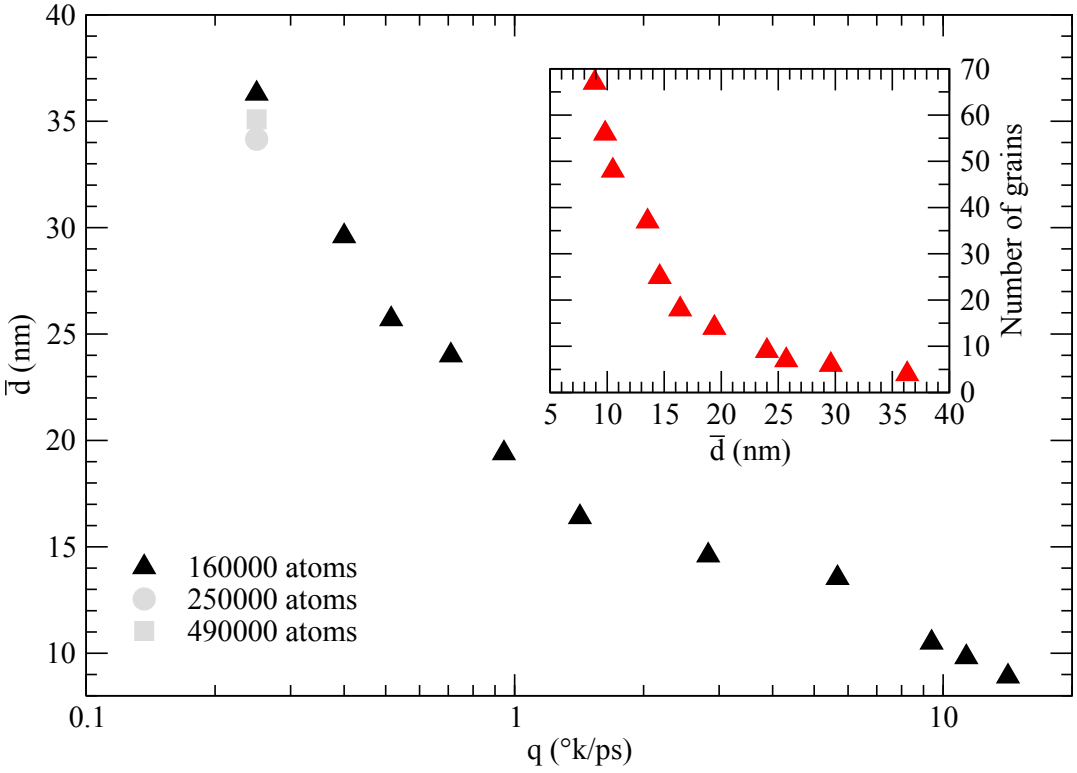

FIGURE 2.10: Variation of the average grain size $\bar{d}$ with respect to the quenching rate q and variation of the number of grains with respect to the average grain size.

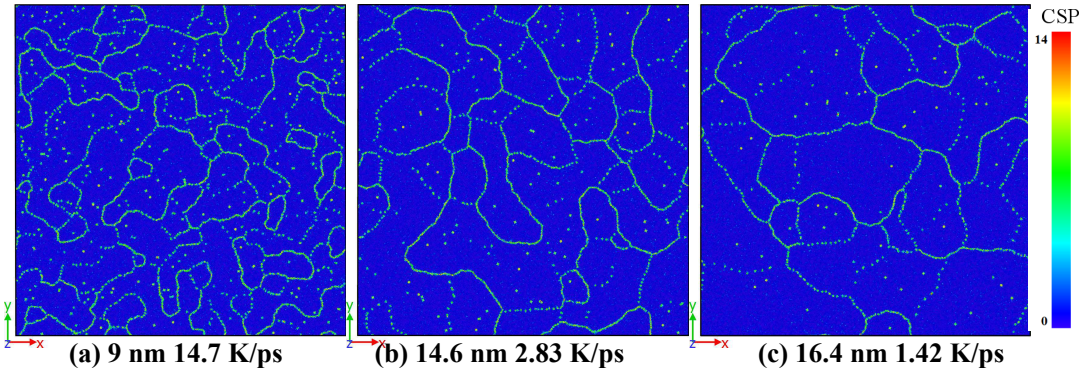

FIGURE 2.11: Different samples with different mean grain sizes. The colour of the atoms corresponds to the value of their CSP: dark blue atoms are in perfect FCC position (CSP<1).

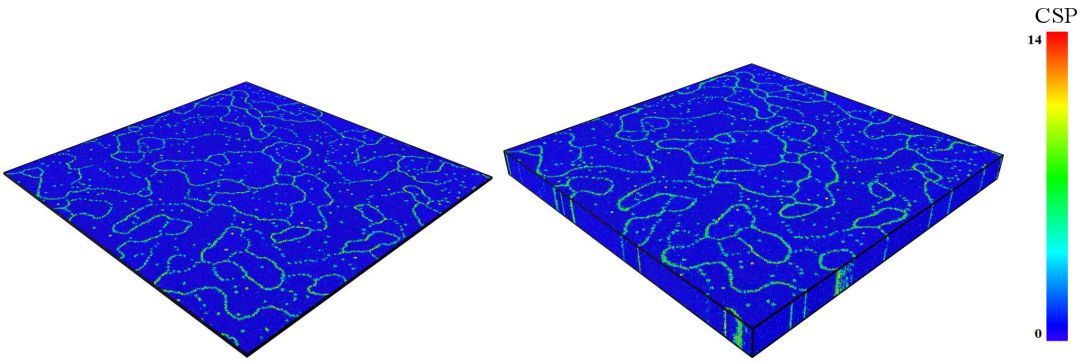

(a) (b)

FIGURE 2.12: NC copper systems generated with the melting-cooling method. The mean grain size is 9 nm. (a) quasi-2D sample, (b) columnar 3D sample. The color of the atoms corresponds to the value of their CSP: dark blue atoms are in perfect fcc position, green atoms correspond to defects or grain boundaries.

20 nm (section 1.2.2). Therefore, the range of our samples is sufficient to predict the critical grain size.

The samples used in this study have an average grain size varying from 9.0 nm (67 grains) to 24 nm (9 grains) as shown in the inset of Figure 2.10. Because the number of atoms is initially the same, the higher is the mean grain size, the lower is the number of grains in the box. Note that the decrease of the mean grain size significantly increases the volume fraction of grain boundaries and defects. Several quenches of the same sample and same cooling rate have been also performed. These simulations lead to the same average grain size while the size distribution and shape might be different. The influence of the size of the initial box has been tested with two configurations containing 250 000 and 490 000 atoms respectively. Simulations have been performed using the smallest cooling rate ($0.25K/ps$), and the results are presented with grey symbols in Figure 2.10. It appears that the number of atoms slightly influences the mean grain size but not significantly.

Columnar 3D system

In order to analyze the deformation mechanism for a 3D structure and to compare the behavior of the 3D structure with the quasi-2D one, we have aimed to replicate the 9 nm quasi-2D system 15 times along the columnar axis. Then, the system has been heated to $900K$ in NPT ensemble at zero external pressure for 100 ps, followed by a relaxation at $900K$ in NPT ensemble for 100 ps. At this T, the diffusion process at the grain boundary becomes possible and hence the atomic diffusion leads to a nearly stabilized grain boundaries. After

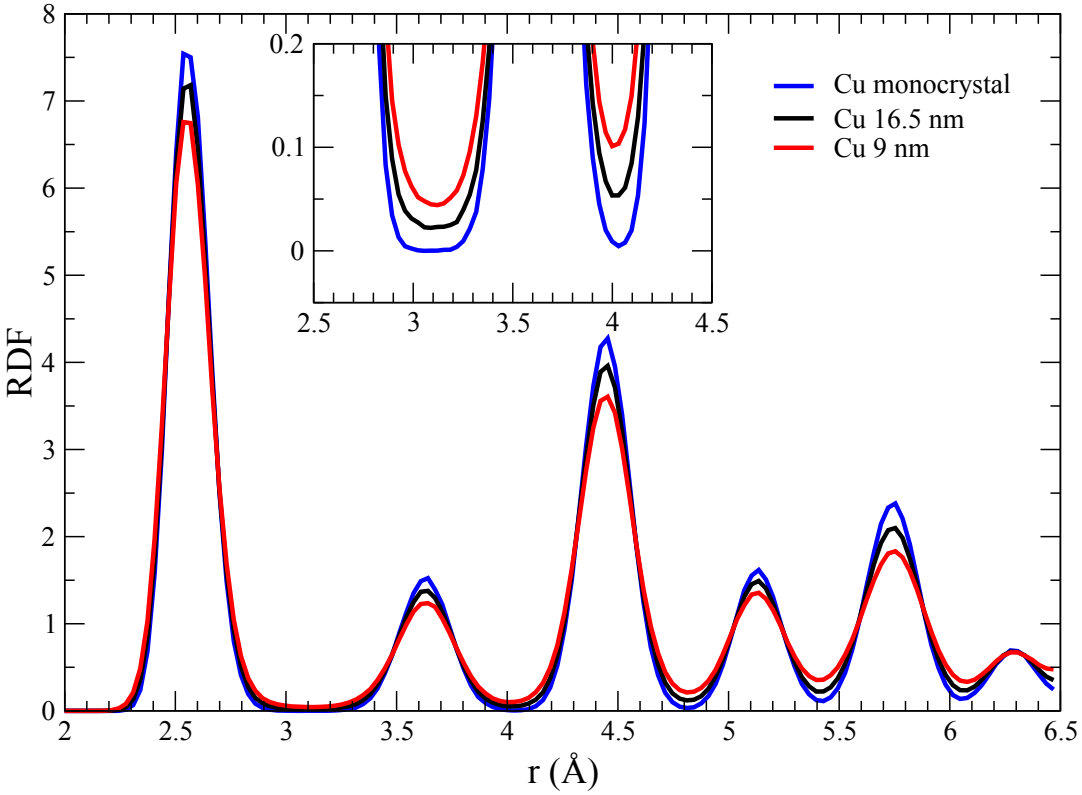

FIGURE 2.13: RDF for quasi-2D nanocrystalline Copper samples with a mean grain size of 9 nm and 16.5 nm obtained by a melting cooling method compared to relaxed Copper monocrystal at 300K.

the relaxation process, the system is cooled down to 300K and then relaxed in NPT ensemble at zero external pressure for 100 ps. The resulting configuration has a 9 nm columnar 3D Copper sample that contains 2 400 000 atoms (Figure 2.12 (b)). Although such a starting configuration might be seen as artificial, it is important to emphasize that this type of microstructure is commonly present in the deposition of nanocrystalline thin films [157–159] and nanotwinned Copper [160, 161].

2.4.2 Grain boundary structure and energy

The radial distribution function (RDF) is a density – density correlation function that indicates the probability to find a particle in the volume element between distance r and r+dr from another particle. RDF is defined as follows:

$$RDF = g(r) = \frac{1}{4\pi r^2 N\rho} \sum_{i=1}^{N} \sum_{\substack{j=1 \\ j\neq i}}^{N} \delta(r - r_{ij}) \tag{2.26}$$

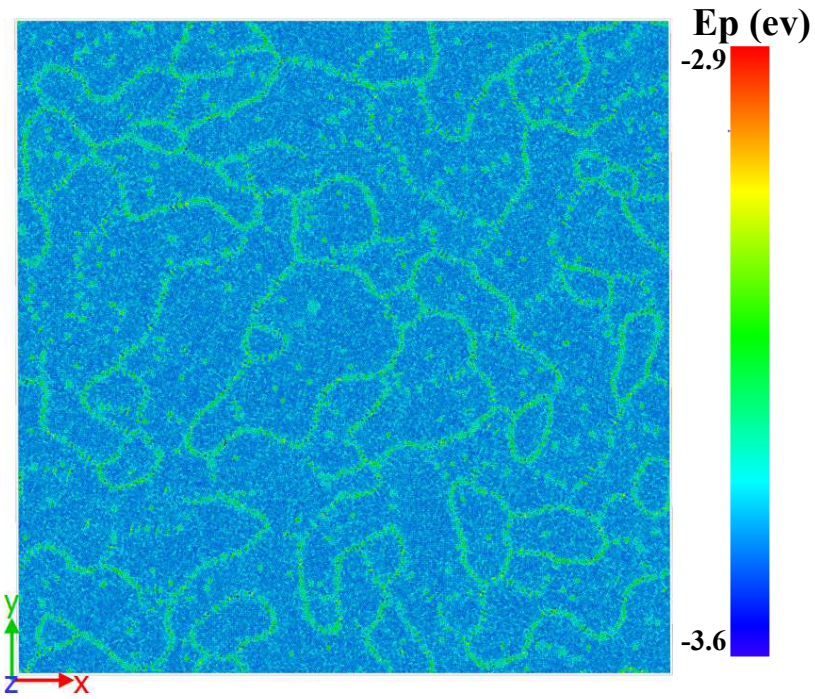

FIGURE 2.14: Atomic configuration of the quasi-2D 9.0 nm sample colored with the atomic potential energy

Where N is the total number of atoms , ρ is the density of the system, r_{ij} is the distance between atom i and j and δ is the Kronecker constant equal to 1 if $r = r_{ij}$.

To characterize the structure of the initial samples generated by melting cooling method, the RDF for each sample has been calculated after the relaxation process (Figure 2.13). The peaks obtained for the monocrystal (colored in blue) are slightly broadened, compared to the sharp peaks expected for a monocrystal. This is due to atomic vibrations at $T \neq 0$ around their equilibrium positions. The RDF for the 9.0 and 16.5 nm samples present well-defined peaks that characterize a well-ordered crystalline material. Although, these peaks are slightly broadened due to the presence of defects (e.g grain boundary). Moreover, we remark that the RDF for the polycrystal 9.0 and 16.5 nm does not exhibit a global minimum between peaks (i.e. $g(r) = 0$), in contrast with the RDF of the monocrystal. This is attributed to the presence of grain boundaries that generate some disorder in the system. The decrease of the mean grain size reduces the peaks amplitude due to the increase of the fraction of grain boundaries.

Figure 2.14 shows a snapshot of the atomic configuration of the quasi-2D 9.0 nm sample colored by potential energy per atom. We can clearly notice that the energy of the grain boundaries and defects inside the grains is higher

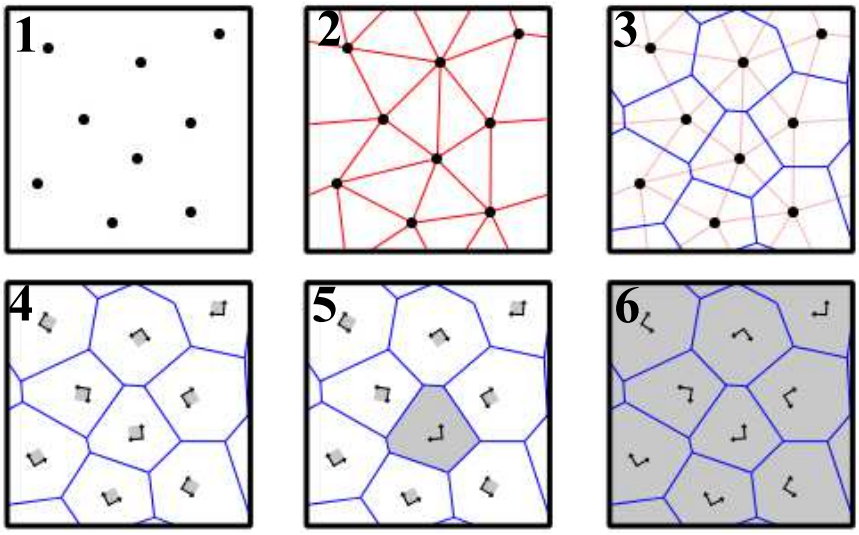

FIGURE 2.15: Schematic plot of the basics of Voronoï tessellation method.

than the intra-granular atoms. We also acknowledge that the present mapping correlates very well with the CSP parameter calculated above (Figures 2.8 (a) and 2.11 (a)) . Still the difference are weak as the average potential energy for atoms in grain boundaries is $-3.4\ eV$, whereas for the intra-granular atoms, one finds $-3.5\ eV$.

2.4.3 Voronoï tessellation

The Voronoï tessellation is a method widely used to generate 3D nanocrystalline samples. We used the ATOMSK software to generate initial configurations by Voronoï tessellation method [152]. Nanocrystalline system construction starts with an empty simulation box containing a number of seed positions Figure 2.16 (1). The number of seed points is determined by the simulation cell size and the desired mean grain size. Then the Voronoï volume or (polyhedral) for each seed is defined with respect to its position from the others. The volumes is then filled by a crystal structure (FCC, HCP....) in a random orientation. If an atom becomes closer to another seed point than to its grain center, the construction is stopped. This is repeated for all grains, and finally results in a three dimensional polycrystal. When the number of grains is sufficiently large, such a construction results in a log-normal grain size distribution [162], that is also found experimentally [163]. A schematic plot of the Voronoï method for a 2D sample for simplicity is shown in Figure 2.15. The steps of this methods are as follows:

1. A number of nodes are introduced randomly in the simulation box.

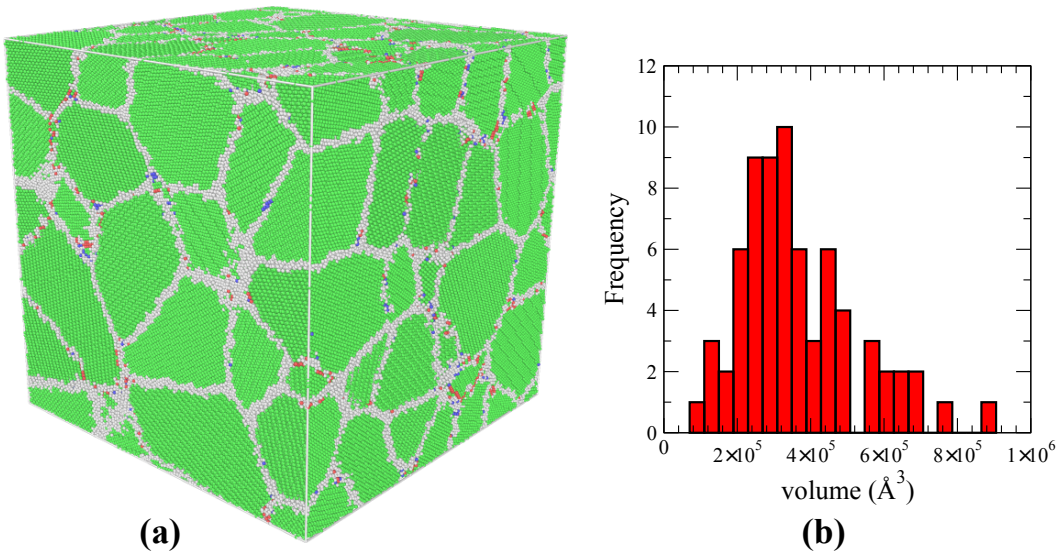

FIGURE 2.16: (a) 3D nanocrystalline Copper sample that contains 70 grains colored by the CNA, green atoms are FCC atoms, gray atoms are disordered atoms at grain boundaries and red atoms are in HCP structure position. (b) Volume distribution of the grains in this sample, the average grain size is 9 nm.

2. All nodes are linked with their neighbors (red lines) [1].

3. The normal to the red lines are found (blue lines). These blue lines define the contours of the future grains, i.e. the grain boundaries.

4. Atomic "seeds" are placed at the positions of the nodes, with the given crystal orientation.

5. A seed is expanded in the three directions of space.

6. After all seeds have been expanded and cut inside their respective grains, one obtains the final polycrystal. Atoms presenting overlap are removed.

In addition, to compare the mechanical behavior of nanocrystalline FCC and HCP structure, initial configurations of full 3D nanocrystalline HCP α-Titanium have been constructed by Voronoï tessellation with $3nm \leqslant d \leqslant 30nm$. Then a fraction of 0.5% of atoms has been removed in order to create some defects such as vacancies and interstitials inside the grains. Each system is then relaxed in the NPT ensemble at $300K$ with zero external pressure in all direction for 300 ps in order to minimize the potential energy and to obtain a system without residual stresses. The interatomic potential used is the modified embedded atomic method by Henning *et al* [136].

[1] This step is called Delaunay tessellation. It is usually used to generate the mesh for the finite elements simulations.

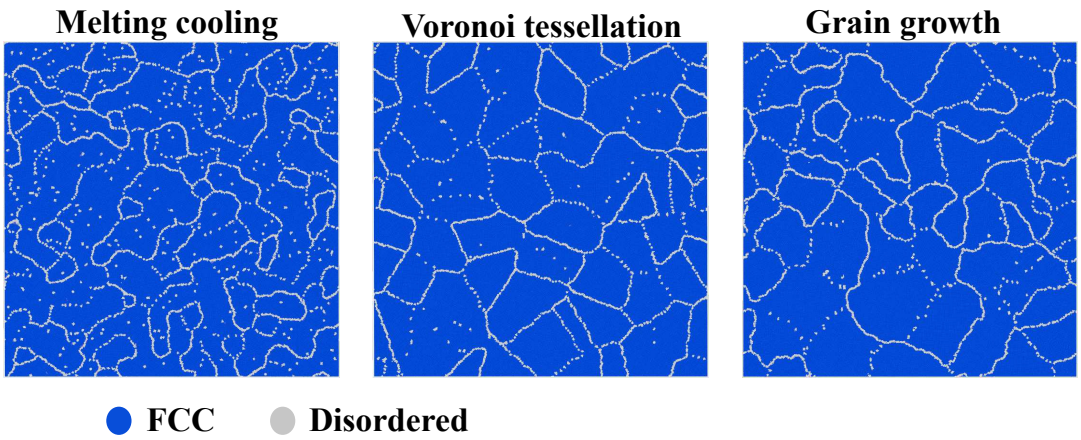

FIGURE 2.17: Initial configurations of a 9 nm sample generated by different methods colored by common neighbor analysis.

Furthermore, we constructed two additional nanocrystalline Copper samples by Voronoï tessellation to compare the mechanical response of 3D structure generated by Voronoï tessellation with the melting cooling method. A full 3D nanocrystalline Copper with a 9 nm mean grain size that contains 70 grains and 2 150 000 atoms (Figure 2.16) and a columnar 3D Copper with 9 nm mean grain size that contains 64 grains. After the generation, these samples are also relaxed in an NPT ensemble at $300K$ for 200 ps and zero external pressure in all direction. In contrast with the melting cooling method, grain boundaries have flat surfaces and the grain interior does not contain any type of defects.

Initial quasi-2D samples have also been generated with other methods to validate the interest of the melting cooling method. The Voronoï tessellation and the grain growth method have been used for this purpose. Two quasi-2D samples have been similarly generated and the mean grain size has been specified, in these cases to be d = 9.0 nm. After the generation, these two samples are relaxed in an NPT ensemble at $300K$ for 200 ps. The atomic configurations obtained for these cases are presented in Figure 2.17, colored with the common neighbor analysis and compared to the one obtained with the melting cooling method.

A summary of all the generated samples that are used to our studies are present in the table 2.6.

TABLE 2.6: Summary of all the generated nanocrystalline samples used in our work

Type	structure	Number of grains	Construction method	mean grain size	geometry
Copper	FCC	67	melting cooling	9 nm	quasi-2D
Copper	FCC	48	melting cooling	10.5 nm	quasi-2D
Copper	FCC	25	melting cooling	14.6 nm	quasi-2D
Copper	FCC	18	melting cooling	16.4 nm	quasi-2D
Copper	FCC	14	melting cooling	19.4 nm	quasi-2D
Copper	FCC	9	melting cooling	24 nm	quasi-2D
Copper	FCC	67	melting cooling	9 nm	columnar-3D
Copper	FCC	64	Voronoï tessellation	9 nm	quasi-2D
Copper	FCC	67	Voronoï tessellation	9 nm	columnar-3D
Copper	FCC	64	grain growth	9 nm	quasi-2D
Copper	FCC	70	Voronoï tessellation	9 nm	3D
α-Titanium	HCP	120	Voronoï tessellation	3 nm	3D
α-Titanium	HCP	90	Voronoï tessellation	5 nm	3D
α-Titanium	HCP	40	Voronoï tessellation	8 nm	3D
α-Titanium	HCP	30	Voronoï tessellation	10 nm	3D
α-Titanium	HCP	24	Voronoï tessellation	12 nm	3D
α-Titanium	HCP	15	Voronoï tessellation	15 nm	3D
α-Titanium	HCP	11	Voronoï tessellation	18 nm	3D
α-Titanium	HCP	10	Voronoï tessellation	20 nm	3D
α-Titanium	HCP	10	Voronoï tessellation	22 nm	3D
α-Titanium	HCP	8	Voronoï tessellation	25 nm	3D
α-Titanium	HCP	5	Voronoï tessellation	30 nm	3D

2.5 Mechanical tests protocol

After the conception of the above samples (table 2.6), we applied a series of uniaxial tensile tests on these samples. The tensile strain is applied in the y direction at constant $\dot{\varepsilon}$ and $T = 300K$. During the loading process, the components of the pressure tensor in the x and z directions were set to zero using an anisotropic Nosé-Hoover barostat. Periodic boundary conditions are applied in all directions (section 2.1.3). The time step used in the simulations is 3 fs.

The macroscopic stress of the system is computed using the virial formulation (section 2.1.2). This stress is considered as a true stress because each time step the new volume is used to compute the macroscopic stress of the system. A logarithmic true strain is recorded in the tensile direction during the deformation:

$$L_y(t) = l_y(0)(1+\dot{\varepsilon}t) \tag{2.27}$$

$$ln(\lambda) = ln\left(\frac{L_y(t)}{L_y(0)}\right) \tag{2.28}$$

where $L_y(t)$ is the instantaneous length of the box. The stress-strain curve can be then plotted and investigated.

Influence of grain size

In the first study of our work, we investigate the influence of the mean grain size on the mechanical behavior of nanocrystalline Copper and α-Titanium. All tensile tests applied in our study are summarized in table 2.7.

To investigate the influence of the initial samples conception method on the mechanical properties of nanocrystalline Copper, we applied uniaxial tensile tests on systems with the same mean grain size but with different conception methods and geometry (table 2.8).

Influence of strain rate

In the second study of our work, the strain rate dependence of the mechanical properties of nanocrystalline Copper has been investigated. To this aim, a series of uniaxial tensile tests have been applied to two nanocrystalline Copper models, a quasi-2D and a columnar 3D with 9 nm mean grain size at different strain rates. It is also important to emphasize that because of the limitation

TABLE 2.7: Summary of all the tensile tests applied to study the influence of the grain size in our work.

Type	structure	mean grain size	geometry	$\dot{\varepsilon}_{yy}$
Copper	FCC	9 nm	quasi-2D	$10^8\ s^{-1}$
Copper	FCC	10.5 nm	quasi-2D	$10^8\ s^{-1}$
Copper	FCC	14.6 nm	quasi-2D	$10^8\ s^{-1}$
Copper	FCC	16.4 nm	quasi-2D	$10^8\ s^{-1}$
Copper	FCC	19.4 nm	quasi-2D	$10^8\ s^{-1}$
Copper	FCC	24 nm	quasi-2D	$10^8\ s^{-1}$
α-Titanium	HCP	3 nm	3D	$10^8\ s^{-1}$
α-Titanium	HCP	5 nm	3D	$10^8\ s^{-1}$
α-Titanium	HCP	8 nm	3D	$10^8\ s^{-1}$
α-Titanium	HCP	10 nm	3D	$10^8\ s^{-1}$
α-Titanium	HCP	12 nm	3D	$10^8\ s^{-1}$
α-Titanium	HCP	15 nm	3D	$10^8\ s^{-1}$
α-Titanium	HCP	18 nm	3D	$10^8\ s^{-1}$
α-Titanium	HCP	20 nm	3D	$10^8\ s^{-1}$
α-Titanium	HCP	22 nm	3D	$10^8\ s^{-1}$
α Titanium	HCP	25 nm	3D	$10^8\ s^{-1}$
α-Titanium	HCP	30 nm	3D	$10^8\ s^{-1}$

in computational power, in order to reach a deformation of $\varepsilon = 0.9\%$, the time sampled by the simulation t_{exp} ranges from e.g. 900 ns to 9 ps for 10^4 to $10^9 s^{-1}$, respectively. All the applied tensile tests are summarized in table 2.9.

Finally, to study the relaxation behavior of the nanocrystalline Copper systems with 9 nm mean grain size, initial configurations of the quasi-2D and the columnar 3D have been extracted from each tensile test experiment at 0.9% and 3% (table 2.9). Then, these configurations have been relaxed in NVT ensemble for 2 ns at $300K$. During the relaxation, the evolution of the stress $\sigma(t) = \sigma_{yy}(t)$ is monitored and analyzed.

TABLE 2.8: Summary of the tensile tests applied to analyze the influence of the sample conception method.

Type	grain size	geometry	Conception method	$\dot{\varepsilon}_{yy}$
(a)				
Copper	9 nm	quasi-2D	melting-cooling	$10^8\ s^{-1}$
Copper	9 nm	quasi-2D	Voronoï tessellation	$10^8\ s^{-1}$
Copper	9 nm	quasi-2D	grain growth	$10^8\ s^{-1}$
(b)				
Copper	9 nm	columnar 3D	melting-cooling	$10^8\ s^{-1}$
Copper	9 nm	columnar 3D	Voronoï tessellation	$10^8\ s^{-1}$
Copper	9 nm	3D	Voronoï tessellation	$10^8\ s^{-1}$

TABLE 2.9: Summary of the tensile tests applied to analyze the strain rate dependence of the mechanical properties of nanocrystalline Copper

Type	grain size	geometry	Conception method	$\dot{\varepsilon}_{yy}$	simulation time (ns)
Copper	9 nm	quasi-2D	melting-cooling	$10^4\ s^{-1}$	7650
Copper	9 nm	quasi-2D	melting-cooling	$10^5\ s^{-1}$	1470
Copper	9 nm	quasi-2D	melting-cooling	$5.10^5\ s^{-1}$	240
Copper	9 nm	quasi-2D	melting-cooling	$10^6\ s^{-1}$	180
Copper	9 nm	quasi-2D	melting-cooling	$5.10^6\ s^{-1}$	60
Copper	9 nm	quasi-2D	melting-cooling	$10^7\ s^{-1}$	30
Copper	9 nm	quasi-2D	melting-cooling	$5.10^7\ s^{-1}$	6
Copper	9 nm	quasi-2D	melting-cooling	$10^8\ s^{-1}$	3
Copper	9 nm	quasi-2D	melting-cooling	$5.10^8\ s^{-1}$	0.6
Copper	9 nm	quasi-2D	melting-cooling	$10^9\ s^{-1}$	0.3
Copper	9 nm	columnar 3D	melting-cooling	$10^7\ s^{-1}$	30
Copper	9 nm	columnar 3D	melting-cooling	$5.10^7\ s^{-1}$	6
Copper	9 nm	columnar 3D	melting-cooling	$10^8\ s^{-1}$	3
Copper	9 nm	columnar 3D	melting-cooling	$5.10^8\ s^{-1}$	0.6
Copper	9 nm	columnar 3D	melting-cooling	$10^9\ s^{-1}$	0.3
Copper	9 nm	columnar 3D	melting-cooling	$5.10^9\ s^{-1}$	0.06
Copper	9 nm	columnar 3D	melting-cooling	$10^10\ s^{-1}$	0.03

Chapter 3

Study of the effect of grain size on the mechanical properties of nanocrystalline materials

Contents

3.1 Introduction

In this chapter, molecular dynamics simulations have been used to study the influence of the grain size on the mechanical behavior of two nanocrystalline materials, an FCC Copper and an HCP α-Titanium. In section 2.5, we have described the protocol of the applied mechanical tests on these materials. In the next, we start by investigating the dependence of the stress-strain response on

the grain size in the elastic and the plastic regime. Secondly, the influence of the grain size on Young's modulus, the yield, and the flow stresses is addressed. In our range of grain size studied, a transition from a Hall Petch to an inverse Hall Petch tendency is expected (see section 1.2.2.2). Thirdly, the influence of the initial samples conception method is examined to show the relevance of the recent melting cooling method. Finally, the deformation mechanisms of these materials have been analyzed on the atomic scale.

Recent experiments have shown that nanocrystalline materials have fascinated mechanical properties linked to their large volume fraction of grain boundaries. Molecular dynamics simulations have also been widely used to investigate the deformation mechanisms of these materials [28, 30, 104]. They have shown that the grain boundaries are sources and sinks to dislocations (section 1.2.2.3) [36, 110]. These simulations have also revealed significant grain boundaries activities accompanied by local discrete atomic events in the grain boundaries (section 1.2.2.1) [27, 32, 82].

Traditional Voronoï tessellation are normally used to generate the initial configurations for molecular dynamics studies. This method is very efficient to produce samples with a wide grain size distribution and polyhedral grains. Nevertheless, the grain boundaries in this method are flat surfaces with high internal stresses [164]. In addition, the interior of the grains lacks initial defects. Therefore, the nanocrystalline sample models used in molecular dynamics studies lack realistic intra-granular defects (e.g. dislocations, vacancies and impurities...) and grain boundaries morphology (e.g. equilibrium and curvature boundaries).

To respond to this lacking, in the previous chapter we show a recent melting cooling method to generate more realistic initial nanocrystalline Copper samples for molecular dynamics simulations (section 2.4.1). These samples have a well ordered crystalline phase with more realistic morphology of grain boundaries (section 2.4.2). The presence of defects inside the grains such as dislocations and vacancies is also one of the main advantages of this method.

After the conception of the nanocrystalline materials (table 2.6), the main objectives of our work are now:

- The understanding of the main deformation mechanisms of the nanocrystalline materials by using molecular dynamics simulations on these realistic initial configurations.
- The study of the influence of the grain size on the mechanical properties of nanocrystalline materials by molecular dynamics simulations.
- To reveal the influence of the method used to generate the initial configurations on the mechanical properties and the deformation mechanisms of those configurations.

3.2 Tensile tests results

In this section, we analyze the results of the applied uniaxial tensile tests on the two nanocrystalline materials, the FCC Copper and the HCP α-Titanium. A description of the applied uniaxial tensile tests has been presented in section 2.5.

3.2.1 Stress strain response

During the tensile deformation, the true stress of the system is monitored and plotted versus the true strain. Figure 3.1 (a) presents the results of the tensile tests applied to the Copper samples generated with the melting–cooling method for different mean grain sizes. The stress linearly increases up to a stress threshold and then fluctuates around a constant value which is the flow stress. Then the ultimate failure occurs by sample fracture. We can clearly see the dependence of the plastic flow stress on the grain size. A zoom on the stress-strain curves below 10% deformation is represented in Figure 3.1 (b). A dependence of the stress in the elastic or linear regime and Young's modulus on the grain size is visible.

The stress-strain curves of fully dense 3D nanocrystalline α-Titanium at different grain sizes are shown in Figure 3.2. Like the Copper samples, the stress of these materials clearly depends on the grain size in the elastic and the plastic flow regimes. The inset of the Figure 3.2 shows a zoom on the stress-strain curves for 2 % strain. We can clearly see the dependence of the elastic response on the grain size. Moreover, we remark the presence of an overshoot in the stress-strain curves before the flow regime for grain sizes above 8 nm. Normally, the tensile limit at which the stress decreases first in the

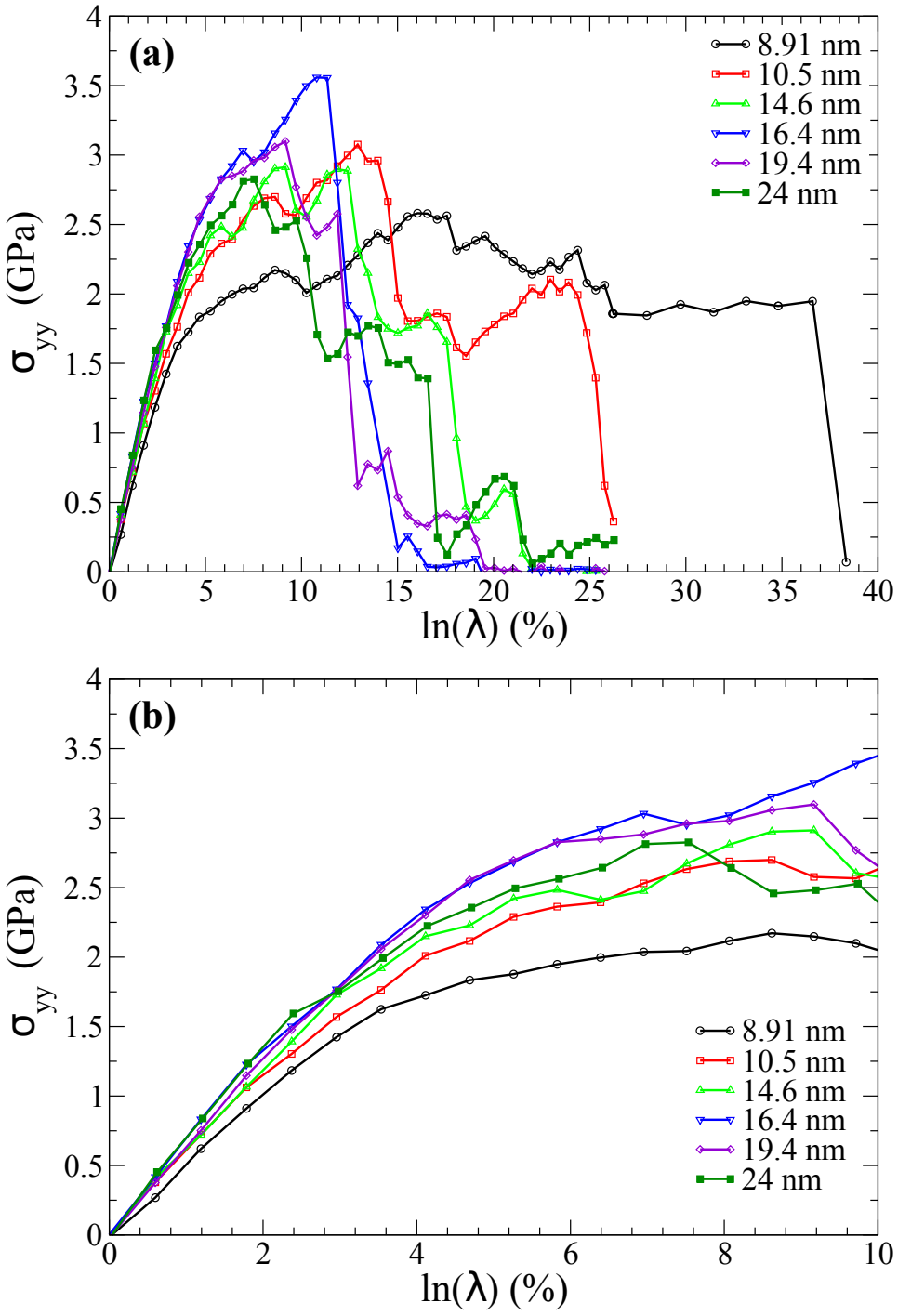

FIGURE 3.1: (a) True stress versus strain curves for nanocrystalline quasi-2D Copper samples with different mean grain sizes at constant strain rate $\dot{\epsilon} = 10^8\ s^{-1}$ and T = 300K; (b) Zoom for a strain below 10%.

stress-strain curve appears by the effective activation of slip (propagation of dislocations) or twinning process in coarse grains materials. In such a way, the macroscopic stress of the material is relaxed by local plastic deformation processes (dislocations or twinning). Here, the decrease of the stress is resulting from the emission of partial dislocations and the nucleation of twins from grain boundaries that cross the entire grains to the opposite boundaries.

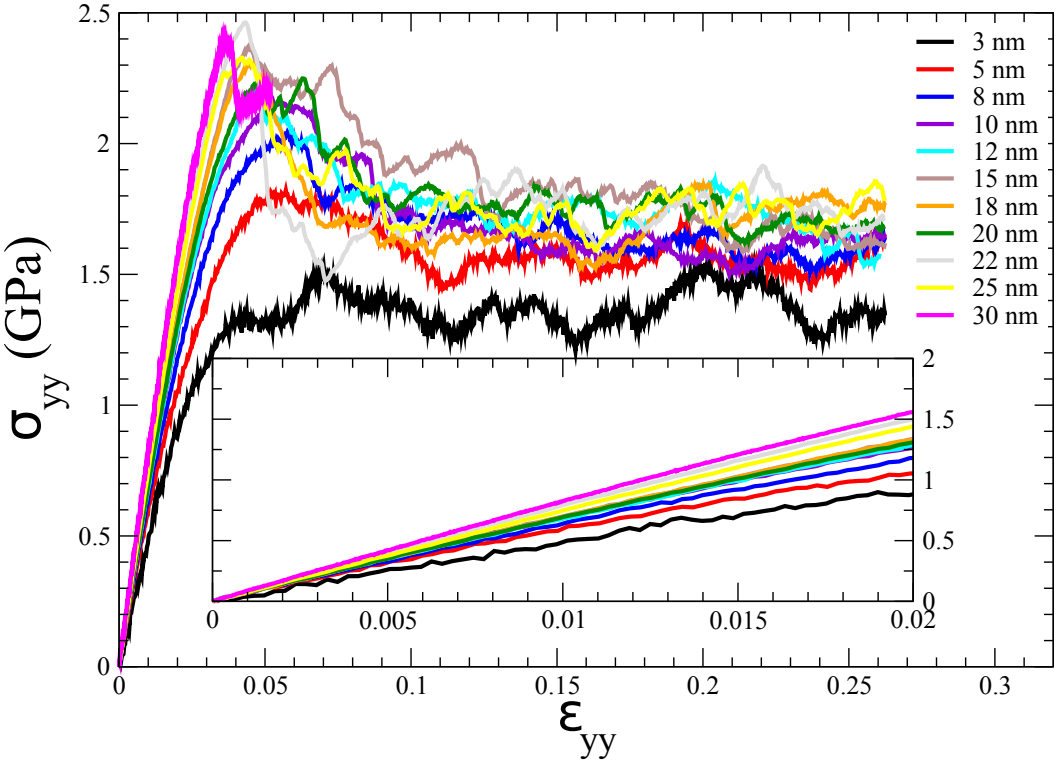

FIGURE 3.2: True stress versus strain curves for the nanocrystalline α-Titanium with fully dense 3D structure at different mean grain sizes deformed at constant strain rate $\dot{\varepsilon} = 10^8\ s^{-1}$ and $T = 300K$. A zoom on the first 2% strain is presented in the inset Figure.

3.2.2 Determination of the elastic domain

In order to analyze the effect of the grain size, we first evaluate the yield, the flow stresses and Young's modulus of these nanocrystals. The yield stress is defined as the maximal stress reached in the elastic domain (reversible phenomena). The flow stress is defined as the average stress of the plateau of the stress–strain curve. The Young modulus is the slope of the stress–strain curve in the elastic domain. Therefore, to define the yield stress and Young's modulus we have aimed to determine the elastic domain.

Two methods are used to identify the elastic domain and thus the yield stress of all the generated nanocrystalline Copper and α-Titanium. The first method consists in unloading the sample to evaluate the reversibility of the deformation. The protocol of the unloading process is as follows: (1) The atomic configurations of the same sample are extracted after being submitted to a different strain level of 0.3, 0.6, 0.9, 1.2, 1.5, 2.0 and 3%. These configurations are used as initial configurations for an unloading test (stress set to zero), (2) Each system is unloaded using a Nose-Hoover barostat in NPT ensemble where all the components of the stress tensor are set to zero for 40 ps, (3) During the unloading process, the strain is monitored as a function of the time.

During the unloading process, the strain follows the sudden decrease of the stress and then stabilize at a final strain (Figure 3.3 (a)). Thus, if the final strain return to zero, the deformation is considered as totally reversible. The final strain is then plotted (black line) as a function of the initial strain on Figure 3.3 (c).

The second method consists in inverting the rate of deformation to evaluate the total work on the sample. The steps of the strain rate inverting process are as follows: (1) The same initial configurations as the ones relaxed in the first method are chosen as initial samples, (2) Each system is then submitted to an inverted rate of deformation $\dot{\varepsilon} = -10^8\ s^{-1}$, (3) the variation of the average stress as a function of the true strain is monitored. The area between the loading and the returning curves corresponding to the work is evaluated (represented in pink in the inset of the Figure 3.3 (b)). Thus, if the area is equal to zero (the loading and returning curves are coincident) the deformation is considered totally reversible. This area is then plotted as a function of the initial strain in Figure 3.3 (c) (pink line).

Figure 3.3 (c) reveals the fact that until one percent of deformation, the material has a reversible behaviour. The curves present a clear change in slope for initial strain between 1 and 2%. The final strain for the unloading process from a strain below 2% is less than 0.2%. Also, experimentally speaking, the macroscopic yield strength is determined taken a 0.2% offset plastic strain criterion [165]. This indicates that the limit of the elastic domain is at 2 % deformation. We thus define the limit of the elastic domain at 2% and the yield stress is computed for a true strain of 2%. The results of both methods are presented on the same Figure and have been rescaled for comparison; remark

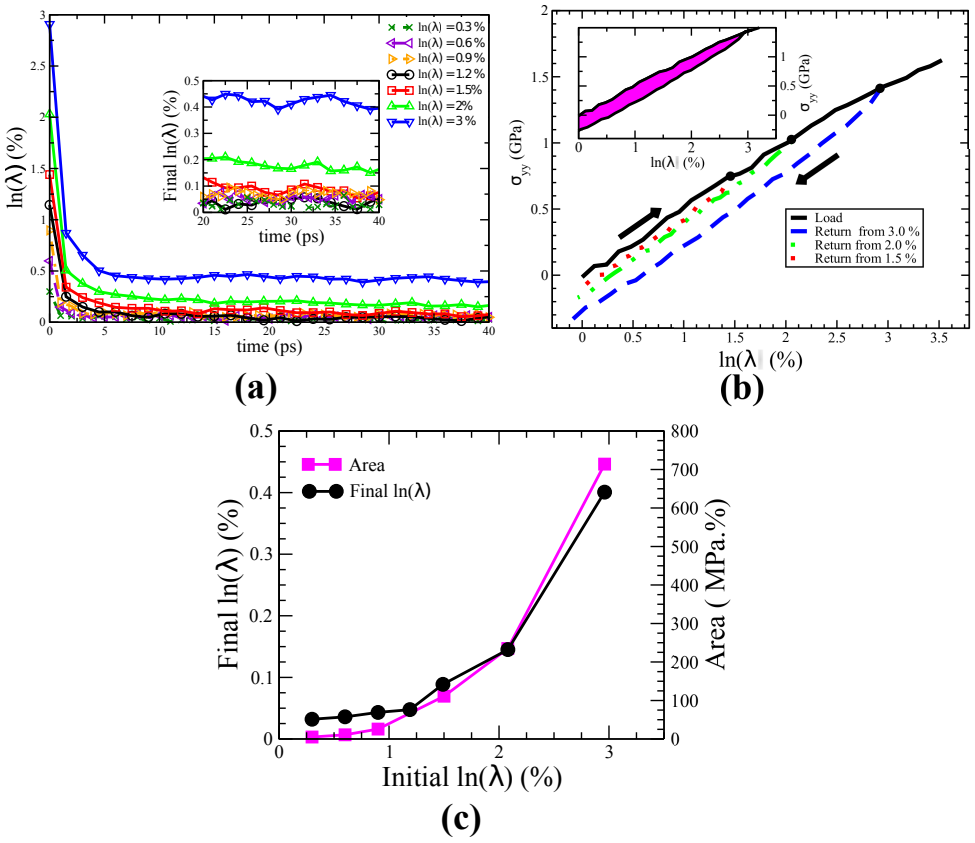

FIGURE 3.3: Determination of the elastic domain. (a) Evolution of the true strain as a function of time at a load equal to zero for a sample with a 9.0 nm mean grain size and from different initial strains. (b) Variation of the stress as a function of the true strain for a loading (black curve) and unloading (red curve) tensile test. (c) Variation of the final true strain as a function of the initial true strain (black curve) for the unloading test (a), and variation of the work (b) as a function of the initial true strain (pink curve) for the unloading test (b).

that both methods present the same tendency (Figure 3.3 (c)).

The determination of the elastic limit following these methods has been performed for all samples with different mean grain sizes. We found that all the tested samples exhibit the same tendency. Hence, the same criteria of elastic limit is used that corresponds to 2 % strain ($ln(\lambda) = 2\%$).

3.2.3 Grain size dependence of the Young modulus

The determination of the elastic domain allows calculating of Young's modulus. The latter is estimated using data taken from the stress-strain curve for a strain less than $ln(\lambda) \leq 0.5\%$ for nanocrystalline Copper. At this strain level, the stress-strain curve is still linear and in the elastic regime. On the other

side, Young's modulus for α-Titanium has been fit from the stress-strain curves for strain less than 0.5 , 1 and 1.5%. This helps one to detect any potential influence of the strain limit on the determination of Young's modulus. Moreover, the relative density with respect to a pure monocrystal is determined for all the generated samples in table 2.6.

Figure 3.4 presents the values obtained for the different mean grain sizes considered for both materials. The values of Young's modulus and the relative density increase with the mean grain size. Two guidelines are plotted in the Figures 3.4 (a) and (b) to facilitate the inspection of the tendency. The values of Young's modulus for nanocrystalline Copper vary from 53 to 71 GPa for mean grain size between 9 and 24 nm. Thus Young's modulus increases with the grain size in nanocrystalline Copper. These results are consistent with the experimental results found by Nieman *et al* [166]. Whereas, the values of Young's modulus for α-Titanium vary from 50 to 80 GPa when the mean grain size increases from 3 to 30 nm. The values of Young's modulus fit from the data taken for strain less than 0.5, 1 and 1.5 % are coherent (Figure 3.4 (b)). Typical values of Young's modulus for commercial polycrystalline pure Titanium at room temperature is in the range of 100 to 110 GPA [167]. However, a low elastic modulus of 85 GPa at 25°C (298K) is predicted for high purity (99.9%) polycrystalline Titanium [167]. This value is close to the value found in our work for d = 30 nm.

In fact, atoms belonging to grain boundaries have a larger potential energy than those inside the grains due to the low density of atoms in this region (section 2.4.2). Therefore, they are easier to displace when an external load is applied. Their contribution to the elastic response is hence reduced compared to the atoms inside the grains. Therefore, Young's modulus decreases with the mean grain size.

The relative density of the two nanocrystalline materials also increases with the mean grain size. First, the grain boundaries are disordered regions where low density of atoms is present in comparison with the grain interior. Therefore, the decrease of the mean grain size increases the fraction of grain boundaries and hence the relative density of the system decreases. The values of the relative density vary from 97.9 % to 98.4 % for nanocrystalline Copper for the mean grain size studied. For nanocrystalline α-Titanium the relative densities vary from 97.18 % to 99.91 % for the mean grain size investigated.

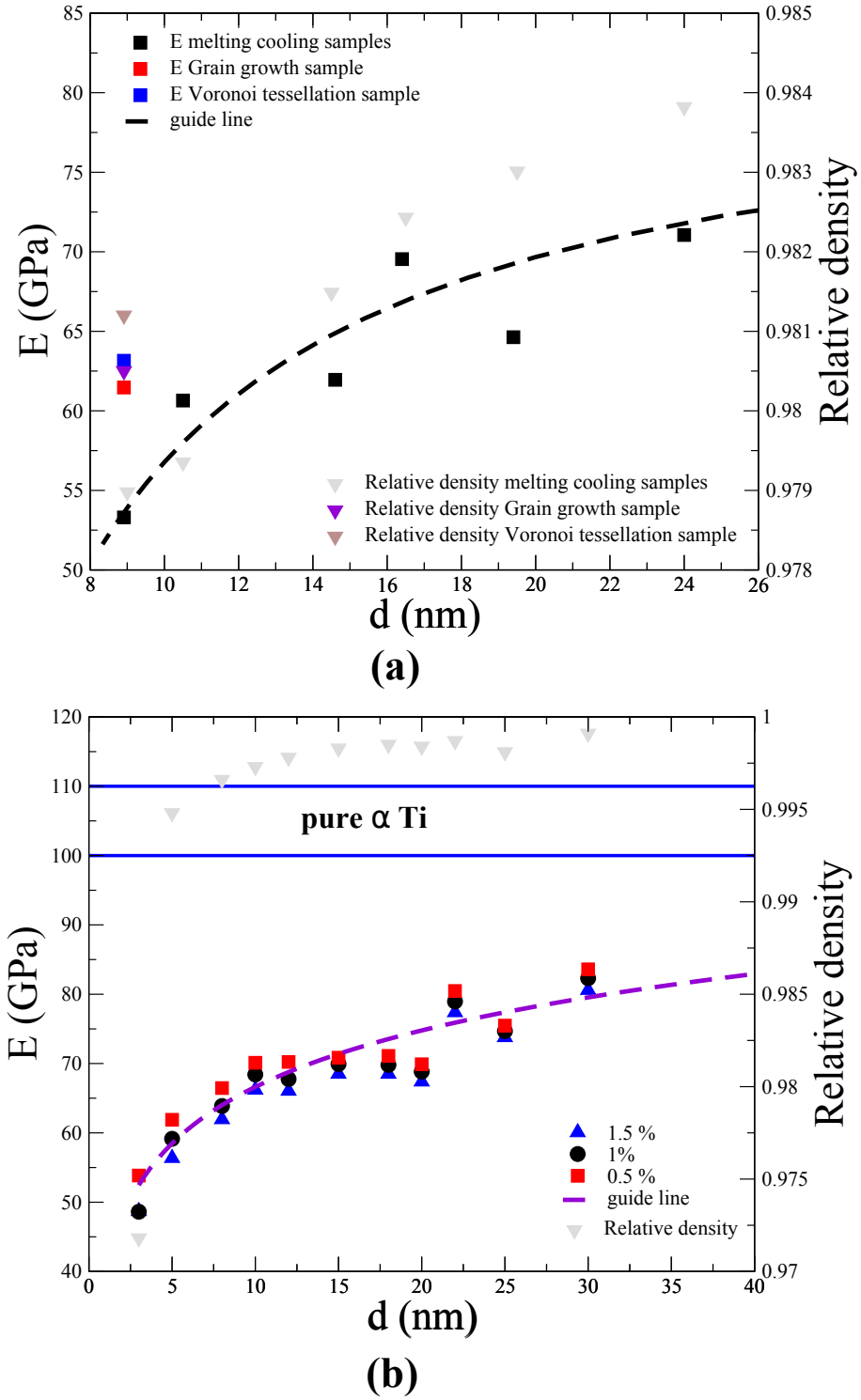

FIGURE 3.4: Variation of Young's modulus and the relative density as function of the mean grain size: (a) For nanocrystalline quasi-2D Copper and (b) For nanocrystalline α-Titanium.

The range of the relative density for our systems is typical for nanocrystalline materials [12, 166]. The values of the relative density of copper are lower than that of the α-Titanium. This is due to the defects present in the grains of the nanocrystalline Copper generated by the melting-cooling method.

3.2.4 Yield and flow stresses as a function of the mean grain size

One of the important phenomenon in nanocrystalline materials is the inverse Hall-Petch response. Strength is usually enhanced, as the grain size decreases. However, when the grain size becomes less than a critical value, the strength begins to decrease due to the prelevance of the role of grain boundaries [24, 28]. After the determination of the elastic region, the yield stress is defined as the stress corresponding to 2 % strain ($\sigma_{2\%}$).

The variation of the yield and flow stresses as a function of the mean grain size has been calculated and presented in Figure 3.5. In Figure 3.5 (a) and (b) the yield and the flow stresses are plotted versus $\overline{d}$ for the quasi-2D nanocrystalline Copper samples. The yield and flow stresses decrease with the decrease of the mean grain size below 16 nm. This tendency indicates a reverse Hall-Petch effect. In Figure 3.5 (a) and (b) two main regimes are present, one that confirms the Hall–Petch tendency for $d \geqslant 16$ nm, in this case the yield and flow stresses decrease with the increase of the mean grain size while the reverse Hall-Petch tendency is observed for $d < 16$ nm. The obtained values are in good agreement with the literature [25, 113].

To find the critical grain size in nanocrystalline α-Titanium, a Hall-Petch plot is constructed in terms of the flow stress calculated as the average stress above 10% strain as shown in Figure 3.5 (c). The crossover from regular to inverse Hall Petch is seen at a critical grain size of 15 nm. This is concluded from the tendency of the flow stress versus the inverse square root of the mean grain size. Moreover, below 15 nm the maximum stress and the yield stress also present an inverse Hall-Petch behavior illustrated by the decrease of the stress with the mean grain size. The critical mean grain size of nanocrystalline α-Titanium is very close to that find for Copper d_c = 16 nm.

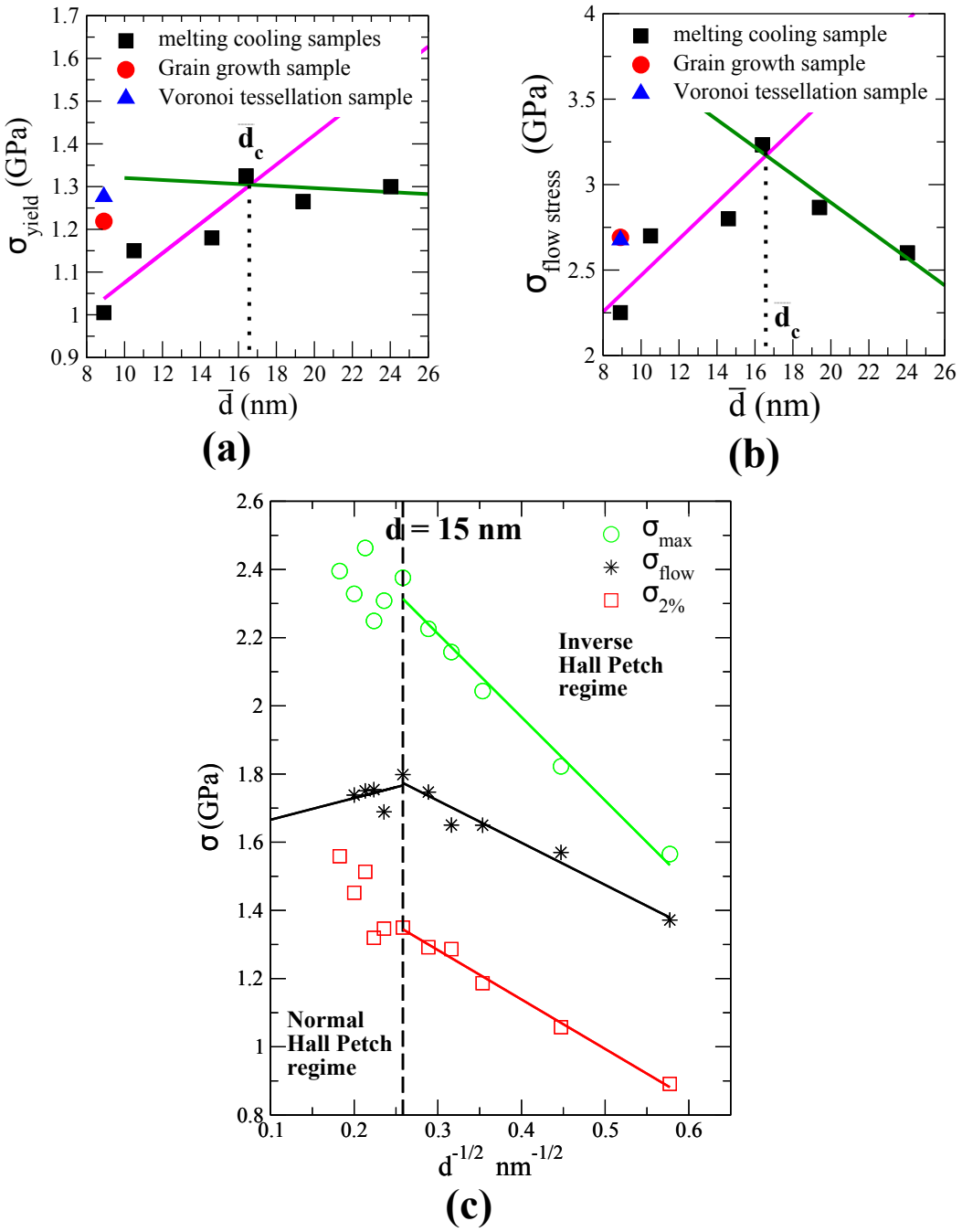

FIGURE 3.5: Effect of grain size on (a) yield stress, and (b) flow stress for nanocrystalline Copper. Panel (c) shows the effect of grain size on the yield, flow and maximum stresses for 3D nanocrystalline α Titanium.

The crossover to inverse Hall-Petch in nanocrystalline α-Titanium is caused by the transition of the dominant deformation mechanisms from dislocations and twinning to grain boundary mediated processes below d_c = 15 nm. In terms of stress-strain relationship, it is clear from Figure 3.2 that the overshoot in the stress-strain curves for mean grain size below 15 nm begins to diminish when the grain size decreases. The overshoot even vanishes for the lower two mean grain size. This confirms that the stress-strain curves for lower mean grain size reach the flow regime smoothly without a stress overshoot related to the nucleation of partial dislocations. Therefore, a clear transition in the deformation behavior to grain boundary mediated process is expected with the decrease of the mean grain size. The regular and inverse Hall Petch slopes for nanocrystalline α-Titanium are 0.64 and 1.24 MPa $mm^{0.5}$.

The normal Hall Petch slope obtained by our molecular dynamics simulations (0.64 MPa.$mm^{0.5}$) is closed to the slope found for coarse-grained commercial pure Titanium (1.1 MPa.$mm^{0.5}$) with a mean grain size between 0.96 and 4.7 μm [168]. Nevertheless, it is instructive to compare simulations and experiments, as this can help to understand the difference of plasticity in HCP and FCC metals. For nanocrystalline Copper, the slope of the Hall Petch computed by molecular dynamics simulations for a mean grain size between 20 and 50 nm by Schiøtz *et al* is 5.9 MPa $mm^{0.5}$. This value is very closed to the experimental value (4.7 MPa.$mm^{0.5}$) [169, 170].

The values of the yield and flow stresses found in our work are higher than that found in experimental work. For example, Sanders *et al* found a $\sigma_{yield} = 300MPa$ for 16 nm nanocrystalline Copper produced by inert gas condensation and warm compaction [12]. However, we should note that nanocrystalline materials are sensitive to the strain rate and the results of the experimental studies are usually obtained using a low strain rate. Indeed, large strain rate sensitivity is found for nanocrystalline Copper as presented above in section 1.1. Therefore, the increase of the strain rate will result in an increase of the yield and flow stresses of the material. This explains the large values found in our work. In the next chapter, the effect of the strain rate on the mechanical properties of nanocrystalline Copper will be investigated.

From the above discussion, one can conclude that the transition to inverse Hall-Petch effect is caused by a change in the dominant plastic deformation

mechanism. For large mean grain size, the emission and propagation of dislocations and twinning dominate the plastic deformation. Whereas, for small grain sizes grain boundary sliding is the dominant deformation mechanism. From the stress-strain response, we can conclude that the macroscopic stress behavior is directly linked to the local plastic deformation mechanism especially to the mobility of dislocations. The objective of our work is now to analyze the evolution of the deformation mechanisms of these nanocrystalline materials at the atomic level.

3.3 Influence of the initial samples conception method and geometry

In this section, two strategies have been applied to evaluate the benefits of melting-cooling method. First, we studied the effect of the construction method on the mechanical response of nanocrystalline Copper. To this aim, we applied a series of uniaxial tensile test on quasi-2D Copper sample with 9 nm mean grain size generated with different methods (table 2.8 (a)). In the second study, the effect of the geometry on the mechanical properties of nanocrystalline Copper has been investigated. We will analyze the results of the uniaxial tensile tests applied on nanocrystalline Copper with the same mean grain size of 9 nm but with different geometries (3D, columnar 3D, and quasi-2D) (table 2.8 (b)).

Influence of the conception method

The results of the uniaxial tensile tests are present in Figure 3.6 (a). The sample generated with the melting–cooling method (blue line) is more ductile than the other samples, furthermore it is yield and flow stresses are lower than these of other samples. This is due to the presence of defects especially edge dislocations inside the grains that play a role in the dissipation of the excess energy of the system before cracking. The Young modulus, the yield, and the flow stresses are extracted from each stress-strain curve.

In Figure 3.4 (a), Young's modulus and the relative density of the samples generated by Voronoï tessellation and the grain growth method are also presented. The values of Young's modulus are higher than that obtained by melting–cooling method. The Young modulus is proportional to the relative density of the system. The Voronoï tessellation sample has the highest relative density and hence the highest Young's modulus. The large fraction of defects inside the

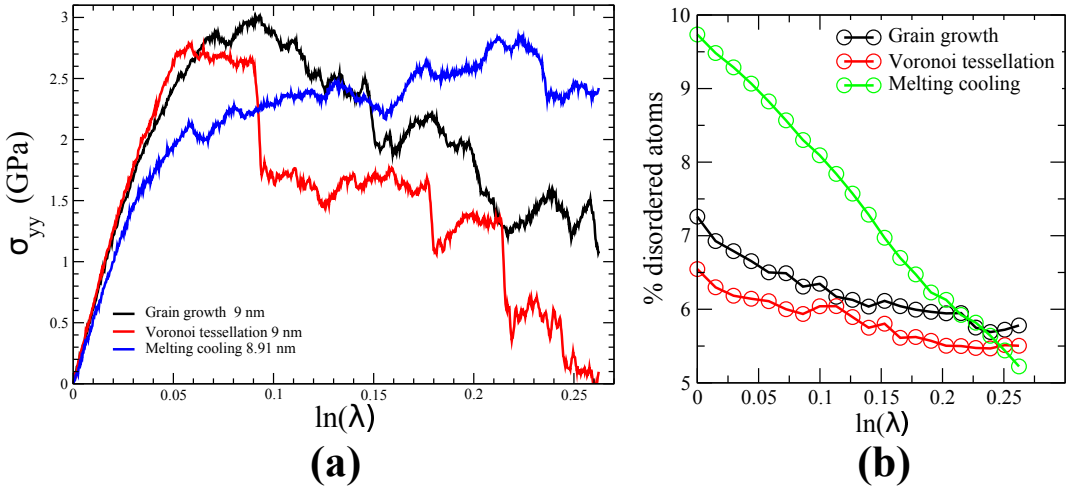

FIGURE 3.6: Comparison of the mechanical behaviour under tensile loading for different samples generated with different methods. (a) True stress versus strain curves for 9 nm samples at $\dot{\varepsilon} = 10^8\ s^{-1}$ and $T = 300°K$, (b) The variation of the fraction of the disordered atoms with the strain for the same samples.

sample generated by melting cooling method explains its low Young's modulus in comparison with other samples.

In Figure 3.6 (b), the variation of the fraction of disordered atoms with the strain is calculated. The disordered atoms are atoms belonging to grain boundaries and defects inside the grains. The fraction of disordered atoms decreases with the increase of the strain. Therefore, the coalescence of grains is an important deformation mechanism for these nanocrystalline samples. However, the rate of the coalescence of grains is higher in the melting cooling method than the other samples. This can be explained by (1) the curvature of the grain boundaries, which promote the grain growth in this sample and (2) The distribution of grain size inside the nanostructure. We have seen that the small grains collapse with the larger ones. Thus, the grain size distribution affects the rate of coalescence. Haslam *et al* also showed that curvature-driven grain boundary migration leads to grain growth. Also, they revealed that the increase of stress enhances the grain boundary migration and grain rotation that lead to grains coalescence [99, 100].

In conclusion, two additional deformation mechanisms are explored by melting cooling method:

1. Curvature driven grain boundary migration that induces grain coalescence.

2. Shear bands generated by the motion of perfect edge dislocations present inside the grains on {110} slip planes that acts to relax the imposed stress level. This mechanism will be discussed in details below.

Influence of the structure of the system

The results of the uniaxial tensile tests applied on systems with different geometries and with 9 nm mean grain size (table 2.8 (b)) are shown in Figure 3.7. The stress strain curve for the full 3D sample increases linearly to reach a plateau then it holds constant in the flow regime. The transition from the elastic to plastic deformation is very smooth without any stress overshoot and with a small plastic strain hardening of nearly 1.8% typical for nanocrystalline materials (see section 1.2.1.3). In contrast, the stress strain behavior for the two columnar 3D samples present a stress overshoot before the flow regime. This overshoot is more pronounced in the Voronoï sample.

The analysis of the atomic configurations shows that the delay of the nucleation and propagation of partial dislocations is the cause of the overshoot in the stress strain curve of the columnar systems. The tensile stress drops sharply once partial dislocations propagate in these samples. The strains at which partial dislocations propagate in these samples are marked in the Figure. Finally, in the flow regime, the tensile stress fluctuates around a constant value the flow stress .

We have calculated the flow stress for all the samples used in this study, the following observation are concluded:

1. The flow stress of the quasi-2D sample is higher than that for the 3D systems.

2. The flow stress of the 3D system is higher than that for the columnar 3D systems.

3. The flow stress of the two columnar 3D systems is nearly the same.

As discussed above, the shape of the stress-strain curve is directly linked to the local plastic deformation mechanisms active in the system. For this reason, we analyzed the atomic configurations of the samples used in this study at different strains to understand the above observations. Concerning the first one, we concluded that the partial dislocations mechanism (see section 1.2.2.3) is not present in the quasi-2D sample, whereas this mechanism is preponderant

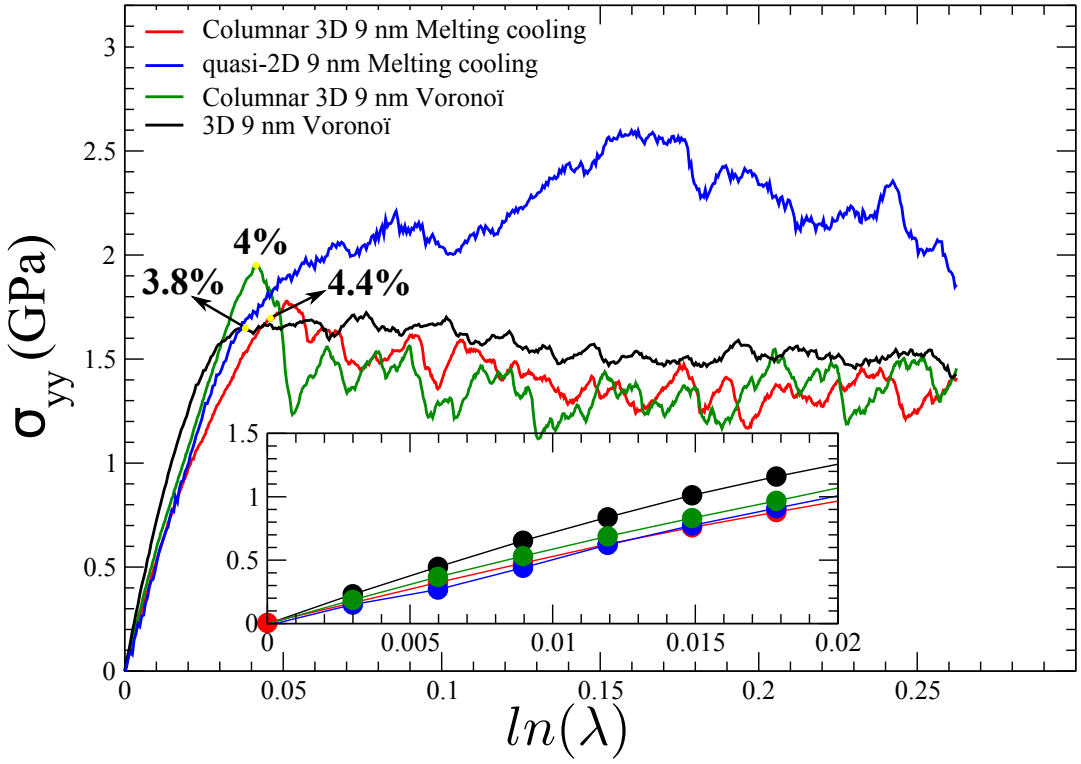

FIGURE 3.7: Comparison of the stress behavior of different nanocrystalline samples submitted to uniaxial tensile test at $\dot{\varepsilon} = 10^8\ s^{-1}$.

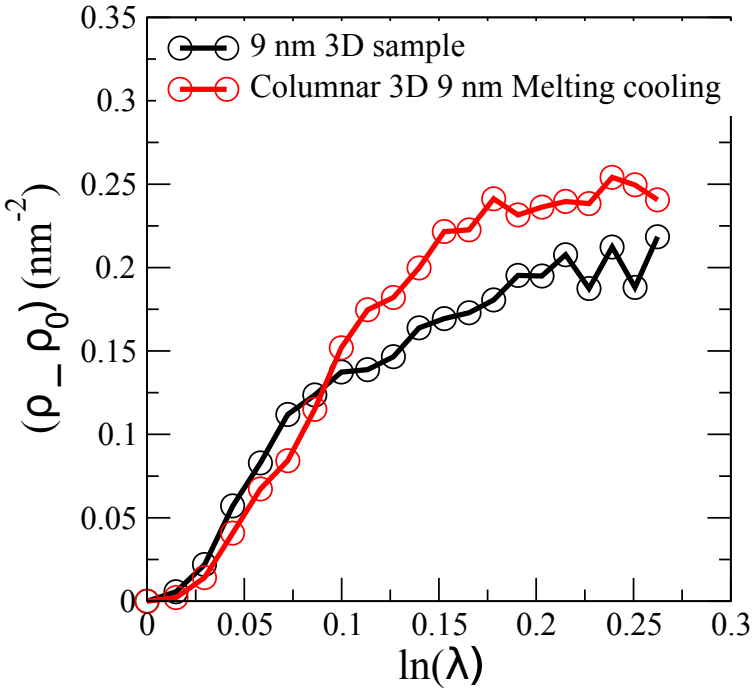

FIGURE 3.8: Comparison of the density of partial dislocations between the columnar 3D and the full 3D samples.

in the 3D samples. This justifies the smaller flow stress of the 3D structures in comparison with the quasi-2D. In fact, when partial dislocations are emitted from grain boundaries the stress on these boundaries is relaxed and hence the macroscopic stress. Also during the propagation of these dislocations, the stress of the system is relaxed by generating local plastic deformation.

The key point to understand the difference of the flow stress between the columnar 3D and the full 3D sample is the calculation of the dislocation density. The flow stress is directly linked to the dislocation density. The increase of the dislocation density decreases the flow stress and vice versa. We calculate the partial dislocation density for the full 3D and the columnar 3D sample generated by melting cooling method using the dislocation extraction algorithm (see section 2.3.4). Figure 3.8 shows the variation of the partial dislocation density versus the strain for the two systems. The density of partial dislocations for the columnar 3D sample in the flow regime is higher than that of the full 3D sample. This explains the second observation regarding the smaller flow stress of the columnar 3D sample generated by melting cooling method.

Moreover, the inset of the Figure 3.7 shows the elastic regime of the stress-strain curve of different systems. We remark that the elastic behavior of the quasi-2D and the columnar 3D samples generated by melting-cooling method overlap.

The lack of defects inside the grains of the full 3D structure and the planar grain boundaries lead to a mechanical response somewhat artificial. The defects present in the samples generated by melting cooling method lead to a possibility of exploring new deformation mechanisms which are not fully accessible for the other samples (e.g. curvature driven grain growth). To this reasons, in the next chapter, we choose to study the effect of the strain on the mechanical properties of the quasi-2D and the columnar 3D system with the 9 nm mean grain size generated by melting cooling method. Moreover, all the deformation mechanisms observed in these samples will be discussed below.

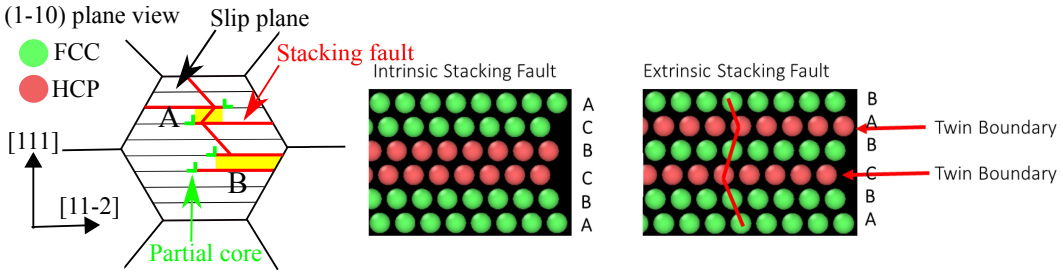

FIGURE 3.9: Schematic plot of the intrinsic and the extrinsic stacking fault formation by Shockley partial dislocations the initial lattice is FCC.

3.4 Deformation mechanisms

3.4.1 Dislocation mediated plasticity

The analysis of the atomic configurations allows one to further identify how each deformation mechanism manifests at the atomic level. For this purpose, a series of snapshots from the atomic configurations has been taken at the different strain levels. Then, different post-treatment analyses (e.g the calculation of the atomic Von Mises strain, the common neighbor analysis) have been done to investigate the evolution of the main deformation mechanisms. The following mechanisms have been seen for nanocrystalline materials:

- **Mechanism 1**: The emission of Shockley partial dislocations from a grain boundary that cross the entire grain to vanish on the opposite grain boundary. While propagating these dislocations left behind some stacking fault planes (section 1.2.2.3).

  For the nanocrystalline HCP α-Titanium, the close-packed planes are (0002) planes. These basal planes are the most observed glide planes in HCP crystals. Unlike the FCC structure, two kinds of intrinsic fault I_1 and I_2 exist [68]. A stacking fault consists of a single FCC plane is generated by the motion of Shockley partial dislocation of the I_1 type. However, a staking fault ribbons consisting of two FCC planes is formed by the motion of this Shockley partials I_2 type.

- **Mechanism 2**: The twinning mechanism has been extensively seen during the deformation of these nanocrystalline samples. Like the partial dislocations, the twinning mechanism seen for nanocrystalline FCC Copper is different from that of HCP α-Titanium.

For the nanocrystalline FCC Copper, the overlapping of the stacking fault ribbons of two Shockley partials gliding on adjacent slip planes is the source of extrinsic stacking fault or micro-twin (Figure 3.9) (see also section 1.2.2.3). However, for the nanocrystalline HCP α-Titanium, the grain boundaries is considered as the source for twinning. Twin boundaries are nucleated from grain boundaries and then cross the entire grains to vanish on the opposite boundaries. While propagating these twin boundaries change the grains orientations.

- **Mechanism 3**: Dislocations emitted from a low angle grain boundaries leading to shear bands inside the grain up to the opposite grain boundary.

  An example of this mechanism is present in Figure 3.10. The misorientation angle between two grains G_1 and G_2 is 15°. The lattice orientation of the two grains is marked by two yellow square in Figure 3.10 (a). A perfect edge dislocation (D_1) is emitted from a low angle grain boundary between G_1 and G_2 (Figure 3.10 (b)). This boundary is formed by perfect edge dislocations with different distances between the cores due to the curvature of the boundary. The dislocation D_1 propagates in the grain to finally vanish on the opposite boundary. The trajectory of this dislocation is detected using the atomic Von Mises strain. Large stress assisted free volume migration is present on the grain boundary. This allows accommodating the core of the dislocation D_1. Which entails a nucleation of another edge dislocation D_3 at the grain boundary ledge (L shape edge on grain boundary). Once the stress concentration on the grain boundary increases the core of this dislocation propagates through the grain to relax this increase, thus generating another shear band (Figure 3.10 (d)).

- **Mechanism 4**: Dislocations emitted from the inside of the grain, precisely, from edge dislocations present inside the grain lead to a sliding up to an adjacent grain boundary. These dislocations are reminiscent from the cooling process. The Burger vector for these dislocations is found to be $\frac{1}{2}\langle 110\rangle$ on a $\{110\}$ sliding planes (Figure 3.11).

  In Figure 3.11 some of the edge dislocations inside the grain have been marked by red (Figure 3.11(a)). In comparing the evolution of the grain, we observe that once the resolved shear stress inside the grain reaches

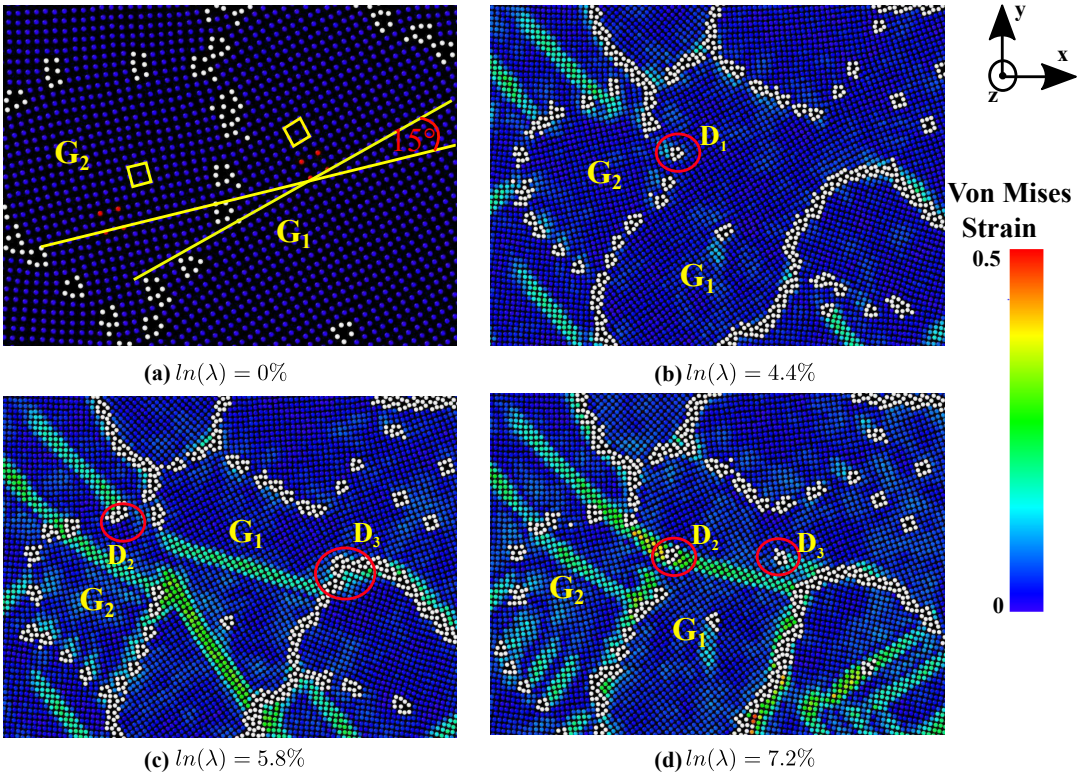

(a) $ln(\lambda) = 0\%$ **(b)** $ln(\lambda) = 4.4\%$

(c) $ln(\lambda) = 5.8\%$ **(d)** $ln(\lambda) = 7.2\%$

FIGURE 3.10: Zoom on two grains inside the quasi-2D nanocrystalline Copper sample with 9 nm mean grain size at different regions and strains where a low angle grain boundary is present with 15° misorientation angle. The atomic configuration is colored by the atomic Von Mises strain calculated with respect to the initial configuration. The defects inside the nanostructure are marked by white and superposed to the atomic Von Mises strain cartography.

the critical stress required to move these dislocations. They will propagate generating sliding planes where large Von Mises strain is present.

Influence of the grain size

In section 3.2.4, we have seen that at $d_c = 16.5nm$ a transition to inverse Hall-Petch is present in nanocrystalline Copper. The atomic configurations of this critical grain size have been analyzed, and the deformation mechanisms have been compared with that of the 9 nm mean grain size (Figure 3.12).

In the snapshots of Figure 3.12, the color of the atoms represents the atomic von Mises strain. It is then possible to distinguish the shear bands, corresponding to a value of the atomic Von Mises strain above 0.1 and colored in green in the Figure. These snapshots show the existence of two types of dislocation mechanisms in these samples (mechanism 3 and 4), some of these dislocations are marked by pink (mechanism 3) and yellow (mechanism 4) circles respectively.

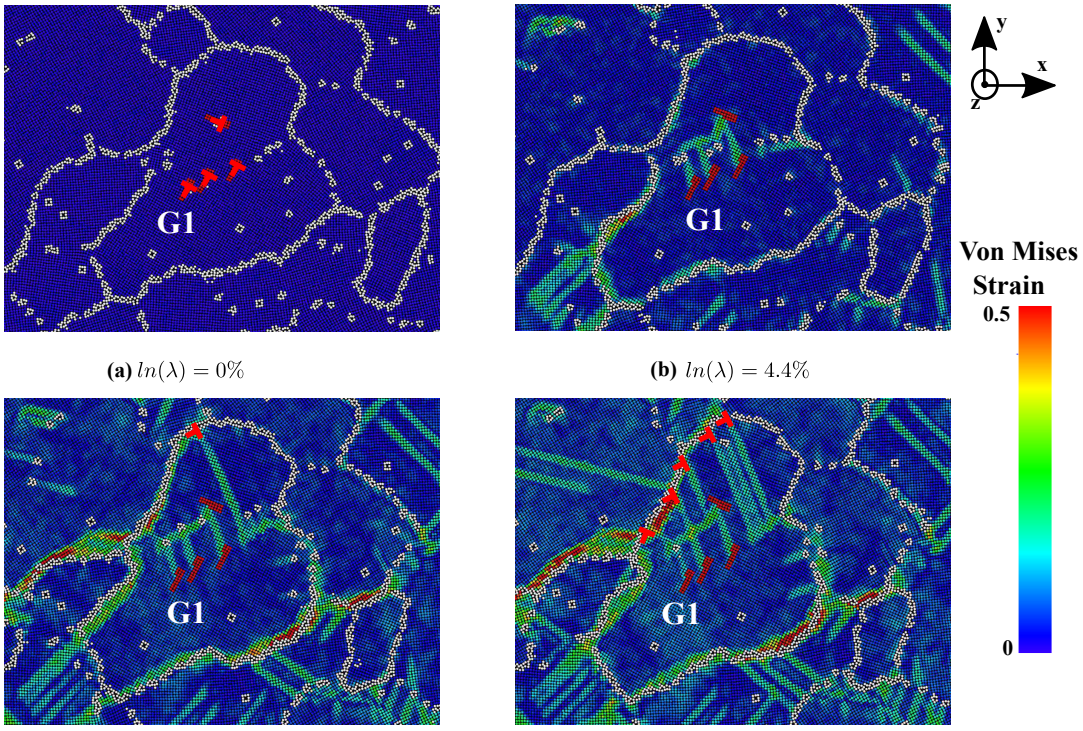

(a) $ln(\lambda) = 0\%$ **(b)** $ln(\lambda) = 4.4\%$

(c) $ln(\lambda) = 7.2\%$ **(d)** $ln(\lambda) = 8.6\%$

FIGURE 3.11: Evolution of a grain G1 in the quasi-2D nanocrystalline Copper during deformation. The grain size of the sample is 9 nm and it is colored by the atomic Von Mises strain calculated with respect to the initial configuration. The grain boundaries and defects are selected by common neighbor analysis and colored by white. Some of the initial edge dislocations are marked by red inside the grain.

Also, we can see several slip systems active in the samples especially at 5.8 % strain. Moreover, the shear bands present on grain boundaries are marked by red ovals.

When comparing the Figure 3.12 (c) and (a) at 2.95 % strain. It is clear the domination of the dislocation process in the sample with 16.5 nm mean grain size. When the grain size increases the fraction of grain boundaries decreases and hence their contribution to plasticity is not relevant. When the strain increases to 5.8 % a combination of dislocations and grain boundaries processes dominate the plastic deformation in the 9 nm sample, whereas dislocations still dominate the plastic deformation in the 16.5 nm sample. Therefore, the deformation mechanism is dominated by dislocations at the critical mean grain size. This suggests that the increase of the contribution of grain boundaries to plasticity is responsible to the crossover to inverse Hall-Petch effect (see section 3.2.4).

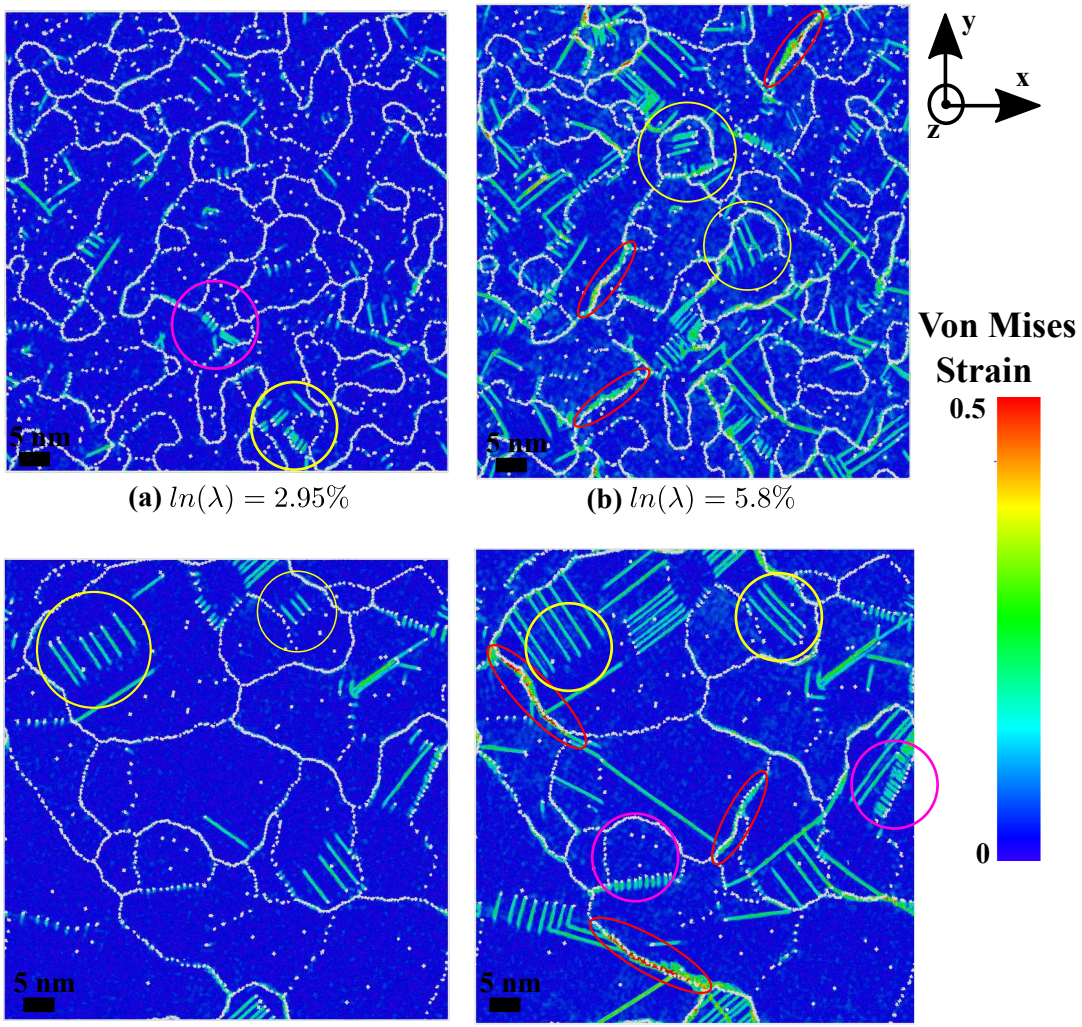

(a) $ln(\lambda) = 2.95\%$ **(b)** $ln(\lambda) = 5.8\%$

(c) $ln(\lambda) = 2.95\%$ **(d)** $ln(\lambda) = 5.8\%$

FIGURE 3.12: Effect of the grain size on the deformation mechanisms of the quasi-2D nanocrystalline Copper samples. Snapshots of the microstructure for 9.0 nm grain size (a) and (b) colored with the atomic von Mises strain and for two different strain levels and for 16.5 nm (c) and (d). White atoms are disordered atoms at grain boundaries, identified by common neighbor analysis. The atomic von Mises strain is calculated with respect to the initial configuration.

Perfect and partial dislocations

The nucleation of the Shockley trailing partial that eliminates the stacking fault ribbon created by the leading partial at the timescale of molecular dynamics has been always an open question (see section 1.2.2.3). As discussed above, the emission of the trailing partials depends on the shape of the generalized stacking fault energy curve (section 2.2.3). More specifically on the ratio of the stacking fault energy to the unstable stacking fault energy. If this ratio is close to one, the emission of the trailing partial is plausible at the timescale of molecular dynamics (as the case of FCC Al) [111]. For the EAM potential used in our work this ratio is 0.11 (see table 2.2) far from one. Therefore, the emission of the trailing partial is not expected at the timescale of the simulations.

However, in our work, the nucleation of the trailing partials has been seen at large plastic strain for nanocrystalline Copper. In fact, the low ratio of 0.11 indicates that the energy barrier to nucleate the trailing partial is large (section 2.2.3). Therefore, sufficient time is needed to re-concentrate the stress at the grain boundary in order to nucleate a trailing partial. Hence, the emission of trailing partial is localized at the high plastic strain. As the case of nanocrystalline Al [36], the trailing partial has been nucleated from a different grain boundary where the leading partial has emitted.

Figure 3.13 presents some snapshots of the atomic configurations of the columnar 9 nm sample during the tensile test. The common neighbor analysis and the atomic Von Mises strain are used to identify the dislocation mobility in these snapshots at each strain level. To analyze the plastic deformation between each strain level, the atomic Von Mises strain have been calculated using different reference configurations. The initial configuration has been taken as a reference for the atomic configuration at 2.95 %. Whereas, the atomic configuration at 2.95 % is used as the reference for the 7.23 % configuration. In addition, the atomic configuration at 7.23 % is considered as the reference for the 11.3 % configuration. In this way, the evolution of the plastic deformation can be detected by comparing different snapshots.

Firstly, the emission of Shockley partial dislocations from grain boundaries that generate stacking faults is present nearly in all grains at 7.23 % (mechanism 1). A schematic presentation of the stacking sequence of an intrinsic

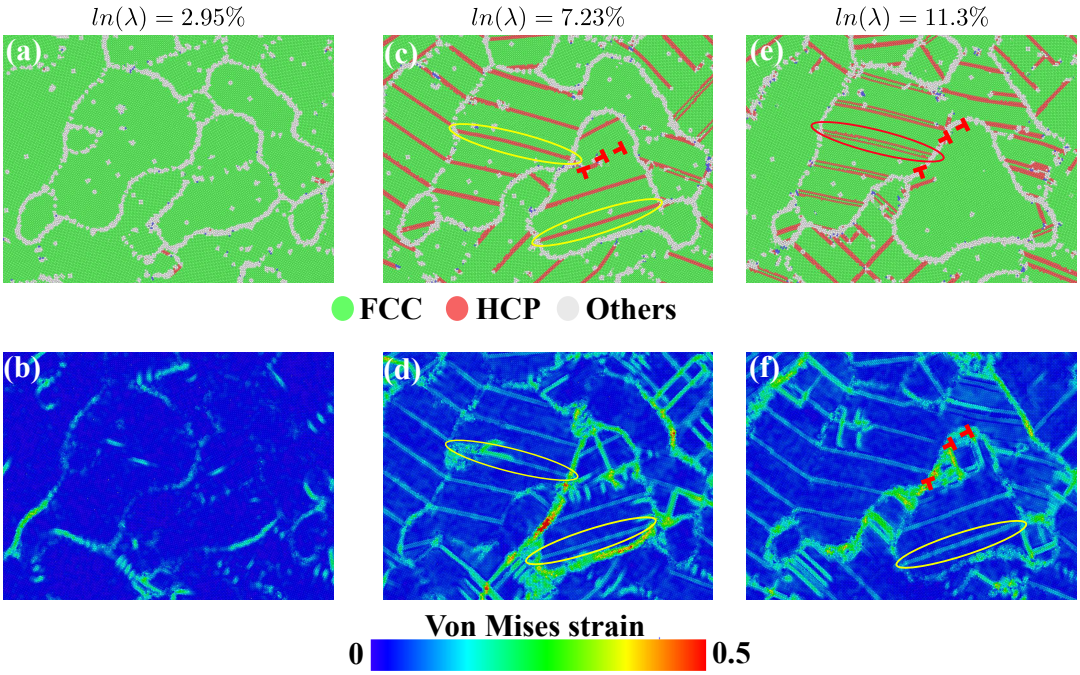

FIGURE 3.13: Zoom on a zone inside the columar 3D 9 nm Copper sample deformed at $\dot{\varepsilon} = 10^8\ s^{-1}$. The atomic configuration at each strain level has been colored by the common neighbor analysis and the atomic Von Mises strain.

stacking fault is presented in Figure 3.9. In Figure 3.13 (c) some of the stacking faults are encircled by yellow ovals. When the atomic Von Mises strain is calculated in Figure (d), we can see that the plastic deformation is localized on these slip systems. Moreover, some edge dislocations inside the grains have been marked by red (T) at 7.23 %. When the strain increases to 11.3 %, these dislocations propagate and vanish on the adjacent grain boundary as seen in Figure (e) (mechanism 4). The atomic Von Mises strain in the Figure (f) indicates the shear bands generated by these dislocations. As mentioned above, these dislocations propagate on {110} sliding planes.

By comparing the snapshots at different strain levels in Figure 3.13 we can see that some stacking faults generated by the motion of partial dislocations have disappeared in Figure 3.13 (e). This indicates the nucleation and propagation of the trailing partials that eliminate the stacking faults before vanishing on the opposite grain boundary. Therefore, even at this timescale, the trailing partials have been emitted from the grain boundary. This indicates that dislocations are not only partials, and perfect dislocations exist even at 9 nm mean grain size (section 1.2.2.3). In Figure 3.13 (f) a yellow oval mark one sliding plane of the trailing partial. In this Figure, as mentioned before the reference configuration for the atomic Von Mises strain is taken at 7.23 %. Therefore,

any plastic events occurred between 7.23 and 11.3 % is detected by the atomic Von Mises strain. The shear bands present inside the grain in Figure 3.13 (f) confirms the emission of the trailing partials.

In conclusion, the high strain rate used in molecular dynamics constraints the time to re-concentrate the stress at grain boundary in order to nucleate trailing partials. Therefore, in our work, the trailing partials are specifically detected at the high plastic strain. This indicates that the emission of perfect dislocations dissociated into two partials is an important deformation mechanism of nanocrystalline materials. Also, an open area is still lacking concerning the effect of the strain rate on the emission of perfect dislocation mechanism. When scaling to the experimental limit or while reducing the strain rate does partial dislocations still exist or all dislocations are perfect dislocations? This will be discussed in the next chapter.

3.4.2 Grain boundary mediated mechanisms

Our simulations also reveal abundant inter-granular processes involving dislocations, grain boundaries interactions and grain boundary based mechanisms such as grain boundary sliding, grain boundary and triple junction migrations. Figure 3.14 focus on a zone inside the 9 nm columnar 3D Copper sample generated by melting cooling at different strain levels. To investigate the inter-granular activity, the grain boundaries in the initial configuration have been superposed to the actual atomic configuration at 5.8% and colored by blue (Figure 3.14(a)).

Firstly, the two grains marked by red circles in the Figure 3.14 (a) have collapsed with the bigger grain and one of them leaves behind an edge dislocation marked by R_1. A zoom on this dislocation is present in the left side on the Figure 3.14. The atomic structure of this dislocation is marked by blue. Secondly, grain boundaries and triple junctions migrations are encircled by yellow ovals in the Figure (a). They are responsible for the relaxation of the stress by generating local plastic deformation before the onset of dislocation emission. In this Figure, the onset of partial dislocation emission is not yet attained. Therefore, these processes are responsible to accommodate the increase of the imposed plastic strain at grain boundaries.

The atomic Von Mises strain is a good measurement of the plastic or irreversible deformation (section 2.3.3). This parameter is computed for the atomic

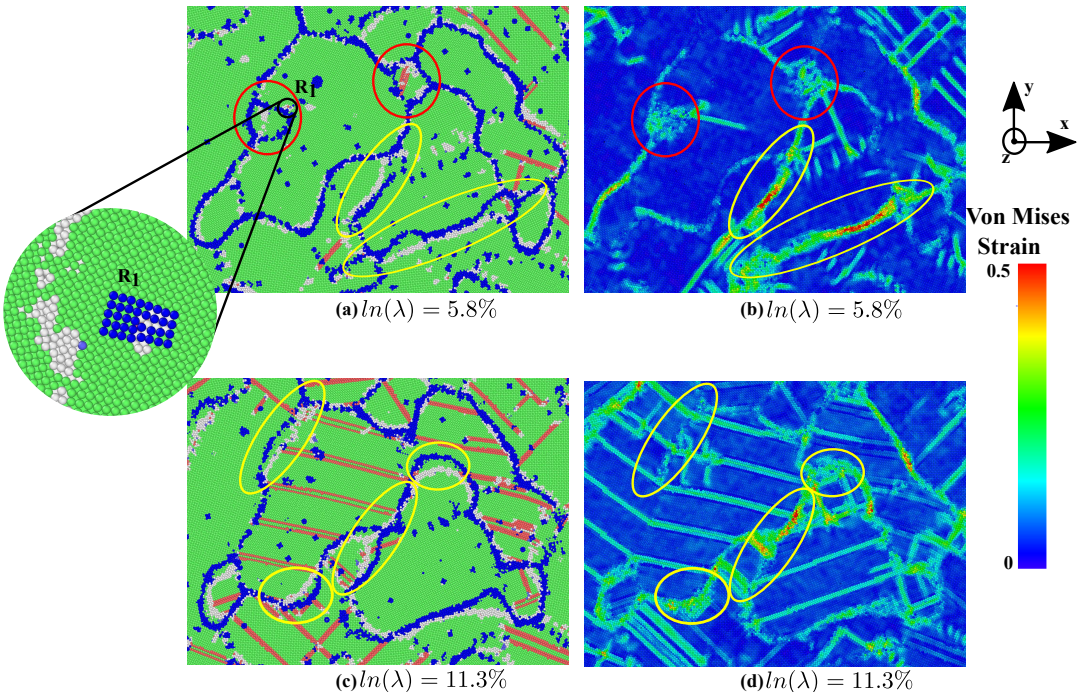

FIGURE 3.14: Zoom on a zone inside the 9 nm sample deformed at $\dot{\varepsilon} = 10^8\ s^{-1}$ at different strain levels. The common neighbor analysis has been used to identify the local structure of each atom in the snapshots (a) and (c). The blue atoms in the atomic configuration (a) are the grain boundaries of the initial configuration. The blue atoms in the atomic configuration at 11.3 % are the grain boundaries of the atomic configuration at 5.8 % strain level. In this way the evolution of the plastic deformation at grain boundary can be detected. The atomic Von Mises strain have been calculated for these configurations and presented in the snapshots (b) and (d). The initial configuration has been taken as a reference for the 5.8% deformed configuration in (b). The atomic configuration at 5.8% has been taken as a reference for the 11.3% deformed configuration in (d).

configuration at 5.8% with respect to the initial one (Figure 3.14 (b)). Large Von Mises strain is present on the grain boundaries (red circles and yellow ovals). In comparing this Figure with the Figure (a) one can distinguish directly that the motion of grain boundaries and triple junctions generate local plastic deformation at grain boundaries (see section 1.2.2.1). Moreover, the coalescence of grains is caused by grain boundary migration hence local plastic deformation is also present when two grains merge.

In conclusion, the motion of grain boundaries and triple junctions leads to grain growth (coalescence of grains) and to relax the stress concentration at grain boundaries by generating local plastic deformation. Now, we want to analyze the effect of the emission and absorption of partial dislocations on grain boundaries processes. For this purpose, first, we extract the atomic configurations of the same grains of Figure 3.14 (a) and (b) but at 11.3 % deformation. At

this plastic strain, partial dislocations and twinning are present inside these grains (Figure 3.14 (c)). Also, the grain boundaries of the atomic configuration at 5.8% are superposed to the Figure 3.14 (c) and marked by blue. In this way, the motion of the grain boundaries from 5.8 to 11.3 % can be detected.

In comparing gray and blue atoms (the actual and initial grain boundaries), it is evidenced the motion of some part of the grain boundaries (yellow ovals in the Figure). This indicates that large grain boundaries processes such as atomic shuffling and stress assisted free volume migration is needed to nucleate and accommodate partial dislocations on grain boundaries (see section 1.2.2.1). Moreover, in Figure 3.14 (d) the atomic Von Mises strain at 11.3% is calculated with respect to the atomic configuration at 5.8%. As mentioned above, the motion of some regions of grain boundaries leads to relaxing the stress by generating plastic deformation (yellow ovals in Figure 3.14 (d)).

3.5 conclusion

Molecular dynamics simulations have been used to study the mechanical behavior of nanocrystalline Copper and α-Titanium. The following conclusions have been drawn:

- The inverse of the Hall Petch relation havs been found at a grain size of 16 nm has been found for nanocrystalline Copper and at 15 nm for nanocrystalline α-Titanium. Below this critical grain size, the yield and flow stresses decrease with the decrease of the mean grain size. A combination of grain boundaries activities (Atomic shuffling, grain boundary and triple junction migrations, grain coalescence) and dislocations mechanisms control the deformation behavior of these samples.

- The transition of the Hall Petch effect is caused by the change of the dominant deformation mechanism from dislocations for large grain size to a combination of dislocations and grain boundary mediated mechanisms for small grain size.

- The Young modulus of the nanocrystalline Copper and α-Titanium decreases with the decrease of the mean grain size.

- A deformation mechanism has been found. When edge dislocations present inside the grains propagate on {110} planes. The propagation of

these dislocations generates shear bands inside the grain and hence relax the stress of the system.

- Basal dislocations and mechanical twinning are the dominant deformation processes in α-Titanium. Twin boundaries are found to nucleate at grain boundaries and then cross the entire grains to vanish on the opposite grain boundaries inducing a complete re-orientation of the grain.

Chapter 4

Study of the strain rate sensitivity of nanocrystalline copper

Contents

4.1 Introduction

In chapter 3 we have shown that a combination of dislocations and grain boundaries mediated processes is responsible for the accommodation of the plasticity in nanocrystalline materials. The study of the strain rate sensitivity of nanocrystalline materials elucidates the rate limiting of the active deformation mechanism [81, 171, 172]. In this way, an important insight into the

contribution of each deformation mechanism to plasticity can be formed. For example, the contribution of grain boundary sliding was found to increase in nanocrystalline materials with the decrease of the loading strain rate in nano-indentation tests applied on nanocrystalline Copper [15–17].

Molecular dynamics simulations have been also used to investigate the effect of the strain rate on the deformation behavior of nanocrystalline FCC metals [29, 37, 64]. The results confirmed the enhancement of the grain boundary activity with decreasing strain rate as proposed by experiments [37]. However, in these studies, the strain rate used varies from 10^7 to 10^{10} s^{-1} typical for molecular dynamics simulations. This range of strain rate remains two to three order of magnitude higher than the experimental limits. Therefore, two main questions arise:

- What is the ability of the nanocrystalline material to relax and equilibrate under the applied mechanical load at the timescale of the molecular dynamics simulations?
- Can the deformation mechanisms seen in molecular dynamics simulations be extended to the experimental range?

Motivated by this lack in the understanding of the strain rate sensitivity of the mechanical behavior of nanocrystalline materials, we applied molecular dynamics simulations of uniaxial tensile tests to study the effect of the strain rate on the plastic deformation mechanisms of two nanocrystalline Copper systems. The range of the strain rate used in our study can be attained experimentally (section 2.9). Two nanocrystalline systems generated by melting cooling method have been used in this study, a quasi-2D and a columnar 3D one with an average grain size of 9 nm. As discussed in chapter 3, in these two models a combination of dislocations, grain boundary sliding and twinning are the main deformation mechanisms. We will discuss the effect of the strain rate on (i) the stress-strain response, (ii) the relaxation behavior and (iii) the atomic scale deformation mechanisms of these models

4.2 Results

4.2.1 Strain rate dependence of the stress strain response

The results of the uniaxial tensile tests applied on the nanocrystalline models are presented in Figure 4.1. For the quasi-2D sample, we stopped the

tensile test at $\dot{\varepsilon} = 10^4 s^{-1}$ (7.6% deformation level) because of the huge computational time required to reach e.g. $\varepsilon_{yy} = 26.3\%$ as for the other simulations performed from $\dot{\varepsilon}$=5.10^6 to 10^9 s^{-1}. Similarly, the tensile test of $\dot{\varepsilon} = 10^5 s^{-1}$ was stopped at 14.6% and that of $\dot{\varepsilon} = 10^6 s^{-1}$ at 17.3%. For the quasi-2D model (Figure 4.1 (a)) the stress increases continuously with strain to reach a threshold then fluctuates around a constant (i.e. the flow stress). For the columnar 3D model the stress exhibits an overshoot before the onset of the plastic flow regime. In the previous chapter, we have shown that the stress strain curves of the quasi-2D and the columnar 3D samples overlapped in the elastic regime (section 3.2.1).

We notice four features in the stress-strain response of the Figure 4.1:

1. The increase of the flow stress with the strain rate.
2. The presence of abrupt stress changes (i.e. jumps) in the plastic flow regime at low strain rate especially in the quasi-2D sample.
3. The overshoot of the columnar 3D sample which is less pronounced with the decrease of the strain rate.
4. The dependence of the Young's modulus on the strain rate indicating the non-equilibrium character of the systems.

The mobility of dislocations controls the response of the macroscopic stress with respect to the increase of the applied strain in materials. Therefore, we have quantified the variation of the dislocation densities inside the two nanocrystalline copper models. This quantification allows understanding the first three above features.

We calculate the fraction of slipped atoms on the sliding planes of the edge dislocations for the quasi-2D sample every 0.9 % strain at different strain rates. To calculate this fraction, we first applied a common neighbor analysis to identify the FCC atoms (atoms inside the grains). Then, we calculate the atomic Von Mises strain between the running and a reference configuration. Finally, we compute the fraction of FCC atoms having Von-Mises strain higher than 0.1. For the columnar 3D sample, we calculated the Shockley partial dislocations density at different strain rates. We used the dislocation extraction analysis to compute the length of all partial dislocation lines. Figure 4.2 (a) shows the variation of the fraction of slipped atoms on the sliding planes of the edge dislocations in the quasi-2D sample as a function of strain at different applied strain rates. This fraction increases with strain and then fluctuate

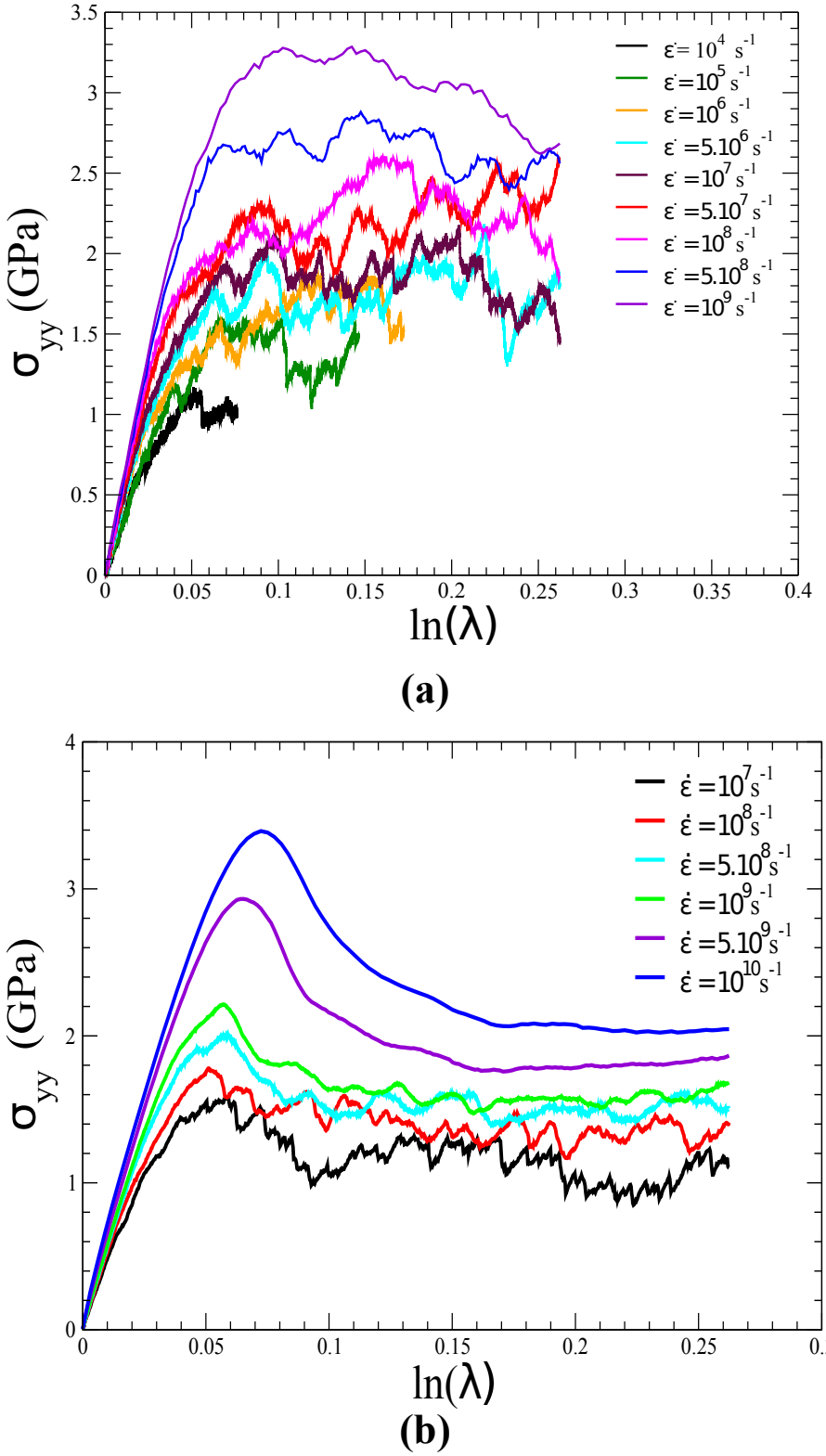

FIGURE 4.1: (a) True stress strain curves of the quasi-2D nanocrystalline Copper with $\bar{d} = 9\ nm$ at strain rates $\dot{\varepsilon}$ ranging from 10^4 to $10^9\ s^{-1}$. (b) True stress-strain curves of columnar 3D nanocrystalline Copper with $\bar{d} = 9\ nm$ at strain rates going from 10^7 to $10^{10}\ s^{-1}$

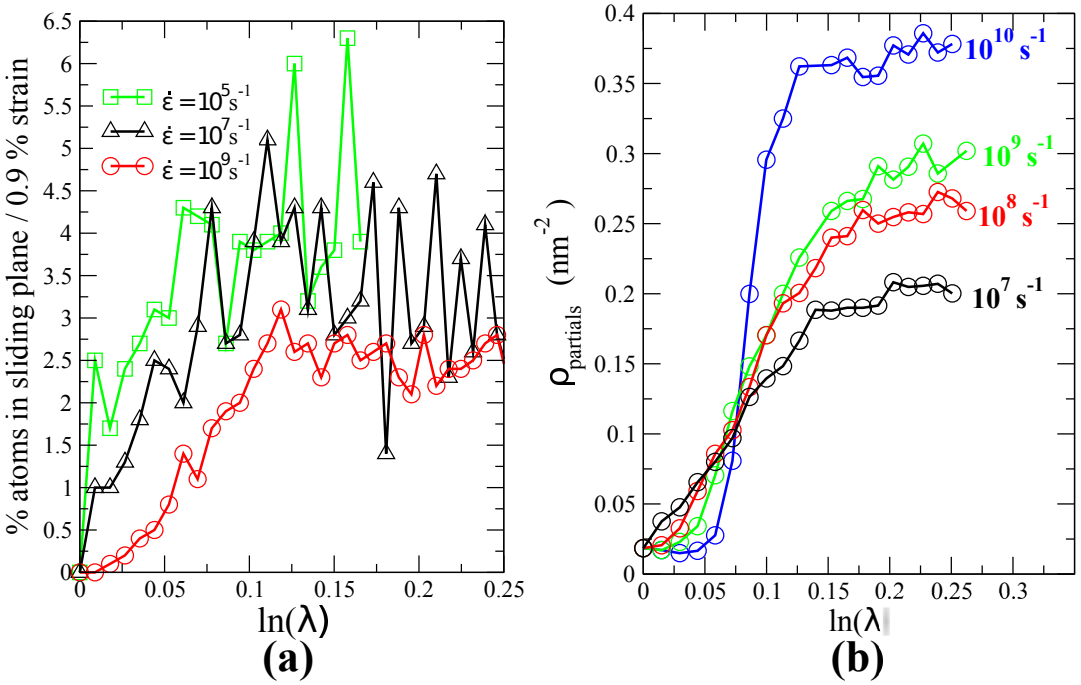

FIGURE 4.2: (a) Evolution of the fraction of slipped atoms on the sliding planes of the edge dislocations in the quasi-2D sample per 0.9% strain versus strain for different strain rates, (b) Density of the Shockley partial dislocations with $b = \frac{1}{6}$ <112> in the columnar 3D sample versus strain for different strain rates.

around a constant value in the plastic flow regime. While comparing the tendency for different strain rates, we can see that this fraction increases with the decrease of the strain rate especially before the occurrence of the plastic flow. Thus, the delay of the onset of the dislocations propagation is responsible for the increase of the flow stress with the strain rate.

For the columnar 3D sample, Figure 4.2 (b) shows the variation of the Shockley partial dislocations density at different strain rates. We notice that the values of our calculated dislocation densities are of the same order ($10^{17} m^{-2}$) as those found in experimental work and molecular dynamics simulations [112, 173, 174]. Two main observations can be distinguished from this Figure:

1. The density of partial dislocations for strain below 7 % decreases as the applied strain rate increases. This indicates the delay of the nucleation of partial dislocations with the increase of the strain rate.

2. The density of partial dislocations in the flow regime increases with the strain rate.

The first observation is responsible for the overshoot present in the stress-strain curve. At high strain rate, the onset of partial dislocation nucleation and

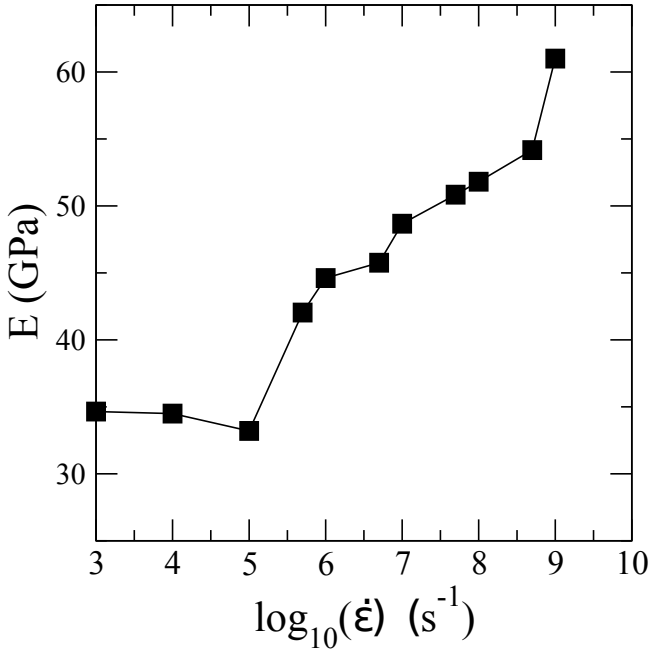

FIGURE 4.3: Variation of the Young's modulus with the strain rate for nanocrystalline quasi-2D sample with 9 nm mean grain size.

propagation is delayed resulting in an increase of the stress. Once, the density of dislocations increases the stress of the system decreases. This explains the decrease of the stress before the flow regime in Figure 4.1 (b). Finally, in the flow regime of the stress-strain curve, an equilibrium between the emission and annihilation of partial dislocations sets on. This is confirmed by the stabilization of the density of partial dislocations.

In the two nanocrystalline models, we have found that the increase of the strain rate results in a delay of the onset of dislocation nucleation and propagation. This will lead to the increase of the flow stress with the strain rate.

For crystalline solids, the elastic regime must display a Hookean behavior independent from the strain rate. Therefore, the dependence of the Young's modulus on the strain rate suggests the occurrence of local irreversible events in the linear regime. Next, we computed the Young's modulus from the slope of the stress-strain curve at deformation less than 0.3 %. Figure 4.3 shows the variation of the Young's modulus as a function of the strain rate. Interestingly, we found a threshold in the Young's modulus at a value of $\dot{\varepsilon}_c \simeq 5\times10^5$ s^{-1}. For lower values, the Young's modulus remains nearly constant and does not depend on $\dot{\varepsilon}$, suggesting a Hookean behavior. For higher values, the Young's modulus increases with the strain rate, a characteristic of non-equilibrium systems.

The equilibrium of the system can be completely inferred if the typical relaxation time of the material is compared to the typical timescale of the experiment. Therefore, to study this basic feature, we performed stress relaxation simulations by starting from configurations obtained at an initial strain in the elastic ($ln(\lambda)$ = 0.9 %) and the plastic (($ln(\lambda)$ = 3 %) regime at given strain rate $\dot{\varepsilon}$ for the quasi-2D model.

4.2.2 Evidence for glassy relaxation

In this section, we demonstrate that the relaxation behavior of nanocrystalline materials follows a Kohlrausch-Williams-Watts (KWW) stretched exponential profile at high strain rate where the system is out of equilibrium.

During the relaxation process the evolution of the stress $\sigma(t) = \sigma_{yy}(t)$ as a function of time is monitored for 2 ns. Figure 4.4 (a) and (b) exhibit such a behavior for various strain rates $\dot{\varepsilon}$, and the decay from $\sigma(0)$ to an *equilibrium* finite value $\sigma(\infty)$ is, indeed, typical of crystalline solids [175], albeit also found in cross-linked polymers [176].

We found that at small $\dot{\varepsilon}$, there is almost no evolution of the stress with time, indicative of very small viscoelastic effects. For strain rates $\dot{\varepsilon} \geqslant 5.10^5 s^{-1}$, σ_{yy} decreases with time until reaching an horizontal asymptote $\sigma(\infty)$. This indicates that for such strain rates the system has not relaxed during the tensile loading. In other words, the sample deformation is very fast in comparison with the timescale of the local relaxation mechanisms in the sample. Therefore, at high strain rate, the system can be considered as being out of equilibrium on the simulation timescale. In contrast, simulations performed at $\dot{\varepsilon} < 5.10^5 s^{-1}$ are able to relax continuously the increase of stress (Figure 4.4), for the two lowest strain rates 10^4 and $10^5 s^{-1}$. In this case, the stress reached during the tensile strain is the equilibrium stress that corresponds to the strain tensor of the sample.

Interestingly, we can see that for the two lowest strain rates the stress fluctuates around the same mean value in Figure 4.4 (a). This is not surprising because the two systems are in the elastic regime and are able to equilibrate. Therefore, the effective Young's modulus for these systems does not depend on the strain rate. This confirms that the stress follows a Hookean behavior with constant effective Young's modulus (Figure 4.3) for the three lowest strain

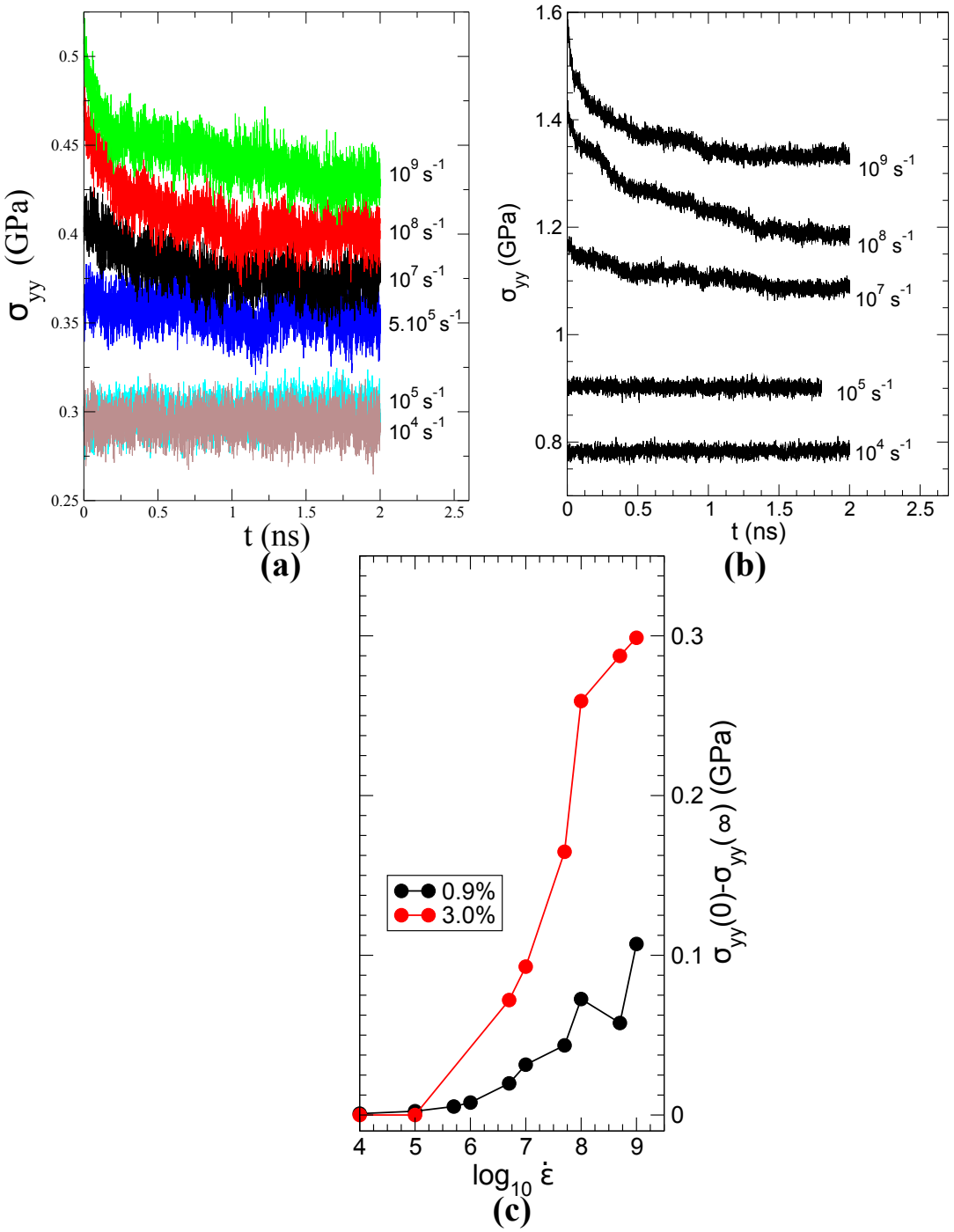

FIGURE 4.4: Stress relaxation curves $\sigma_{yy}(t)$ from initial configurations (t=0) obtained at fixed (a) $ln(\lambda)$=0.9% and (b) $ln(\lambda)$=3% for different strain rates $\dot{\varepsilon}$, (c) Evolution of $\sigma_{yy}(0) - \sigma_{yy}(\infty)$ with strain rate $\dot{\varepsilon}$

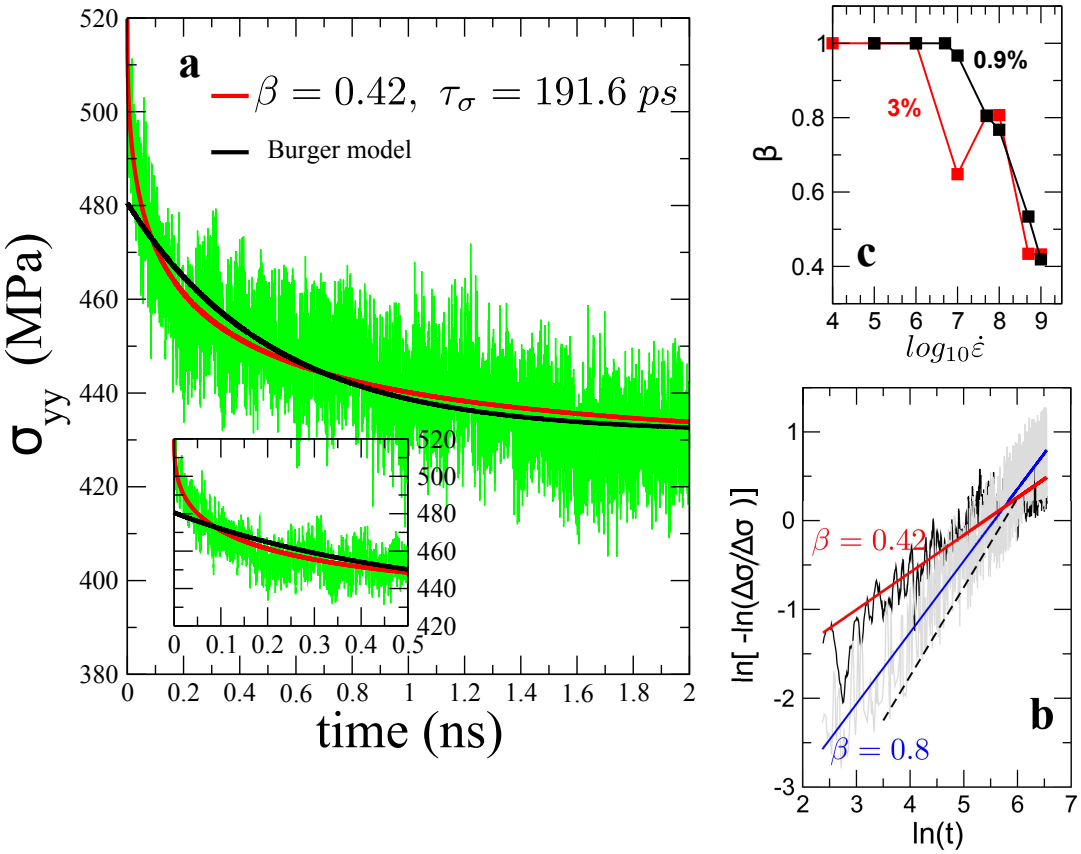

FIGURE 4.5: a) Fitting procedure (KWW (red) and Burger's model (black)) of a typical stress relaxation curve $\Phi(t)$ (for $\log_{10}\dot{\epsilon}$=9 and starting $ln(\lambda)$=0.9%). b) Representation of $\log[-\log\Phi(t)]$ with respect to $\log(t)$ for $\dot{\epsilon}$=10^9 s^{-1} (black) and 5×10^7 s^{-1} (gray), together with corresponding KWW fits and obtained parameter β (red and blue lines) which permits one to detect that $\Phi(t)$ has a KWW form. The broken line corresponds to an exponential Debye relaxation (β=1). c) Obtained KWW stretched exponent β as a function of $\log_{10}\dot{\epsilon}$.

rates. When the difference $\sigma(0)-\sigma(\infty)$ is represented (Figure 4.4 (c)), we furthermore realize that the threshold value $\dot{\varepsilon}_c$ detected for the Young's modulus is nearly recovered from the evolution of $\sigma(0)-\sigma(\infty)$ (Figure 4.4 (c)).

A usual means to quantify the viscoelastic behavior relies on a combination of Maxwell and Voigt-Kelvin cells leading to a four parameters Burger's model [177] which contains two exponentials with characteristic times τ_1 and τ_2 [178]. We found that this model is, however, unable to accurately fit the obtained stress relaxation profile at high deformation rate (Figure 4.5 (a)). In fact, such a model fails to describe correctly the behavior at short and intermediate times and the curve deviates substantially at small times.

The decay of the corresponding relaxation function $\Phi(t) = \Delta\sigma/\Delta\sigma_0 = (\sigma(t)-$

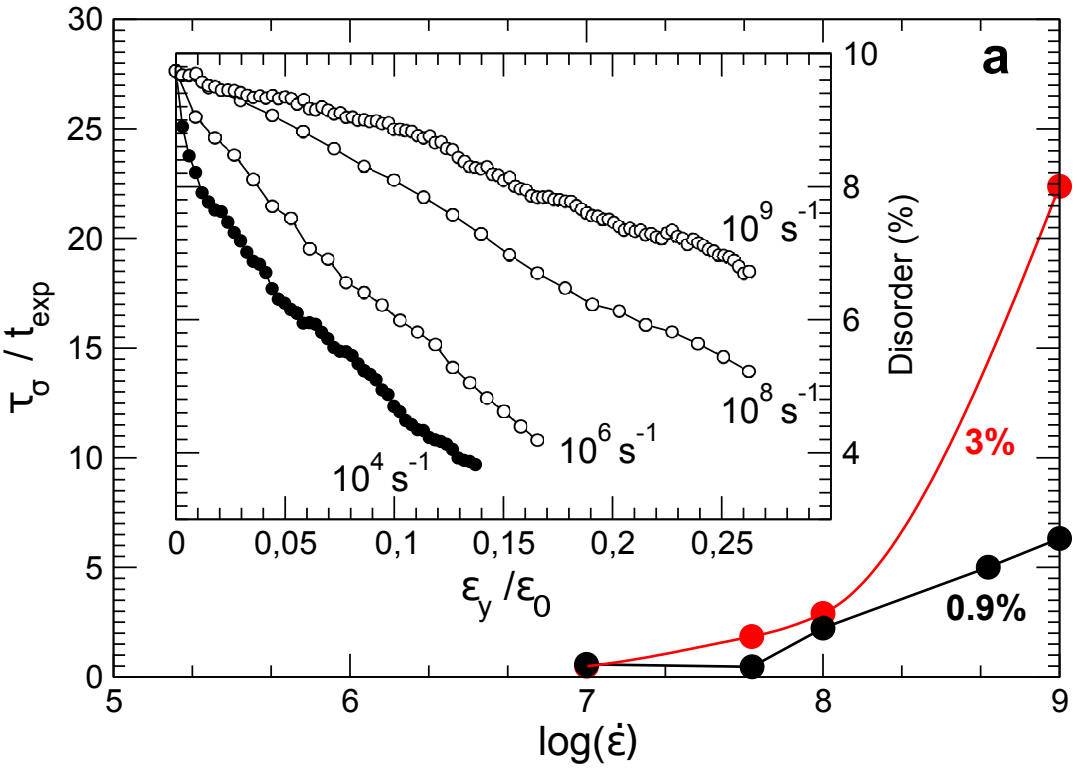

FIGURE 4.6: Behavior of τ_σ/t_{exp} as a function of strain rate $\dot{\epsilon}$ for ϵ_0=0.9 % and 3.0 %. The inset shows the fraction of atoms in a disordered environment as a function of strain for different $\dot{\epsilon}$.

$\sigma(\infty))/(\sigma(0)-\sigma(\infty))$ is found to be more accurately fitted with a KWW profile of the form $\exp[-(t/\tau_\sigma)^\beta]$, and this can be fully evidenced from an appropriate plot (Figure 4.5 (b)) which represents $\log[-\log[\Delta\sigma/\Delta\sigma_0]]$ as a function of $\log(t)$ and leads to a straight line for the stress relaxation, the slope being equal to the stretching exponent β of the KWW form. Interestingly, β also exhibits the threshold-like behavior (Figure 4.5 (c)), previously noticed for the Young's modulus and $\sigma(0)-\sigma(\infty)$. The value of β decreases from β=1 for $\dot{\epsilon}$=5×10^5 s^{-1} down to β=0.42 for 10^9 s^{-1}.

The KWW behavior for stress relaxation at high strain rate, typical of the α-relaxation in glasses [179], is an indication of a "*glassy*" out-off equilibrium behavior, and $\dot{\epsilon}$ plays here a similar role to the cooling rate $\dot{T}$ in supercooled liquids. In fact, polycrystals deformed at low $\dot{\epsilon}$ can equilibrate on the simulation timescales and results in a total energy and stress that remain constant with time for an initial $ln(\lambda)$. Conversely, for large $\dot{\epsilon}$, the system is unable to equilibrate and relax the imposed stress (Figure 4.6), the relaxation time t_σ is higher than the time of the tensile experiment simulation t_{exp}.

Now a question arises whether this relaxation behavior is specific for the quasi-2D samples or if it is typical for nanocrystalline models at the timescale of molecular dynamics. To address this issue, we applied three additional relaxation tests on two different nanocrystalline models. Two relaxation tests have been applied to the columnar 3D sample with 9 nm mean grain size from an initial strain of 3 % at two strain rates ($10^7$and $10^9 s^{-1}$). Another relaxation test has been applied to the 3D nanocrystalline sample with 9 nm mean grain size from the same initial strain but at a strain rate of $10^8\ s^{-1}$. We found the same relaxation behavior as the quasi-2D sample. The KWW model fits very well the stress relaxation profile of these models. The values of β found are less than 1 e.g $\beta = 0.48$ for the columnar 3D sample where $\dot{\varepsilon} = 10^9 s^{-1}$ relaxed at $ln(\lambda) = 3\%$.

4.2.3 What is the microstructural origin of the stress relaxation?

In this section we show that the following local mechanisms are responsible for the relaxation of the stress:

- The uncorrelated atomic shuffling processes on grain boundaries lead to the relaxation of the stress by generating local plastic deformation at these boundaries.
- The stress assisted grain boundary migration also entails a relaxation of the stress during the migration.
- The propagation of dislocations located initially inside the grains relax the stress by creating shear bands with high plastic deformation.

Uncorrelated atomic shuffling and grain boundary migration: In order to quantify the local mechanisms that lead to stress relaxation at the atomic scale, the microstructures of the two extreme strain rates ($10^9$and $10^4 s^{-1}$) have been analyzed. The atomic configuration at $\varepsilon_{yy} = 0.9\%$ after 2 ns relaxation time has been mapped by the atomic Von Mises strain calculated with respect to the unrelaxed configuration as a reference configuration (Figure 4.7). Figure 4.7(a) reveals the presence of irreversible deformation at grain boundaries, as marked by white 1 to 4 in the Figure. The relaxation of the stress at grain boundaries is caused by grain boundary migration and uncorrelated atomic shuffling. Figure 4.8 shows a zoom on the zones marked 1 to 6 in Figure

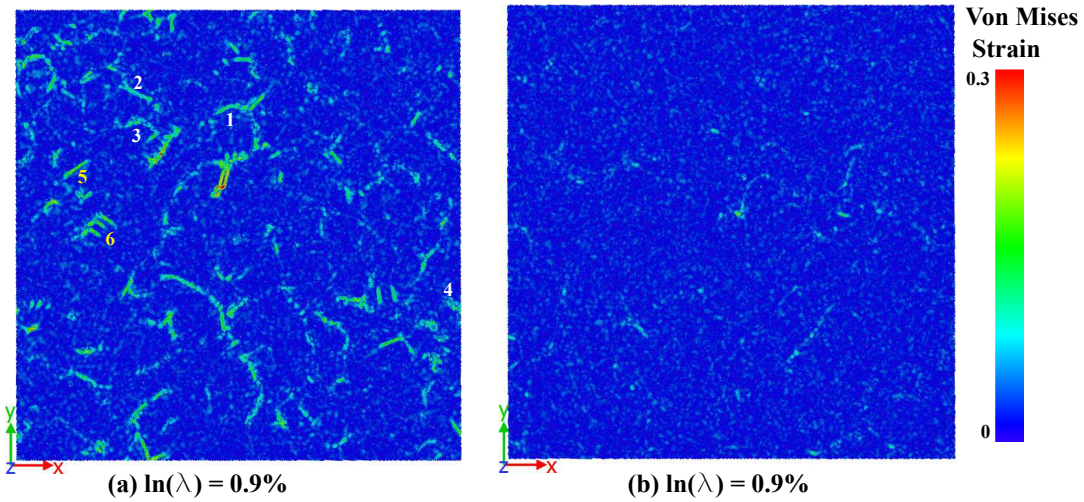

FIGURE 4.7: Von Mises strain cartography of quasi-2D nanocrystalline sample at $\varepsilon_{yy} = 0.9\%$ after the relaxation process seen in Figure 4.4 (a). The Von Mises strain is calculated with respect to the atomic configuration before the relaxation, (a) $\dot{\varepsilon} = 10^9\ s^{-1}$, (b) $\dot{\varepsilon} = 10^4\ s^{-1}$.

4.7 (a) where high Von Mises strain have been detected. The initial defects on grain boundaries and inside the grains prior to relaxation are marked by red and are superposed to the snapshots of Figure 4.8. A selection of snapshots reveals that atoms move into the interior of the neighboring grain during the relaxation, and this atomic shuffling induces a relaxation of the shear stress close to these boundaries. Atomic shuffling processes have also been shown to facilitate grain boundary sliding in FCC and BCC nanocrystalline materials [27, 31, 96]. Complementary migration mechanisms can also be evidenced such as the migration of a grain boundary by a distance of $\delta \approx 1nm$ which is nothing else than a stress-induced grain boundary migration.

Dislocations propagation: The shear bands inside the grains contribute to the local plastic deformation such as the zones marked 5 and 6 in Figure 4.7 (a). These bands are formed by the propagation of edge dislocations located initially inside the grains and are reminiscent of the initial cooling process. Thus, the decrease of $\sigma(t)$ during relaxation is caused by the plastic deformation at grain boundaries and the grain interior which decreases the energy of the system. In Figure 4.8, snapshots 5 and 6 illustrate the propagation of edge dislocations during the relaxation process. As shown, high Von Mises strain is present on the shear bands generated by the propagation of these edge dislocations. The core of the dislocation after relaxation is marked by a black circle in the snapshot 5. Also, in the snapshot 6, the edge dislocations are absorbed by the adjacent grain boundary which induces large atomic activity on grain boundary

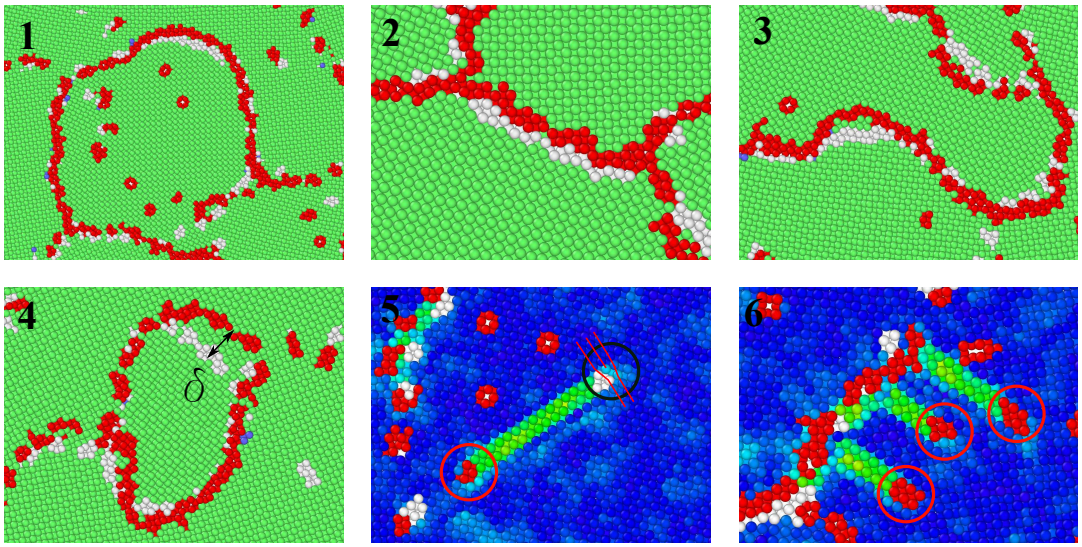

FIGURE 4.8: Zoom on zones 1 to 6 marked in Figure 4.7 (a) where high atomic Von Mises strain is detected. These snapshots allow identifying the local processes contributing to stress relaxation. The initial defects on grain boundaries and grain interiors are marked by red and are included in these snapshots, whereas white atoms indicate the defects after 2 ns relaxation. When no atomic activity on Grain boundary is present the Grain boundary marked by red atoms coincide with that of white atoms. In the snapshots 1 to 4, FCC atoms are marked in green. We used adaptive common neighbor analysis to distinguish between the atoms in a disordered environment and on an FCC lattice [144]. In snapshots 5 and 6, atoms are colored by their Von Mises strain as in Figure 4.7. The core of the edge dislocations before the relaxation is marked by red circles whereas the position of the core after relaxation is marked by a black circle in snapshot 5. The edge dislocations in snapshot 6 are absorbed by the neighboring Grain boundary marked by red and white atoms.

to accommodate the dislocation cores. Therefore, high Von Mises strain is seen on this boundary.

Finally, Figure 4.7 (b) shows the atomic configuration after relaxation for $\dot{\varepsilon} = 10^4 s^{-1}$. The atomic configuration is colored by the atomic Von Mises strain with respect to the atomic configuration before the relaxation. There is no evidence of a large local plastic deformation in this sample. This indicates that the system has an increased reversibility. This is confirmed by the fact that this strain level is still in the linear or elastic regime of the curve.

4.2.4 Strain rate sensitivity of the flow stress

We have calculated the flow stress for different tensile experiments with changing the strain rate (Figure 4.1). Figure 4.9 summarizes the behavior by representing in (a) a log-log plot the flow stress σ_f with respect to the strain rate $\dot{\varepsilon}$ for the quasi-2D and the columnar 3D samples. As mentioned above, the

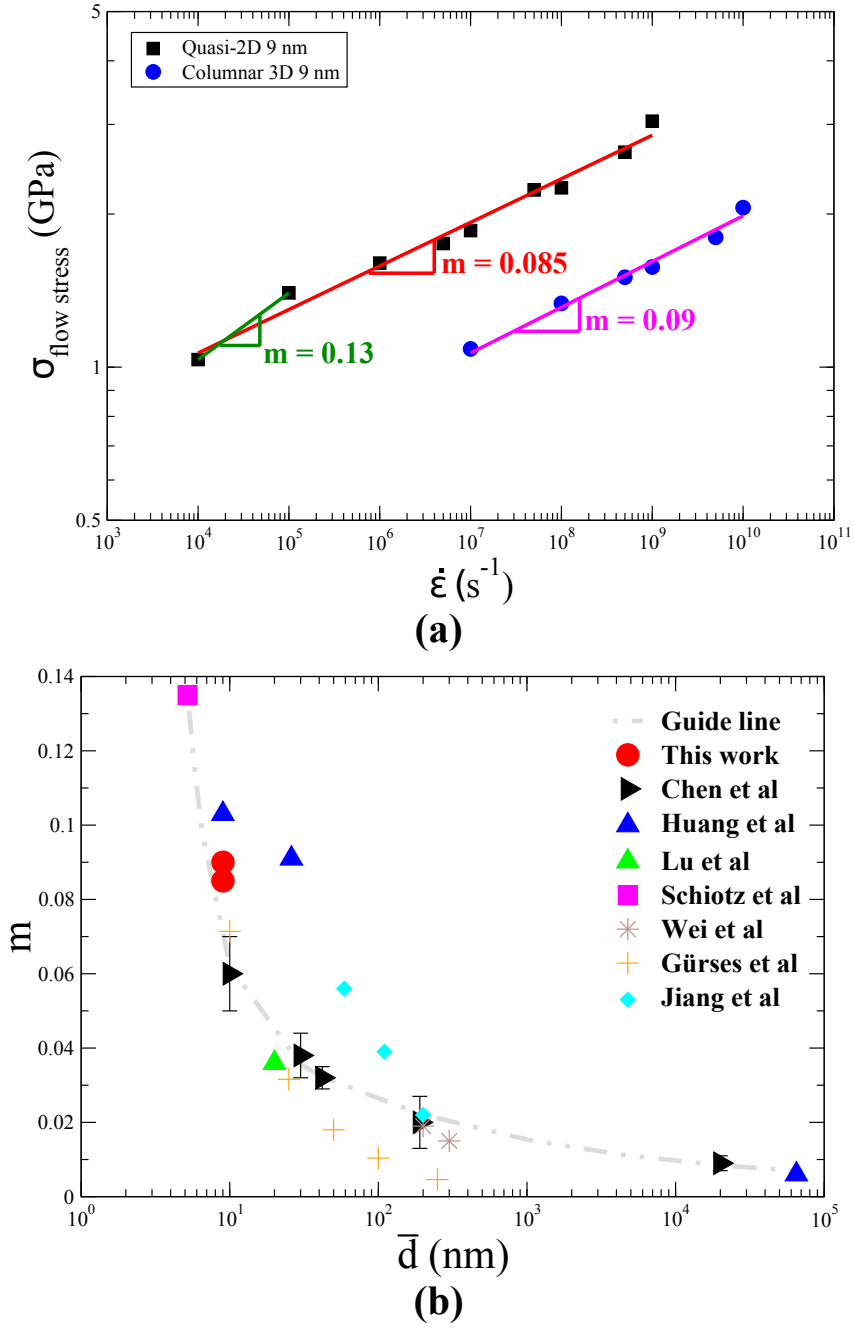

FIGURE 4.9: Log-log plot of the flow stress σ_f versus strain rate $\dot{\varepsilon}$ for the simulated nanocrystalline samples having $\bar{d}$=9 nm. The slope permits one to estimate m for a fixed $\bar{d}$, (b) Variation of m as a funanocrystallinetion of the average grain size $\bar{d}$ in nanocrystalline Copper, compared to experimental data from the literature : Chen et al. [15], Schiøtz et al. [24], Huang et al. [17], Wei et al. [57], Lu et al. [62], Gurses et al. [180], Jiang et al [181].

flow stress increases with the strain rate. The strain rate sensitivity of the flow stress can be calculated from the slope of this log-log curve $m = \frac{\partial ln(\sigma_f)}{\partial ln(\dot{\varepsilon})}$. We find $m = 0.085$ and $m = 0.09$ for the quasi-2D sample and the columnar 3D sample, respectively. These results are consistent with the experimental determination of m for nanocrystalline copper having similar grain size ($\approx$ 9 nm). Chen *et al* [15] found a $m = 0.06 \pm 0.01$ for 10 nm mean grain size sample measured by nanoindentation tests, a value that is also close to our results (Figure 4.9), even if the microstructures of these samples might be different between the numerical and experimental work. The values obtained for m are somewhat lower than those proposed for Lifshitz creep [79] and Rachinger Grain boundary sliding [182] even in the case of quasi-2D sample where the activation energy for Grain boundary diffusion is lowered due to the small thickness of the simulation box.

Figure 4.9 (b) displays the values of m found in the literature with respect to the mean grain size $\bar{d}$. Here, m increases as the grain size decreases, the values of m for the FCC nanocrystalline materials being one to two orders of magnitude higher than those of the microcrystalline ones, suggesting an enhanced strain rate sensitivity for materials having $\bar{d} \leq 100\ nm$. From the strain rate sensitivity, we computed the activation volume using equation (1.3). We find $V^* = 2.5b^3$ for the quasi-2D system and $V^* = 3.1b^3$ for the columnar 3D one. These small activation volumes in nanocrystalline Copper have been also measured experimentally by Chen *et al.* [15, 123]. And these authors found $V^* = 8b^3$ for $\bar{d}$ = 10 nm and $V^* = 23\ b^3$ for $\bar{d} = 42nm$. While our results agree with the experimental findings, it is important to emphasize that such small activation volumes are typical of nanocrystalline materials. Indeed, for coarse-grained polycrystalline materials, the forest lattice dislocations nucleated from Frank-Read sources lead to $V^* \simeq 1000b^3$ [183]. Conversely, for nanoscale grain size such Frank-Read sources do not exist due to energetic and grain size considerations [10, 103]. As we have seen, grain boundaries act as sources and sinks to dislocations, and the contribution of the grain boundaries mediated mechanisms to plasticity is improved. As a result, as m increases, V^* decreases.

4.3 Deformation mechanisms

Now we discuss the strain rate dependence of the main deformation mechanisms of the columnar 3D model with 9 nm mean grain size.

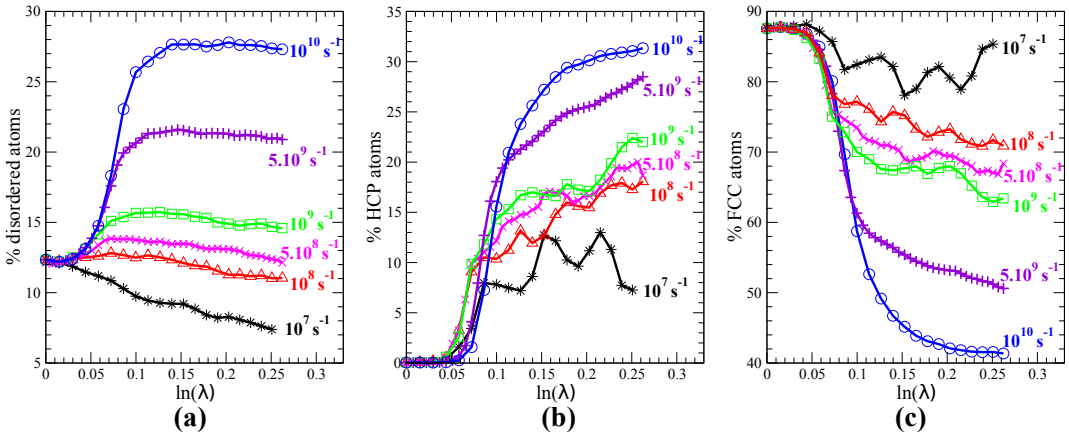

FIGURE 4.10: Fraction of atoms inside the microstructure with respect to the true strain for different tensile strain rates applied on columnar 3D nanocrystalline copper sample: (a) disordered atoms, (b) HCP atoms and (c) FCC atoms.

4.3.1 Influence of the strain rate on dislocations

The density of the partial dislocations increases with the strain rate (Figure 4.2 (b)). The partial dislocations do not have the time to propagate due to the high strain rate. Therefore, large fraction of stacking faults are hindered inside all grains. Figure 4.10 (b) illustrates the variation of the fraction of HCP atoms with the strain at different strain rates. The fraction of HCP atoms indicates the presence of stacking fault ribbons inside the grains. The results correlate very well with the density of partial dislocations (Figure 4.2 (b)). The fraction of HCP atoms increases with the strain rate.

Figure 4.11 shows the evolution of the grain (G1) inside the columnar 3D sample deformed at a strain rate of $10^7 s^{-1}$. The FCC atoms are suppressed to clearly observe the dislocation activity inside the grain. In Figure 4.11 (3) a partial dislocation with burger vector $B\alpha$ is nucleated at 5.8 % and propagates inside the grain. In the Figure a projection of the slip system, the dislocation line and the burger vector to the (xy) is presented. The pinning sites of the dislocation glide along the grain boundaries. As strain is increased to 7.2%, new partial dislocation is nucleated from the triple junction between the G1, G2, and G3. This dislocation will be absorbed by the grain boundary due to the interaction with the first partial with burger vector $B\alpha$. At this strain rate and at high plastic strain, a trailing partial αC is nucleated from the triple junction between G1, G5, and G6. This partial eliminates the stacking faults generated by the leading partials and then it is absorbed by grain boundaries (Figure 4.11 (5)). This indicates that the nucleation of the trailing partial is not necessary

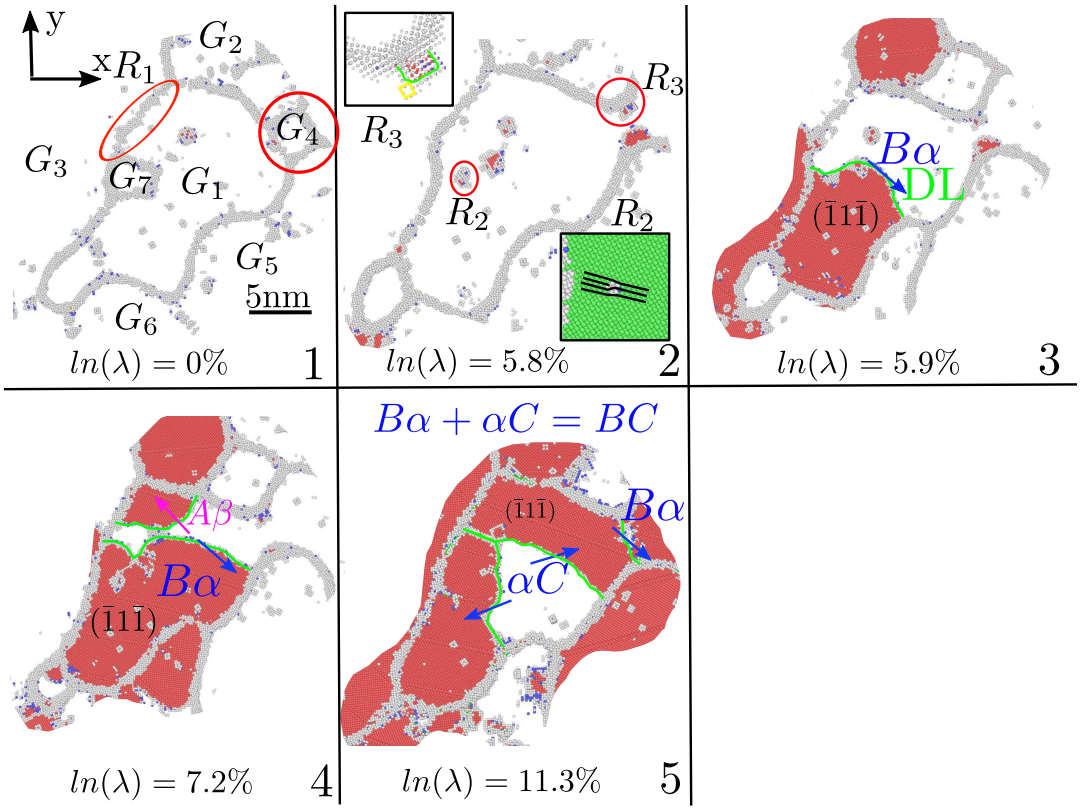

FIGURE 4.11: Evolution of a grain (G1) inside the columnar 3D sample loaded at $\dot{\varepsilon} = 10^7 s^{-1}$. The FCC atoms are omitted, only defects gray atoms and HCP red atoms are present. The projection of the slip plane and the burger vectors to the (xy) plane are present in the Figure. The burger vectors are noted using the Thompson tetrahedron [68]. The dislocation extraction analysis is used to calculate the burger vector of each Dislocation Line. A zoom on R_3 in the inset of Figure 2 shows a vacancy marked by yellow square and a dislocation line of a partial dislocation that are just nucleated marked by a green line.

localized on the same grain boundary as the leading partial.

After the absorption of the trailing partial, one cannot detect any evidence that a perfect dislocation has propagated inside the grain i.e. no defects in the grain are left behind the trailing partial. Perfect dislocation has not been observed at high strain rate above $10^8\ s^{-1}$. In Figure 4.10 (c) we can notice that the fraction of FCC atoms in the flow regime have a large fluctuation for $10^7 s^{-1}$ and it correlate very well with the fraction of HCP atoms in Figure 4.10 (b). For $\dot{\varepsilon} = 10^7\ s^{-1}$ in the flow regime once the fraction of FCC atoms increases, the fraction of HCP atoms decreases and vice versa. Therefore, this fluctuation is due to the nucleation of the trailing partial that clean the stacking fault ribbon generated by the leading partial, and hence the fraction of HCP atoms decreases.

Moreover, the nucleation of a trailing partial has been extensively observed at low strain rate to form a perfect dislocation (Figure 4.11). Therefore, one can predict an increase in the contribution of perfect dislocation to the total strain as the strain rate decreases. In fact, the increase of the strain rate reduces the time needed to concentrate the stress necessary to nucleate the trailing partial from the same grain boundary on the timescale of molecular dynamics. In consequence, the fraction of perfect dislocation is reduced at high strain rate.

4.3.2 Influence of the strain rate on twinning

The twinning mechanism is enhanced with the increase of the strain and the strain rate since the fraction of stacking faults increases (Figure 4.13 (b)). The presence of these faults inside the grains especially at high strain rate will increase the possibility of forming micro-twins. These micro-twins are resulting from the overlapping of the stacking faults of two partials on adjacent slip planes.

Figure 4.12 (1) and (3) show a grain at strain rate of 10^7 and $10^{10}\ s^{-1}$ respectively. It is clear that the fraction of twin boundaries increases in the grain deformed at higher strain rate. In fact, the flow stress increases with the strain rate to reach the onset of twinning nucleation. Therefore, we can predict a transition from dislocations to twinning with the increase of the strain rate. However, this transition is also dependent on the grain size.

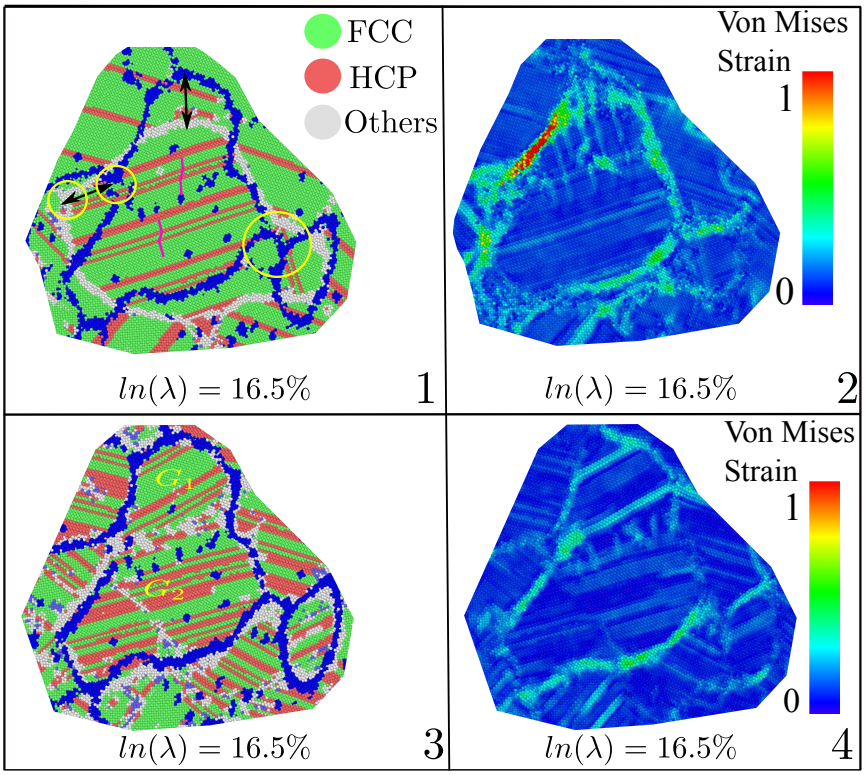

FIGURE 4.12: A zoom on different grains inside the columnar 3D sample at different strains and strain rates to focus on the plastic deformation mechanisms seen: In (1) and (2) the same grain have been taken from the tensile test at $\dot{\varepsilon} = 10^7 s^{-1}$. The grain is colored by the common neighbor analysis in (3)and the atomic Von Mises strain in (4) calculated with respect to the initial configuration at zero strain. The blue atoms in (3) are the grain boundaries of the same grain in the initial configuration, hence a comparison can be done. The snapshots (3) and (4) are respectively the same as (1) and (2) but the initial configuration is deformed at $\dot{\varepsilon} = 10^{10} s^{-1}$.

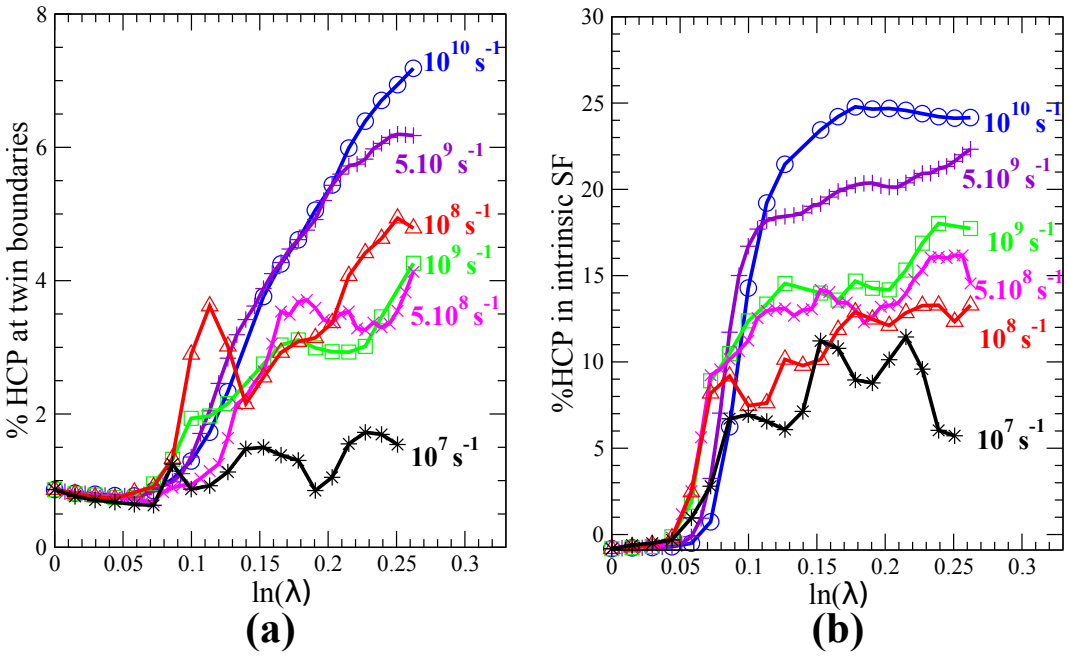

FIGURE 4.13: (a) Fraction of atoms at twin boundaries versus strain, (b) Fraction of atoms in intrinsic stacking fault ribbons generated by partial dislocations versus strain.

Figure 4.13 (a) shows the variation of the fraction of HCP atoms in twin boundaries and in intrinsic stacking fault ribbons versus the strain for different strain rate loading. The total fraction of HCP atoms obtained (Figure 4.10 (b)) is resulting from two main contributions: (i) twinning and (ii) partial dislocation contributions, and the fraction of each part can be calculated. The tendency to twin increases with the strain rate (Figure 4.13 (a)). Also, for a strain rate of $10^7 s^{-1}$ the fraction of atoms in twin boundaries is nearly constant. This suggests that at this mean grain size the twinning mechanism is not dominant at low strain rate.

Moreover, in comparing the fraction of HCP atoms (Figure 4.13) the partial dislocations dominate with respect to twinning, the contribution of the latter increasing with the strain rate. This suggests the presence of a possible crossover between a mechanical behavior driven by either partial dislocations or twinning. This seems at least confirmed by a recent study. A molecular dynamics insight on the ultimate limit of metal plasticity at high strain rate shown that above a strain rate of $8.10^8 s^{-1}$ tantalum BCC single crystals cannot dissipate the imposed mechanical load by dislocations and twinning becomes the dominant mode of dynamic response [112].

4.3.3 Influence of the strain rate on the grain boundaries processes

In this section, we demonstrate that the influence of the strain rate on the grain boundaries processes is as follows:

- The grain boundary and free volume migration are enhanced with the decrease of the strain rate.
- The grain growth mechanism is limited at high strain rate.
- Even at high strain rate, in order to absorb partial dislocations in nanocrystalline materials a large amount of grain boundary activity is necessary to accommodate the core of the partial dislocations at this boundary.

Figure 4.11 shows the evolution of a grain (G1) inside the columnar 3D sample loaded at $\dot{\varepsilon} = 10^7 s^{-1}$. A comparison of G1 at 5.8% strain with the initial state of the grain indicates the collapse of the grains G7 and G4 in the G1. The G7 left behind a pure edge dislocation core encircled by red (R2) in Figure 4.11 (2). A zoom on the atomic configuration at the position of this dislocation is illustrated in the inset of Figure 4.11 (2). Also, the coalescence of the G4 with G1 left behind a vacancy marked by R3 is acknowledged in the Figure. These phenomena indicate large grain boundary activities such as grain boundary and free volume migrations. The evolution of the same grain at $\dot{\varepsilon} = 10^8\ s^{-1}$ presented in Figure 3.14 indicates that the vacancy has not been emitted during the coalescence of G4 with G1. This confirms the enhancement of the activity of grain boundary processes with reducing the strain rate.

In Figure 4.12 (1) and (3) the initial grain boundaries or the defects of the grain before loading is superposed on these snapshots to investigate the motion of the grain boundaries. At the lowest strain rate of $10^7\ s^{-1}$ which corresponds to the Figure 4.12 (1), we can clearly observe the grain boundary and triple junction migrate (yellow circle and black arrows in the Figure). The atomic Von Mises strain is calculated for this deformed grain with respect to the initial configuration (Figure 4.12 (2)). In comparing the two Figures, we observe that high Von Mises strain is present when grain boundary and triple junction move. Also, the small grain present in the lower right region of the Figure 4.12 (1) collapses with the bigger grain. However, when the strain rate increases we have seen that the microstructure is roughly frozen during deformation. In Figure 4.12 (3) the grain boundaries in the deformed and the undeformed grain

overlap. Thus, the grain growth mechanisms are limited when the strain rate is high.

As the strain rate increases, we have observed that the system is much more disordered during the tensile loading. The density of atoms in grain boundaries increases (Figure 4.10 (a)) which in turn induces a thickening of the grain boundaries. Therefore, the barrier to the motion of dislocation is reinforced, hence the flow stress increases. However, at strain rate below $10^8\ s^{-1}$ a decrease of the fraction of disordered atoms with strain is shown indicative of grain coalescence mechanism is present at low strain rate due to the increase of the grain boundary activity especially grain boundary migration with the decrease of the strain rate.

In Figure 4.12 (3), the grain has been decomposed on two subgrains G1 and G2 marked by yellow in the Figure. In fact, the initial grain contains defects such as perfect edge dislocations left over from the cooling process. When deformed at low strain rate these dislocations are nucleated from the grain interior and then absorbed by the neighboring grain boundary. However, at high strain rate, these dislocations are stuck inside the grains and form a low angle boundary inside the grain. The nucleation and absorption of partial dislocations will increase the misorientation angle and hence the grain is divided into two subgrains.

Furthermore, Figure 4.12 (4) shows the grain at 16.5% strain deformed at $10^{10}\ s^{-1}$ colored by the atomic Von Mises strain with respect to the initial configuration. Large plastic deformation is present on the grain boundaries even at such high strain rate. Consequently, this indicates that in order to absorb partial dislocations in nanocrystalline materials, a large amount of grain boundary activity is necessary to accommodate the core of the partial dislocations. We have seen that a large number of free volume is emitted from grain boundary once a dislocation is absorbed by this boundary. In addition, as discussed above the partial dislocation is nucleated and propagates inside the grain while being pinned to the grain boundary which in turn induce large atomic activity on the grain boundary to facilitate the pinning unpinning process of this dislocation. This picture seems to be consistent with Van Swygenhoven *et al* who have studied the nucleation and propagation of full dislocations in nanocrystalline FCC Al. They also revealed that the emission of perfect dislocation is

accompanied by atomic shuffling and usually stress assisted free volume migration [36].

4.4 Conclusion

MD simulations have been carried out to study the effect of the strain rate on the plastic deformation of two nanocrystalline copper systems, a quasi-2D and a columnar 3D one. Uniaxial tensile tests have been applied on these models at strain rate varying from 10^4 to 10^9 s^{-1} for the quasi-2D sample and from 10^7 to 10^{10} s^{-1} for the columnar 3D sample. Moreover, a series of relaxation tests for 2 ns have been applied on these samples from the elastic and the plastic regime. The following results have been found:

- While deforming at $\dot{\varepsilon} \geqslant 5.10^5$ nanocrystalline copper models are not able to relax entirely at the numerical experiment timescale at high strain rate and the system is out of equilibrium.
- A stretched exponential model typical for supercooled liquids relaxation fits very well the stress relaxation curves at high strain rate.
- The grain boundary accommodation mechanisms are enhanced while reducing the strain rate especially grain boundary and triple junction migrations and grain growth corresponding to an increase of the strain rate sensitivity of nanocrystalline copper.
- The increase of the strain rate has been found to increase the disorder of the system and to delay the onset of dislocation nucleation and propagation resulting in an increase of the flow stress.
- At low strain rate, trailing partials have been observed at large plastic strain at a timescale of molecular dynamics. Also, the nucleation of these partials is not necessarily on the same grain boundary region where the leading partial is nucleated.
- The contribution of twinning mechanism to plasticity increases with the strain rate but is not yet the dominant deformation mechanism even at very high strain rate ($\dot{\varepsilon} = 10^{10}$ s^{-1}).

Chapter 5

Conclusions and perspectives

5.1 Conclusions

In this thesis, molecular dynamics simulations have been extensively used to investigate the mechanical behavior of nanocrystalline metals and their nano-scale deformation mechanisms. The influence of the mean grain size and the strain rate on the deformation mechanisms of these materials have been deeply examined. A recent melting-cooling method has been employed to generate initial configurations with a more realistic intra and intergranular defects. This method is able to produce curved grain boundaries and point and line defects inside the grains.

In chapter 3 the effect of the grain size on the mechanical properties of columnar nanocrystalline FCC Copper generated by the melting-cooling method and 3D nanocrystalline HCP α-Titanium generated by Voronoï tessellation have been studied. A clear transition to inverse Hall-Petch effect has been observed on both materials at a certain grain size. The deformation mechanisms responsible for such a transition have been explored at the atomic level. The deformation behavior of these materials depends upon the grain boundary mediated processes and dislocation movements. At low plastic strain, grain boundary sliding is dominating the plastic deformation. Whereas, at high plastic strain, dislocations and twinning become the dominant deformation mechanisms.

Our contributions can be summarized as follows:

- the influence of the sample generation method on the mechanical behavior has been studied. Three methods were compared: (i) the melting-cooling of a mono-crystal, (ii) the Voronoï tessellation, and (iii) the simultaneous grain growth. The sample generated with the melting-cooling method presents more ductility than the others because of the defects inside the grains.

- A crossover to inverse Hall-Petch effect has been found at d_c equal to 16 nm for nanocrystalline Copper and at 15 nm for nanocrystalline α-Titanium. Below this d_c a softening of the material has been observed. This softening is illustrated by the decrease of the yield and flow stresses with respect to the mean grain size.

- The Young modulus of the nanocrystalline Copper and α-Titanium decreases with the decrease of the mean grain size.

- A new deformation mechanism has been found when edge dislocations propagate on {110} planes to finally vanish on an adjacent grain boundary. While propagating, these dislocations generate shear bands inside the grains where high local shear strain is present.

- Deformation by twinning mechanism plays an important role at a high plastic strain. The main twinning mechanism results from the overlapping of the stacking fault ribbons of two partial dislocations on adjacent slip systems.

- Basal dislocations and mechanical twinning are the dominant deformation mechanisms in nanocrystalline α-Titanium. Twinning boundaries are found to nucleate from grain boundary and cross the entire grain to vanish on the opposite boundary. Hence the grains are reoriented after the passage of these boundaries.

In chapter 4 the effect of the strain rate on the deformation mechanisms of two nanocrystalline Copper systems have been studied. Two nanocrystallines Copper samples quasi-2D and columnar 3D have been generated by melting cooling methods with a mean grain size of 9 nm. These samples are then submitted to tensile tests at different strain rates going from $10^4 s^{-1}$ to $10^9 s^{-1}$ for the quasi-2D sample and from $10^7 s^{-1}$ to $10^{10} s^{-1}$ for the columnar 3D sample. The investigation of the mechanical behavior of these samples with respect to strain rate reveals a certain threshold of a strain rate from which Young's modulus becomes rate dependent. Same observation was also found for the stress recovery in case of stress relaxation tests. These latter were performed on elastically and plastically strained specimens. For both cases, the stress recovery was found to be rate dependent.

At low strain rate ($\dot{\varepsilon} < \dot{\varepsilon}_c \simeq 5.10^5\ s^{-1}$), materials are able to be in equilibrium with the ongoing deformation over the ns timescale. Whereas, ultra-fast deformations bring the system out of equilibrium on the same timescale. The

time evolution of the stress relaxation curves is investigated. A stretched exponential function was used to fit the stress-time curve for stress relaxation results of specimens strained with a high strain rate.

A strong strain rate sensitivity of nanocrystalline Copper has been found. The dislocation propagation activity is highly strain-rate dependent which in his turn influences the stress-strain curve. A delay of the onset of dislocation propagation has been quantitatively showed resulting in an increase of the flow stress with the strain rate. In the columnar system, this delay results in an overshoot in the stress-strain curve. Moreover, the density of dislocations increases with the strain rate. An increase of the contribution of twinning to the plastic deformation is found at high plastic strain and high strain rate. This suggests a transition in the plastic deformation mechanism to twinning with the increase of the strain and strain rate. Detailed analysis at the atomic level demonstrates that the motion of grain boundary is enhanced with the decrease of the strain rate. This indicates the increasing importance of the grain boundary mediated processes with the decrease of the strain rate.

5.2 Perspectives

In spite of the considerable progress made in the understanding of the mechanical behavior of the nanocrystalline materials, there are still a large number of intriguing directions for future work.

The melting cooling method used in our work is an advantageous way to generate more realistic samples with grain boundary curvature and intragranular defects in the initial configuration. However, in our work, the limiting computational power constraints us to generate only columnar nanocrystalline systems. Phillpot *et al* have constructed nanocrystalline materials from the crystallisation of a melt [154]. However, pre-oriented single crystal seeds are embedded in the melt to accelerate the growth and to specified the orientation of each grain. In spite of the relevance of the microstructure obtained, the randomness of the grain orientations is not respected. Also, no grain size distribution can be obtained in their models, all the grains are of the same size. Thus, the generation of a 3D structure by melting cooling method without initial seeds deserves more interests. This will allow one to obtain more realistic models for atomistic simulations with more equilibrated grain boundaries and

triple junctions.

The presented simulations were performed on impurity-free samples. However, experimental nanocrystalline structures — even in highly pure systems — have impurities which can segregate at the grain boundary and can affect the mechanical behavior [184] and the stability of the initial microstructure against grain growth [185]. With this in mind, the influence of grain boundary segregation/matrix on mechanical behavior must be studied. In this case, atomistic simulations would again be extremely beneficial for studying how segregation modifies the local properties, the structure of grain boundaries, and the deformation mechanisms of the material.

The development of better potentials which accurately describe the mechanical properties relative to the composition (e.g., the composition dependence of stacking fault energy) will be a necessary preliminary step for such work.

A remaining research area still exists concerning the relaxation and equilibrium behavior of nanocrystalline materials. The study of the effect of grain size and/or grain boundary defects in the microstructure on the relaxation time still lacking. Moreover, the study of the characteristic relaxation time of a single crystal with a high density of dislocations is important. This will allow one to compare the relaxation behavior of a polycrystal with a single crystal. Also, the effect of the strain rate on d_c where the crossover from Hall-Petch to inverse Hall Petch is still needed.

One of the purposes of the use of molecular dynamisc simulations in our work is the investigation of the grain refinement mechanisms during the SMAT of 316L stainless steel. To this aim, during this thesis, a pre-study of the compression of a monocrystalline Fe14Ni18Cr has been applied to understand how the grains form during the SMAT of a monocrystal 316L stainless steel. The first results of this study are described in the Appendix A.

Bibliography

[1] Herbert Gleiter. “Nanocrystalline materials”. In: *Advanced Structural and Functional Materials*. Springer, 1991, pp. 1–37.

[2] C Suryanarayana. “Nanocrystalline materials”. In: *International Materials Reviews* 40.2 (1995), pp. 41–64.

[3] Ke Lu. “Nanocrystalline metals crystallized from amorphous solids: nanocrystallization, structure, and properties”. In: *Materials Science and Engineering: R: Reports* 16.4 (1996), pp. 161–221.

[4] C Suryanarayana and CC Koch. “Nanocrystalline materials–Current research and future directions”. In: *Hyperfine Interactions* 130.1-4 (2000), p. 5.

[5] Marc A Meyers, A Mishra, and David J Benson. “Mechanical properties of nanocrystalline materials”. In: *Progress in materials science* 51.4 (2006), pp. 427–556.

[6] Eric N Hahn and Marc A Meyers. “Grain-size dependent mechanical behavior of nanocrystalline metals”. In: *Materials Science and Engineering: A* 646 (2015), pp. 101–134.

[7] EO Hall. “The deformation and ageing of mild steel: III discussion of results”. In: *Proceedings of the Physical Society. Section B* 64.9 (1951), p. 747.

[8] Norman J Petch. “The cleavage strengh of polycrystals”. In: *J. of the Iron and Steel Inst.* 174 (1953), pp. 25–28.

[9] CS Pande, RA Masumura, and RW Armstrong. “Pile-up based Hall-Petch relation for nanoscale materials”. In: *Nanostructured materials* 2.3 (1993), pp. 323–331.

[10] TG Nieh and J Wadsworth. “Hall-Petch relation in nanocrystalline solids”. In: *Scripta Metallurgica et Materialia* 25.4 (1991), pp. 955–958.

[11] AH Chokshi et al. “On the validity of the Hall-Petch relationship in nanocrystalline materials”. In: *Scripta Metallurgica* 23.10 (1989), pp. 1679–1683.

[12] Paul G Sanders, JA Eastman, and JR Weertman. “Elastic and tensile behavior of nanocrystalline copper and palladium”. In: *Acta materialia* 45.10 (1997), pp. 4019–4025.

[13] Jason R Trelewicz and Christopher A Schuh. “The Hall–Petch breakdown at high strain rates: optimizing nanocrystalline grain size for impact applications”. In: *Applied Physics Letters* 93.17 (2008), p. 171916.

[14] GW Nieman, JR Weertman, and RW Siegel. “Mechanical behavior of nanocrystalline Cu and Pd”. In: *Journal of Materials Research* 6.5 (1991), pp. 1012–1027.

[15] J Chen, L Lu, and K Lu. “Hardness and strain rate sensitivity of nanocrystalline Cu”. In: *Scripta Materialia* 54.11 (2006), pp. 1913–1918.

[16] S Cheng et al. “Tensile properties of in situ consolidated nanocrystalline Cu”. In: *Acta materialia* 53.5 (2005), pp. 1521–1533.

[17] P Huang et al. “Dependence of strain rate sensitivity upon deformed microstructures in nanocrystalline Cu”. In: *Acta Materialia* 58.15 (2010), pp. 5196–5205.

[18] Roland Würschum, Simone Herth, and Ulrich Brossmann. “Diffusion in nanocrystalline metals and alloys—a status report”. In: *Advanced Engineering Materials* 5.5 (2003), pp. 365–372.

[19] NR Tao et al. “An investigation of surface nanocrystallization mechanism in Fe induced by surface mechanical attrition treatment”. In: *Acta materialia* 50.18 (2002), pp. 4603–4616.

[20] HW Zhang et al. “Formation of nanostructured surface layer on AISI 304 stainless steel by means of surface mechanical attrition treatment”. In: *Acta materialia* 51.7 (2003), pp. 1871–1881.

[21] Ke Lu and Jian Lu. “Nanostructured surface layer on metallic materials induced by surface mechanical attrition treatment”. In: *Materials Science and Engineering: A* 375 (2004), pp. 38–45.

[22] NR Tao et al. “Surface nanocrystallization of iron induced by ultrasonic shot peening”. In: *Nanostructured Materials* 11.4 (1999), pp. 433–440.

[23] X Wu et al. “Microstructure and evolution of mechanically-induced ultrafine grain in surface layer of Al-alloy subjected to USSP”. In: *Acta materialia* 50.8 (2002), pp. 2075–2084.

[24] Jakob Schiøtz, Francesco D Di Tolla, and Karsten W Jacobsen. “Softening of nanocrystalline metals at very small grain sizes”. In: *Nature* 391.6667 (1998), p. 561.

[25] Jakob Schiøtz et al. “Atomic-scale simulations of the mechanical deformation of nanocrystalline metals”. In: *Physical Review B* 60.17 (1999), p. 11971.

[26] H Van Swygenhoven and A Caro. “Plastic behavior of nanophase Ni: A molecular dynamics computer simulation”. In: *Applied Physics Letters* 71.12 (1997), pp. 1652–1654.

[27] H Van Swygenhoven and PM Derlet. “Grain-boundary sliding in nanocrystalline fcc metals”. In: *Physical Review B* 64.22 (2001), p. 224105.

[28] Jakob Schiøtz and Karsten W Jacobsen. “A maximum in the strength of nanocrystalline copper”. In: *Science* 301.5638 (2003), pp. 1357–1359.

[29] Christian Brandl, Peter M Derlet, and Helena Van Swygenhoven. “Strain rates in molecular dynamics simulations of nanocrystalline metals”. In: *Philosophical Magazine* 89.34-36 (2009), pp. 3465–3475.

[30] Tomotsugu Shimokawa, A Nakatani, and H Kitagawa. “Grain-size dependence of the relationship between intergranular and intragranular deformation of nanocrystalline Al by molecular dynamics simulations”. In: *Physical Review B* 71.22 (2005), p. 224110.

[31] Yizhe Tang, Eduardo M Bringa, and Marc A Meyers. “Inverse Hall–Petch relationship in nanocrystalline tantalum”. In: *Materials Science and Engineering: A* 580 (2013), pp. 414–426.

[32] Diana Farkas, Anders Frøseth, and Helena Van Swygenhoven. “Grain boundary migration during room temperature deformation of nanocrystalline Ni”. In: *Scripta Materialia* 55.8 (2006), pp. 695–698.

[33] Diana Farkas, Som Mohanty, and Joshua Monk. “Strain-driven grain boundary motion in nanocrystalline materials”. In: *Materials Science and Engineering: A* 493.1-2 (2008), pp. 33–40.

[34] F Sansoz and JF Molinari. “Mechanical behavior of Σ tilt grain boundaries in nanoscale Cu and Al: A quasicontinuum study”. In: *Acta Materialia* 53.7 (2005), pp. 1931–1944.

[35] A Hasnaoui, H Van Swygenhoven, and PM Derlet. “Cooperative processes during plastic deformation in nanocrystalline fcc metals: A molecular dynamics simulation”. In: *Physical Review B* 66.18 (2002), p. 184112.

[36] H Van Swygenhoven, PM Derlet, and AG Frøseth. “Nucleation and propagation of dislocations in nanocrystalline fcc metals”. In: *Acta Materialia* 54.7 (2006), pp. 1975–1983.

[37] Maxime Dupraz et al. “Dislocation interactions at reduced strain rates in atomistic simulations of nanocrystalline Al”. In: *Acta Materialia* 144 (2018), pp. 68–79.

[38] V Yamakov et al. “Deformation-mechanism map for nanocrystalline metals by molecular-dynamics simulation”. In: *Nature materials* 3.1 (2004), p. 43.

[39] KS Kumar, H Van Swygenhoven, and S Suresh. “Mechanical behavior of nanocrystalline metals and alloys1”. In: *Acta Materialia* 51.19 (2003), pp. 5743–5774.

[40] D Wolf et al. “Deformation of nanocrystalline materials by molecular-dynamics simulation: relationship to experiments?” In: *Acta Materialia* 53.1 (2005), pp. 1–40.

[41] M Dao et al. “Toward a quantitative understanding of mechanical behavior of nanocrystalline metals”. In: *Acta Materialia* 55.12 (2007), pp. 4041–4065.

[42] NR Tao, Jian Lu, and Ke Lu. “Surface nanocrystallization by surface mechanical attrition treatment”. In: *Materials science forum*. Vol. 579. Trans Tech Publ. 2008, pp. 91–108.

[43] Jalal Azadmanjiri et al. “Development of surface nano-crystallization in alloys by surface mechanical attrition treatment (SMAT)”. In: *Critical Reviews in Solid State and Materials Sciences* 40.3 (2015), pp. 164–181.

[44] Thierry Roland et al. “Fatigue life improvement through surface nanostructuring of stainless steel by means of surface mechanical attrition treatment”. In: *Scripta Materialia* 54.11 (2006), pp. 1949–1954.

[45] K Wang et al. “Plastic strain-induced grain refinement at the nanometer scale in copper”. In: *Acta Materialia* 54.19 (2006), pp. 5281–5291.

[46] KY Zhu et al. “Nanostructure formation mechanism of α-titanium using SMAT”. In: *Acta Materialia* 52.14 (2004), pp. 4101–4110.

[47] Yimin Lin et al. “Surface nanocrystallization by surface mechanical attrition treatment and its effect on structure and properties of plasma nitrided AISI 321 stainless steel”. In: *Acta Materialia* 54.20 (2006), pp. 5599–5605.

[48] Thierry Roland et al. “Enhanced mechanical behavior of a nanocrystallised stainless steel and its thermal stability”. In: *Materials Science and Engineering: A* 445 (2007), pp. 281–288.

[49] HQ Sun et al. “Plastic strain-induced grain refinement in the nanometer scale in a Mg alloy”. In: *Acta Materialia* 55.3 (2007), pp. 975–982.

[50] H Gleiter. “Nanostructured materials: basic concepts and microstructure”. In: *Acta materialia* 48.1 (2000), pp. 1–29.

[51] TD Shen et al. “On the elastic moduli of nanocrystalline Fe, Cu, Ni, and Cu–Ni alloys prepared by mechanical milling/alloying”. In: *Journal of Materials Research* 10.11 (1995), pp. 2892–2896.

[52] Guo-Jie J Gao, Yun-Jiang Wang, and Shigenobu Ogata. “Studying the elastic properties of nanocrystalline copper using a model of randomly packed uniform grains”. In: *Computational Materials Science* 79 (2013), pp. 56–62.

[53] P Valat-Villain, J Durinck, and PO Renault. “Grain Size Dependence of Elastic Moduli in Nanocrystalline Tungsten”. In: *Journal of Nanomaterials* 2017 (2017).

[54] Mohammed Cherkaoui and Laurent Capolungo. *Atomistic and continuum modeling of nanocrystalline materials*. Springer, 2009.

[55] R Bohn et al. “Nanocrystalline intermetallic compounds—an approach to ductility?” In: *Scripta metallurgica et materialia* 25.4 (1991), pp. 811–816.

[56] Yinmin Wang et al. “High tensile ductility in a nanostructured metal”. In: *Nature* 419.6910 (2002), p. 912.

[57] Q Wei et al. “Effect of nanocrystalline and ultrafine grain sizes on the strain rate sensitivity and activation volume: fcc versus bcc metals”. In: *Materials Science and Engineering: A* 381.1-2 (2004), pp. 71–79.

[58] F Dalla Torre et al. “Deformation behaviour and microstructure of nanocrystalline electrodeposited and high pressure torsioned nickel”. In: *Acta Materialia* 53.8 (2005), pp. 2337–2349.

[59] Verena Maier et al. “Nanoindentation strain-rate jump tests for determining the local strain-rate sensitivity in nanocrystalline Ni and ultrafine-grained Al”. In: *Journal of materials research* 26.11 (2011), pp. 1421–1430.

[60] T Kruml, O Coddet, and JL Martin. “The investigation of internal stress fields by stress reduction experiments”. In: *Materials Science and Engineering: A* 387 (2004), pp. 72–75.

[61] T Kruml et al. “Stress reduction experiments during constant-strain-rate tests in Cu and Ge”. In: *Philosophical magazine letters* 83.11 (2003), pp. 651–658.

[62] L Lu, SX Li, and K Lu. “An abnormal strain rate effect on tensile behavior in nanocrystalline copper”. In: *Scripta Materialia* 45.10 (2001), pp. 1163–1169.

[63] PM Derlet, A Hasnaoui, and H Van Swygenhoven. “Atomistic simulations as guidance to experiments”. In: *Scripta materialia* 49.7 (2003), pp. 629–635.

[64] Ting Zhang, Kai Zhou, and ZQ Chen. “Strain rate effect on plastic deformation of nanocrystalline copper investigated by molecular dynamics”. In: *Materials Science and Engineering: A* 648 (2015), pp. 23–30.

[65] V Yamakov et al. “Grain-boundary diffusion creep in nanocrystalline palladium by molecular-dynamics simulation”. In: *Acta Materialia* 50.1 (2002), pp. 61–73.

[66] Helena Van Swygenhoven and Julia R Weertman. “Deformation in nanocrystalline metals”. In: *Materials today* 9.5 (2006), pp. 24–31.

[67] James Chen-Min Li. *Microstructure and Properties of Materials:(Volume 2)*. Vol. 2. World Scientific Publishing Company, 2000.

[68] John P Hirth and Jens Lothe. “Theory of dislocations”. In: (1982).

[69] CAO Henning, FW Boswell, and JM Corbett. “Mechanical properties of vacuum-deposited metal films—I. Copper films”. In: *Acta Metallurgica* 23.2 (1975), pp. 177–185.

[70] MD Merz and SD Dahlgren. “Tensile strength and work hardening of ultrafine-grained high-purity copper”. In: *Journal of Applied Physics* 46.8 (1975), pp. 3235–3237.

[71] RA Masumura, PM Hazzledine, and CS Pande. “Yield stress of fine grained materials”. In: *Acta Materialia* 46.13 (1998), pp. 4527–4534.

[72] CS Pande and KP Cooper. “Nanomechanics of Hall–Petch relationship in nanocrystalline materials”. In: *Progress in Materials Science* 54.6 (2009), pp. 689–706.

[73] Hans Conrad. “Grain-size dependence of the flow stress of Cu from millimeters to nanometers”. In: *Metallurgical and Materials Transactions A* 35.9 (2004), pp. 2681–2695.

[74] V Yamakov et al. “Length-scale effects in the nucleation of extended dislocations in nanocrystalline Al by molecular-dynamics simulation”. In: *Acta Materialia* 49.14 (2001), pp. 2713–2722.

[75] Vesselin Yamakov et al. “Dislocation processes in the deformation of nanocrystalline aluminium by molecular-dynamics simulation”. In: *Nature materials* 1.1 (2002), p. 45.

[76] CA Schuh, TG Nieh, and T Yamasaki. “Hall–Petch breakdown manifested in abrasive wear resistance of nanocrystalline nickel”. In: *Scripta Materialia* 46.10 (2002), pp. 735–740.

[77] H Van Swygenhoven, A Caro, and D Farkas. “A molecular dynamics study of polycrystalline fcc metals at the nanoscale: grain boundary structure and its influence on plastic deformation”. In: *Materials Science and Engineering: A* 309 (2001), pp. 440–444.

[78] Krishan Kumar Chawla and MA Meyers. *Mechanical behavior of materials*. Prentice Hall, 1999.

[79] RL Coble. “A model for boundary diffusion controlled creep in polycrystalline materials”. In: *Journal of applied physics* 34.6 (1963), pp. 1679–1682.

[80] Paul C Millett et al. “Atomistic simulations of diffusional creep in a nanocrystalline body-centered cubic material”. In: *Acta Materialia* 56.14 (2008), pp. 3688–3698.

[81] Ravi S Kottada and Atul H Chokshi. “Low temperature compressive creep in electrodeposited nanocrystalline nickel”. In: *Scripta materialia* 53.8 (2005), pp. 887–892.

[82] John W Cahn, Yuri Mishin, and Akira Suzuki. “Coupling grain boundary motion to shear deformation”. In: *Acta materialia* 54.19 (2006), pp. 4953–4975.

[83] Joshua Monk, Brian Hyde, and Diana Farkas. “The role of partial grain boundary dislocations in grain boundary sliding and coupled grain boundary motion”. In: *Journal of materials science* 41.23 (2006), pp. 7741–7746.

[84] Zhiwei Shan et al. “Grain boundary-mediated plasticity in nanocrystalline nickel”. In: *Science* 305.5684 (2004), pp. 654–657.

[85] YB Wang et al. “Deformation-induced grain rotation and growth in nanocrystalline Ni”. In: *Applied Physics Letters* 92.1 (2008), p. 011903.

[86] GE Fougere et al. “Grain-size dependent hardening and softening of nanocrystalline Cu and Pd”. In: *Scripta metallurgica et materialia* 26.12 (1992), pp. 1879–1883.

[87] KS Kumar et al. “Deformation of electrodeposited nanocrystalline nickel”. In: *Acta Materialia* 51.2 (2003), pp. 387–405.

[88] Kai Zhang, JR Weertman, and JA Eastman. “Rapid stress-driven grain coarsening in nanocrystalline Cu at ambient and cryogenic temperatures”. In: *Applied Physics Letters* 87.6 (2005), p. 061921.

[89] M Jin, AM Minor, and JW Morris Jr. “Strain-induced coarsening in nano-grained films”. In: *Thin Solid Films* 515.6 (2007), pp. 3202–3207.

[90] S Brandstetter et al. “Grain coarsening during compression of bulk nanocrystalline nickel and copper”. In: *Scripta Materialia* 58.1 (2008), pp. 61–64.

[91] Marc Legros, Daniel S Gianola, and Kevin J Hemker. “In situ TEM observations of fast grain-boundary motion in stressed nanocrystalline aluminum films”. In: *Acta Materialia* 56.14 (2008), pp. 3380–3393.

[92] TJ Rupert et al. “Experimental observations of stress-driven grain boundary migration”. In: *Science* 326.5960 (2009), pp. 1686–1690.

[93] H Van Swygenhoven and A Caro. “Plastic behavior of nanophase metals studied by molecular dynamics”. In: *Physical Review B* 58.17 (1998), p. 11246.

[94] H Van Swygenhoven, Diana Farkas, and Alfredo Caro. “Grain-boundary structures in polycrystalline metals at the nanoscale”. In: *Physical Review B* 62.2 (2000), p. 831.

[95] H Van Swygenhoven, M Spaczer, and A Caro. “Microscopic description of plasticity in computer generated metallic nanophase samples: a comparison between Cu and Ni”. In: *Acta Materialia* 47.10 (1999), pp. 3117–3126.

[96] PM Derlet and H Van Swygenhoven. “Atomic positional disorder in fcc metal nanocrystalline grain boundaries”. In: *Physical Review B* 67.1 (2003), p. 014202.

[97] Jakob Schiøtz. “Strain-induced coarsening in nanocrystalline metals under cyclic deformation”. In: *Materials Science and Engineering: A* 375 (2004), pp. 975–979.

[98] Mario Velasco, H Van Swygenhoven, and Christian Brandl. “Coupled grain boundary motion in a nanocrystalline grain boundary network”. In: *Scripta Materialia* 65.2 (2011), pp. 151–154.

[99] AJ Haslam et al. “Stress-enhanced grain growth in a nanocrystalline material by molecular-dynamics simulation”. In: *Acta Materialia* 51.7 (2003), pp. 2097–2112.

[100] AJ Haslam et al. “Mechanisms of grain growth in nanocrystalline fcc metals by molecular-dynamics simulation”. In: *Materials Science and Engineering: A* 318.1-2 (2001), pp. 293–312.

[101] VI Yamakov. “The mechanical behavior of nanostructured metals based on molecular dynamics computer simulations”. In: *Nanostructured Metals and Alloys*. Elsevier, 2011, pp. 459–480.

[102] H Van Swygenhoven, PM Derlet, and A Hasnaoui. “Atomic mechanism for dislocation emission from nanosized grain boundaries”. In: *Physical Review B* 66.2 (2002), p. 024101.

[103] PM Derlet, H Van Swygenhoven, and A Hasnaoui. “Atomistic simulation of dislocation emission in nanosized grain boundaries”. In: *Philosophical Magazine* 83.31-34 (2003), pp. 3569–3575.

[104] V Yamakov et al. “Deformation mechanism crossover and mechanical behaviour in nanocrystalline materials”. In: *Philosophical Magazine Letters* 83.6 (2003), pp. 385–393.

[105] Zeljka Budrovic et al. “Plastic deformation with reversible peak broadening in nanocrystalline nickel”. In: *Science* 304.5668 (2004), pp. 273–276.

[106] Anders Gudmund Frøseth, Peter Michael Derlet, and Helena Van Swygenhoven. “Twinning in nanocrystalline fcc metals”. In: *Advanced Engineering Materials* 7.1-2 (2005), pp. 16–20.

[107] YT Zhu, XZ Liao, and XL Wu. “Deformation twinning in nanocrystalline materials”. In: *Progress in Materials Science* 57.1 (2012), pp. 1–62.

[108] MA Meyers, O Vöhringer, and VA Lubarda. “The onset of twinning in metals: a constitutive description”. In: *Acta materialia* 49.19 (2001), pp. 4025–4039.

[109] H Van Swygenhoven et al. “Competing plastic deformation mechanisms in nanophase metals”. In: *Physical Review B* 60.1 (1999), p. 22.

[110] V Yamakov et al. “Dislocation–dislocation and dislocation–twin reactions in nanocrystalline Al by molecular dynamics simulation”. In: *Acta materialia* 51.14 (2003), pp. 4135–4147.

[111] H Van Swygenhoven, PM Derlet, and AG Frøseth. “Stacking fault energies and slip in nanocrystalline metals”. In: *Nature materials* 3.6 (2004), p. 399.

[112] Luis A Zepeda-Ruiz et al. “Probing the limits of metal plasticity with molecular dynamics simulations”. In: *Nature* 550.7677 (2017), p. 492.

[113] Kai Zhou et al. “Effects of grain size and shape on mechanical properties of nanocrystalline copper investigated by molecular dynamics”. In: *Materials Science and Engineering: A* 615 (2014), pp. 92–97.

[114] XZ Liao et al. “Deformation mechanism in nanocrystalline Al: Partial dislocation slip”. In: *Applied Physics Letters* 83.4 (2003), pp. 632–634.

[115] XL Wu and YT Zhu. “Inverse grain-size effect on twinning in nanocrystalline Ni”. In: *Physical review letters* 101.2 (2008), p. 025503.

[116] Xiao-Lei Wu, YT Zhu, and E Ma. “Predictions for partial-dislocation-mediated processes in nanocrystalline Ni by generalized planar fault energy curves: An experimental evaluation”. In: *Applied physics letters* 88.12 (2006), p. 121905.

[117] XL Wu, Y Qi, and YT Zhu. “Partial-mediated slips in nanocrystalline Ni at high strain rate”. In: *Applied physics letters* 90.22 (2007), p. 221911.

[118] YT Zhu, XZ Liao, and XL Wu. “Deformation twinning in bulk nanocrystalline metals: experimental observations”. In: *Jom* 60.9 (2008), p. 60.

[119] YT Zhu et al. “Twinning partial multiplication at grain boundary in nanocrystalline fcc metals”. In: *Applied Physics Letters* 95.3 (2009), p. 031909.

[120] YT Zhu et al. “Grain size effect on deformation twinning and detwinning”. In: *Journal of Materials Science* 48.13 (2013), pp. 4467–4475.

[121] Lihua Wang et al. “New twinning route in face-centered cubic nanocrystalline metals”. In: *Nature communications* 8.1 (2017), p. 2142.

[122] NQ Vo et al. “Quantitative description of plastic deformation in nanocrystalline Cu: Dislocation glide versus grain boundary sliding”. In: *Physical Review B* 77.13 (2008), p. 134108.

[123] J Chen, YN Shi, and K Lu. “Strain rate sensitivity of a nanocrystalline Cu–Ni–P alloy”. In: *Journal of materials research* 20.11 (2005), pp. 2955–2959.

[124] Daan Frenkel et al. “Understanding molecular simulation”. In: *Computers in Physics* 11.4 (1997), pp. 351–354.

[125] Michele Parrinello and Aneesur Rahman. “Polymorphic transitions in single crystals: A new molecular dynamics method”. In: *Journal of Applied physics* 52.12 (1981), pp. 7182–7190.

[126] Glenn J Martyna, Douglas J Tobias, and Michael L Klein. “Constant pressure molecular dynamics algorithms”. In: *The Journal of Chemical Physics* 101.5 (1994), pp. 4177–4189.

[127] Mark E Tuckerman et al. “A Liouville-operator derived measure-preserving integrator for molecular dynamics simulations in the isothermal–isobaric ensemble”. In: *Journal of Physics A: Mathematical and General* 39.19 (2006), p. 5629.

[128] Wataru Shinoda, Motoyuki Shiga, and Masuhiro Mikami. “Rapid estimation of elastic constants by molecular dynamics simulation under constant stress”. In: *Physical Review B* 69.13 (2004), p. 134103.

[129] Steve Plimpton. “Fast parallel algorithms for short-range molecular dynamics”. In: *Journal of computational physics* 117.1 (1995), pp. 1–19.

[130] Arun K Subramaniyan and CT Sun. “Continuum interpretation of virial stress in molecular simulations”. In: *International Journal of Solids and Structures* 45.14-15 (2008), pp. 4340–4346.

[131] MS Daw. “MS Daw and MI Baskes, Phys. Rev. B 29, 6443 (1984).” In: *Phys. Rev. B* 29 (1984), p. 6443.

[132] SM Foiles, MI Baskes, and Murray S Daw. “Embedded-atom-method functions for the fcc metals Cu, Ag, Au, Ni, Pd, Pt, and their alloys”. In: *Physical review B* 33.12 (1986), p. 7983.

[133] Giovanni Bonny et al. “Interatomic potential to study plasticity in stainless steels: the FeNiCr model alloy”. In: *Modelling and simulation in materials science and engineering* 19.8 (2011), p. 085008.

[134] MI Baskes. “Application of the embedded-atom method to covalent materials: a semiempirical potential for silicon”. In: *Physical review letters* 59.23 (1987), p. 2666.

[135] Thomas J Lenosky et al. “Highly optimized empirical potential model of silicon”. In: *Modelling and Simulation in Materials Science and Engineering* 8.6 (2000), p. 825.

[136] RG Hennig et al. “Classical potential describes martensitic phase transformations between the α, β, and ω titanium phases”. In: *Physical Review B* 78.5 (2008), p. 054121.

[137] NW Ashcroft. *ND Mermin Solid State Physics WB Saunders Company*. 1976.

[138] Eric A Brandes and GB Brook. *Smithells metals reference book*. Elsevier, 2013.

[139] Gene Simmons, Herbert Wang, et al. “Single crystal elastic constants and calculated aggregate properties”. In: (1971).

[140] Jonathan A Zimmerman, Huajian Gao, and Farid F Abraham. “Generalized stacking fault energies for embedded atom FCC metals”. In: *Modelling and Simulation in Materials Science and Engineering* 8.2 (2000), p. 103.

[141] Christian Brandl. “Deformation mechanism in nanocrystalline FCC metals studied by atomistic simulations”. In: (2010).

[142] Shigenobu Ogata, Ju Li, and Sidney Yip. “Ideal pure shear strength of aluminum and copper”. In: *Science* 298.5594 (2002), pp. 807–811.

[143] Z Sun et al. “Experimental study of microstructure changes due to low cycle fatigue of a steel nanocrystallised by Surface Mechanical Attrition Treatment (SMAT)”. In: *Materials Characterization* 124 (2017), pp. 117–121.

[144] Alexander Stukowski. “Visualization and analysis of atomistic simulation data with OVITO–the Open Visualization Tool”. In: *Modelling and Simulation in Materials Science and Engineering* 18.1 (2009), p. 015012.

[145] Cynthia L Kelchner, SJ Plimpton, and JC Hamilton. “Dislocation nucleation and defect structure during surface indentation”. In: *Physical review B* 58.17 (1998), p. 11085.

[146] J Dana Honeycutt and Hans C Andersen. “Molecular dynamics study of melting and freezing of small Lennard-Jones clusters”. In: *Journal of Physical Chemistry* 91.19 (1987), pp. 4950–4963.

[147] Daniel Faken and Hannes Jónsson. “Systematic analysis of local atomic structure combined with 3D computer graphics”. In: *Computational Materials Science* 2.2 (1994), pp. 279–286.

[148] Alexander Stukowski. “Structure identification methods for atomistic simulations of crystalline materials”. In: *Modelling and Simulation in Materials Science and Engineering* 20.4 (2012), p. 045021.

[149] Futoshi Shimizu, Shigenobu Ogata, and Ju Li. “Theory of shear banding in metallic glasses and molecular dynamics calculations”. In: *Materials transactions* 48.11 (2007), pp. 2923–2927.

[150] Alexander Stukowski, Vasily V Bulatov, and Athanasios Arsenlis. “Automated identification and indexing of dislocations in crystal interfaces”. In: *Modelling and Simulation in Materials Science and Engineering* 20.8 (2012), p. 085007.

[151] Alexander Stukowski and Karsten Albe. “Extracting dislocations and non-dislocation crystal defects from atomistic simulation data”. In: *Modelling and Simulation in Materials Science and Engineering* 18.8 (2010), p. 085001.

[152] Pierre Hirel. “Atomsk: a tool for manipulating and converting atomic data files”. In: *Computer Physics Communications* 197 (2015), pp. 212–219.

[153] B Mantisi. “Generation of polycrystalline material at the atomic scale”. In: *Computational Materials Science* 118 (2016), pp. 245–250.

[154] SR Phillpot, D Wolf, and H Gleiter. “Molecular-dynamics study of the synthesis and characterization of a fully dense, three-dimensional nanocrystalline material”. In: *Journal of applied physics* 78.2 (1995), pp. 847–861.

[155] SR Phillport et al. “Computer simulation of the structure and dynamical properties of grain boundaries in a nanocrystalline model material”. In: *Materials Science and Engineering: A* 204.1-2 (1995), pp. 76–82.

[156] SR Phillpot, D Wolf, and H Gleiter. “A structural model for grain boundaries in nanocrystalline materials”. In: *Scripta metallurgica et materialia* 33.8 (1995).

[157] M-S Colla et al. “Dislocation-mediated relaxation in nanograined columnar palladium films revealed by on-chip time-resolved HRTEM testing”. In: *Nature communications* 6 (2015), p. 5922.

[158] H Gong et al. “Nano-crystalline Cu-doped ZnO thin film gas sensor for CO”. In: *Sensors and Actuators B: Chemical* 115.1 (2006), pp. 247–251.

[159] PB Barna and M Adamik. “Fundamental structure forming phenomena of polycrystalline films and the structure zone models”. In: *Thin solid films* 317.1-2 (1998), pp. 27–33.

[160] Thomas LaGrange et al. “Topological view of the thermal stability of nanotwinned copper”. In: *Applied Physics Letters* 102.1 (2013), p. 011905.

[161] Y Morris Wang et al. “Defective twin boundaries in nanotwinned metals”. In: *Nature materials* 12.8 (2013), p. 697.

[162] AG Frøseth, PM Derlet, and H Van Swygenhoven. “Vicinal twin boundaries providing dislocation sources in nanocrystalline Al”. In: *Scripta materialia* 54.3 (2006), pp. 477–481.

[163] F Dalla Torre, H Van Swygenhoven, and M Victoria. “Nanocrystalline electrodeposited Ni: microstructure and tensile properties”. In: *Acta Materialia* 50.15 (2002), pp. 3957–3970.

[164] Yong-Bo Guo, Tao Xu, and Mo Li. “Atomistic calculation of internal stress in nanoscale polycrystalline materials”. In: *Philosophical Magazine* 92.24 (2012), pp. 3064–3083.

[165] Stefan Brandstetter et al. “From Micro-to Macroplasticity”. In: *Advanced Materials* 18.12 (2006), pp. 1545–1548.

[166] GW Nieman, JR Weertman, and RW Siegel. *Mechanical behavior of nanocrystalline metals*. Tech. rep. Argonne National Lab., IL (USA), 1990.

[167] Gerhard Welsch, Rodney Boyer, and EW Collings. *Materials properties handbook: titanium alloys*. ASM international, 1993.

[168] Dong-Hwan Kang and Tae-Won Kim. “Mechanical behavior and microstructural evolution of commercially pure titanium in enhanced multi-pass equal channel angular pressing and cold extrusion”. In: *Materials & Design* 31 (2010), S54–S60.

[169] Niels Hansen and B Ralph. “The strain and grain size dependence of the flow stress of copper”. In: *Acta Metallurgica* 30.2 (1982), pp. 411–417.

[170] S Nagarjuna, M Srinivas, and KK Sharma. “The grain size dependence of flow stress in a Cu–26Ni–17Zn alloy”. In: *Acta materialia* 48.8 (2000), pp. 1807–1813.

[171] S Van Petegem et al. “Creep in nanocrystalline Ni during X-ray diffraction”. In: *Scripta Materialia* 60.5 (2009), pp. 297–300.

[172] Atul H Chokshi. “Unusual stress and grain size dependence for creep in nanocrystalline materials”. In: *Scripta Materialia* 61.1 (2009), pp. 96–99.

[173] RMJ Cotterill. “Does dislocation density have a natural limit?” In: *Physics Letters A* 60.1 (1977), pp. 61–62.

[174] XZ Liao et al. “Deformation twinning in nanocrystalline copper at room temperature and low strain rate”. In: *Applied physics letters* 84.4 (2004), pp. 592–594.

[175] J Hessinger and K Knorr. “Field-cooling experiments on the quadrupolar-glass state of (KBr) 0.47 (KCN) 0.53”. In: *Physical review letters* 65.21 (1990), p. 2674.

[176] Stephan A Baeurle, Atsushi Hotta, and Andrei A Gusev. “A new semi-phenomenological approach to predict the stress relaxation behavior of thermoplastic elastomers”. In: *Polymer* 46.12 (2005), pp. 4344–4354.

[177] Ellad B Tadmor, Ronald E Miller, and Ryan S Elliott. *Continuum mechanics and thermodynamics: from fundamental concepts to governing equations*. Cambridge University Press, 2012.

[178] Yann Gueguen et al. “A relationship between non-exponential stress relaxation and delayed elasticity in the viscoelastic process in amorphous solids: Illustration on a chalcogenide glass”. In: *Mechanics of Materials* 85 (2015), pp. 47–56.

[179] Matthieu Micoulaut. “Relaxation and physical aging in network glasses: a review”. In: *Reports on Progress in Physics* 79.6 (2016), p. 066504.

[180] Ercan Gürses and Tamer El Sayed. “Constitutive modeling of strain rate effects in nanocrystalline and ultrafine grained polycrystals”. In: *International Journal of Solids and Structures* 48.10 (2011), pp. 1610–1616.

[181] Yue Jiang et al. “Strain rate dependence of tensile strength and ductility of nano and ultrafine grained coppers”. In: *Materials Science and Engineering: A* 712 (2018), pp. 341–349.

[182] Heinz Lüthy, Richard A White, and Oleg D Sherby. “Grain boundary sliding and deformation mechanism maps”. In: *Materials Science and Engineering* 39.2 (1979), pp. 211–216.

[183] Reza Abbaschian and Robert E Reed-Hill. *Physical metallurgy principles*. Cengage Learning, 2008.

[184] A Elsener et al. “Variable-charge method applied to study coupled grain boundary migration in the presence of oxygen”. In: *Acta Materialia* 57.6 (2009), pp. 1988–2001.

[185] DS Gianola et al. “Stress-assisted discontinuous grain growth and its effect on the deformation behavior of nanocrystalline aluminum thin films”. In: *Acta Materialia* 54.8 (2006), pp. 2253–2263.

Appendix A

Grain refinement mechanism in $FeNi_{14}Cr_{18}$

A.1 Grain refinement in $FeNi_{14}Cr_{18}$

To create a monocrystalline $FeNi_{14}Cr_{18}$, an FCC lattice structure with a_0 = 3.4987 is replicated along x, y and z direction for 50x50x300 unit cells respectively that contains 3,000,000 atoms. The equilibrium lattice distance a_0 of an FCC Fe is used to generate the initial simulation domain. Then, the number of atoms corresponding to each weighting fraction of element is calculated. Atoms are randomly chosen and the type of these atoms is changed in order to match the weighting fraction of each element. An energy minimization is then applied to the system in order to reach a minimum potential energy. Once the system is in a minimum potential energy the equilibrium lattice distance is calculated and the value corresponds to the one reported in table 2.3 ($a_0 = 3.511$).

In order to create some realistic defects inside the monocrystalline $FeNi_{14}Cr_{18}$, a fraction of 0.1% of atoms has been also removed from the system. This will generate a number of vacancies inside the microstructure. Then, the system is relaxed following the stated steps:

1. The system is relaxed in the NPT ensemble at $300K$ and zero external pressure in all directions for 30 ps. The external pressure is controlled by an anisotropic barostat.

2. Heating of the system so that the temperature reaches $900K$ in NPT ensemble for 30 ps with zero external pressure.

3. The system is then relaxed in the NPT ensemble at $900K$ and zero external pressure in all directions for 30 ps. Followed by, a decrease in the temperature to $300K$ for 30 ps.

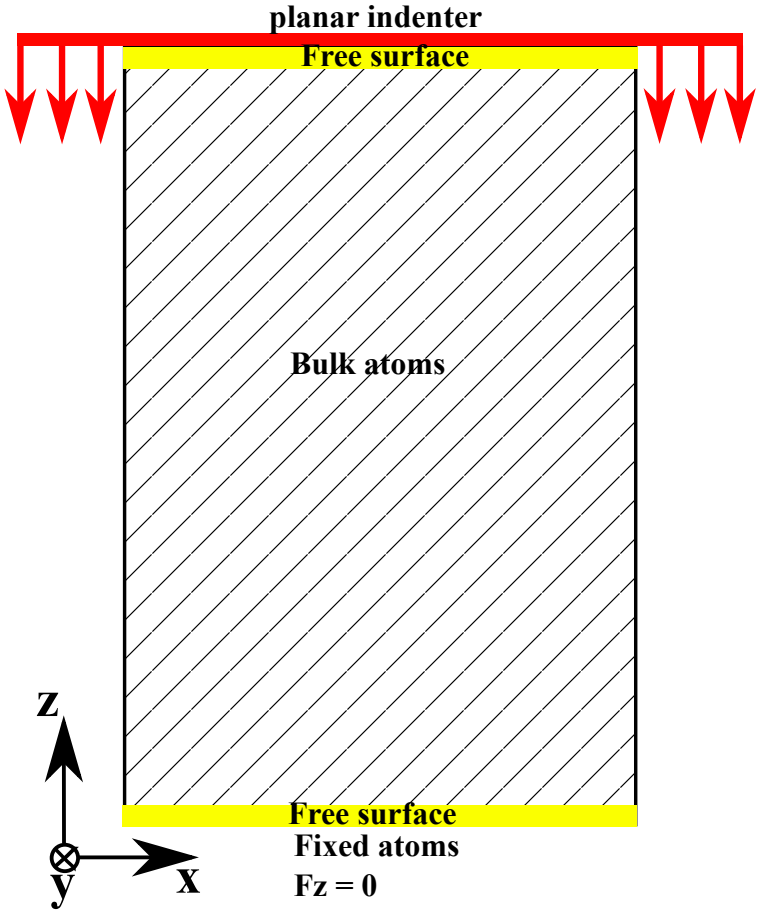

FIGURE A.1: Schematic plot of the compression process applied on the $FeNi_{14}Cr_{18}$ monocrystal.

4. Finally, we relax the system at $300K$ and zero external pressure for 30 ps.

We finally obtained a system with a minimum potential energy and the components of the pressure tensor are equal to zero in all directions. The boundaries conditions are kept periodic in x and y, but the z direction is changed to a free boundary condition. Therefore, the system now describes a thin film of a monocrystalline iron alloy.

A uniaxial compression tests is applied in the z direction at $\dot{\varepsilon} = 5.10^9\ s^{-1}$ and T = $300K$. Figure A.1 shows a schematic plot of the compression setup. The F_z for atoms with a distance less than $2a_0$ from the lower side of the simulation domain have been set to zero. Therefore, these atoms cannot move in the z direction.

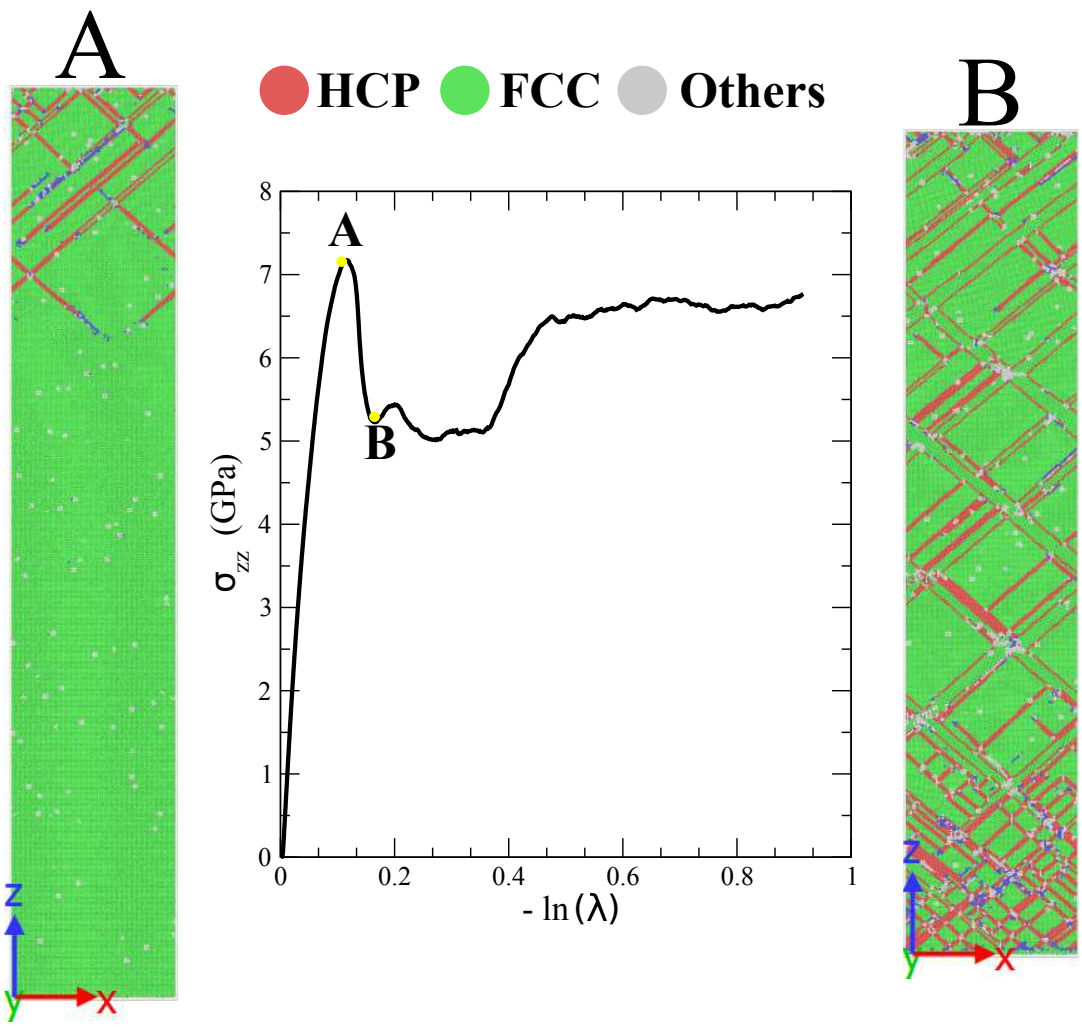

FIGURE A.2: Stress strain curve of the monocrystalline Fe14Ni18Cr submitted to uniaxial compression test at $\dot{\varepsilon} = 5.10^9 s^{-1}$, A and B are two snapshots of the atomic configuration at different strain level colored by the common neighbor analysis.

A.2 Preliminary results

The result of the uniaxial compression test applied on the monocrystalline Fe14Ni18Cr is present in Figure A.2. Two main observations can be extracted from the Figure: (1) The stress strain curve exhibit an overshoot before reaching the plastic flow regime, and (2) the stress in the flow regime above 40% deformation re-increase to reach another flow stress regime. Two snapshots of the atomic configurations have been taken at the two different strains (A and B above and below the drop of stress) as marked by yellow on the stress-strain curve (Figure A.2). The heterogeneity of the strain is in the origin of such overshoot of the stress in the stress-strain curve. Once dislocations are presents along all the thickness of the sample, the stress attains the flow regime.

The second observation is caused by the interaction between partial dislocations and twin boundaries or stacking fault ribbons. These faults act as barrier to the motion of dislocations and hence increase the flow stress of the system.

We found that the final microstructure consists of columnar nanograins, a combination of dislocation slip and mechanical twinning have been found as the main refinement mechanisms. High density of dislocations and twins nucleation can be distinguished on the surface. Moreover, large density of twin boundaries have been observed that decompose the monocrystal into lamellar twin-matrix blocks with a nanometer-sized thickness. Finally, twin-twin and twin-dislocation interaction are found to be responsible for the transformation of the twin-matrix blocks to small grains. At the end, the refinement mechanism can be described as follows:

1. Emission of Shockley partial from the mobile surface below the planar indenter on $(1\bar{1}1)$ and $(\bar{1}\bar{1}1)$ planes (Figure A.3 (a)).

2. The overlapping of the partial dislocations on adjacent slip planes will lead to the nucleation of coherent twin boundaries (Figure A.3 (b)).

3. The thickness of the twinned area begin to increase due to the propagation of partial dislocations on adjacent slip planes of the twin boundaries.

4. Several twin systems are activate and the intersection of these twin boundaries lead to the creation of rhombic blocks inside the matrix (Figure A.3 (c)).

5. High density of deformation twins break up the original grains and the dislocations are trapped between the twin boundaries. Hence, the interaction between partial dislocations and twin boundaries lead to the transition from coherent twin boundary to incoherent high angle grain boundary (Figure A.3 (d)).

Finally, The interaction between dislocations and twin boundaries and/or stacking faults should be deeply investigated. The transition from twin boundaries to high angle grain boundaries leading to grain refinement should also be analyzed in terms of the possible dislocation reactions at twin boundaries.

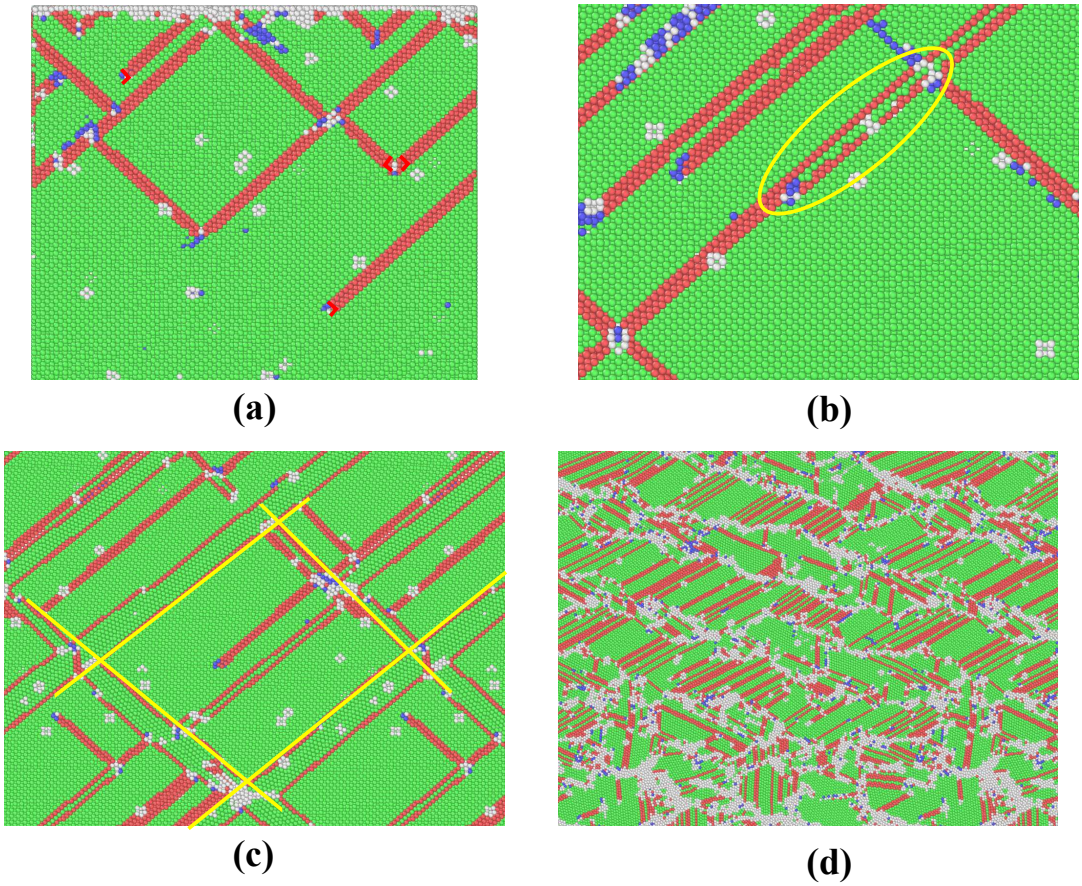

FIGURE A.3: Snapshots focusing on a specific deformation mechanism in the atomic configuration during the grain refinement process.

Appendix B

List of publications

The following journal and conference papers have been produced as parts of outcomes of this research:

Refereed publications

- Rida, A., Rouhaud, E., Makke, A., Micoulaut, M., & Mantisi, B. (2017). Study of the effects of grain size on the mechanical properties of nanocrystalline copper using molecular dynamics simulation with initial realistic samples. Philosophical Magazine, 97(27), 2387-2405.
- Understanding the strain rate sensitivity of nanocrystalline copper using molecular dynamics simulations, A. Rida, M. Micoulaut, E. Rouhaud, A. Makke (In preparation).
- Evidence for glassy relaxation in crystals at high deformation rate, A. Rida, M. Micoulaut, E. Rouhaud, A. Makke, (In preparation).

Conference publications

- Rida, A., Makke, A., Rouhaud, E., & Micoulaut, M. (2017, October). Influence of grain size on the mechanical properties of nano-crystalline copper; insights from molecular dynamics simulation. In AIP Conference Proceedings (Vol. 1896, No. 1, p. 160012). AIP Publishing (ESAFORM 2017).
- Rida, A., Rouhaud, E., Micoulaut, M., Makke, A., & Retraint, D. Molecular dynamics investigations for surface mechanical attrition treatment (ICSP 2017).

Résumé

Introduction

En pratique, la plupart des défaillances de matériaux métalliques proviennent de la surface et sont sensibles à la microstructure et les propriétés mécaniques. Les matériaux nanocristallins ont été trouvés à être plus résistants et à avoir une dureté et des propriétés physiques améliorées par rapport à des systèmes présentant des grains microcristallins. Un procédé de traitement de surface, le SMAT (Surface Mechanical Attrition Treatment) a été développé à l'UTT dans notre équipe pour améliorer le comportement de la surface de pièces mécaniques métalliques en créant des nanostructures superficielles par des déformations plastiques sévères ce qui permet d'améliorer leur propriétés mécaniques et d'augmenter la durée de vie de ces pièces. Le SMAT permet de développer un gradient de taille moyenne de grains de quelques nanomètres près de la surface (couche nanocristalline) jusqu'à quelques micromètres au coeur du matériau. L'effet du gradient de la taille moyenne de grains joue un rôle primordial dans le comportement mécanique des matériaux "*smattés*". On produit ainsi un durcissement local de la surface toute en conservant le coeur du matériau ductile. La conciliation de la dureté superficielle à la ductilité du cœur est un enjeu majeur pour ce type de matériaux. La compréhension des déformations locales et des contraintes locales qui se développent dans la couche superficielle nanocristalline lors d'une sollicitation est cruciale pour la modélisation.

Un challenge essentiel en mécanique des matériaux est de comprendre et de modéliser les mécanismes qui entrent en jeu à plusieurs échelles lors d'une déformation plastique. Une approche expérimentale a été mise en oeuvre dans l'équipe LASMIS de l'UTT pour étudier les propriétés mécaniques locales de cette couche nanocristalline : la compression de micro-piliers. La compréhension des mécanismes qui interviennent à plusieurs échelles lors de la compression de micro-piliers ou d'une manière générale lors de la déformation plastique de matériaux polycristallins est nécessaire, voire indispensable pour bien modéliser le comportement mécanique et comprendre le procédé. Pour combler cette lacune, la simulation par dynamique moléculaire (MD) est une méthode efficace qui permet de comprendre l'évolution de la nanostructure lors d'une

sollicitation mécanique. La relation nanostructure-réponse mécanique peut, à terme, devenir totalement exploitable à plusieurs échelles.

Dans cette thèse, un intérêt tout particulier sera porté sur l'analyse des mécanismes de déformation de la couche nanocristalline. À l'échelle nanométrique, des simulations de dynamique moléculaire sont effectuées pour étudier l'effet des joints de grains, de la taille moyenne des grains et du taux de déformation sur les mécanismes de déformation des matériaux métalliques nanocristallins. Ces objectifs nous permettent de renforcer la compréhension fine du rôle de la structure sur les mécanismes de plasticité et d'endommagement aux échelles locales.

Chapter 1

Méthodologie

1.1 Génération des échantillons

Plusieurs méthodes ont été proposées dans la littérature afin de générer les configurations initiales pour les simulations MD. Le pavage de Voronoï est le plus répandu pour fabriquer des échantillons colonnaires et 3D [1]. Les échantillons générés par cette méthode possèdent cependant des joints de grains linéaires ainsi que des contraintes résiduelles importantes le long des joints grains. De plus, il n'existe pas de défauts à l'intérieur des grains comme des lacunes, des interstitielles et des dislocations qui reflètent aussi la réalité des matériaux nanocristallins. Une nécessité est donc de développer une nouvelle méthode qui permet de générer ces défauts réalistes afin de mieux comprendre leur rôle dans la réponse mécanique et les mécanismes de déformations des matériaux nanocristallins.

Nous avons développé une nouvelle méthode pour construire les configurations initiales avec des joints de grains courbés et des défauts caractéristique à l'intérieur des grains par fusion suivi d'un refroidissement d'un monocristal. La méthode consiste à chauffer un monocristal de Cu jusqu'à $2000K$ dans un ensemble NPT pendant 60 ps. Les conditions aux bords sont périodiques et la pression dans toutes les directions est nulle afin de laisser le système évoluer sans contraintes extérieures. Les dimensions de la boite de simulation sont 72.3 nm x 72.3 nm x 0.3615 nm et elle contient 160 000 atomes de Cu. Le potentiel inter-atomique utilisé est un potentiel de type EAM développé par Foiles *et al* [2]. Après la fusion, le liquide a été relaxé dans un ensemble NPT à $2000K$ avec une pression nulle dans toutes les directions pendant 60 ps afin d'équilibrer le système. Cette procédure permet l'augmentation du volume de la boite de simulation lors de l'augmentation de la température (T).

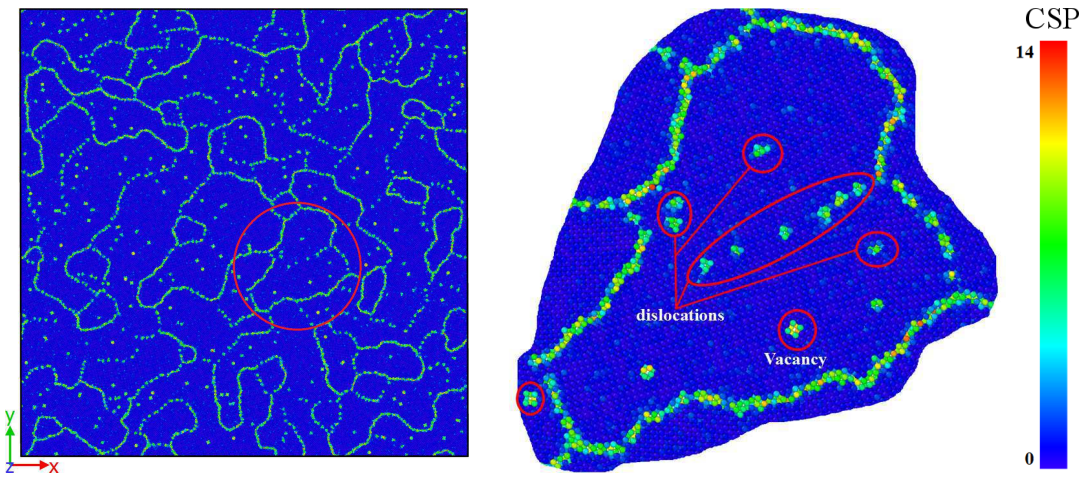

FIGURE 1.1: (a) Un échantillon de Cu nanocristallin généré par fusion refroidissement avec une taille moyenne de grains de 9 nm coloré par la valeur des coefficients centrosymétriques, (b) Zoom sur un grain encerclé en rouge dans (a) pour visualiser les défauts inter- et intra-granulaires.

Après la fusion et la relaxation du liquide, le système est refroidi jusqu'au $300K$ dans un ensemble NPT à différent taux de refroidissement. La vitesse du trempe est un paramètre essentiel qui permet de contrôler la taille moyenne des grains. Plus le taux de refroidissement augmente, plus la taille moyenne de grains diminue. Après la refroidissement, le système est relaxé dans un ensemble NPT à $300K$ et une pression nulle pour 200 ps. Figure 1.1 (a) présente un échantillon de Cu nanocristallin généré par fusion refroidissement. Un Zoom sur un grain (encerclé en rouge dans cet échantillon) est présenté dans la Figure 1.1 (b). Il y apparaissent les défauts intra-granulaires comme des dislocations coins et des lacunes. De plus, les joints de grains sont courbés avec la présence de coins et des joints triples.

Comme mentionné ci-dessus, la taille moyenne de grains est contrôlée par le taux de refroidissement. L'augmentation du taux de refroidissement diminue le temps nécessaire pour la recristallisation. Ceci induit la formation des petits grains qui n'ont pas le temps d'augmenter leurs tailles par aggrégation périodique des atomes environnants. Par conséquent, la taille moyenne de grains diminue avec l'augmentation de la vitesse de refroidissement. La Figure 1.2 présente la variation de la taille moyenne de grains pour les échantillons construits par la méthode de fusion refroidissement, la taille moyenne de grains variant de 9.0 nm (67 grains) à 36 nm (4 grains) (Figure 1.2). Les dimensions de la boite de simulation et le nombre d'atomes dans cette boite sont les mêmes pour tous les échantillons. Cela implique que l'augmentation de la taille

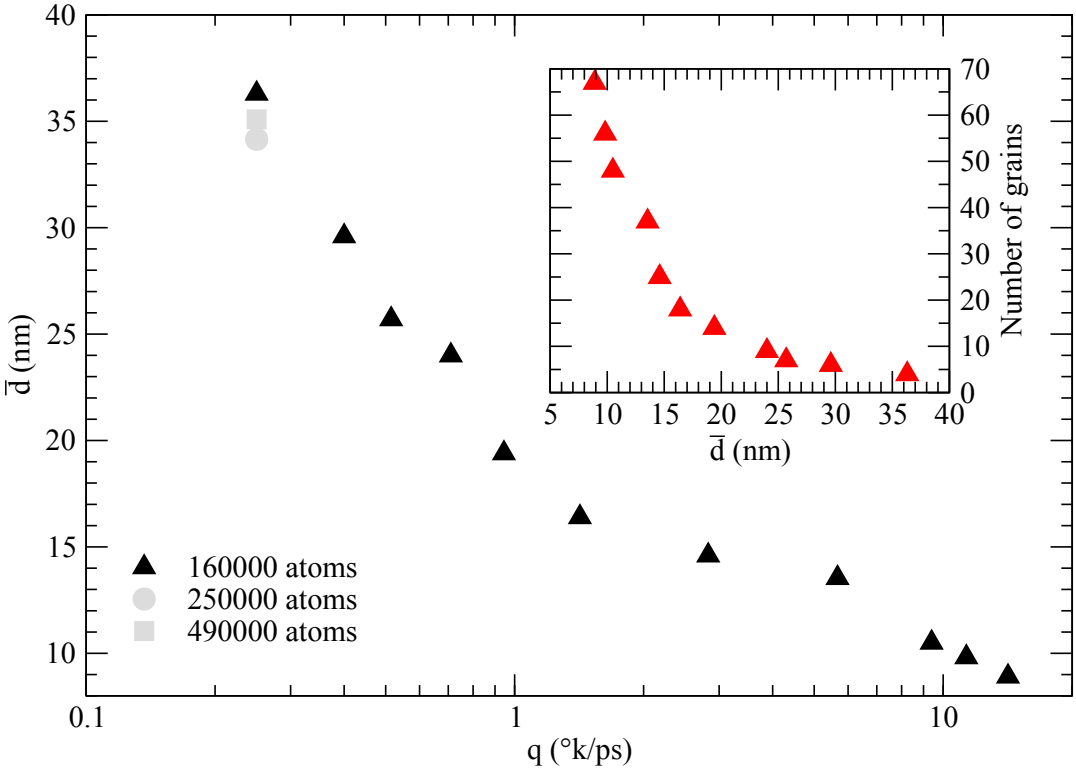

FIGURE 1.2: Variation de la taille moyenne de grains en fonction du taux de refroidissement et la variation de la nombre de grains dans le système en fonction de la taille moyenne de grains.

moyenne de grains diminue le nombre de grains dans le système.

Il faut noter que la diminution de la taille moyenne des grains augmente considérablement la fraction volumique des joints de grains et des défauts. Pour s'assurer d'une bonne statistique et d'une bonne reproductibilité, plusieurs trempes d'un même échantillon avec le même taux de refroidissement ont été également effectués. Ces simulations conduisent à la même taille moyenne de grains, mais la distribution de taille de grains peut être différente. L'influence de la taille de la boîte initiale a été testée avec deux configurations contenant respectivement 250 000 et 490 000 atomes. Les simulations ont été effectuées en utilisant le plus petit taux de refroidissement ($0,25 \pm K/ps$). Les résultats sont présentés avec des marques grises sur la Figure 1.2. Il semble que le nombre d'atomes influence légèrement la taille moyenne des grains. La Figure 1.3 présente les 2 échantillons quasi-2D et colonnaires 3D générés par fusion refroidissement. Les échantillons 3D en colonnes ont été créés pour étudier plus en détail les mécanismes de déformation des matériaux nanocristallins qui pourraient être absents à plus faible dimension (2D).

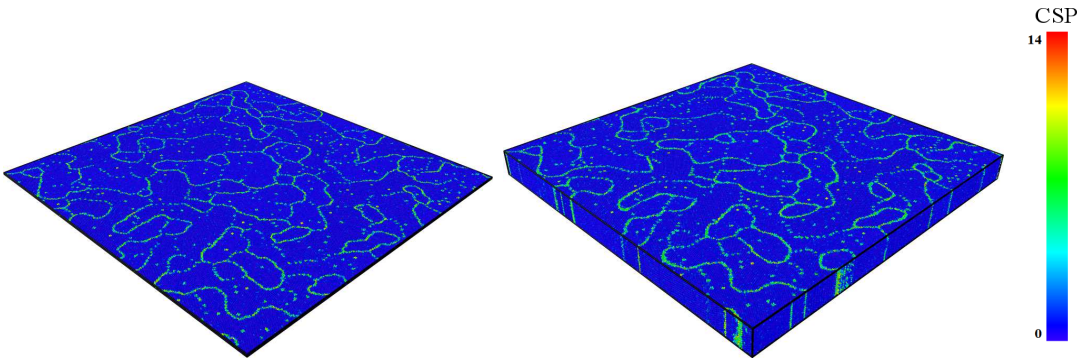

(a) (b)

FIGURE 1.3: 2 systèmes de Cu nanocristallins générés par fusion refroidissement avec une taille moyenne de grains de 9 nm. (a) quasi-2D, (b) colonnaire 3D. La couleur des atomes correspond à la valeur du coefficient centrosymétrique.

1.2 Structure et énergie des joints de grains

La fonction de distribution radiale (RDF) est une fonction de corrélation de densité-densité qui indique la probabilité de trouver une particule dans l'élément de volume entre la distance r et r + dr d'une autre particule. La RDF est définie par :

$$RDF = g(r) = \frac{1}{4\pi r^2 N\rho} \sum_{i=1}^{N} \sum_{\substack{j=1 \\ j\neq i}}^{N} \delta(r - r_{ij}) \tag{1.1}$$

où N est le nombre total des atomes, ρ est la densité de système, r_{ij} est la distance entre l'atome i et l'atome j et δ est la constante de Kronecker égale à 1 si $r = r_{ij}$.

Afin de caractériser la structure des échantillons initiaux générés par la méthode de fusion refroidissement, la RDF pour chaque échantillon a été calculée après la relaxation à $300K$. La Figure 1.4 présente la RDF de 2 échantillons de Cu nanocristallins de taille moyenne de 9.0 et 16.5 nm générés avec la méthode de fusion refroidissement. De plus, un échantillon constitué d'un cuivre monocristallin est présenté à titre de comparaison. Les pics obtenus pour le monocristal (coloré en bleu) sont légèrement élargis, en les comparant aux pics pointus attendus pour un monocristal. Ceci est dû à la relaxation du système à $300K$ qui crée un léger désordre dans le cristal de structure parfaite. La RDF pour les échantillons de 9.0 et 16.5 nm présente des pics bien définis qui caractérisent un matériau cristallin ordonné. Cependant, ces pics sont

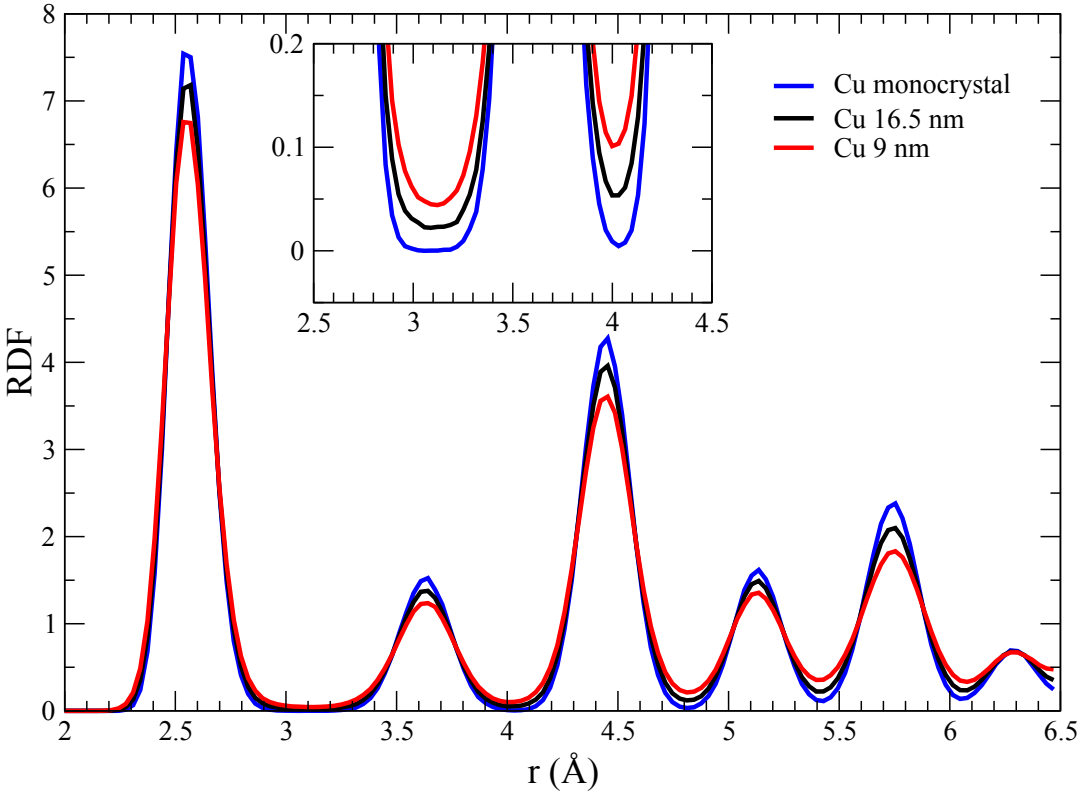

FIGURE 1.4: RDF pour les échantillons de Cu quasi-2D de taille moyenne de grains de 9.0 et 16.5 nm, en comparaison avec un monocristal de Cu relaxé à $300°K$.

légèrement décalés du monocristal relaxé en raison de la présence de défauts (par exemple les joints de grains). De plus, nous remarquons que la RDF pour les polycristaux 9.0 et 16.5 nm ne présente pas de minimum nul entre les deux premiers pics, contrairement à la RDF du monocristal. Ceci est attribué à la présence des joints de grains qui génèrent des désordres dans le système. Nous pouvons également voir à partir de la RDF de la Figure que la diminution de la taille moyenne de grains réduit les pics de la RDF suite à l'augmentation de la fraction de joints de grains.

Chapter 2

Effet de la taille de grains sur les propriétés mécaniques des matériaux nanocristallins

Les études expérimentales ont montré la présence d'une transition dans les propriétés mécaniques de matériaux nanocristallins avec la diminution de la taille moyenne des grains. Dans un premier temps, un durcissement de matériaux a lieu avec la diminution de la taille de grains (effet dits de Hall Petch) jusqu'à une taille critique où un adoucissement aura lieu avec la diminution de la taille de grains. En-dessous de cette taille critique, on est en présence d'un effet inverse de Hall Petch [3–7]. On assiste en effet à une transition entre de la déformation plastique induite par le mouvement des dislocations et une plasticité localisée sur les joints de grains essentiellement. La MD a été largement utilisée pour élucider la localisation de la taille critique de grains avec une analyse de la transition entre ces deux mécanismes de déformation. Cette taille critique est connue pour plusieurs matériaux [8–10].

Les simulations MD ont montré que les joints de grains à cette échelle constituent des sources et des barrières pour les dislocations. De plus, les dislocations partielles de type Shockley sont émises des joints grains et elles se propagent à l'intérieur des grains en créant des défauts d'empilements pour finalement être absorbées par les joints de grains opposés [11, 12]. De plus, les simulations MD ont montré des activités significatives des joints de grains lors de la déformation des modèles atomistiques des matériaux nanocristallins. Ces activités sont accompagnées d'événements atomiques localisés sur les joints de grains (rebond/adsorption d'atomes sur les grains, migration des petits volumes vides sur les joints grains suite à des gradients de contrainte, et diffusion des lacunes) [13–15].

Dans ce contexte, nous avons utilisé des simulations MD pour étudier l'influence de la taille moyenne de grains sur les propriétés mécaniques du Cu FCC et du HCP α-Ti nanocristallins avec une taille de grain moyenne variant entre 9 et 24 nm générés par la méthode de fusion refroidissement pour le Cu et du 3 à 30 nm pour le α-Ti générés par la méthode de pavage de Voronoï . Dans cette gamme de taille de grains, une transition de l'effet Hall Petch à un effet Hall Petch inverse est attendue. De plus, les mécanismes de déformation de ces matériaux ont été analysés au niveau atomique.

2.1 Méthode

Après la génération des configurations atomiques, des essais de traction uniaxiale sont appliqués à ces échantillons dans la direction y et avec un taux de déformation $\dot{\varepsilon}_{yy} = 10^8\ s^{-1}$ à $300K$. Les composantes de la tenseur de contrainte suivant x et z sont maintenues nulle par un barostat de Nosé Hoover dans un ensemble NPT lors de la traction. Des conditions aux bords périodiques sont appliquées dans toutes les directions. Le pas du temps utilisé est 3 fs. La boite de simulation est allongée dans la direction y jusqu'à 26.2 % déformation réel qui correspond à 3 ns temps physique de simulation pour ce taux de déformation.

2.2 Réponse mécaniques

Les résultats des essais de traction appliqués aux échantillons du Cu quasi-2D générés avec la méthode de fusion-refroidissement sont présentés dans la Figure 2.1 (a) pour différentes tailles moyennes de grains. La contrainte augmente linéairement jusqu'à une contrainte seuil puis fluctue autour d'une valeur constante (la contrainte d'écoulement) avant que la rupture soit atteinte. Nous pouvons clairement voir dans la Figure la dépendance de la contrainte d'écoulement plastique en fonction de la taille moyenne de grains. De plus, un zoom sur les courbes de contrainte-déformation à 10 % est représentée dans la Figure 2.1 (b). La contrainte dans le régime élastique ou linéaire dépend clairement de la taille moyenne de grains.

Afin de comparer le comportement mécanique des matériaux nanocristallins FCC comme le Cu avec des matériaux nanocristallins HCP, nous avons également étudié l'influence de la taille moyenne de grains sur les propriétés mécaniques du α-Ti nanocristallin de géométrie hexagonale compacte. Les

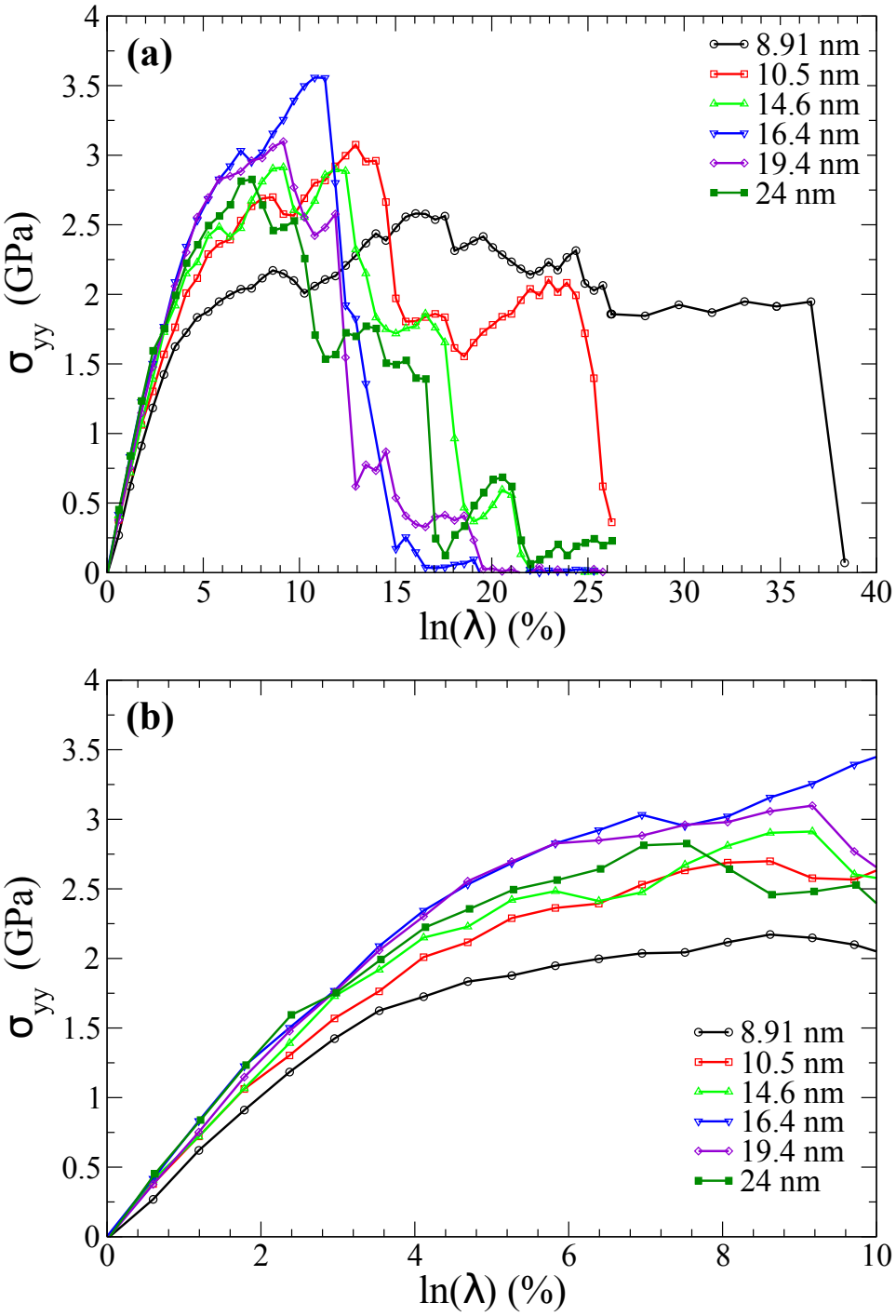

FIGURE 2.1: (a) Les courbes contraintes déformation des essais de tractions uniaxiaux appliqués au Cu nanocristallin pour différent tailles moyennes de grains.(b) un Zoom sur 10 % de ces courbes.

courbes de contrainte - déformation de Ti nanocristallin 3D sont présentées dans la Figure 2.2, avec une taille moyenne de grains variant de 3 nm à 30 nm. Nous remarquons la présence d'un pic (un "overshoot") dans les courbes de contrainte - déformation avant le régime d'écoulement plastique pour les tailles moyennes de grains supérieurs à 8 nm. La diminution de la contrainte avant l'écoulement plastique résulte de l'émission de dislocations partielles à partir des joints de grains et/ou de la nucléation de joints de macles sur les joints de grains et celles-ci traversent les grains jusqu'aux joints de grains opposés.

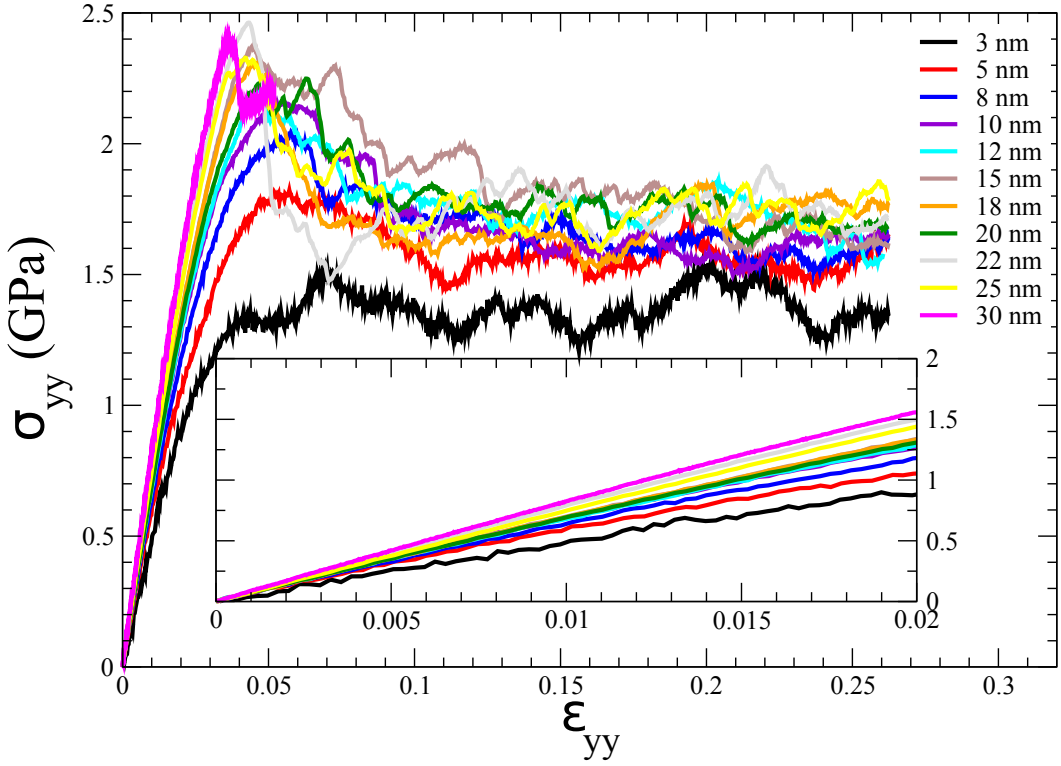

FIGURE 2.2: Courbes de contrainte-déformation pour le α-Ti nanocristallins 3D déformés à $\dot{\varepsilon} = 10^8 s^{-1}$. Un zoom à 2 % de déformation est présenté dans l'encart de la Figure.

Afin d'analyser l'effet de la taille moyenne de grains, nous avons calculé la limite élastique, la contrainte d'écoulement et le module de Young de ces nanocristaux. La limite élastique est définie comme la contrainte maximale atteinte dans le domaine élastique correspondant à des phénomènes essentiellement réversibles. La contrainte d'écoulement est définie comme la contrainte moyenne du plateau de la courbe contrainte-déformation.

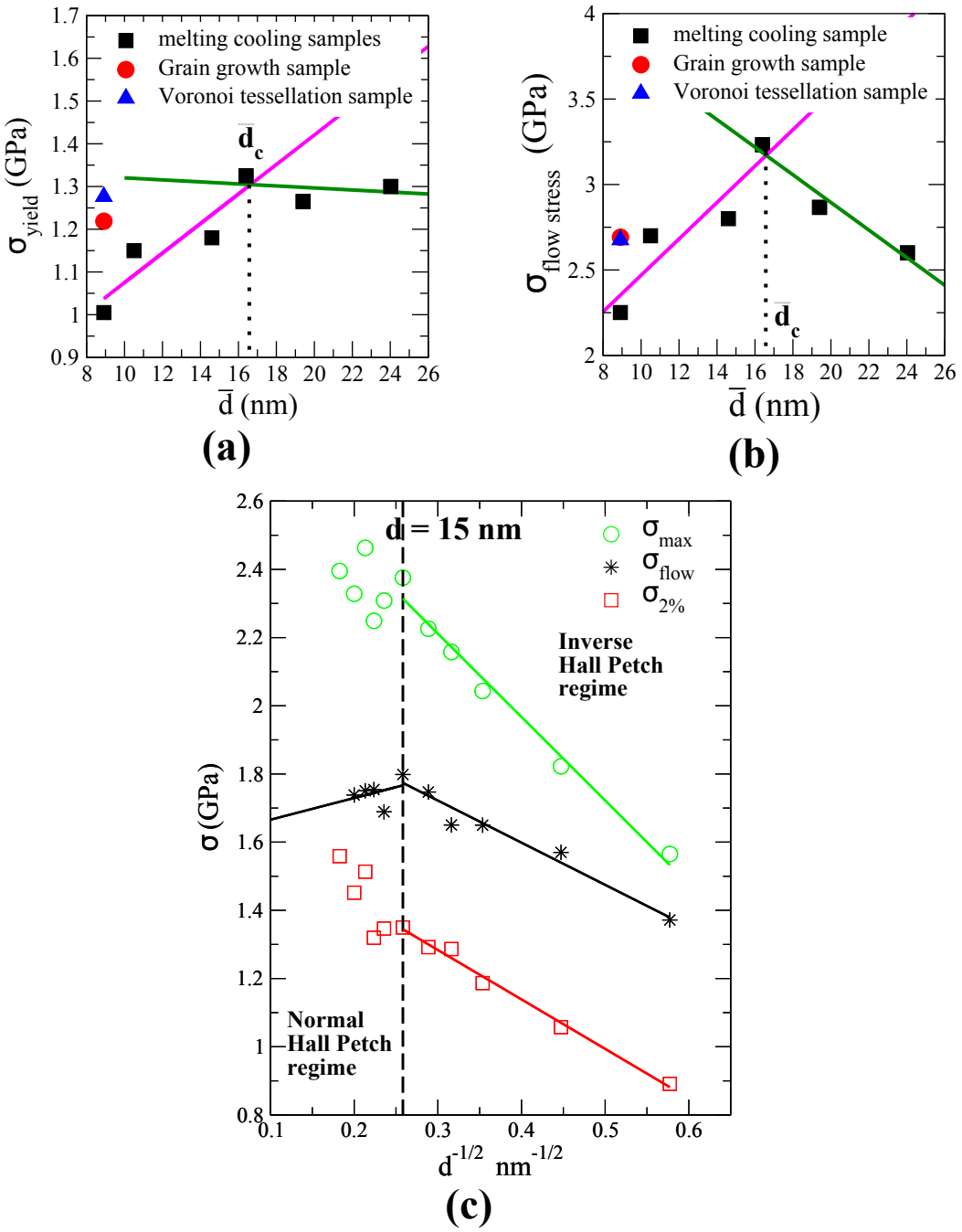

FIGURE 2.3: Effet de la taille moyenne de grains sur (a) la limite élastique ,(b) la contrainte d'écoulement du Cu nanocristallin et (c) Effet de la taille moyenne de grains sur la limite élastique, la contrainte d'écoulement et la contrainte maximale du α-Ti nanocristallins.

2.3 Inverse de la relation de Hall-Petch

Après la détermination du régime élastique, la variation de la limite élastique et la contrainte d'écoulement en fonction de la taille moyenne de grains est présentée dans la Figure 2.3. Les Figures 2.3 (a) et (b) présentent la variation de la limite élastique et la contrainte d'écoulement en fonction de $\overline{d}$ pour les échantillons de Cu quasi-2D nanocristallins. La limite élastique diminue avec la taille moyenne de grains en dessous de d = 16 nm. Cette tendance indique donc bien un effet Hall-Petch inversé. Les Figures 2.3 (a) et (b) indiquent également la présence de deux régimes principaux, un premier confirmant la tendance de Hall-Petch pour $d \geqslant 16$ nm. Dans ce cas, la limite élastique et la contrainte d'écoulement diminuent avec l'augmentation de la taille moyenne de grains alors que l'on observe l'inverse pour $d < 16$ nm. Les valeurs obtenues sont en bon accord avec la littérature [16, 17].

Afin de trouver la taille moyenne de grain critique pour le Ti nanocristallin, nous traçons nos résultats sur un graphe adapté avec une contrainte d'écoulement calculée comme la contrainte moyenne au-dessus de 10%, tracée en fonction de $d^{-1/2}$ (Figure 2.3 (c)). On y remarque une transition de Hall Petch vers Hall Petch inverse à une taille moyenne de grain de 15 nm. De plus, en dessous de 15 nm, la contrainte maximale et la limite élastique présentent également une tendance de Hall-Petch inversé. Cette tendance est illustrée par la diminution de la contrainte avec la taille moyenne de grains.

La taille moyenne de grains critique du Ti est proche de celle du Cu nanocristallin. Comme signalé plus haut, cette transition est due à un changement du mécanisme de déformation dominant avec un passage progressif d'effets dus à des dislocations et des maclages vers des processus inter-granulaires. Du point de vue macroscopique, les courbes contrainte-déformation (Figure 2.2) signalent que le maximum avant l'écoulement plastique commence à diminuer pour une taille moyenne de grains inférieure à 15 nm afin de finalement disparaître aux deux dernières taille moyenne de grains. Par conséquent, une transition nette du comportement de déformation à des processus inter-granulaires est mise en évidence avec la diminution de la taille moyenne de grains. Les pentes de Hall Petch et inverse Hall Petch pour le Ti nanocristallin sont de 0.64 et 1.24 MPa $mm^{0,5}$.

2.4 Module de Young

Le module de Young (E) est défini par la pente de la courbe contrainte-déformation dans le domaine élastique. Nous avons déterminé E en faisant une régression de la courbe contrainte déformation tenant en compte les données pour $ln(\lambda) < 0.5\%$ pour assurer la présence dans le régime linéaire. La Figure 2.4 (a) présente les valeurs obtenues pour les différents tailles moyennes de grains considérées. Les valeurs du module de Young varient de 53 GPa pour une taille moyenne de grains de 9.0 nm à 79 GPa pour une taille de grain moyenne de 36 nm. La densité relative varie de 97.9 % à 98.4 % pour ces échantillons de Cu.

L'encart de la Figure 2.2 montre un zoom sur les courbes de contrainte déformation à 2%. La dépendance du module de Young à la taille moyenne de grains est claire. Le module de Young augmente avec la taille moyenne de grains. Comme dans le cas du Cu nanocristallin, la diminution de la taille moyenne de grains conduit à l'augmentation de la fraction des joints de grains. Par conséquent, la densité relative du système diminue et par suite le module de Young. La Figure 2.4 (b) présente les valeurs mesurées pour le module de Young en fonction de la taille moyenne de grains pour le α-Ti nanocristallin. Le module de Young est calculé des données des courbes de contrainte déformation pour des déformations inférieures à 0,5 %, 1 % et 1,5 % et les résultats sont très cohérents. Le module de Young effectif varie de 50 GPa à 80 GPa pour notre gamme de taille moyenne de grain. Les valeurs de la densité relative varient de 97,18 % à 99,91 % à cette plage de taille moyenne de grains. Les valeurs typiques du module de Young pour le Ti pur à température ambiante sont de l'ordre de 100 à 110 GPa [18]. Cependant, un module de Young de 85 GPa à $25°C$ $(298K)$ est prévu à partir de l'équation suivante [18]:

$$E(GPa) = 104.5 - 0.0645T \tag{2.1}$$

où T est la température (K). Cette équation est valide pour un Ti pur $(99,9\%)$ à une température inférieure à $500K$.

En fait, les atomes dans les joints de grains ont une plus grande énergie potentielle que ceux à l'intérieur des grains à cause de la faible densité des atomes sur les joints de grains. Donc, ils sont plus faciles à déplacer lorsqu'une

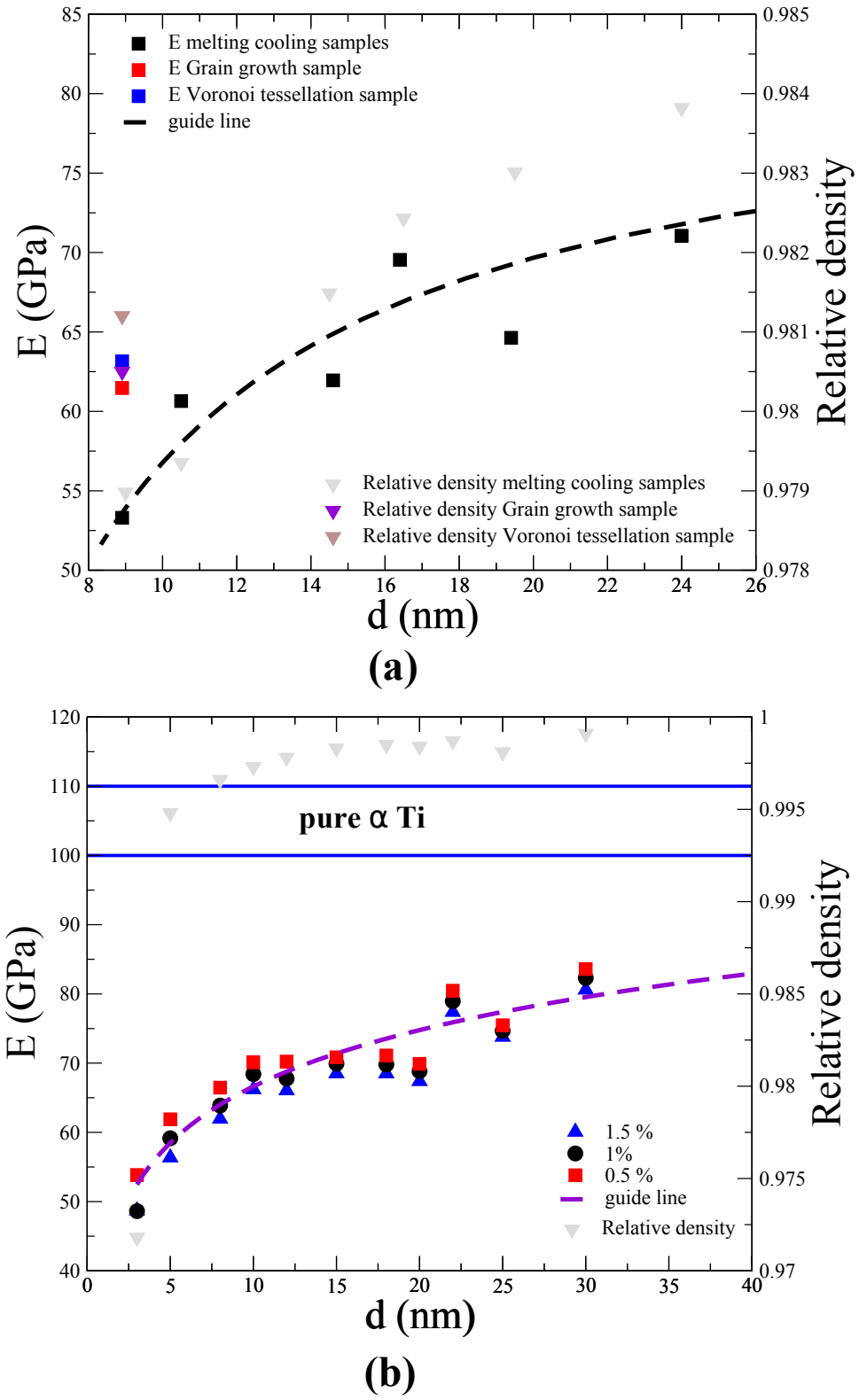

FIGURE 2.4: Variation du module de Young et de la densité relative en fonction de la taille moyenne de grains : (a) Pour le Cu quasi-2D nanocristallin et (b) pour le α Ti nanocristallin.

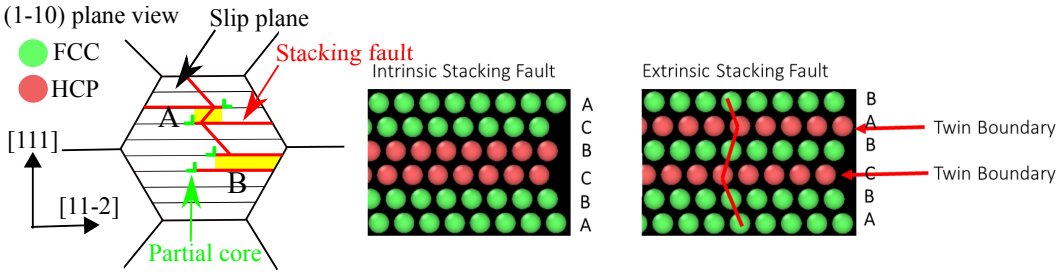

FIGURE 2.5: Schéma de la formation des défauts d'empilements intrinsèque et extrinsèque par la propagation des dislocations partielles de Shockley.

charge externe est appliquée. Ceci implique que leur contribution à la résistance élastique est réduite par rapport aux atomes de l'intérieur de grains. Les résultats de calcul de la densité relative sont très compatibles avec les échantillons préparés par condensation de gaz suivi de compactage à chaud [4].

2.5 Mécanismes de déformation

L'analyse des configurations atomiques permet d'identifier plus précisément comment chaque mécanisme de déformation se manifeste au niveau atomique. Une série des configurations instantanée ont été analysées à différents niveaux de déformation (par exemple le calcul de la déformation atomique de Von Mises, l'analyse de la structure locale). Les mécanismes suivants ont été observés pour les matériaux nanocristallins :

- **Mécanisme 1**: L'émission de dislocations partielles de Shockley à partir des joints de grains qui traversent les grains afin d'être finalement absorbés par les joints de grains opposés. Lors de la propagation de ces dislocations, des plans de défauts d'empilements sont générés.

- **Mécanisme 2**: Les joints de macles ont été largement observés au cours de la déformation de ces échantillons nanocristallins. Comme les dislocations partielles, le mécanisme de maclage observé pour le FCC Cu nanocristallin est différent de celui du HCP α-Ti.

  Pour le FCC Cu nanocristallin, le chevauchement des 2 rubans de défauts d'empilements générés par deux dislocations partielles de type Shockley glissants sur des plans adjacents est la source de création d'un nouveau défaut d'empilement nommé extrinsèque ou micro-macle (Figure 2.5). Ces micro-macles sont issues de deux processus différents illustrés dans

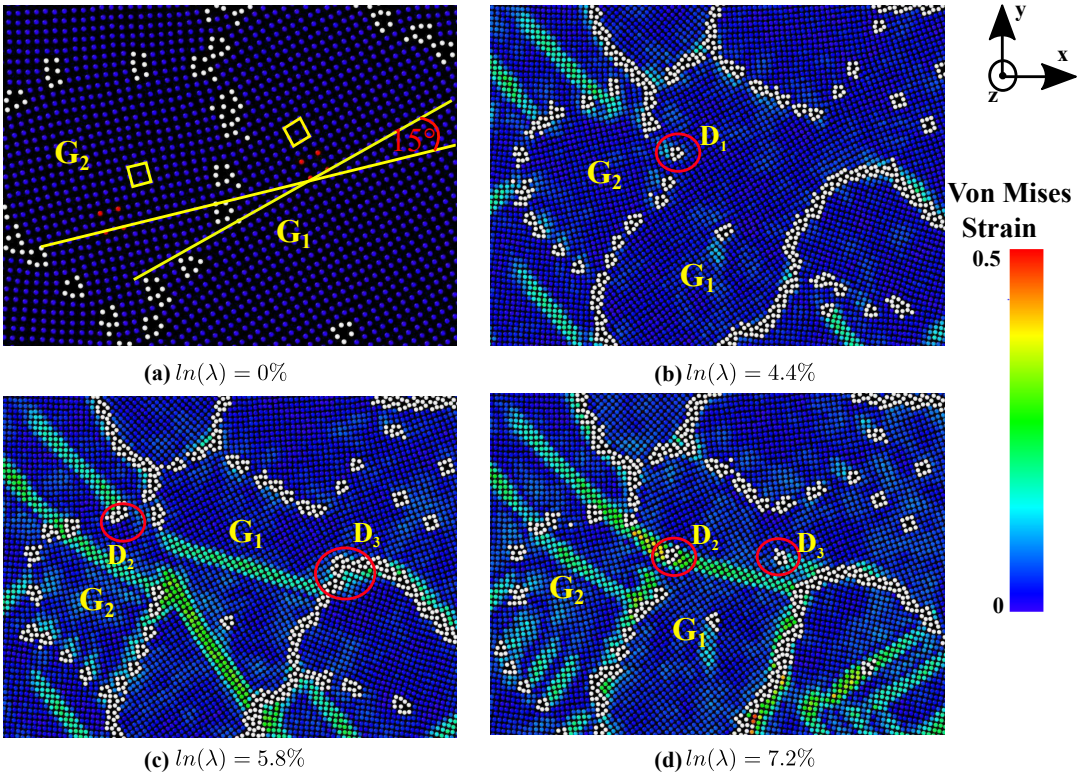

(a) $ln(\lambda) = 0\%$ **(b)** $ln(\lambda) = 4.4\%$

(c) $ln(\lambda) = 5.8\%$ **(d)** $ln(\lambda) = 7.2\%$

FIGURE 2.6: Un zoom sur deux grains à l'intérieur de l'échantillon de Cu nanocristallin quasi-2D avec une taille moyenne de grains de 9 nm dans différentes régions de la boîte de simulation et avec différentes déformations. L'angle de désorientation entre les deux grains est faible (15°). La configuration atomique est colorée suivant la valeur de la déformation atomique de Von Mises calculée par rapport à la configuration initiale. Les défauts à l'intérieur de la nanostructure sont marquées en blanc et superposés à la cartographie atomique de la déformation de Von Mises.

la Figure 2.5. Les défauts d'empilements extrinsèques peuvent être formés par le chevauchement des rubans de type A ou de type B (voir figure). La zone commune où les deux peuvent coexister est illustrée dans la Figure. Une symétrie miroir est créée entre la matrice et la zone maclée. Ce mécanisme a été prédit dans la littérature et semble être typique des déformations plastiques élevées.

Cependant, pour le α-Ti, les joints de grains sont considérés comme la source des joints de macles. Les joints de macles sont nucléés à partir des joints de grains, puis traversent les grains pour enfin disparaître aux joints opposés. La propagation de ces joints change l'orientation des grains.

- **Mechanism 3**: Les dislocations émises par des joints de grains à faible angle de désorientation entraînent un glissement à l'intérieur du grain

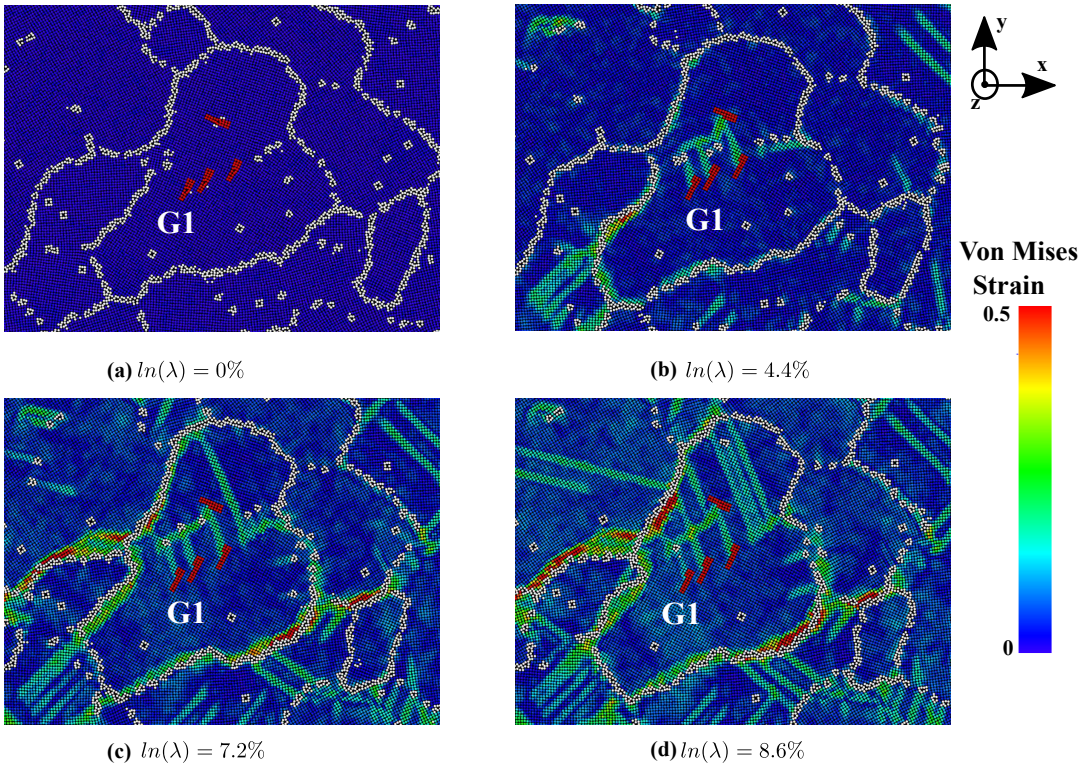

(a) $ln(\lambda) = 0\%$ **(b)** $ln(\lambda) = 4.4\%$

(c) $ln(\lambda) = 7.2\%$ **(d)** $ln(\lambda) = 8.6\%$

FIGURE 2.7: Évolution d'un grain G1 dans l'échantillon de Cu nanocristallin quasi-2D (taille moyenne de grain de 9 nm) colorée par la valeur de la déformation atomique de Von Mises calculée par rapport à la configuration initiale. Les joints de grains et les défauts sont sélectionnés par l'analyse de la structure local de chaque atome et colorés en blanc. Certaines des dislocations coins initiales sont marquées par du rouge à l'intérieur du grain.

jusqu'au joint de grains opposé (Figure 2.6). Ces dislocations se propagent sur les plans {110} et conduisent à une coalescence des deux grains.

- **Mécanisme 4**: Les dislocations émises depuis l'intérieur du grain, précisément à partir des dislocations coins présentes à l'intérieur du grain, induisent un glissement jusqu'au joints de grains adjacents. La Figure 2.7 présente l'évolution d'un grain dans l'échantillon quasi-2D. En comparant l'évolution du grain, nous observons que lorsque la contrainte de cisaillement résolue à l'intérieur du grain (projection sur l'orientation cristallographique du grain) atteint le seuil critique nécessaire pour déplacer ces dislocations, elles se propagent en générant des plans de glissement avec une grande valeur de déformation de Von Mises. Le vecteur de Burger de ces dislocations est $\frac{1}{2}\langle 110\rangle$ sur les plans de glissement {110}.

Nos simulations révèlent également des processus inter-granulaires abondants impliquant l'interaction entre les dislocations et les joints de grains et des

mécanismes associés à ces défauts tels que le glissement d'un joint de grains et la migration d'un joint de grain ou d'un joint triple.

2.6 Conclusion

Des simulations de dynamique moléculaire ont été utilisées pour étudier le comportement mécanique de Cu et de α-Ti nanocristallins. Une nouvelle méthode de fusion refroidissement a été développée pour produire des échantillons de Cu nanocristallins avec des défauts plus réalistes à l'intérieur des grains et des joints de grains courbés. Afin d'étudier les mécanismes de déformation de Cu, deux types d'échantillons ont été étudiés : des échantillons 3D colonnaires et des quasi 2D, avec une taille de grain moyenne entre 9 et 24 nm. Nous avons trouvé un diamètre critique de 16 nm en dessous de laquelle la relation de Hall Petch n'est plus applicable pour le Cu et un diamètre critique de 15 nm pour le α-Ti.

Une combinaison d'activités des joints de grains (rebond/adsorption d'atomes su les grains, migrations des joints de grains et des joints triples, coalescence de grains) et de mécanismes de dislocations contrôlent le comportement mécanique de ces échantillons. De plus, nous avons trouvé un nouveau mécanisme de déformation illustré par l'émission de dislocations coins présentes à l'intérieur des grains suite au processus de refroidissement. Lorsque ces dislocations se propagent, elles génèrent des bandes de cisaillement à l'intérieur du grain et par conséquent relaxent la contrainte du système. De plus, on voit que ces dislocations se propagent sur des plans {110}.

Chapter 3

Effet du taux de déformation sur le comportement mécanique du Cu nanocristallin

Dans ce chapitre, des simulations MD ont été réalisées pour étudier l'effet de la vitesse de déformation sur le comportement mécanique de deux systèmes Cu nanocristallins générés par fusion refroidissement, un quasi-2D et un 3D colonnaire, les deux systèmes ayant une taille moyenne des grains de 9 nm. Une série d'essais de traction uniaxiale a été appliquée à ces systèmes avec un taux de déformation variant entre 10^4 à $10^9 s^{-1}$ pour le système quasi-2D et de 10^7 à $10^{10} s^{-1}$ pour le système colonnaire 3D suite à des limitations du temps de calcul. Il est à noter que le taux de déformation minimal est inférieur de trois ordres de grandeur à celui utilisés habituellement dans les études de MD. Les configurations atomiques déformées extraites du régime élastique et plastique ont ensuite été soumises à des essais de relaxation de contrainte pendant 2 ns. L'évolution dans le temps de la contrainte est étudiée lors de la relaxation. De plus la dépendance du taux de déformation de la réponse contrainte/déformation est discutée en termes de mécanismes de déformation observés au niveau atomique.

3.1 méthode

Des simulations MD d'essais de traction uniaxiale dans la direction y ont été appliquées à deux modèles nanocristallins : un échantillon quasi-2D et un échantillon 3D colonnaire générés par la méthode de fusion refroidissement ayant $\bar{d} = 9nm$ à $T = 300K$. Le potentiel interatomique utilisé est celle développée par Foiles *et al* [2]. Il est également important de souligner qu'en raison de la limitation de la puissance de calcul, afin d'atteindre une déformation de $\varepsilon = 0.9\%$, les temps de simulation physique t_{exp} vont par exemple de 900 ns à 9

ps pour 10^4 à $10^9 s^{-1}$, respectivement. Les composants du tenseur de contraintes dans les directions x et z ont été mises à zéro pendant le chargement. Le pas de temps utilisé dans les simulations est 3 ~ fs. Les conditions aux bords sont périodiques dans toutes les directions. Une déformation logarithmique a été calculée dans la direction de la traction pendant l'essai. Le tenseur de contraintes moyen a été calculé en utilisant le théorème du viriel.

3.2 Résultats

3.2.1 Réponse mécaniques à différents taux de déformations

Les résultats des essais de traction uniaxiale appliqués sur les modèles nanocristallins sont présentés dans la Figure 3.1. Pour le modèle quasi-2D (Figure 3.1(a)), la contrainte augmente avec la déformation pour atteindre un seuil puis fluctue autour d'une valeur constante (la contrainte d'écoulement). Pour le modèle 3D en colonne, la courbe contrainte déformation présente un maximum avant le début du régime d'écoulement plastique à des taux de déformations élevés.

Nous remarquons quatre caractéristiques dans la réponse mécanique en fonction du taux de déformation (Figure3.1):

1. L'augmentation de la contrainte d'écoulement avec le taux de déformation.

2. La présence de changements brusques de contrainte (des sauts) dans le régime d'écoulement plastique à faible vitesse de déformation, en particulier dans l'échantillon quasi-2D.

3. Le maximum dans la courbe de l'échantillon 3D colonnaire avant le régime d'écoulement plastique à des taux de déformations élevés.

4. La dépendance du module de Young au taux de déformation indiquant le caractère non-équilibré des systèmes.

La mobilité des dislocations contrôle la réponse mécanique macroscopique de la contrainte à l'augmentation de la déformation appliquée aux matériaux. Par conséquent, nous avons quantifié la variation des densités de dislocations dans les deux modèles de Cu nanocristallin. Cette quantification permet

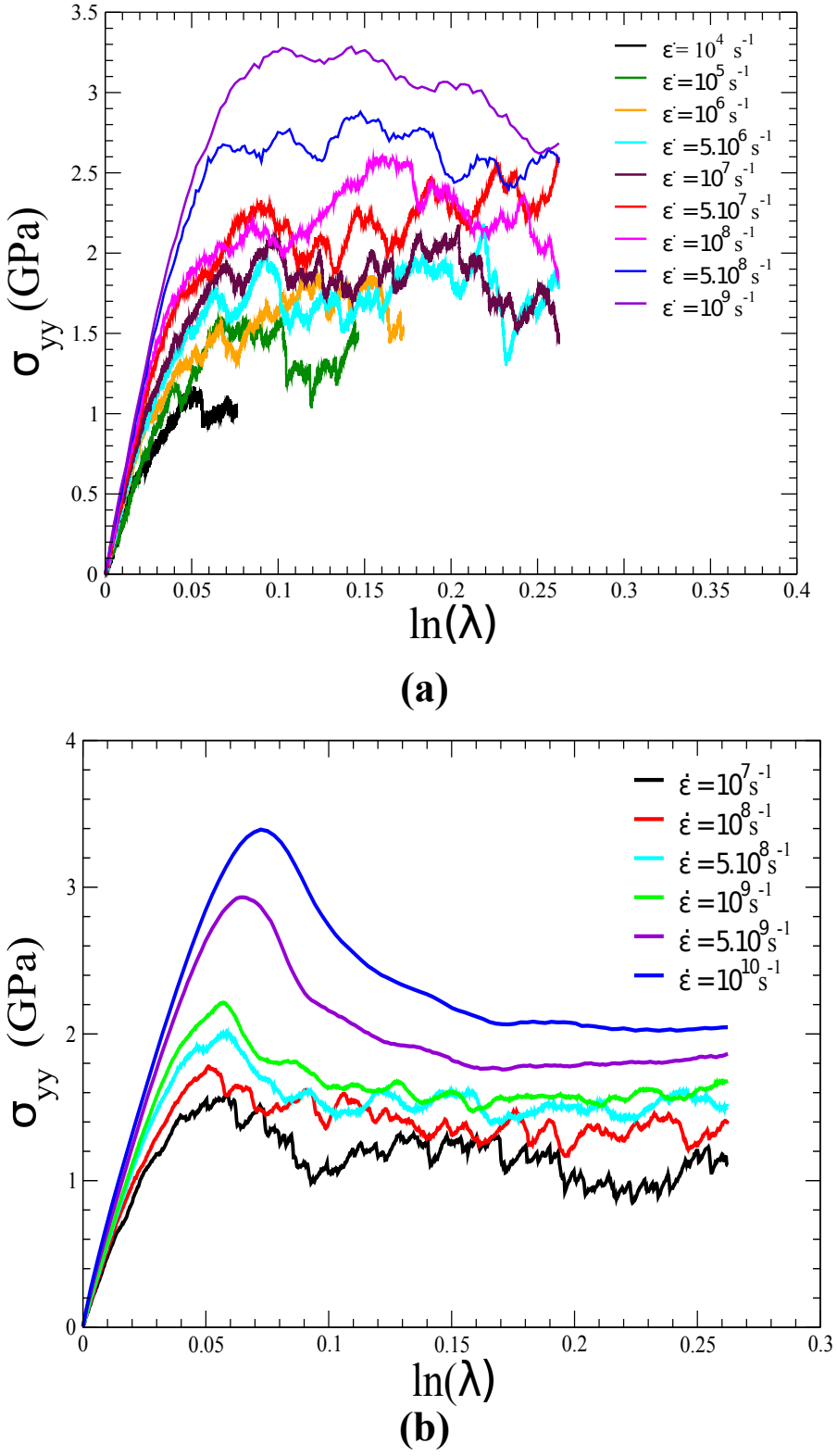

FIGURE 3.1: Variation de la contrainte en fonction de la déformation à différent taux de déformation pour: (a) un quasi-2D Cu avec 9 nm taille moyenne de grains, (b) un 3D colonnaire avec 9 nm taille moyenne de grains.

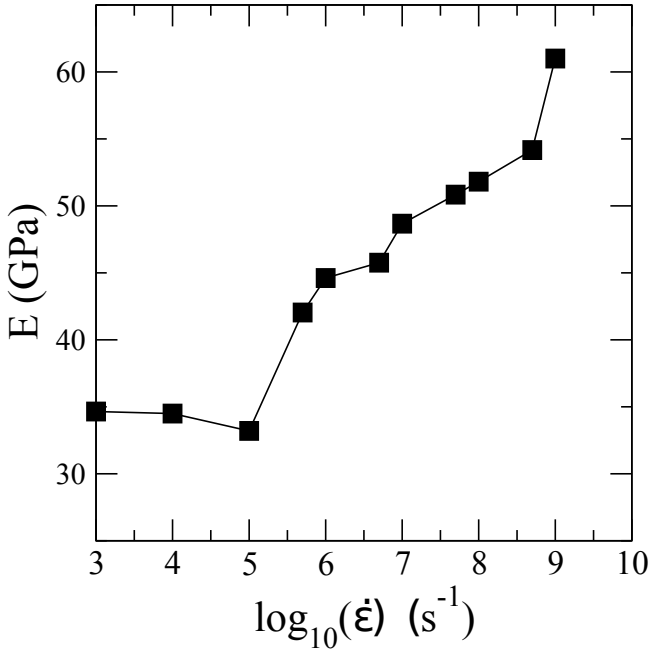

FIGURE 3.2: Variation du module de Young avec le aux de déformation pour l'échantillon quasi-2D de taille moyenne de grains de 9 nm.

de comprendre les trois premières caractéristiques ci-dessus. Dans les deux modèles nanocristallins, nous avons constaté que l'augmentation du taux de déformation entraîne un retard de la nucléation et de la propagation des dislocations. Cela conduit à l'augmentation de la contrainte d'écoulement avec le taux de déformation.

La réponse élastique de ces échantillons présente également une dépendance du taux de déformation. Ceci indique l'apparition des événements irréversibles locaux même dans le régime élastique (linéaire). Les valeurs du module de Young calculées sont présentées dans la Figure 2.4. Un seuil est mis en évidence dans la Figure à $\dot{\varepsilon}_c \simeq 5\times10^5$ s^{-1}. Pour les valeurs de $\dot{\varepsilon}$ inférieures à $\dot{\varepsilon}_c$, E reste constant et ne dépend pas de $\dot{\varepsilon}$. Ceci est également une indication que pour $\dot{\varepsilon} < \dot{\varepsilon}_c$, le système présente un comportement newtonien c'est-à-dire que ses propriétés mécaniques ne dépendent pas du taux de déformation.

3.2.2 Évidence d'une relaxation vitreuse

Pour étudier l'équilibre du système après la déformation, nous avons calculé la relaxation de la contrainte dans l'ensemble NVT pendant 2 ns en partant des configurations initiales déformées à ($ln(\lambda)$ = 0.9 % et 3 %) à chaque taux de déformation $\dot{\varepsilon}$. Ensuite l'évolution de la contrainte $\sigma(t) = \sigma_{yy}(t)$ a été suivie en

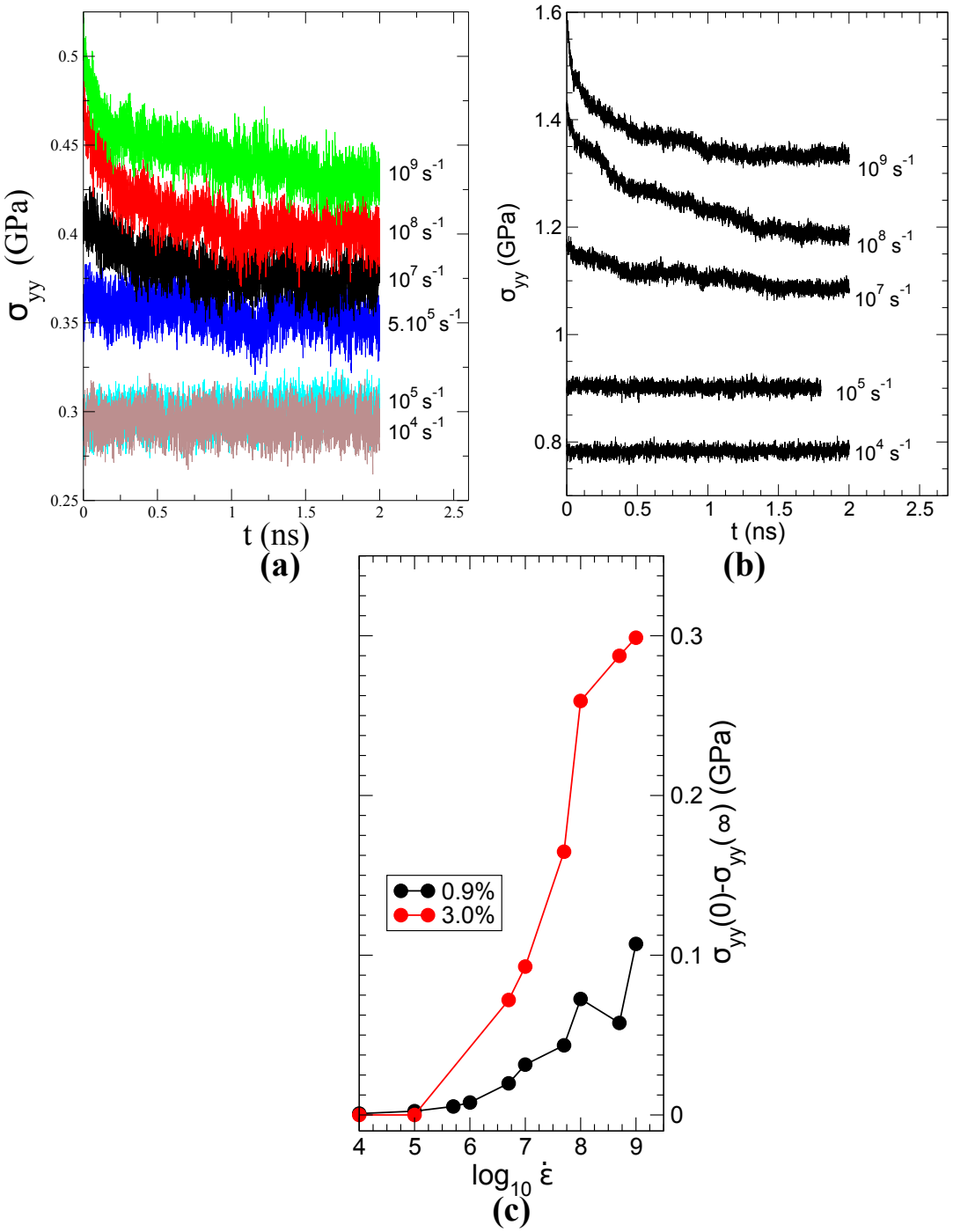

FIGURE 3.3: les courbes de relaxation de la contrainte $\sigma(t)$ en fonction du temps pour des échantillons initiaux de (a) $ln(\lambda)$=0.9% et (b) $ln(\lambda)$=3% pour différents taux de déformations $\dot{\varepsilon}$, (c) Évolution de $\sigma(0) - \sigma(\infty)$ en fonction du taux de déformation $\dot{\varepsilon}$

fonction du temps, le tenseur de déformation de la configuration étant maintenu constant pendant la relaxation.

La Figure 3.3 (a) et (b) présente les courbes de l'évolution de la contrainte pour différents taux de déformation $\dot{\varepsilon}$. À faible $\dot{\varepsilon}$, il n'y a presque pas d'évolution de la contrainte avec le temps ce qui signale de faibles effets viscoélastiques. Pour les taux de déformation $\dot{\varepsilon} \geqslant 5.10^5 s^{-1}$, $sigma_{yy}$ diminue avec le temps jusqu'à atteindre une asymptote horizontale $\sigma(\infty)$. Ceci indique que pour de tels taux de déformation, le système n'est pas relaxé complètement durant la traction. En d'autres termes, la déformation de l'échantillon est très rapide par rapport à l'échelle temporelle des mécanismes de relaxation locaux dans l'échantillon. La différence $\sigma(0) - \sigma(\infty)$ est présentée dans la Figure 3.3 (c) et l'on voit clairement que la valeur seuil $\dot{\varepsilon}_c$ précisée pour le module de Young est proche de celle déterminée à partir de l'évolution de $\sigma(0) - \sigma(\infty)$ (Figure 3.3 (c)).

3.2.3 Sensibilité de la contrainte d'écoulement au taux de déformation

La Figure 3.4 (a) montre en représentation log-log la contrainte d'écoulement σ_f en fonction du taux de déformation $\dot{\varepsilon}$ pour les échantillons quasi-2D et 3D colonnaire. Comme indiquée ci-dessus, la contrainte d'écoulement augmente avec l'augmentation du taux de déformation. La sensibilité au taux de déformation de la contrainte d'écoulement peut être calculée à partir de la pente de cette courbe log-log. une pente $m = 0,085$ et $m = 0,09$ pour l'échantillon quasi-2D et l'échantillon 3D colonnaire respectivement.

Ces résultats sont en accord avec les valeurs expérimentales de m pour le cuivre nanocristallin ayant une taille de grain moyenne autour de 9 nm. Chen *et al* ont trouvé $m = 0.06 \pm 0.01$ pour un échantillon de taille moyenne de grain de 10 nm mesuré par des essais de nanoindentation, une valeur proche de nos résultats (Figure 3.4 (b)). Pour cette taille moyenne de grain, une combinaison entre les dislocations et des processus sur les joints de grains dominent la déformation plastique. Les valeurs obtenues pour m sont inférieures à celles proposées par des techniques expérimentales (Lifshitz creep [26] et et Rachinger GB sliding [27]) même dans le cas d'un échantillon quasi-2D où l'énergie d'activation de la diffusion sur les joints de grains est faible à cause de l'épaisseur réduite de la boîte de simulation.

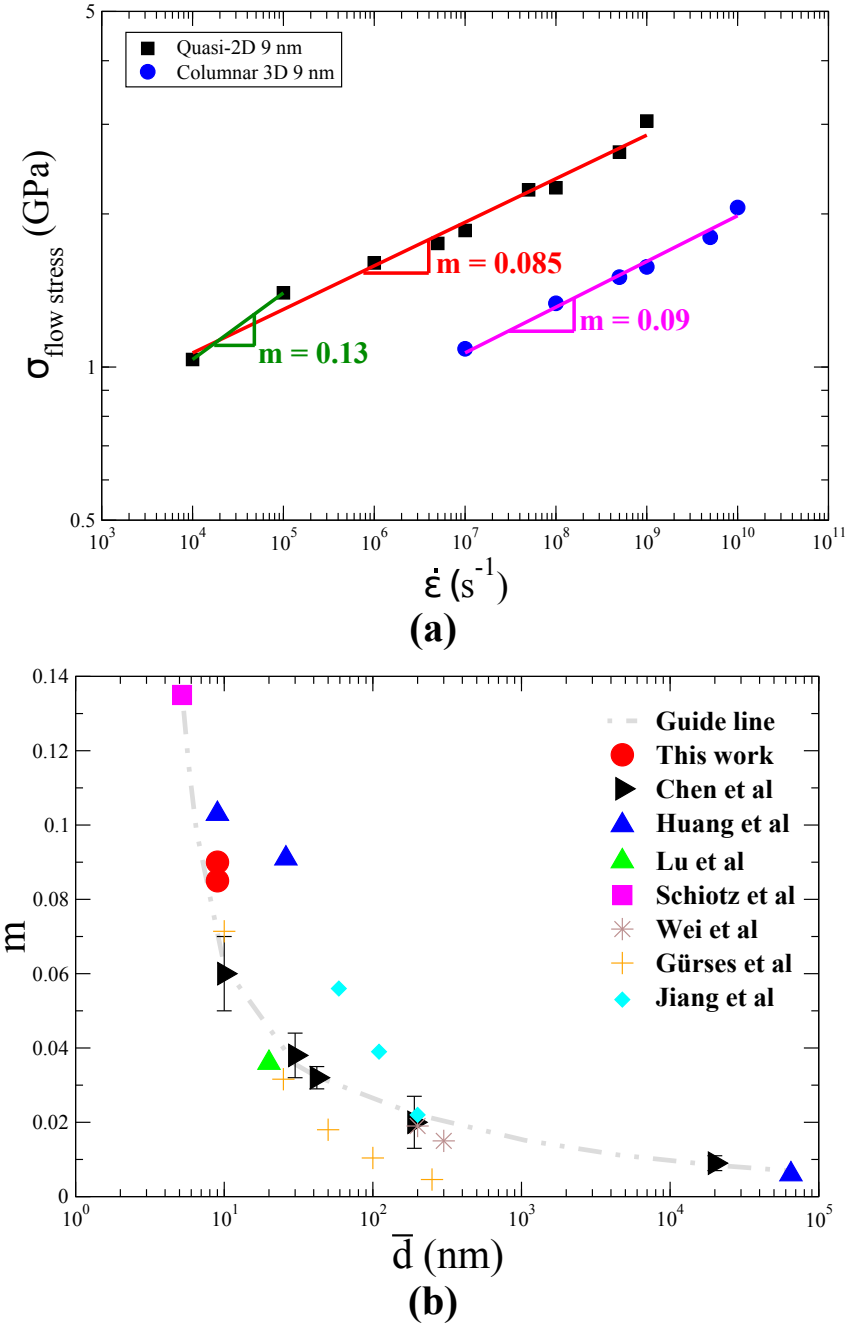

FIGURE 3.4: Représentation log-log de la contrainte d'écoulement σ_f en fonction du taux de déformation $\dot{\varepsilon}$ pour les échantillons quasi-2D et 3D colonnaire avec $\bar{d}$=9 nm. la sensibilité au taux de déformation (m) est la pente de cette courbe log-log, (b) Variation de m en fonction de la taille moyenne de grains $\bar{d}$ pour le cuivre nanocristallin, nos valeurs sont comparés avec ceux des études éxperimentales : Chen et al. [19], Schiøtz et al. [20], Huang et al. [21], Wei et al. [22], Lu et al. [23], Gurses et al. [24], Jiang et al [25].

3.3 Conclusion

Des simulations MD ont été réalisées pour étudier l'effet du taux de déformation sur la déformation plastique de deux modèles de Cu nanocristallins, un quasi-2D et un 3D colonnaire. Une série d'essais de traction uniaxiale est appliquée sur ces modèles à une vitesse de déformation variant de 10^4 à 10^9 s^{-1} pour l'échantillon quasi-2D et de 10^7 à 10^{10} s^{-1} pour le 3D colonnaire. la relaxation de la contrainte est ensuite analysée sur ces échantillons en régime élastique et plastique. Les résultats suivants ont été trouvés :

- Lors de la déformation des modèles de Cu nanocristallins à $\dot{\varepsilon} \geqslant 5.10^5$, nous avons trouvés que ces systèmes ne sont pas capables de relaxer la contrainte imposée à l'échelle de l'expérience numérique aux taux de déformation élevés. Par conséquent, ces systèmes ne sont pas équilibrés lors de la déformation.

- La relaxation de la contrainte suit un modèle d'exponentiel étiré typique de la relaxation de liquides surfondus et des verres avec des valeurs de β plus petit que 1, particulièrement à des taux de déformations élevés.

- Les mécanismes de déformations inter-granulaires sont promus en réduisant le taux de déformation, notamment les migrations de joints de grains et des jonctions triples et la croissance des grains. Cela est validé par l'augmentation de la sensibilité au taux de déformation du Cu nanocristallin par rapport au Cu microcristallin.

- L'augmentation du taux de déformation augmente le désordre du système et retarde la nucléation et la propagation des dislocations, ce qui entraîne une augmentation de la contrainte d'écoulement.

- La contribution du maclage à la plasticité augmente avec le taux de déformation. Une transition du mécanisme de déformation des dislocations au maclage est prévue avec l'augmentation du taux de déformation.

Bibliography

[1] Pierre Hirel. “Atomsk: a tool for manipulating and converting atomic data files”. In: *Computer Physics Communications* 197 (2015), pp. 212–219.

[2] SM Foiles, MI Baskes, and Murray S Daw. “Embedded-atom-method functions for the fcc metals Cu, Ag, Au, Ni, Pd, Pt, and their alloys”. In: *Physical review B* 33.12 (1986), p. 7983.

[3] AH Chokshi et al. “On the validity of the Hall-Petch relationship in nanocrystalline materials”. In: *Scripta Metallurgica* 23.10 (1989), pp. 1679–1683.

[4] Paul G Sanders, JA Eastman, and JR Weertman. “Elastic and tensile behavior of nanocrystalline copper and palladium”. In: *Acta materialia* 45.10 (1997), pp. 4019–4025.

[5] RA Masumura, PM Hazzledine, and CS Pande. “Yield stress of fine grained materials”. In: *Acta Materialia* 46.13 (1998), pp. 4527–4534.

[6] CA Schuh, TG Nieh, and T Yamasaki. “Hall–Petch breakdown manifested in abrasive wear resistance of nanocrystalline nickel”. In: *Scripta Materialia* 46.10 (2002), pp. 735–740.

[7] GE Fougere et al. “Grain-size dependent hardening and softening of nanocrystalline Cu and Pd”. In: *Scripta metallurgica et materialia* 26.12 (1992), pp. 1879–1883.

[8] Jakob Schiøtz and Karsten W Jacobsen. “A maximum in the strength of nanocrystalline copper”. In: *Science* 301.5638 (2003), pp. 1357–1359.

[9] Tomotsugu Shimokawa, A Nakatani, and H Kitagawa. “Grain-size dependence of the relationship between intergranular and intragranular deformation of nanocrystalline Al by molecular dynamics simulations”. In: *Physical Review B* 71.22 (2005), p. 224110.

[10] V Yamakov et al. “Deformation mechanism crossover and mechanical behaviour in nanocrystalline materials”. In: *Philosophical Magazine Letters* 83.6 (2003), pp. 385–393.

[11] H Van Swygenhoven, PM Derlet, and AG Frøseth. “Nucleation and propagation of dislocations in nanocrystalline fcc metals”. In: *Acta Materialia* 54.7 (2006), pp. 1975–1983.

[12] V Yamakov et al. “Dislocation–dislocation and dislocation–twin reactions in nanocrystalline Al by molecular dynamics simulation”. In: *Acta materialia* 51.14 (2003), pp. 4135–4147.

[13] H Van Swygenhoven and PM Derlet. “Grain-boundary sliding in nanocrystalline fcc metals”. In: *Physical Review B* 64.22 (2001), p. 224105.

[14] John W Cahn, Yuri Mishin, and Akira Suzuki. “Coupling grain boundary motion to shear deformation”. In: *Acta materialia* 54.19 (2006), pp. 4953–4975.

[15] Diana Farkas, Anders Frøseth, and Helena Van Swygenhoven. “Grain boundary migration during room temperature deformation of nanocrystalline Ni”. In: *Scripta Materialia* 55.8 (2006), pp. 695–698.

[16] Kai Zhou et al. “Effects of grain size and shape on mechanical properties of nanocrystalline copper investigated by molecular dynamics”. In: *Materials Science and Engineering: A* 615 (2014), pp. 92–97.

[17] Jakob Schiøtz et al. “Atomic-scale simulations of the mechanical deformation of nanocrystalline metals”. In: *Physical Review B* 60.17 (1999), p. 11971.

[18] Gerhard Welsch, Rodney Boyer, and EW Collings. *Materials properties handbook: titanium alloys*. ASM international, 1993.

[19] J Chen, L Lu, and K Lu. “Hardness and strain rate sensitivity of nanocrystalline Cu”. In: *Scripta Materialia* 54.11 (2006), pp. 1913–1918.

[20] Jakob Schiøtz, Francesco D Di Tolla, and Karsten W Jacobsen. “Softening of nanocrystalline metals at very small grain sizes”. In: *Nature* 391.6667 (1998), p. 561.

[21] P Huang et al. “Dependence of strain rate sensitivity upon deformed microstructures in nanocrystalline Cu”. In: *Acta Materialia* 58.15 (2010), pp. 5196–5205.

[22] Q Wei et al. “Effect of nanocrystalline and ultrafine grain sizes on the strain rate sensitivity and activation volume: fcc versus bcc metals”. In: *Materials Science and Engineering: A* 381.1-2 (2004), pp. 71–79.

[23] L Lu, SX Li, and K Lu. “An abnormal strain rate effect on tensile behavior in nanocrystalline copper”. In: *Scripta Materialia* 45.10 (2001), pp. 1163–1169.

[24] Ercan Gürses and Tamer El Sayed. “Constitutive modeling of strain rate effects in nanocrystalline and ultrafine grained polycrystals”. In: *International Journal of Solids and Structures* 48.10 (2011), pp. 1610–1616.

[25] Yue Jiang et al. “Strain rate dependence of tensile strength and ductility of nano and ultrafine grained coppers”. In: *Materials Science and Engineering: A* 712 (2018), pp. 341–349.

[26] RL Coble. “A model for boundary diffusion controlled creep in polycrystalline materials”. In: *Journal of applied physics* 34.6 (1963), pp. 1679–1682.

[27] Heinz Lüthy, Richard A White, and Oleg D Sherby. “Grain boundary sliding and deformation mechanism maps”. In: *Materials Science and Engineering* 39.2 (1979), pp. 211–216.

Ali RIDA

Doctorat : Matériaux, Mécanique, Optique, Nanotechnologie

Année 2018

Etude des propriétés mécaniques des matériaux métalliques nanocristallins par des simulations de dynamique moléculaire

Le SMAT est un procédé de traitement de surface répandu dans le domaine industriel. Ce procédé est capable de nanocristalliser la surface de pièces traitées et produit ainsi un durcissement local de la surface toute en conservant la ductilité du cœur du matériau. Dans ce contexte, la caractérisation des mécanismes de déformations à différentes échelles (du micron au nanomètre) est indispensable afin de créer des modèles constitutifs permettant de décrire précisément le comportement mécanique des pièces traitées.

Les mécanismes de déformations de la couche nanocristalline sont assez mal compris. La densité élevée des joints de grains dans cette couche change radicalement la réponse mécanique par rapport à des grains de taille micrométrique. Pour ces raisons, la dynamique moléculaire a été utilisée pour exploiter les mécanismes de déformations des matériaux métalliques nanocristallins à l'échelle atomique.

Dans la première partie de cette thèse, nous avons développé une nouvelle méthode de génération des échantillons numériques nanocristallins par fusion-refroidissement d'un monocristal.

Dans une deuxième partie, nous avons étudié l'effet de la taille des grains sur les propriétés mécaniques du cuivre FCC et d'une forme cristalline du titane (α-Ti HCP) nanocristallins. Les mécanismes de déformations de ces matériaux ont été étudiés et caractérisés à l'échelle atomique, en lien avec les propriétés mécaniques. Finalement, l'influence du taux de déformation sur la réponse mécanique du cuivre nanocristallin a été étudiée.

Mots clés : dynamique moléculaire – matériaux nanostructurés – dislocations dans les métaux – plasticité – joints de grains – matériaux, propriétés mécaniques.

Study of the Mechanical Properties of Nanocrystalline Materials by Molecular Dynamics Simulations

Surface mechanical attrition treatment (SMAT) is a type of surface treatment process widely used in industrial applications. SMAT is able to nanocrystallize the surface, and to generate a gradient of grain size along with increasing material depth, thereby combining strength and ductility. In this context, the characterization of the deformation mechanisms of each layer from the micro to the nanoscale is timely and desirable. This should lead to multiscale constitutive models able to describe accurately the mechanical behavior of the treated specimens.

The mechanical behavior of the nanocrystalline materials still not well understood. The high density of grain boundaries changes radically the mechanical response in comparison with materials containing only micro-grains. To this aim, molecular dynamics simulations (MD) have been employed in order to study the mechanical behavior of the nanocrystalline surface layer that results from SMAT at the atomic scale.

First, a new melting cooling method has been developed to generate realistic numerical initial atomic configurations for MD simulations. Secondly, the effect of the grain size on the mechanical behavior of FCC nanocrystalline Copper and HCP nanocrystalline Titanium (-Ti) has been investigated. The deformation mechanisms of these systems are explored and analyzed at the atomic level.

Finally, the strain rate dependence of the mechanical and the relaxation behavior of nanocrystalline Copper models is studied.

Keywords: molecular dynamics – nanostructured materials – dislocations in metals – plasticity – grain boundaries – materials, mechanical properties.

Thèse réalisée en partenariat entre :

Ecole Doctorale "Sciences pour l'Ingénieur"